

A three-dimensional model of skeletal muscle for physiological, pathological and experimental mechanical simulations

Ein dreidimensionales Skelettmuskel-Modell für physiologische,
pathologische und experimentelle mechanische Simulationen

DISSERTATION

zur Erlangung des akademischen Grades
Doktor-Ingenieur (Dr.-Ing.)
an der Fakultät Bauingenieurwesen
der Bauhaus-Universität Weimar

vorgelegt von
Dipl.-Ing. M.Sc. Benjamin Winkel
aus Bergen auf Rügen

Gutachter:

Prof. Dr.-Ing. habil. Carsten Könke, Bauhaus-Universität Weimar

Prof. Dipl.-Ing. Dr. techn. Christian Bucher, Technische Universität Wien

Prof. Dr. rer. nat. Olaf Ueberschär, Hochschule Magdeburg-Stendal

Tag der Disputation: 02. September 2020

Abstract

In recent decades, a multitude of concepts and models were developed to understand, assess and predict muscular mechanics in the context of physiological and pathological events. Most of these models are highly specialized and designed to selectively address fields in, e.g., medicine, sports science, forensics, product design or CGI; their data are often not transferable to other ranges of application.

A single universal model, which covers the details of biochemical and neural processes, as well as the development of internal and external force and motion patterns and appearance could not be practical with regard to the diversity of the questions to be investigated and the task to find answers efficiently. With reasonable limitations though, a generalized approach is feasible.

The objective of the work at hand was to develop a model for muscle simulation which covers the phenomenological aspects, and thus is universally applicable in domains where up until now specialized models were utilized. This includes investigations on active and passive motion, structural interaction of muscles within the body and with external elements, for example in crash scenarios, but also research topics like the verification of in vivo experiments and parameter identification.

For this purpose, elements for the simulation of incompressible deformations were studied, adapted and implemented into the finite element code `SIlang`. Various anisotropic, visco-elastic muscle models were developed or enhanced. The applicability was demonstrated on the base of several examples, and a general base for the implementation of further material models was developed and elaborated.

Kurzfassung

In den vergangenen Jahrzehnten wurde eine Vielzahl verschiedener Konzepte und Modelle entwickelt, um muskuläre Mechanik im Kontext physiologischer und pathologischer Vorgänge zu verstehen, zu bewerten und vorhersagen zu können. Aufgrund der enormen Anwendungsvielfalt - von Medizin, Trainingswissenschaften und Forensik bis hin zu Produktdesign und CGI - sind diese Modelle größtenteils hochspezialisiert. Daten, die die jeweiligen Modelle stützen, sind häufig nicht übertragbar.

Ein generalisiertes Modell, das sowohl die Simulation neurologischer und biochemischer Prozesse, als auch die Ermittlung von Texturen und externen Kraft- und Bewegungsverläufen umspannt, ist aus Effizienzgründen und vor dem Hintergrund der Diversität der Fragestellungen wenig zweckmäßig.

Das Anliegen der vorliegenden Arbeit war jedoch, ein Modell zur Muskelsimulation zu entwickeln, das die phänomenologischen Aspekte abdeckt und damit zur querschnittlichen Anwendung in Bereichen geeignet ist, in denen bislang spezialisierte, exklusive Modelle zum Einsatz kamen. Das umschließt Untersuchungen der aktiven und passiven Bewegung, der strukturdynamischen Wechselwirkungen von Muskeln innerhalb des Körpers wie auch mit externen Elementen in z.B. Crash-Szenarien, aber auch Forschungsaspekte wie die Verifikation von in-vivo Experimenten und Parameter-Identifikation.

Zu diesem Zweck wurden Elemente zur Simulation inkompressibler Deformationen sowie verschiedene Materialgesetze und Funktionen zur Muskelmodellierung entwickelt bzw. verbessert und in das Finite-Elemente-Programm SLang implementiert. Die Anwendbarkeit wurde anhand mehrerer Beispiele dokumentiert, und es wurden Grundlagen zur Implementierung weiterführender Materialformulierungen erarbeitet.

Contents

Notation	v
1 Introduction	1
1.1 Motivation	1
1.2 Aims of the present work	2
1.3 Outline of the work	2
2 Continuum mechanics	5
2.1 Continuum kinematics	5
2.1.1 Motion	5
2.1.2 Deformation measures	6
2.1.3 Time derivatives	8
2.2 Balance Laws	9
2.2.1 Conservation of mass	10
2.2.2 Balance of momentums	10
2.2.3 Kinetic energy balance and entropy	11
2.2.4 Energy conjugates	12
2.3 Constitutive Equations	12
2.3.1 Objectivity	13
2.3.2 Isotropic hyperelasticity	13
2.3.3 Transversely isotropic hyperelasticity	14
2.3.4 Alternative transversely isotropic invariant sets	15
2.3.5 General formulae for stress and elasticity tensors	17
2.3.6 Transformation of 1D laws to 3D	21
2.3.7 Hypo- and non-elastic materials	22

3	Finite Element Modeling	23
3.1	Theoretical basis	23
3.1.1	Approximations to differential equation systems	23
3.1.2	Linearization	24
3.1.3	Spatial discretization	27
3.2	Finite Elements	29
3.2.1	Voigt notation	29
3.2.2	The H1-element (UL)	30
3.2.3	Volumetric locking	31
3.2.4	The F-bar element	33
3.2.5	Inconsistent F-bar element	39
3.2.6	Reduced integration elements	41
3.2.7	Numerical tests	42
3.3	Solution techniques	46
3.3.1	Iteration procedures	47
3.3.2	Time integration	50
4	A general model of skeletal muscle	55
4.1	Properties of skeletal muscle	55
4.1.1	Muscle physiology	56
4.1.2	Contraction mechanism	56
4.1.3	Activation mechanism	58
4.1.4	Muscle geometry and force	59
4.1.5	Three-dimensional properties	61
4.2	Review and extension of straight-line models	62
4.2.1	Rheological models	62
4.2.2	Biophysical models	71
4.3	History of three-dimensional muscle models	72
4.4	Proposed modeling approach	74
4.4.1	Proposed passive constitutive equations	74
4.4.2	Proposed active constitutive equations	76
4.4.3	Complementary: aponeurosis constitutive equations	76
4.5	Validation example: Squid tentacle strike	77
4.5.1	Introduction	77
4.5.2	Model derivation	79

5	Model application	87
5.1	Investigations on M. soleus of rattus norvegicus	87
5.1.1	Introduction	87
5.1.2	Data base	88
5.1.3	Model derivation	90
5.1.4	Computation	94
5.1.5	Results, optimization and evaluation	94
5.1.6	Summary	99
5.2	Muscle activation as means of injury prevention	100
5.2.1	Introduction	100
5.2.2	Background	101
5.2.3	Sample object: Thorax	102
5.2.4	Model derivation	103
5.2.5	Computation	107
5.2.6	Results and evaluation	107
5.2.7	Summary and discussion	112
6	Conclusion	113
6.1	Summary	113
6.2	Discussion and outlook	114
	Appendix	115
A.1	Mathematical preliminaries	115
A.1.1	Tensor calculus	115
A.1.2	Numerical integration	125
A.2	Complementary continuum mechanics	125
A.2.1	Transformation and deformation	126
A.2.2	Objectivity	127
A.2.3	Invariants addendum	131
A.2.4	Material tensor addendum to section 2.3.5	133
A.3	Finite element addendum	136
A.3.1	Linear elements for finite incompressibility	136
A.3.2	Variational base for mixed element formulations	139
	References	152

Notation

This section provides a list of the operators, symbols and abbreviations used in this work. Items which occur only once in the main text or only in the appendix are omitted here and explained there. Components of higher order entities, distinguishable by italic font style and italic indeces, are omitted as well. (Indeces in regular font style are abbreviations.) Continuum mechanics symbols are re-used in the FEM sections. If mistakable, they are marked by underlines or by a hat in the main text, but not listed here either.

Symbols

Continuum mechanics

δ_j^i	Kronecker symbol
λ	stretch
ρ	density
θ	modified dilatation
ε_{ijk}	Levi-Cevit� symbol
$\mathcal{B}, \mathcal{V}, \mathcal{S}$	correlating domains: body, volume, surface
\mathcal{P}	material point in \mathcal{B}
a	area (reference configuration: A)
e	error measure
f	function
J	dilatation
m	mass
s	distance (reference configuration: S)
t	time
v	volume (reference configuration: V)
W	work, strain energy function

ϵ	engineering strain
σ	Cauchy stress
τ	Kirchhoff stress
\mathbf{b}	force per unit mass
\mathbf{C}	right Cauchy-Green tensor
\mathbf{c}	left Cauchy-Green tensor
\mathbf{d}	rate of deformation
\mathbf{E}	Green-Lagrange strain
\mathbf{e}	Almansi strain
\mathbf{e}_i	right-handed Cartesian base vector
\mathbf{F}	deformation gradient
f	tensor valued function
\mathbf{g}_i	arbitrary right-handed base vector (reference configuration: \mathbf{G}_i)
\mathbf{I}	identity tensor
\mathbf{n}	normalized direction vector (reference configuration: \mathbf{N})
\mathbf{P}	1st Piola-Kirchhoff stress
\mathbf{S}	2nd Piola-Kirchhoff stress
\mathbf{t}	force per unit surface, traction vector (reference configuration: \mathbf{T})
\mathbf{u}	displacement vector
\mathbf{v}	material velocity vector
\mathbf{x}	position vector (reference configuration: \mathbf{X})
\mathbb{C}	elasticity tensor (material notation)
\mathbb{c}	elasticity tensor (spatial notation)
\mathbb{V}	viscoelastic tensor (material notation)
\mathbb{v}	viscoelastic tensor (spatial notation)

Finite element method

\mathbf{b}_l	linear strain-displacement matrix
\mathbf{b}_{nl}	nonlinear strain-displacement matrix
\mathbf{D}	damping matrix
\mathbf{f}	force vector
\mathbf{h}	shape function matrix
\mathbf{J}	Jacobian
\mathbf{K}	stiffness matrix

\mathbf{K}_l	linear stiffness matrix
\mathbf{K}_{nl}	nonlinear stiffness matrix
\mathbf{K}_v	viscous stiffness matrix
\mathbf{M}	mass matrix

Operators

$\det \bullet$	determinant of \bullet
$\operatorname{div} \bullet$	divergence of \bullet
$\operatorname{Exp} \bullet$	natural exponentiation of \bullet
$\operatorname{grad} \bullet$	gradient of \bullet
$\ln \bullet$	natural logarithm of \bullet
$\operatorname{sym} \bullet$	symmetric part of \bullet
$\operatorname{tr} \bullet$	trace of \bullet
$\Phi_\star \bullet$	push-forward of \bullet
$\Phi^\star \bullet$	pull-back of \bullet
\bullet_0	quantity \bullet in reference configuration
$\bullet_{,\star}$	derivative of \bullet with respect to \star
$\bullet_{i,j}$	derivative of component i of \bullet with respect to X_j
$\bullet_{i;j}$	derivative of component i of \bullet with respect to x_j
$\dot{\bullet}$	time derivative of \bullet
$\mathring{\bullet}$	Lie derivative of \bullet
$\delta \bullet$	variation of \bullet
$\mathring{\delta} \bullet$	Lie variation of \bullet
$\Delta \bullet$	linearized increment of \bullet
\bullet^T	transposition of \bullet
$ \bullet $	absolut value of \bullet
$\ \bullet\ $	Euclidean norm of \bullet

For tensor operators with more than one argument refer to sections A.1.1.2 and A.1.1.3.

Abbreviations

AIS	Abbreviated Injury Scale
BMI	Body Mass index

CAS	Computer Assisted Surgery
CE	Contractile Element
CGI	Computer-Generated Imagery
CSA	Cross-Sectional Area
FEA	Finite Element Analysis
FEM	Finite Element Method
ISM	Institute of Structural Mechanics
H1	Hexhedron w/ 1st order interpolation
MRT	Magnetic Resonance Tomography
PE	Parallel Element
PMHS	Post-Mortal Human Subject
RMS	Root Mean Square
SE	Serial Element
SLM	Straight-Line Models
SRI	Selective Reduced Integration
T1	Tetrahedron w/ 1st order interpolation
TL	Total Lagrangian
UL	Updated Lagrangian
URI	Uniform Reduced Integration
VHP	Virtual Human Project

Chapter 1

Introduction

1.1 Motivation

Amongst the many fields of mechanics, biomechanics is one of the most exciting and gratifying domains of study. This is due to the vast variety of applications, the inherent optimization which drives natural design, and the immensely complex processes involved in the control and generation of animate mobility. Not least, this is also due to every researcher's personal life-long experience with the topic. However, due to limited reproducibility and the ethical implications of in vivo experiments, biomechanics is in many ways also more reliant on simulation-based research than other fields of mechanics.

Even in the very specific field of muscle simulation, with special emphasis on the muscle's unique capability to generate force and motion, a multitude of unrelated models have been developed to address topics in even more specific sub-domains. Examples are branches in neurology (paths and patterns to initiate, perceive, control and inhibit motion), biochemistry (muscle energy provision, conversion, depletion, exhaustion), pathology and medicine (malfunctions of any of the aforementioned, and potential ways to cure them), sports science (performance optimization and conditioning), ergonomics, forensics, computer-generated imagery (CGI), and computer-assisted surgery (CAS).

An universal approach to cover all these fields in one type of model will not be feasible in the foreseeable future. But the desirable consolidation on the modeling side is viable. This is evident from recent publications, and will be substantiated by the work at hand for the field of phenomenological three-dimensional modeling.

1.2 Aims of the present work

The objective of this work is to develop a simulation framework for three-dimensional (3D) modeling of skeletal muscle, universally applicable where body motion, movement, force generation or specific aspects of body composition are of interest. Processes on molecular level, i.e. neurological and biochemical aspects, will be disregarded or averaged appropriately in order to simulate phenomenological processes at reasonable efficiency.

Based on state-of-the-art parametric one-dimensional (1D) descriptions of muscle behavior and in conjunction with anisotropic hyperelastic 3D material formulations, a stimule visco-elastic muscle model shall be developed, and embedded in an appropriate finite element code. The deduced theoretical base as well as the implementation has to provide the flexibility to adapt to new or different material formulations, governing variables and parameter sets.

Application examples shall validate concept and implementation, but also by themselves provide meaningful results.

1.3 Outline of the work

This thesis is structured as follows:

Chapter 2 introduces the reader to the continuum mechanic concepts, notation and fundamentals which are required for subsequent parts of the work. Generalized formula for the implementation of arbitrary invariant-based materials are derived and documented.

Chapter 3 introduces the finite element method in general, and documents specifically the development and implementation of elements for simulating incompressible hyperelastic structures. Benchmarks and comparison for several such elements are provided.

Chapter 4 starts with an introduction to skeletal muscle, its properties and the various established approaches towards modeling. On this basis, specific enhancements are presented, the fundamental ideas of the proposed modeling approach are explained, and its development and implementation is elaborated on. The simulation of a squid tentacle strike is used to validate this work's model.

Chapter 5 comprises two studies which utilize the previously implemented elements and models. a) Reproducing the contraction of a rat's soleus muscle, and a subsequent material parameter identification. b) Assessment of the rib fracture potential during a car front-collision depending on the activation state of the anterior thoracic muscles.

The work is concluded in chapter 6 with summary and outlook. Beyond that, the appendix provides helpful complementary information which is considered to be outside the core scope of the main text.

Chapter 2

Continuum mechanics

The present work deals primarily with mechanical aspects of muscle modeling. For better accessibility, this chapter provides an introduction to the utilized continuum mechanical approach and to the nomenclature used. Consider section A.2 for more details, and the textbooks of Holzapfel [2000] and Weichert and Başar [2000] for more in-depth information on the topic.

Continuum mechanics is based on the postulation of material as continuously distributed in a body's domain, thereby neglecting its distinctive composition below a certain threshold scale. Its basic purpose is to describe the internal mechanical behavior of bodies when interacting or subjected to a dynamic set of boundary conditions. Since kinematic and material properties are averaged phenomenologically, the findings are valid only for structures that are large in comparison to their mechanically significant components. The structures considered in the course of this work comply with this condition.

2.1 Continuum kinematics

This section introduces briefly the theory of deformation of solid bodies and provides the definition of several stretch, strain and deformation rate measures.

2.1.1 Motion

The material body \mathcal{B} be a continuous set of elements \mathcal{P} called material point or particle. In a reference configuration \mathcal{B}_0 , selected arbitrarily, any \mathcal{P} is associated with its coordinates $\mathbf{X} = X^i \mathbf{e}_i$ in a Cartesian base system $\{\mathbf{e}_i\}$. These X^i are referred to as Lagrangian,

referential or material coordinates. (Variables and operators in the reference configuration will be denoted by upper-case letters or marked by the index 0.)

In a configuration \mathcal{B}_t , the point $\mathbf{x} = x^i \mathbf{e}_i$ marks the location of a material element \mathcal{P} at the time t . These x^i are Eulerian or spatial coordinates and this state is labeled current or deformed configuration. The deformation of \mathcal{B} may be considered as a continuous sequence of such configurations with the time-dependent one-to-one mapping

$$\mathbf{x} = \mathbf{x}(\mathbf{X}, t) = \mathbf{X} + \mathbf{u}(\mathbf{X}, t). \quad (2.1)$$

At $t = 0$ current and reference configuration are identical.

The displacement \mathbf{u} in (2.1) is given in the so-called material or Lagrangian description, where material coordinates serve as independent variables. When instead spatial coordinates are considered as independent, i.e. $\mathbf{u}(\mathbf{x}, t) = \mathbf{x} - \mathbf{X}(\mathbf{x}, t)$, it is referred to as spatial or Eulerian description.

In the former case, X^i are utilized as convective coordinates, uniquely identifying any $\mathcal{P} \in \mathcal{B}$ by the same values in any deformation state. They also constitute a valid specification of general curvilinear coordinates. As detailed in (A.50), the corresponding co- and contravariant base systems $\{\mathbf{g}_i\}$ and $\{\mathbf{g}^i\}$ of a deformed configuration are then defined by

$$\mathbf{g}_i = \frac{\partial \mathbf{x}}{\partial X^i} = \frac{\partial x^j}{\partial X^i} \mathbf{e}_j \quad \text{and} \quad \mathbf{g}^i = \frac{\partial X^i}{\partial x_j} \mathbf{e}^j. \quad (2.2)$$

For the reference configuration, this corresponds to¹

$$\mathbf{G}_i = \mathbf{e}_i = \mathbf{e}^i = \mathbf{G}^i. \quad (2.3)$$

When a tensor's base is given as either \mathbf{G}_i , \mathbf{g}_i or both, it is accordingly labeled material, spatial or two-point tensor.

2.1.2 Deformation measures

Based on the transformation rules for vectorial line elements (A.50), the deformation gradient \mathbf{F} can be established as a second-order tensor to relate the bases \mathbf{G}_i and \mathbf{g}_i .

$$\mathbf{F} = \mathbf{g}_i \otimes \mathbf{G}^i = \frac{\partial x^i}{\partial X^j} \mathbf{e}_i \otimes \mathbf{e}_j = \frac{\partial \mathbf{x}}{\partial \mathbf{X}} = \text{Grad } \mathbf{x} \quad (2.4)$$

¹ The rules for index positioning may be relaxed in Cartesian systems due to the identity of co- and contravariant base vectors.

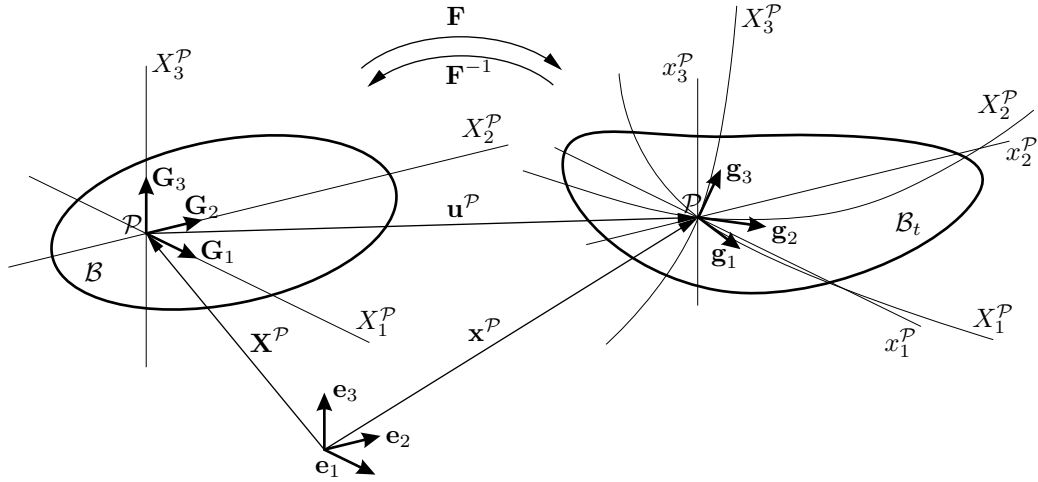


Figure 2.1: Deformation from reference to current configuration. Notational anomaly: X_i^P marks a line on which points differ only in their respective X_i coordinates from point P .

Hence \mathbf{F} maps an arbitrary infinitesimal line element from reference to current configuration and describes its rotation and deformation during the motion of \mathcal{B} . The mapping of infinitesimal area (dA) and volume elements (dV) may be deduced from A.1.1.2:

$$\begin{aligned} d\mathbf{x} &= \mathbf{F} d\mathbf{X} \\ \mathbf{n}_a da &= J \mathbf{F}^{-T} \mathbf{N}_A dA \\ dv &= J dV \end{aligned} \tag{2.5}$$

where \mathbf{N}_A and \mathbf{n}_a are the unit normal vectors to dA and da , respectively. The Jacobian determinant $J = \det \mathbf{F}$ will henceforth denote the dilatation. Inversed and transposed forms of \mathbf{F} are quoted in A.2.

Based on the stretch $\lambda = ds/dS$ with $ds = |d\mathbf{x}|$ and $dS = |d\mathbf{X}|$, a variety of strain functions $f(\lambda)$ may be defined as measures for the elongation of a material line element $d\mathbf{X}$. The approach

$$f(\lambda) = \begin{cases} \frac{1}{n}(\lambda^n - 1) & \text{for } n \neq 0 \\ \ln \lambda & \text{for } n = 0 \end{cases} \tag{2.6}$$

fulfills the characteristic conditions $f(1) = 0$, $f_{,\lambda}(1) = 1$, and $f_{,\lambda}(\lambda) > 0$. The class of Lagrangian strain tensors is analogously defined, by substituting λ in (2.6) with the stretch tensor \mathbf{U} that follows from a polar decomposition of \mathbf{F} (see A.71). For an even-numbered n the rotational influence vanishes and therefore the decomposition becomes obsolete. E.g.,

the Green-Lagrange strain tensor \mathbf{E} and the Almansi strain tensor \mathbf{e} are derived with $n = 2$ and $n = -2$ as

$$\begin{aligned}\mathbf{E} &= \frac{1}{2}(\mathbf{F}^T \mathbf{F} - \mathbf{I}) = \frac{1}{2}(\mathbf{g}_i \cdot \mathbf{g}_j - \mathbf{G}_i \cdot \mathbf{G}_j) \mathbf{G}^i \otimes \mathbf{G}^j \\ \mathbf{e} &= \frac{1}{2}(\mathbf{I} - \mathbf{F}^{-T} \mathbf{F}^{-1}) = \frac{1}{2}(\mathbf{g}_i \cdot \mathbf{g}_j - \mathbf{G}_i \cdot \mathbf{G}_j) \mathbf{g}^i \otimes \mathbf{g}^j.\end{aligned}\tag{2.7}$$

Obviously, both feature identical components, although with respect to different bases. The component description with respect to the Cartesian base $\mathbf{e}_i \otimes \mathbf{e}_j$ (by 2.1 and 2.2) reads

$$\begin{aligned}E_{ij} &= \frac{1}{2}(u_{i,j} + u_{j,i} + u_{k,i} u_{k,j}) \\ e_{ij} &= \frac{1}{2}(u_{i,j} + u_{j,i} - u_{k,i} u_{k,j})\end{aligned}\tag{2.8}$$

with $u_{i,j} = \partial u_i / \partial X^j$ and $u_{i,j} = \partial u_i / \partial x^j$. This notation will be kept within the scope of this work. Also, when not explicitly stated otherwise, tensors in indicial notation will always refer to a right-handed Cartesian base with indices in alphabetical order.

Both strains \mathbf{E} and \mathbf{e} represent the squared length change of a convective element $d\mathbf{X}$ in reference and current configuration.

$$ds^2 - dS^2 = 2 d\mathbf{X} \mathbf{E} d\mathbf{X} = 2 d\mathbf{x} \mathbf{e} d\mathbf{x}\tag{2.9}$$

As closely related deformation measures, the right Cauchy-Green tensor \mathbf{C} and left Cauchy-Green tensor \mathbf{c} , sometimes also denoted Finger tensor, are established as

$$\begin{aligned}\mathbf{C} &= \mathbf{F}^T \mathbf{F} = \mathbf{g}_i \cdot \mathbf{g}_j \mathbf{G}^i \otimes \mathbf{G}^j \\ \mathbf{c} &= \mathbf{F} \mathbf{F}^T = \mathbf{G}^i \cdot \mathbf{G}^j \mathbf{g}_i \otimes \mathbf{g}_j.\end{aligned}\tag{2.10}$$

For sufficiently small deformations, any strain may be reduced to the so-called engineering strain $\epsilon_{ij} = 1/2(u_{i,j} + u_{j,i})$.

2.1.3 Time derivatives

The material time derivative $\dot{\mathbf{f}}$ is obtained by differentiating any field variable \mathbf{f} with respect to time t , holding the material coordinates \mathbf{X} fixed. Therefore, if \mathbf{f} is given as

$f(\mathbf{X}, t)$ the material time derivative equals the partial time derivative.

$$\dot{f} = \frac{df}{dt} = \frac{\partial f(\mathbf{X}, t)}{\partial t} = \dot{f}_{ij} \mathbf{G}^i \otimes \mathbf{G}^j \quad (2.11)$$

If f is provided in spatial description as $f(\mathbf{x}, t)$ the material time derivative is

$$\dot{f} = \frac{df}{dt} = \text{grad } f \mathbf{v} + \frac{\partial f}{\partial t} = f_{ij}(\dot{\mathbf{g}}^i \otimes \mathbf{g}^j + \mathbf{g}^i \otimes \dot{\mathbf{g}}^j) + \dot{f}_{ij} \mathbf{g}^i \otimes \mathbf{g}^j \quad (2.12)$$

where

$$\mathbf{v} = \dot{\mathbf{x}} = \dot{\mathbf{u}} \quad (2.13)$$

denotes the material velocity vector. The last element in (2.12), $\dot{f}_{ij} \mathbf{g}^i \otimes \mathbf{g}^j$, is labeled Lie-derivative \mathring{f} , the time derivative of a spatial variable considering the deformed basis constant. In analogy to (2.9) its relevance becomes more obvious:

$$\frac{d}{dt}(ds^2 - dS^2) = 2 d\mathbf{X} \dot{\mathbf{E}} d\mathbf{X} = 2 d\mathbf{x} \dot{\mathbf{e}} d\mathbf{x}. \quad (2.14)$$

The Lie-derivative of a spatial tensor can be obtained by subsequent pull-back (Φ^*) , derivative, and push-forward (Φ_*) operations, written as

$$\mathring{f} = \Phi_* \frac{d}{dt} (\Phi^* f). \quad (2.15)$$

See (A.68) for the operator rules. For a covariant tensor $\mathbf{f} = f_{ij} \mathbf{g}^i \otimes \mathbf{g}^j$ this leads to

$$\mathring{f} = \dot{f} - \text{grad } \mathbf{v} f - f (\text{grad } \mathbf{v})^T \quad (2.16)$$

with the spatial velocity gradient $\text{grad } \mathbf{v}$. Its symmetric part - the rate of deformation tensor \mathbf{d} - is identical to the Lie-derivative of the Almansi strain tensor.

$$\mathbf{d} = \text{sym}(\text{grad } \mathbf{v}) = \dot{\mathbf{e}} \quad (2.17)$$

2.2 Balance Laws

The balance equations for mass, linear and angular momentum, energy and entropy provide the essential framework to thermodynamics and rule a body's behavior in a given

environment. They apply to the body as a whole, but, presuming continuity and sufficient smoothness of the considered fields, they might as well be utilized on subdomains $\tilde{\mathcal{B}}$, or be transformed into field equations which are valid at every material point within the body. Subsequently, they are summarized in the latter, local form and their consequences are briefly discussed.

2.2.1 Conservation of mass

The mass m of $\tilde{\mathcal{B}}$ remains unchanged during arbitrary deformations of \mathcal{B} . This may be written as

$$m(\tilde{\mathcal{B}}, t) = \int_{\mathcal{V}} dm = \int_{\mathcal{V}} \rho \, dv = \text{const.} \quad (2.18)$$

with $\tilde{\mathcal{B}}$ occupying a region \mathcal{V} enclosed by the smooth boundary surface \mathcal{S} . v and ρ denote current volume and density¹. One equivalent local form

$$\rho_0/J = \rho \quad (2.19)$$

follows from (2.5). Applying $\dot{J} = J \operatorname{div} \mathbf{v}$ (A.73) to the time derivative of (2.19) leads directly to (2.20), known as continuity equation.

$$\dot{\rho} + \rho \operatorname{div} \mathbf{v} = 0 \quad (2.20)$$

2.2.2 Balance of momentums

The balance of momentum equations describe the equilibrium relations between an external force on $\tilde{\mathcal{B}}$ and the rate of change of $\tilde{\mathcal{B}}$'s linear momentum (2.21), and between an external moment and the rate of change of $\tilde{\mathcal{B}}$'s angular momentum (2.22).

$$\frac{d}{dt} \int_{\mathcal{V}} \rho \mathbf{v} \, dv = \int_{\mathcal{S}} \mathbf{t} \, da + \int_{\mathcal{V}} \rho \mathbf{b} \, dv \quad (2.21)$$

$$\frac{d}{dt} \int_{\mathcal{V}} \mathbf{x} \times \rho \mathbf{v} \, dv = \int_{\mathcal{S}} \mathbf{x} \times \mathbf{t} \, da + \int_{\mathcal{V}} \mathbf{x} \times \rho \mathbf{b} \, dv \quad (2.22)$$

¹ The notational inconsistency between velocity vector \mathbf{v} and infinitesimal volumes dv and dV is not resolved here.

Herein, $\tilde{\mathcal{B}}$ is subjected to \mathbf{b} , volume forces per unit mass, and to \mathbf{t} , contact forces per unit surface area.

By means of Cauchy's stress theorem (2.23), the Cauchy stress tensor $\boldsymbol{\sigma} = \sigma^{ij} \mathbf{g}_i \otimes \mathbf{g}_j$ is established, which relates an infinitesimal surface area $da \subset \mathcal{S}$, identified by its unit normal vector \mathbf{n} , to the traction vector acting upon it.

$$\mathbf{t}(\mathbf{x}, t, \mathbf{n}) = \boldsymbol{\sigma}(\mathbf{x}, t) \mathbf{n} \quad (2.23)$$

Applying (2.23) and the divergence theorem (A.72), the Cauchy equation of motion is obtained as the local form of (2.21):

$$\rho \dot{\mathbf{v}} = \operatorname{div} \boldsymbol{\sigma} + \rho \mathbf{b}. \quad (2.24)$$

The second term in (2.22) may be transformed in accordance with the divergence theorem as well, providing

$$\int_{\mathcal{S}} \mathbf{x} \times \mathbf{t} \, da = \int_{\mathcal{V}} \mathbf{x} \times \operatorname{div} \boldsymbol{\sigma} + \boldsymbol{\varepsilon} : \boldsymbol{\sigma}^T \, dv \quad (2.25)$$

using $\boldsymbol{\varepsilon}$ the Levi-Cevita symbol (A.8). With this substitution, a comparison of the local form of (2.22) with (2.24) then leads to $\boldsymbol{\varepsilon} : \boldsymbol{\sigma} = \mathbf{0}$. Thus, the main consequence of (2.22) is the symmetry of the Cauchy stress tensor $\boldsymbol{\sigma}$.

2.2.3 Kinetic energy balance and entropy

Equation (2.26) is obtained after some transformations through expansion of (2.24) with the velocity \mathbf{v} , and application of the divergence theorem. It describes the rate of change of kinematic energy to equal the power of external surface and volume forces and the stress power. By (2.17), the latter is determined to $\boldsymbol{\sigma} : \operatorname{grad} \mathbf{v} = \boldsymbol{\sigma} : \mathbf{d}$.

$$\frac{d}{dt} \int_{\mathcal{V}} \frac{1}{2} \rho \mathbf{v} \mathbf{v} \, dv = \int_{\mathcal{S}} \mathbf{t} \mathbf{v} \, da + \int_{\mathcal{V}} \rho \mathbf{b} \mathbf{v} \, dv + \int_{\mathcal{V}} \boldsymbol{\sigma} : \mathbf{d} \, dv \quad (2.26)$$

This energy conservation law corresponds to a reduced form of the first law of thermodynamics, neglecting heat flux and generation.

According to the second law of thermodynamics, the entropy of a closed thermodynamic system can never decrease. A positive entropy gradient marks the irreversibility of an energy converting process, whereas a null-gradient defines reversible processes. The

latter precludes any energy dissipation, and thus provides the basis for elastic constitutive equations in section 2.3.

2.2.4 Energy conjugates

In (2.23), the Cauchy stress tensor $\boldsymbol{\sigma}$ has been introduced as the mapping of a unit normal vector $\mathbf{n}(da)$ to the Cauchy stress vector \mathbf{t} , where $\mathbf{t} da$ is the force acting upon the surface element da . As each of these quantities refers to the current physical configuration, $\boldsymbol{\sigma}$ is also known as true stress. Often though, it is convenient to use stresses which reference other configurations, e.g. the first or second Piola-Kirchhoff stresses \mathbf{P} and \mathbf{S} , or the Kirchhoff stress $\boldsymbol{\tau}$.

$$\begin{aligned} \mathbf{P} &= J\boldsymbol{\sigma}\mathbf{F}^{-T} &= \boldsymbol{\tau}\mathbf{F}^{-T} &= \mathbf{F}\mathbf{S} &= P^{ij}\mathbf{G}_i \otimes \mathbf{G}_j \\ \mathbf{S} &= J\mathbf{F}^{-1}\boldsymbol{\sigma}\mathbf{F}^{-T} = \mathbf{F}^{-1}\boldsymbol{\tau}\mathbf{F}^{-T} = \mathbf{F}^{-1}\mathbf{P} &= S^{ij}\mathbf{G}_i \otimes \mathbf{G}_j \\ \boldsymbol{\tau} &= J\boldsymbol{\sigma} &= \mathbf{P}\mathbf{F}^T &= \mathbf{F}\mathbf{S}\mathbf{F}^T = \tau^{ij}\mathbf{g}_i \otimes \mathbf{g}_j \end{aligned} \quad (2.27)$$

The material traction vector corresponding to (2.23) reads

$$\mathbf{T} = \mathbf{t} \frac{da}{dA} = \mathbf{P} \mathbf{N} \quad (2.28)$$

with the undeformed infinitesimal surface element dA and its unit normal \mathbf{N} .

Equivalent to $\boldsymbol{\sigma}$ in (2.26), the above and other stress tensors might be used to describe the stress power, as long as the related deformation rate is chosen accordingly. The following combinations are energy conjugated:

$$J\boldsymbol{\sigma} : \mathbf{d} = \boldsymbol{\tau} : \mathbf{d} = \mathbf{P} : \dot{\mathbf{F}} = \mathbf{S} : \dot{\mathbf{E}}. \quad (2.29)$$

All of these terms correspond to the same unit volume.

2.3 Constitutive Equations

The aforementioned kinematic and balance equations do not reflect the dependence of a body's deformation and stress state on its material properties. In order to uniquely describe the body's behavior under given boundary conditions, complementary equations are required, which link stresses to kinematic and possibly other field quantities. They are commonly denoted as constitutive equations or material laws.

2.3.1 Objectivity

An essential requirement for any material description is its compliance with the principle of material objectivity. In the present context, it translates to the deformation process being frame-invariant, i.e. energy conversion and dissipation have to be independent of the observer.

This is usually achieved by utilizing invariants of energy conjugated strain and stress tensors. In engineering literature though, objectivity is often attributed to certain stress and strain tensors alone. Some authors [Holzapfel 2000, Ogden 1997] distinguish Lagrangian, Eulerian and two-point objectivity depending on the transformation behavior of the respective tensors. Other sources refer exclusively to tensors of the first [Altenbach and Altenbach 1994, Mase and Mase 1999, Greve 2003] or of the second kind [Hill 1978] as “objective tensors”. As any true tensor is frame-indifferent by definition, it appears advisable to refrain from the use of that term. See appendix A.2.2 for additional remarks.

2.3.2 Isotropic hyperelasticity

Hyperelastic materials are a class of elastic materials characterized by the existence of a strain-energy function $W = W(\mathbf{F})$, which is defined per unit reference volume [Truesdell and Noll 1965]. Considering (2.26), this also implies a bijective correlation between deformation and stress. Since neither stress nor strain-energy must be influenced by the rotational part of \mathbf{F} , they might as well be expressed in terms of invariants of Cauchy-Green tensors or the corresponding strains (see section 2.1.2). From $\dot{W} = \mathbf{S} : \dot{\mathbf{E}}$, the unspecific constitutive equations are deduced.

$$\mathbf{S} = \frac{\partial W}{\partial \mathbf{E}} = 2 \frac{\partial W}{\partial \mathbf{C}} \quad (2.30)$$

$$\boldsymbol{\tau} = 2 \frac{\partial W}{\partial \mathbf{c}} \mathbf{c} = 2 \mathbf{c} \frac{\partial W}{\partial \mathbf{c}} \quad (2.31)$$

A generalized representation of the stress tensors is conveniently based on the principal invariants of \mathbf{C} , for which also applies $I_i(\mathbf{C}) = I_i(\mathbf{c})$.

$$\begin{aligned} I_1(\mathbf{C}) &= \text{tr } \mathbf{C} = \text{tr } \mathbf{c} \\ I_2(\mathbf{C}) &= \frac{1}{2} \left((\text{tr } \mathbf{C})^2 - \text{tr } \mathbf{C}^2 \right) = \frac{1}{2} \left((\text{tr } \mathbf{c})^2 - \text{tr } \mathbf{c}^2 \right) \\ I_3(\mathbf{C}) &= \det \mathbf{C} = \det \mathbf{c} = J^2 \end{aligned} \quad (2.32)$$

See (A.37) and (A.42) for invariant deduction and differentiation. From (2.30) follows

$$\mathbf{S} = 2 \left(\left(\frac{\partial W}{\partial I_1} + I_1 \frac{\partial W}{\partial I_2} \right) \mathbf{I} - \frac{\partial W}{\partial I_2} \mathbf{C} + I_3 \frac{\partial W}{\partial I_3} \mathbf{C}^{-1} \right) \quad (2.33)$$

$$\boldsymbol{\tau} = 2 \left(I_3 \frac{\partial W}{\partial I_3} \mathbf{I} + \left(\frac{\partial W}{\partial I_1} + I_1 \frac{\partial W}{\partial I_2} \right) \mathbf{c} - \frac{\partial W}{\partial I_2} \mathbf{c}^2 \right). \quad (2.34)$$

The time derivative of equation (2.30) provides the definition of a fourth-order elasticity tensor \mathbb{C} which relates stress and strain rates in the material description.

$$\dot{\mathbf{S}} = \mathbb{C} : \dot{\mathbf{E}} \quad \text{with} \quad \mathbb{C} = \frac{\partial^2 W}{\partial \mathbf{E} \partial \mathbf{E}} = 4 \frac{\partial^2 W}{\partial \mathbf{C} \partial \mathbf{C}} \quad (2.35)$$

\mathbb{C} is also referred to as the stress-strain tangent modulus, since $\dot{\mathbf{S}} = (\partial \mathbf{S} / \partial \mathbf{E}) : \dot{\mathbf{E}}$. The spatial elasticity tensor \mathbb{c} is defined analogously to (2.35), but might as well be derived as push-forward of \mathbb{C} .

$$\dot{\boldsymbol{\tau}} = \mathbb{c} : \dot{\mathbf{e}} \quad \text{with} \quad \mathbb{c} = \boldsymbol{\Phi}_* \mathbb{C} = 4 \mathbf{c} \frac{\partial^2 W}{\partial \mathbf{c} \partial \mathbf{c}} \quad (2.36)$$

Invariant-based closed representations of \mathbb{C} corresponding to the form of (2.33) are provided in 2.3.4.

2.3.3 Transversely isotropic hyperelasticity

Fiber reinforcement is an ubiquitous measure in biological and artificial structures to withstand very specific loading conditions. A non-homogeneous fiber distribution causes anisotropy, i.e. directional dependence of mechanical properties. The particular case of exclusively parallel fiber orientation results in transverse isotropy, with isotropic material behavior orthogonal to the distinguished direction \mathbf{N} . During the deformation of the body, the fiber direction changes according to

$$\lambda \mathbf{n} = \mathbf{F} \mathbf{N} \quad (2.37)$$

with fiber stretch λ and normalized fiber directions \mathbf{N} and \mathbf{n} in reference and current configuration, respectively. In order to incorporate the directional dependence into the

work equation, it is necessary to define two further deformation invariants, e.g.:

$$\begin{aligned} I_4 &= I_4(\mathbf{C}, \mathbf{N}) = \mathbf{N}\mathbf{C}\mathbf{N} = \lambda \mathbf{n} \cdot \lambda \mathbf{n} = \lambda^2 \\ I_5 &= I_5(\mathbf{C}, \mathbf{N}) = \mathbf{N}\mathbf{C}^2\mathbf{N} = \lambda^2 \mathbf{n}\mathbf{c}\mathbf{n}. \end{aligned} \quad (2.38)$$

The strain energy function W of any hyperelastic, transversely isotropic material is describable by means of five invariants (see (A.37) to (A.39)). Following an equipresence hypothesis, the work equations for isotropic matrix behavior and one-dimensional fiber description can be superposed: $W = W_{\text{mat}} + W_{\text{fib}}$. Accordingly, the right hand sides of equations (2.33) and (2.34) are extended by

$$2 \left(\frac{\partial W}{\partial I_4} \mathbf{N} \otimes \mathbf{N} + \frac{\partial W}{\partial I_5} (\mathbf{N} \otimes \mathbf{C}\mathbf{N} + \mathbf{N}\mathbf{C} \otimes \mathbf{N}) \right) \quad (2.39)$$

and

$$2 \left(I_4 \frac{\partial W}{\partial I_4} \mathbf{n} \otimes \mathbf{n} + I_4 \frac{\partial W}{\partial I_5} (\mathbf{n} \otimes \mathbf{c}\mathbf{n} + \mathbf{n}\mathbf{c} \otimes \mathbf{n}) \right), \quad (2.40)$$

respectively.

Note that there is no equivalence between the newly introduced invariants with respect to either right or left Cauchy-Green tensor: $I_i = I_i(\mathbf{C}, \mathbf{N}) \neq I_i(\mathbf{c}, \mathbf{n})$ for $i = 4, 5$.

2.3.4 Alternative transversely isotropic invariant sets

The given set of principal invariants may be inefficient for some material formulations, and it has one specific flaw when it comes to experimental verification: The determination of constitutive parameters is very difficult as, for example, an isochore fiber stretch perturbs I_1, I_2, I_4 and I_5 , and a change in dilatation affects all five invariants. Only the latter might be circumvented by using the dilatation-adjusted modified set \hat{I}_i , and except for I_3 , \hat{I}_3 and I_4 none has an apparent physical meaning¹. Here \hat{I}_i are defined in terms of principal invariants:

$$\hat{I}_1 = I_1 I_3^{-\frac{1}{3}} \quad \hat{I}_2 = I_2 I_3^{-\frac{2}{3}} \quad \hat{I}_3 = I_3^{\frac{1}{2}} = J \quad \hat{I}_4 = I_4 I_3^{-\frac{1}{3}} \quad \hat{I}_5 = I_5 I_3^{-\frac{2}{3}}. \quad (2.41)$$

¹ In most publications, the invariants \hat{I}_i are marked by an overbar. This is omitted here in order to avoid confusion with the \mathbf{F} -notation in 3.2.4.

The invariant set proposed by Ehret et al. [2011] comprises an \tilde{I}_5 which is a measure for the change of the cross-fiber cross-sections.

$$\begin{aligned}
\tilde{I}_1 &= \text{tr } \mathbf{C} = \text{tr } \mathbf{c} \\
\tilde{I}_2 &= \text{tr } \mathbf{C}^{-1} = \text{tr } \mathbf{c}^{-1} \\
\tilde{I}_3 &= \det \mathbf{C} = \det \mathbf{c} = J^2 \\
\tilde{I}_4 &= \mathbf{N} \mathbf{C} \mathbf{N} = (\mathbf{n} \mathbf{c}^{-1} \mathbf{n})^{-1} = \lambda^2 \\
\tilde{I}_5 &= \mathbf{N} \mathbf{C}^{-1} \mathbf{N} = \tilde{I}_4 \mathbf{n} \mathbf{c}^{-2} \mathbf{n} = J^{-2} da^2 / dA^2
\end{aligned} \tag{2.42}$$

This set will be utilized for the material formulation in section 4.4.

Criscione et al. [2001] developed a set of invariants which can be very helpful in the experiment-based development and parameter identification of material laws. These invariants I'_i define dilatation (I'_1), isochoric fiber stretch (I'_2), cross-fiber shear (I'_3), along-fiber shear (I'_4), and the orientation of the along-fiber shear plane relative to the cross-fiber shear diagonals (I'_5).

$$\begin{aligned}
I'_1 &= (\det \mathbf{C})^{\frac{1}{2}} = J \\
I'_2 &= (\det \mathbf{C})^{-\frac{1}{6}} (\mathbf{N} \cdot \mathbf{C} \mathbf{N})^{\frac{1}{2}} = J^{-\frac{1}{3}} \lambda \\
I'_3 &= \left(\frac{\mathbf{N}_2 \cdot \mathbf{C}^{-1} \mathbf{N}_2}{\mathbf{N}_1 \cdot \mathbf{C}^{-1} \mathbf{N}_1} \right)^{\frac{1}{4}} = \psi_{\perp} + \sqrt{\psi_{\perp}^2 + 1} \\
I'_4 &= \left(\frac{\mathbf{N} \cdot \mathbf{C}^2 \mathbf{N}}{(\mathbf{N} \cdot \mathbf{C} \mathbf{N})^2} - 1 \right)^{\frac{1}{2}} = \psi_{\parallel} \\
I'_5 &= \frac{(\mathbf{N}_1 \cdot \mathbf{C} \mathbf{N})^2 - (\mathbf{N}_2 \cdot \mathbf{C} \mathbf{N})^2}{(\mathbf{N}_1 \cdot \mathbf{C} \mathbf{N})^2 + (\mathbf{N}_2 \cdot \mathbf{C} \mathbf{N})^2} = \cos^2 \gamma - \sin^2 \gamma
\end{aligned} \tag{2.43}$$

The unit vectors \mathbf{N}_1 and \mathbf{N}_2 are normal to those two planes that contain \mathbf{N} and are perpendicular to each other in both, reference and current configuration. \mathbf{n}_1 and \mathbf{n}_2 mark hereby the principal cross-fiber stretch directions. These vectors are determined by the following set of equations: $\mathbf{N} \cdot \mathbf{N}_1 = 0$, $\mathbf{N} \cdot \mathbf{N}_2 = 0$, $\mathbf{N}_1 \cdot \mathbf{N}_2 = 0$, $\mathbf{n}_1 \cdot \mathbf{n}_2 = \mathbf{N}_1 \cdot \mathbf{C}^{-1} \mathbf{N}_2 = 0$, and for uniqueness $\mathbf{N}_1 \cdot \mathbf{C}^{-1} \mathbf{N}_1 \leq \mathbf{N}_2 \cdot \mathbf{C}^{-1} \mathbf{N}_2$. ψ_{\perp} denotes the major cross-fiber shear, and γ denotes the angle between \mathbf{n}_1 and the plane of the major along-fiber shear ψ_{\parallel} .

So far, there are few approaches to base material laws upon Criscione et al.'s invariants, and in this work they are only utilized as damage measures. But presuming adequate testing, their advantageous properties can be used for the adaptation of established material laws by means of a successive parameter conversion to principal invariants. The conversion

formula between the different invariant sets were completed for this work and are provided in section A.2.3.1 of the appendix.

2.3.5 General formulae for stress and elasticity tensors

Stress and material tensors for any hyperelastic transversely isotropic material can be built directly and with little additional analytical effort from the strain energy function by means of few selected formula. These depend on the respective set of invariants, and are based on (2.30) and (2.35) by application of the product rule, e.g.

$$\frac{\partial W}{\partial \mathbf{C}} = \frac{\partial W}{\partial I_i} \frac{\partial I_i}{\partial \mathbf{C}} \quad (2.44)$$

where $\{I_i\}$ may be any complete set of invariants of (\mathbf{C}, \mathbf{N}) . Whereas the actual structure of the first part on the right-hand side of (2.44) is specific to the material formulation, the second part may be derived independent of the specific material, and thus stress and material tensors may be generalized.

Subsequently, the formulae are presented for those invariant sets that were utilized during the course of this work. They serve as implementation base for the specific material formulations provided later. All terms are factorized with respect to combinations of \mathbf{C} and \mathbf{N} in order to provide an accessible and verifiable structure.

In this generalized and complete form, these formulae were not found published elsewhere.

2.3.5.1 Based on principal invariants

For constitutive equations which are expressed in terms of the previously defined principal invariants $I_i = I_i(\mathbf{C}, \mathbf{N})$, the 2nd Piola-Kirchhoff stress tensor can be computed according to (2.45), which is a more convenient representation of equations (2.33) and (2.39). Here, the term W_i substitutes $\partial W / \partial I_i$, and W_{ij} substitutes $\partial^2 W / (\partial I_i \partial I_j)$.

$$\mathbf{S} = 2 \left(W_1 \mathbf{I} + W_2 (I_1 \mathbf{I} - \mathbf{C}) + W_3 I_3 \mathbf{C}^{-1} + W_4 \mathbf{N} \otimes \mathbf{N} + W_5 (\mathbf{N} \otimes \mathbf{C} \mathbf{N} + \mathbf{N} \mathbf{C} \otimes \mathbf{N}) \right) \quad (2.45)$$

From (2.35) follows $\mathbb{C} = 2\partial\mathbf{S}/\partial\mathbf{C}$ and thus

$$\begin{aligned} \mathbb{C} = & 4 \left(\delta_1 \mathbf{I} \otimes \mathbf{I} + \delta_4 \mathbf{C} \otimes \mathbf{C} + \delta_6 \mathbf{C}^{-1} \otimes \mathbf{C}^{-1} + \delta_7 \mathbf{C}^{-1} \odot \mathbf{C}^{-1} \right. \\ & + \delta_8 \mathbf{I} \odot \mathbf{I} + \delta_9 \mathbf{N} \otimes \mathbf{N} \otimes \mathbf{N} \otimes \mathbf{N} + \delta_{10} (\mathbf{I} \odot (\mathbf{N} \otimes \mathbf{N}) + (\mathbf{N} \otimes \mathbf{N}) \odot \mathbf{I}) \\ & + \delta_{18} (\mathbf{N} \otimes \mathbf{C}\mathbf{N} + \mathbf{N}\mathbf{C} \otimes \mathbf{N}) \otimes (\mathbf{N} \otimes \mathbf{C}\mathbf{N} + \mathbf{N}\mathbf{C} \otimes \mathbf{N}) \\ & + \text{sym} \left[\delta_2 \mathbf{I} \otimes \mathbf{C} + \delta_3 \mathbf{I} \otimes \mathbf{C}^{-1} + \delta_5 \mathbf{C} \otimes \mathbf{C}^{-1} + (\delta_{11} \mathbf{I} + \delta_{12} \mathbf{C} + \delta_{13} \mathbf{C}^{-1}) \otimes \mathbf{N} \otimes \mathbf{N} \right. \\ & \left. \left. + (\delta_{14} \mathbf{I} + \delta_{15} \mathbf{C} + \delta_{16} \mathbf{C}^{-1} + \delta_{17} \mathbf{N} \otimes \mathbf{N}) \otimes (\mathbf{N} \otimes \mathbf{C}\mathbf{N} + \mathbf{N}\mathbf{C} \otimes \mathbf{N}) \right] \right) \end{aligned} \quad (2.46)$$

with

$$\begin{aligned} \delta_1 &= W_{11} + 2I_1 W_{12} + W_2 + I_1^2 W_{22} & \delta_2 &= -2(W_{12} + I_1 W_{22}) \\ \delta_3 &= 2(I_3 W_{13} + I_1 I_3 W_{23}) & \delta_4 &= W_{22} & \delta_5 &= -2I_3 W_{23} & \delta_6 &= I_3 W_3 + I_3^2 W_{33} \\ \delta_7 &= -I_3 W_3 & \delta_8 &= -W_2 & \delta_9 &= W_{44} & \delta_{10} &= W_5 & \delta_{11} &= 2(W_{14} + I_1 W_{24}) \\ \delta_{12} &= -2W_{24} & \delta_{13} &= 2I_3 W_{34} & \delta_{14} &= 2(W_{15} + I_1 W_{25}) & \delta_{15} &= -2W_{25} \\ \delta_{16} &= 2I_3 W_{35} & \delta_{17} &= 2W_{45} & \delta_{18} &= W_{55}. \end{aligned} \quad (2.47)$$

The same factors apply in the following spatial formulation, which is derived through the push-forward operations $\boldsymbol{\tau} = \Phi_* \mathbf{S}$ and $\mathbb{c} = \Phi_* \mathbb{C}$.

$$\boldsymbol{\tau} = 2 \left(W_1 \mathbf{c} + W_2 (I_1 \mathbf{c} - \mathbf{c}^2) + W_3 I_3 \mathbf{I} + W_4 I_4 \mathbf{n} \otimes \mathbf{n} + W_5 I_4 (\mathbf{n} \otimes \mathbf{c}\mathbf{n} + \mathbf{n}\mathbf{c} \otimes \mathbf{n}) \right) \quad (2.48)$$

$$\begin{aligned} \mathbb{c} = & 4 \left(\delta_1 \mathbf{c} \otimes \mathbf{c} + \delta_4 \mathbf{c}^2 \otimes \mathbf{c}^2 + \delta_6 \mathbf{I} \otimes \mathbf{I} + \delta_7 \mathbf{I} \odot \mathbf{I} + \delta_8 \mathbf{c} \odot \mathbf{c} \right. \\ & + \delta_9 I_4^2 \mathbf{n} \otimes \mathbf{n} \otimes \mathbf{n} \otimes \mathbf{n} + \delta_{10} I_4 (\mathbf{c} \odot (\mathbf{n} \otimes \mathbf{n}) + (\mathbf{n} \otimes \mathbf{n}) \odot \mathbf{c}) \\ & + \delta_{18} I_4^4 (\mathbf{n} \otimes \mathbf{c}^2 \mathbf{n} + \mathbf{n}\mathbf{c}^2 \otimes \mathbf{n}) \otimes (\mathbf{n} \otimes \mathbf{c}^2 \mathbf{n} + \mathbf{n}\mathbf{c}^2 \otimes \mathbf{n}) \\ & + \text{sym} \left[\delta_2 \mathbf{c} \otimes \mathbf{c}^2 + \delta_3 \mathbf{c} \otimes \mathbf{I} + \delta_5 \mathbf{c}^2 \otimes \mathbf{I} + I_4 (\delta_{11} \mathbf{c} + \delta_{12} \mathbf{c}^2 + \delta_{13} \mathbf{I}) \otimes \mathbf{n} \otimes \mathbf{n} \right. \\ & \left. \left. + I_4 (\delta_{14} \mathbf{c} + \delta_{15} \mathbf{c}^2 + \delta_{16} \mathbf{I} + \delta_{17} I_4 \mathbf{n} \otimes \mathbf{n}) \otimes (\mathbf{n} \otimes \mathbf{c}^2 \mathbf{n} + \mathbf{n}\mathbf{c}^2 \otimes \mathbf{n}) \right] \right) \end{aligned} \quad (2.49)$$

Derivation details are provided in A.2.4.1.

2.3.5.2 Based on modified invariants acc. to (2.41)

The following formulae apply when the strain-energy function is provided in terms of the invariants $\hat{I}_i = \hat{I}_i(\mathbf{C}, \mathbf{N})$, see (2.41). With $\hat{\mathbf{C}} = J^{-\frac{2}{3}} \mathbf{C}$ holds $\hat{I}_i(\mathbf{C}, \mathbf{N}) = \hat{I}_i(\hat{\mathbf{C}}, \mathbf{N}) = I_i(\hat{\mathbf{C}}, \mathbf{N})$

for all $i \neq 3$. The 2nd Piola-Kirchhoff stress tensor can be computed through

$$\mathbf{S} = 2\hat{I}_3^{-\frac{2}{3}} \left(W_1 \mathbf{I} + W_2 (\hat{I}_1 \mathbf{I} - \hat{\mathbf{C}}) + W_4 \mathbf{N} \otimes \mathbf{N} + W_5 (\mathbf{N} \otimes \hat{\mathbf{C}} \mathbf{N} + \mathbf{N} \hat{\mathbf{C}} \otimes \mathbf{N}) \right. \\ \left. - \frac{1}{3} (W_1 \hat{I}_1 + 2W_2 \hat{I}_2 - \frac{3}{2} W_3 \hat{I}_3 + W_4 \hat{I}_4 + 2W_5 \hat{I}_5) \hat{\mathbf{C}}^{-1} \right) \quad (2.50)$$

with $W_i = \partial W / \partial \hat{I}_i$. The modified invariants \hat{I}_i are usually utilized in decoupled work equations, i.e. with $W_{ij} = \partial^2 W / (\partial \hat{I}_i \partial \hat{I}_j)$, $W_{i3} = W_{3i} = 0$ applies for all $i \neq 3$. The derivation details in A.2.4.2 contain these W_{i3} terms, but they are omitted in the following representation of the material tensor

$$\mathbb{C} = 4\hat{I}_3^{-\frac{4}{3}} \left(\delta_1 \mathbf{I} \otimes \mathbf{I} + \delta_4 \hat{\mathbf{C}} \otimes \hat{\mathbf{C}} + \delta_6 \hat{\mathbf{C}}^{-1} \otimes \hat{\mathbf{C}}^{-1} + \delta_7 \hat{\mathbf{C}}^{-1} \odot \hat{\mathbf{C}}^{-1} \right. \\ + \delta_8 \mathbf{I} \odot \mathbf{I} + \delta_9 \mathbf{N} \otimes \mathbf{N} \otimes \mathbf{N} \otimes \mathbf{N} + \delta_{10} (\mathbf{I} \odot (\mathbf{N} \otimes \mathbf{N}) + (\mathbf{N} \otimes \mathbf{N}) \odot \mathbf{I}) \\ + \delta_{18} (\mathbf{N} \otimes \hat{\mathbf{C}} \mathbf{N} + \mathbf{N} \hat{\mathbf{C}} \otimes \mathbf{N}) \otimes (\mathbf{N} \otimes \hat{\mathbf{C}} \mathbf{N} + \mathbf{N} \hat{\mathbf{C}} \otimes \mathbf{N}) \\ + \text{sym} \left[\delta_2 \mathbf{I} \otimes \hat{\mathbf{C}} + \delta_3 \mathbf{I} \otimes \hat{\mathbf{C}}^{-1} + \delta_5 \hat{\mathbf{C}} \otimes \hat{\mathbf{C}}^{-1} + (\delta_{11} \mathbf{I} + \delta_{12} \hat{\mathbf{C}} + \delta_{13} \hat{\mathbf{C}}^{-1}) \otimes \mathbf{N} \otimes \mathbf{N} \right. \\ \left. + (\delta_{14} \mathbf{I} + \delta_{15} \hat{\mathbf{C}} + \delta_{16} \hat{\mathbf{C}}^{-1} + \delta_{17} \mathbf{N} \otimes \mathbf{N}) \otimes (\mathbf{N} \otimes \hat{\mathbf{C}} \mathbf{N} + \mathbf{N} \hat{\mathbf{C}} \otimes \mathbf{N}) \right] \quad (2.51)$$

with

$$\delta_1 = W_{11} + 2\hat{I}_1 W_{12} + W_2 + \hat{I}_1^2 W_{22} \quad \delta_2 = -2(W_{12} + \hat{I}_1 W_{22}) \quad \delta_4 = W_{22} \\ \delta_3 = -\frac{2}{3}(W_1 + 2\hat{I}_1 W_2 + \hat{I}_1 W_{11} + 2\hat{I}_1 \hat{I}_2 W_{22} + (\hat{I}_1^2 + 2\hat{I}_2)W_{12} + \hat{I}_4 W_{14} + 2\hat{I}_5 W_{15} \\ + \hat{I}_1 \hat{I}_4 W_{24} + 2\hat{I}_1 \hat{I}_5 W_{25}) \quad \delta_5 = \frac{2}{3}(2W_2 - 2W_{22} + \hat{I}_1 W_{12} + \hat{I}_4 W_{24} + 2\hat{I}_5 W_{25}) \\ \delta_6 = \frac{1}{8} \hat{I}_3 W_3 + \frac{1}{4} W_{33} + \frac{1}{9} (\hat{I}_1 W_1 + 4\hat{I}_2 W_2 + \hat{I}_4 W_4 + 4\hat{I}_5 W_5 + \hat{I}_1^2 W_{11} + 4\hat{I}_2^2 W_{22} + \hat{I}_4^2 W_{44} \\ + 4\hat{I}_5^2 W_{55} + 4\hat{I}_1 \hat{I}_2 W_{12} + 2\hat{I}_1 \hat{I}_4 W_{14} + 4\hat{I}_1 \hat{I}_5 W_{15} + 4\hat{I}_2 \hat{I}_4 W_{24} + 8\hat{I}_2 \hat{I}_5 W_{25} + 4\hat{I}_4 \hat{I}_5 W_{45}) \quad (2.52) \\ \delta_7 = -\frac{1}{4} \hat{I}_3 W_3 + \frac{1}{3} (\hat{I}_1 W_1 + 2\hat{I}_2 W_2 + \hat{I}_4 W_4 + 2\hat{I}_5 W_5) \quad \delta_8 = -W_2 \quad \delta_9 = W_{44} \\ \delta_{10} = W_5 \quad \delta_{11} = 2(W_{14} + \hat{I}_1 W_{24}) \quad \delta_{12} = -2W_{24} \quad \delta_{14} = 2(W_{15} + \hat{I}_1 W_{25}) \\ \delta_{13} = -\frac{2}{3}(W_4 + \hat{I}_4 W_{44} + \hat{I}_1 W_{14} + 2\hat{I}_2 W_{24} + 2\hat{I}_5 W_{45}) \quad \delta_{15} = -2W_{25} \\ \delta_{16} = -\frac{2}{3}(2W_5 + 2\hat{I}_5 W_{55} + \hat{I}_1 W_{15} + 2\hat{I}_2 W_{25} + \hat{I}_4 W_{45}) \quad \delta_{17} = 2W_{45} \quad \delta_{18} = W_{55}.$$

The push-forward operation leads to the spatial formulation, utilizing $\hat{\mathbf{c}} = J^{-\frac{2}{3}}\mathbf{c}$ and the same δ -factors.

$$\begin{aligned} \boldsymbol{\tau} = 2 \Big(& W_1 \hat{\mathbf{c}} + W_2 (\hat{I}_1 \hat{\mathbf{c}} - \hat{\mathbf{c}}^2) + W_3 \hat{I}_3 \mathbf{I} + W_4 \hat{I}_4 \mathbf{n} \otimes \mathbf{n} + W_5 \hat{I}_4 (\mathbf{n} \otimes \hat{\mathbf{c}} \mathbf{n} + \mathbf{n} \hat{\mathbf{c}} \otimes \mathbf{n}) \\ & - \frac{1}{3} (W_1 \hat{I}_1 + 2W_2 \hat{I}_2 - \frac{3}{2} W_3 \hat{I}_3 + W_4 \hat{I}_4 + 2W_5 \hat{I}_5) \mathbf{I} \Big) \end{aligned} \quad (2.53)$$

$$\begin{aligned} \mathfrak{c} = 4 \Big(& \delta_1 \hat{\mathbf{c}} \otimes \hat{\mathbf{c}} + \delta_4 \hat{\mathbf{c}}^2 \otimes \hat{\mathbf{c}}^2 + \delta_6 \mathbf{I} \otimes \mathbf{I} + \delta_7 \mathbf{I} \odot \mathbf{I} + \delta_8 \hat{\mathbf{c}} \odot \hat{\mathbf{c}} \\ & + \delta_9 \hat{I}_4^2 \mathbf{n} \otimes \mathbf{n} \otimes \mathbf{n} \otimes \mathbf{n} + \delta_{10} \hat{I}_4 (\hat{\mathbf{c}} \odot (\mathbf{n} \otimes \mathbf{n}) + (\mathbf{n} \otimes \mathbf{n}) \odot \hat{\mathbf{c}}) \\ & + \delta_{18} \hat{I}_4^4 (\mathbf{n} \otimes \hat{\mathbf{c}}^2 \mathbf{n} + \mathbf{n} \hat{\mathbf{c}}^2 \otimes \mathbf{n}) \otimes (\mathbf{n} \otimes \hat{\mathbf{c}}^2 \mathbf{n} + \mathbf{n} \hat{\mathbf{c}}^2 \otimes \mathbf{n}) \\ & + \text{sym} \Big[\delta_2 \hat{\mathbf{c}} \otimes \hat{\mathbf{c}}^2 + \delta_3 \hat{\mathbf{c}} \otimes \mathbf{I} + \delta_5 \hat{\mathbf{c}}^2 \otimes \mathbf{I} + \hat{I}_4 (\delta_{11} \hat{\mathbf{c}} + \delta_{12} \hat{\mathbf{c}}^2 + \delta_{13} \mathbf{I}) \otimes \mathbf{n} \otimes \mathbf{n} \\ & + \hat{I}_3^{\frac{2}{3}} \hat{I}_4 (\delta_{14} \hat{\mathbf{c}} + \delta_{15} \hat{\mathbf{c}}^2 + \delta_{16} \mathbf{I} + \delta_{17} \hat{I}_4 \mathbf{n} \otimes \mathbf{n}) \otimes (\mathbf{n} \otimes \hat{\mathbf{c}}^2 \mathbf{n} + \mathbf{n} \hat{\mathbf{c}}^2 \otimes \mathbf{n}) \Big] \Big) \end{aligned} \quad (2.54)$$

2.3.5.3 Based on invariants acc. to Ehret et al. [2011]

The following formulae apply when the strain-energy function is provided in terms of the invariants \tilde{I}_i (as in Ehret et al. [2011]). When no arguments are provided, these invariants will refer to the right Cauchy-Green tensor and \mathbf{N} (2.37): $\tilde{I}_i = \tilde{I}_i(\mathbf{C}, \mathbf{N})$.

The 2nd Piola-Kirchhoff stress tensor can be computed through

$$\mathbf{S} = 2 \Big(W_1 \mathbf{I} - W_2 \mathbf{C}^{-2} + W_3 \tilde{I}_3 \mathbf{C}^{-1} + W_4 \mathbf{N} \otimes \mathbf{N} - W_5 \mathbf{C}^{-1} \mathbf{N} \otimes \mathbf{N} \mathbf{C}^{-1} \Big) \quad (2.55)$$

with W_i substituting $\partial W / \partial \tilde{I}_i$. From $\mathbb{C} = 2\partial \mathbf{S} / \partial \mathbf{C}$ follows

$$\begin{aligned} \mathbb{C} = 4 \Big(& \delta_1 \mathbf{I} \otimes \mathbf{I} + \delta_4 \mathbf{C}^{-2} \otimes \mathbf{C}^{-2} + \delta_6 \mathbf{C}^{-1} \otimes \mathbf{C}^{-1} + \delta_7 \mathbf{C}^{-1} \odot \mathbf{C}^{-1} \\ & + \delta_8 (\mathbf{C}^{-2} \odot \mathbf{C}^{-1} + \mathbf{C}^{-1} \odot \mathbf{C}^{-2}) + \delta_9 \mathbf{N} \otimes \mathbf{N} \otimes \mathbf{N} \otimes \mathbf{N} \\ & + \delta_{10} \Big((\mathbf{C}^{-1} \mathbf{N} \otimes \mathbf{N} \mathbf{C}^{-1}) \odot \mathbf{C}^{-1} + \mathbf{C}^{-1} \odot (\mathbf{C}^{-1} \mathbf{N} \otimes \mathbf{N} \mathbf{C}^{-1}) \Big) \\ & + \delta_{18} (\mathbf{C}^{-1} \mathbf{N} \otimes \mathbf{N} \mathbf{C}^{-1}) \otimes (\mathbf{C}^{-1} \mathbf{N} \otimes \mathbf{N} \mathbf{C}^{-1}) + \text{sym} \Big[\delta_2 \mathbf{I} \otimes \mathbf{C}^{-2} \\ & + \delta_3 \mathbf{I} \otimes \mathbf{C}^{-1} + \delta_5 \mathbf{C}^{-2} \otimes \mathbf{C}^{-1} + (\delta_{11} \mathbf{I} + \delta_{12} \mathbf{C}^{-2} + \delta_{13} \mathbf{C}^{-1}) \otimes \mathbf{N} \otimes \mathbf{N} \\ & + (\delta_{14} \mathbf{I} + \delta_{15} \mathbf{C}^{-2} + \delta_{16} \mathbf{C}^{-1} + \delta_{17} \mathbf{N} \otimes \mathbf{N}) \otimes \mathbf{C}^{-1} \mathbf{N} \otimes \mathbf{N} \mathbf{C}^{-1} \Big] \Big) \end{aligned} \quad (2.56)$$

with W_{ij} substituting $\partial^2 W / (\partial \tilde{I}_i \partial \tilde{I}_j)$ and

$$\begin{aligned}
\delta_1 &= W_{11} & \delta_2 &= -2W_{12} & \delta_3 &= 2\tilde{I}_3 W_{13} & \delta_4 &= W_{22} & \delta_5 &= -2\tilde{I}_3 W_{23} \\
\delta_6 &= \tilde{I}_3 W_3 + \tilde{I}_3^2 W_{33} & \delta_7 &= -\tilde{I}_3 W_3 & \delta_8 &= -2W_2 & \delta_9 &= W_{44} \\
\delta_{10} &= W_5 & \delta_{11} &= 2W_{14} & \delta_{12} &= -2W_{24} & \delta_{13} &= 2\tilde{I}_3 W_{34} & \delta_{14} &= -2W_{15} \\
\delta_{15} &= 2W_{25} & \delta_{16} &= -2\tilde{I}_3 W_{35} & \delta_{17} &= -2W_{45} & \delta_{18} &= W_{55}.
\end{aligned} \tag{2.57}$$

The same factors apply in the following spatial formulation.

$$\boldsymbol{\tau} = 2 \left(W_1 \mathbf{c} - W_2 \mathbf{c}^{-1} + W_3 \tilde{I}_3 \mathbf{I} + W_4 \tilde{I}_4 \mathbf{n} \otimes \mathbf{n} - W_5 \tilde{I}_4 \mathbf{c}^{-1} \mathbf{n} \otimes \mathbf{n} \mathbf{c}^{-1} \right) \tag{2.58}$$

$$\begin{aligned}
\mathbf{c} &= 4 \left(\delta_1 \mathbf{c} \otimes \mathbf{c} + \delta_4 \mathbf{c}^{-1} \otimes \mathbf{c}^{-1} + \delta_6 \mathbf{I} \otimes \mathbf{I} + \delta_7 \mathbf{I} \odot \mathbf{I} + \delta_8 (\mathbf{c}^{-1} \odot \mathbf{I} + \mathbf{I} \odot \mathbf{c}^{-1}) \right. \\
&\quad + \delta_9 \tilde{I}_4 \mathbf{n} \otimes \mathbf{n} \otimes \mathbf{n} \otimes \mathbf{n} + \delta_{10} \tilde{I}_4 \left((\mathbf{c}^{-1} \mathbf{n} \otimes \mathbf{n} \mathbf{c}^{-1}) \odot \mathbf{I} + \mathbf{I} \odot (\mathbf{c}^{-1} \mathbf{n} \otimes \mathbf{n} \mathbf{c}^{-1}) \right) \\
&\quad + \delta_{18} \tilde{I}_4^2 (\mathbf{c}^{-1} \mathbf{n} \otimes \mathbf{n} \mathbf{c}^{-1}) \otimes (\mathbf{c}^{-1} \mathbf{n} \otimes \mathbf{n} \mathbf{c}^{-1}) + \text{sym} \left[\delta_2 \mathbf{c} \otimes \mathbf{c}^{-1} + \delta_3 \mathbf{c} \otimes \mathbf{I} \right. \\
&\quad + \delta_5 \mathbf{c}^{-1} \otimes \mathbf{I} + \tilde{I}_4 (\delta_{11} \mathbf{c} + \delta_{12} \mathbf{c}^{-1} + \delta_{13} \mathbf{I}) \otimes \mathbf{n} \otimes \mathbf{n} \\
&\quad \left. + \tilde{I}_4 (\delta_{14} \mathbf{c} + \delta_{15} \mathbf{c}^{-1} + \delta_{16} \mathbf{I} + \delta_{17} \tilde{I}_4 \mathbf{n} \otimes \mathbf{n}) \otimes \mathbf{c}^{-1} \mathbf{n} \otimes \mathbf{n} \mathbf{c}^{-1} \right] \Big)
\end{aligned} \tag{2.59}$$

Derivation details are provided in A.2.4.3.

2.3.6 Transformation of 1D laws to 3D

In the context of muscle modeling, it is necessary to incorporate one-dimensional stress-strain relations into three-dimensional constitutive descriptions. These 1D descriptions often stem from force measurements, and thus correspond to a stress function which does not account for a change in cross-section. Hence, the force to cross-section ratio can be regarded as first Piola-Kirchhoff stress P_{1D} . Under the assumption of ideal isovolumetric deformation,

$$P_{1D} = \tau_{1D} / \lambda = S_{1D} \lambda \tag{2.60}$$

applies with the stretch λ in the direction of the 1D stress component, see (2.27). The derivation of equivalent stress tensors follows from rotating a \mathbf{n} -aligned coordinate system

into the global coordinate system:

$$\mathbf{S} = S_{1D} \mathbf{N} \otimes \mathbf{N} \quad (2.61)$$

$$\boldsymbol{\tau} = \tau_{1D} \mathbf{n} \otimes \mathbf{n}. \quad (2.62)$$

Any functional dependence on λ has to be replaced by the corresponding invariant, e.g. $\sqrt{I_4} = \lambda$.

The equations are less straightforward when there's a deviation from the premise of ideal isovolumetric deformation. Section 4.5 discusses this by means of a specific example for the deduction of a three-dimension muscle material.

2.3.7 Hypo- and non-elastic materials

The deductions of the previous sections were based on hyperelastic material behavior, which allows for the determination of a stress state from the deformation state only. In many cases though, there is no strain-energy function W to validate equations (2.30) and (2.31), and deviating from (2.35) and (2.36), stress rates may depend on, e.g., deformation history or other variable's quantity and change rate.

The validity of balance and derived equations are unaffected by the lack of an explicit strain-energy function; e.g., the determination of the internal mechanical work rate (2.29) remains valid. On this base, terms associated with non-hyperelastic material behavior will be introduced ad hoc in subsequent sections.

Chapter 3

Finite Element Modeling

While the system of differential equations provided in chapter 2 is sufficient to describe a structure's response to predefined boundary conditions mechanically, one has to acknowledge that there are very few cases to which specific analytical solutions are accessible and feasible. Approximation techniques are therefore essential in order to derive unrestrained solution algorithms.

Several such methods are established, with ample literature on the most important ones: Finite Element Method (FEM), Finite Difference Method, Finite Volume Method and Boundary Element Method. The FEM is predominant in the field of solid mechanics, especially if geometric or material nonlinearity is involved. This is mainly due to the favorable structure of the involved matrices and the resulting superior numerical efficiency.

3.1 Theoretical basis

3.1.1 Approximations to differential equation systems

There are several approaches to derive the governing equations of the finite element method. The method of weighted residuals and its specific realization as Galerkin's method are described in most inaugural books, and provide a very general access to the topic (see, e.g., Bathe [2002], Belytschko [1999]). Providing the same equations, and more intuitively related to the previous chapter, the variational method will be described here.

The vector-valued differential form of Cauchy's equation of motion (2.24) applies throughout and in every point of the body \mathcal{B} , and is thus considered the strong form of equilibrium. By expanding this form with a test function ϕ and subsequent integration over the body's

domain,

$$\int_{\mathcal{V}} \phi \cdot (\operatorname{div} \boldsymbol{\sigma} + \rho(\mathbf{b} - \ddot{\mathbf{x}})) \, dv = 0 \quad (3.1)$$

is obtained, referred to as the weak form of equilibrium. Both forms are equivalent and exact. Only by specifying a single ϕ out of the set of admissible test functions, equation (3.1) becomes an approximation to the equilibrium conditions. Introducing a variational or virtual displacement $\delta \mathbf{u}$ as test function, the admissibility depends on the compliance with the kinematic boundary conditions at the Dirichlet boundary \mathcal{S}^u of \mathcal{B} . Application of (A.19), (A.58), and Gauss' integral theorem (A.72) finally delivers

$$\int_{\mathcal{V}} \rho (\mathbf{b} - \ddot{\mathbf{x}}) \delta \mathbf{u} \, dv + \int_{\mathcal{S}^t} \mathbf{t} \cdot \delta \mathbf{u} \, da - \int_{\mathcal{V}} \boldsymbol{\sigma} : \mathring{\delta} \mathbf{e} \, dv = 0. \quad (3.2)$$

The symbol $\mathring{\delta}$ for the variation of spatial quantities, e.g. $\mathring{\delta} \mathbf{e}$, refers to the Lie-variation. Adopting the concept of the Lie-derivative (2.15), it describes the variation of a spatial tensor, holding the deformed base vectors constant. For the present case follows

$$\mathring{\delta} \mathbf{e} = \boldsymbol{\Phi}_\star(\delta(\boldsymbol{\Phi}^\star(\mathbf{e}))) = \boldsymbol{\Phi}_\star(\delta \mathbf{E}) = \operatorname{sym}(\operatorname{grad} \delta \mathbf{u}). \quad (3.3)$$

Consequently, the equalities of energy conjugate stress-strain pairings in (2.29) remain valid if the corresponding variation substitutes the time derivative. Rewriting (3.2) for the material description yields

$$\int_{\mathcal{V}} \rho_0 (\mathbf{b} - \ddot{\mathbf{x}}) \delta \mathbf{u} \, dV + \int_{\mathcal{S}^t} \mathbf{T} \cdot \delta \mathbf{u} \, dA - \int_{\mathcal{V}} \mathbf{S} : \delta \mathbf{E} \, dV = 0. \quad (3.4)$$

Both equations are referred to as the principle of virtual work: $W_{\text{ext}}(\delta \mathbf{u}) - W_{\text{int}}(\delta \mathbf{u}) = 0$.¹

3.1.2 Linearization

Generally, equation (3.2) is nonlinear in terms of displacements and possibly other independent variables. Linearization is indispensable in order to apply the necessary iterative solution algorithms. Here, a linear approximation is marked by the linearization operator $\Delta(\cdot)$, and may be specified as the sum of all independent Gâteaux derivatives (see A.1.1.5).

¹ W_{int} and W_{ext} denote internal and external physical work, not a strain-energy function as in 2.3.2.

Exemplary for a 2nd Piola-Kirchhoff stress \mathbf{S} , which shall depend on two variables:

$$\begin{aligned}\Delta \mathbf{S} &= \Delta_{\mathbf{u}} \mathbf{S}(\mathbf{u}, \dot{\mathbf{u}}) + \Delta_{\dot{\mathbf{u}}} \mathbf{S}(\mathbf{u}, \dot{\mathbf{u}}) \\ &= \frac{d}{d\varepsilon} \mathbf{S}(\mathbf{u} + \varepsilon \Delta \mathbf{u}, \dot{\mathbf{u}}) \Big|_{\varepsilon=0} + \frac{d}{d\gamma} \mathbf{S}(\mathbf{u}, \dot{\mathbf{u}} + \gamma \Delta \dot{\mathbf{u}}) \Big|_{\gamma=0}\end{aligned}\quad (3.5)$$

As with material time derivative and variation, the linearization of spatial quantities follows the concept of directional derivatives with the deformed base fixed. Whereas the Lie-derivative describes the change of a spatial quantity relative to the spatial velocity field, the Lie-variation and -linearization refer to virtual and incremental displacement fields, respectively. Exemplarily for the Kirchhoff stress (see (2.27)), this leads to

$$\Delta \boldsymbol{\tau} = \boldsymbol{\Phi}_*(\Delta(\boldsymbol{\Phi}^*(\boldsymbol{\tau}))) = \mathbf{F}(\Delta \mathbf{S})\mathbf{F}^T. \quad (3.6)$$

Subsequently, the linearization of the virtual work equations (3.2,3.4) will be limited to the terms which constitute W_{int} , presuming $\Delta W_{\text{ext}} = 0$. This corresponds to deformation independent surface loads and external mass forces.

In the spatial description, $\boldsymbol{\sigma}$ is substituted by the Kirchhoff stress $\boldsymbol{\tau}$ to prepare for the FE-algorithms used later on. Adjusting the integration domain gives

$$\Delta \int_{\mathcal{V}} \boldsymbol{\sigma} : \mathring{\delta} \mathbf{e} \, dv = \Delta \int_{\mathcal{V}} \boldsymbol{\tau} : \mathring{\delta} \mathbf{e} \, dV. \quad (3.7)$$

In this chapter, stress items are supposed to be a function of deformation and deformation rate only, although the number of independent parameters is not limited in general. Taking advantage of the material tensors' symmetry and applying (2.35) and (2.36) leads to

$$\begin{aligned}\Delta \delta W_{\text{int}} &= \Delta \int_{\mathcal{V}} \boldsymbol{\tau} : \mathring{\delta} \mathbf{e} \, dV + \Delta \int_{\mathcal{V}} \rho_0 \ddot{\mathbf{x}} \delta \mathbf{u} \, dV \\ &= \int_{\mathcal{V}} (\Delta \mathbf{e} : \mathbb{C} + \Delta \dot{\mathbf{e}} : \mathbb{V}) : \mathring{\delta} \mathbf{e} + \boldsymbol{\tau} : \Delta \mathring{\delta} \mathbf{e} + \rho_0 \Delta \ddot{\mathbf{u}} \delta \mathbf{u} \, dV\end{aligned}\quad (3.8)$$

$$\begin{aligned}\Delta \delta W_{\text{int}} &= \Delta \int_{\mathcal{V}} \mathbf{S} : \delta \mathbf{E} \, dV + \Delta \int_{\mathcal{V}} \rho_0 \ddot{\mathbf{x}} \delta \mathbf{u} \, dV \\ &= \int_{\mathcal{V}} (\Delta \mathbf{E} : \mathbb{C} + \Delta \dot{\mathbf{E}} : \mathbb{V}) : \delta \mathbf{E} + \mathbf{S} : \Delta \delta \mathbf{E} + \rho_0 \Delta \ddot{\mathbf{u}} \delta \mathbf{u} \, dV\end{aligned}\quad (3.9)$$

with the viscoelastic tensors \mathbb{V} and \mathbb{V} which account for the deformation rate dependent

change in the material stiffness. The utilized strain items are derived as

$$\begin{aligned}\Delta \mathbf{e} &= \text{sym}(\text{grad } \Delta \mathbf{u}) &= \text{sym}(\Delta u_{i;j}) \mathbf{e}_i \otimes \mathbf{e}_j \\ \Delta \dot{\mathbf{e}} &= \text{sym}(\text{grad}^T \Delta \mathbf{u} \text{ grad } \delta \mathbf{u}) &= \text{sym}(\Delta u_{k;i} \delta u_{k;j}) \mathbf{e}_i \otimes \mathbf{e}_j\end{aligned}\tag{3.10}$$

$$\begin{aligned}\delta \mathbf{E} &= \text{sym}(\mathbf{F}^T \text{Grad } \delta \mathbf{u}) &= \text{sym}(\delta u_{i,j} + \delta u_{k,i} u_{k,j}) \mathbf{e}_i \otimes \mathbf{e}_j \\ \Delta \mathbf{E} &= \text{sym}(\mathbf{F}^T \text{Grad } \Delta \mathbf{u}) &= \text{sym}(\Delta u_{i,j} + \Delta u_{k,i} u_{k,j}) \mathbf{e}_i \otimes \mathbf{e}_j \\ \Delta \delta \mathbf{E} &= \text{sym}(\text{Grad}^T \Delta \mathbf{u} \text{ Grad } \delta \mathbf{u}) &= \text{sym}(\Delta u_{k,i} \delta u_{k,j}) \mathbf{e}_i \otimes \mathbf{e}_j\end{aligned}\tag{3.11}$$

with the notation $\Delta u_{i,j} = (\text{Grad } \Delta \mathbf{u})_{ij}$ and $\Delta u_{i;j} = (\text{grad } \Delta \mathbf{u})_{ij}$. The rate expressions read

$$\begin{aligned}\Delta \dot{\mathbf{e}} &= \text{sym}(\text{grad } \Delta \dot{\mathbf{u}} + \text{grad}^T \dot{\mathbf{u}} \text{ grad } \Delta \mathbf{u}) \\ &= \text{sym}(\Delta \dot{u}_{i;j} + \Delta u_{k;i} \dot{u}_{k;j}) \mathbf{e}_i \otimes \mathbf{e}_j\end{aligned}\tag{3.12}$$

$$\begin{aligned}\Delta \dot{\mathbf{E}} &= \text{sym}(\text{Grad } \Delta \dot{\mathbf{u}} + \text{Grad}^T \dot{\mathbf{u}} \text{ Grad } \Delta \mathbf{u} + \text{Grad}^T \Delta \dot{\mathbf{u}} \text{ Grad } \mathbf{u}) \\ &= \text{sym}(\Delta \dot{u}_{i,j} + \Delta u_{k,i} \dot{u}_{k,j} + \Delta \dot{u}_{k,i} u_{k,j}) \mathbf{e}_i \otimes \mathbf{e}_j.\end{aligned}\tag{3.13}$$

Equations (3.2) and (3.8) were referred to as spatial formulation, featuring the Almansi strain \mathbf{e} and its rate in their variational and linearized forms as deformation measure. Analogies to the respective forms of the Green-Langrange \mathbf{E} strain become apparent in the above indicial notations.

Postulating the reference configuration to be the current rather than the undeformed configuration leads to $u_i \equiv 0$ and the derivational equivalence $\Delta u_{i,j} = \Delta u_{i;j}$. The linearized and variational forms of \mathbf{E} evaluated with respect to this updated reference are identical to the corresponding forms of \mathbf{e} . For example, $\Delta \mathbf{e}$ may be considered to be either the linearization of the Almansi strain, or the linearization of the Green-Langrange strain referring to the current configuration. In conjunction with the Kirchhoff stress $\boldsymbol{\tau}$ being identical to the 2nd Piola-Kirchhoff stress \mathbf{S} with deformed base, the latter approach is commonly labeled Updated Lagrangian (UL). It is utilized in the following element formulations.

For further details on linearization, refer to the literature, e.g. to Holzapfel [2000].

3.1.3 Spatial discretization

The basic idea of the Finite Element Method is the subdivision of the domain Ω into disjoint subdomains Ω^e , whose behavior is then approximated by comparatively simple functions. The subdomains are governed by the same equations as the domain, and boundary conditions are directly transferred to the affected Γ^e . By means of local compatibility conditions between the subdomains, any global integral may be assembled as $\int_{\Omega}() = \bigcup \int_{\Omega^e}()$.

In structural mechanics, Ω may be identified with the body \mathcal{B} , and Γ may be regarded as Dirichlet surface \mathcal{S}^u with prescribed displacements, or Neumann boundary \mathcal{S}^t with prescribed traction. The subdomains are referred to as elements, and specific points - nodes - serve as interpolation roots for the state quantities within the element.

Test functions and weighting parameters introduced in 3.1.1 are now represented by shape functions $h_n^e(\mathbf{X})$ and nodal values (marked by a hat), such that, for example, displacements within an element are approximated as

$$u_i^e(\mathbf{X}) \cong h_n^e(\mathbf{X}) \hat{u}_i^{ne} \quad \text{or} \quad u_i^e(\mathbf{x}) \cong h_n^e(\mathbf{x}) \hat{u}_i^{ne} \quad (3.14)$$

and their derivatives as

$$u_{i,j}^e(\mathbf{X}) \cong h_{n,j}^e(\mathbf{X}) \hat{u}_i^{ne} \quad \text{or} \quad u_{i,j}^e(\mathbf{x}) \cong h_{n,j}^e(\mathbf{x}) \hat{u}_i^{ne} \quad (3.15)$$

with the index n running through the nodes of the element. Thus, instead of continuous field quantities, only a limited set of nodal variables remains to be solved for.

Without regard to element specific formulations, the discrete equilibrium equation

$$\hat{\mathbf{f}}_{\text{ext}}^e - \hat{\mathbf{f}}_{\text{int}}^e = 0 \quad (3.16)$$

as well as the linearization

$$\Delta \hat{\mathbf{f}}_{\text{int}}^e = \mathbf{K}^e \Delta \hat{\mathbf{u}}^e + \mathbf{D}^e \Delta \hat{\mathbf{u}}^e + \mathbf{M}^e \Delta \hat{\mathbf{u}}^e \quad (3.17)$$

may be deduced by identifying the following expressions in (3.2), (3.4), (3.8) and (3.9),

and subsequent elimination of $\delta \hat{\mathbf{u}}^e$ from those terms.

$$(\delta \hat{\mathbf{u}}^e)^T \hat{\mathbf{f}}_{\text{ext}}^e = \int_{\mathcal{S}^t} \delta \mathbf{u} \cdot \mathbf{T} \, dA^e + \int_{\mathcal{V}} \rho_0 \mathbf{b}_0 \delta \mathbf{u} \, dV^e \quad (3.18)$$

$$\begin{aligned} (\delta \hat{\mathbf{u}}^e)^T \hat{\mathbf{f}}_{\text{int}}^e &= \int_{\mathcal{V}} \boldsymbol{\tau} : \dot{\delta} \mathbf{e} \, dV^e + \int_{\mathcal{V}} \rho_0 \ddot{\mathbf{u}} \delta \mathbf{u} \, dV^e \\ &= \int_{\mathcal{V}} \mathbf{S} : \delta \mathbf{E} \, dV^e + \int_{\mathcal{V}} \rho_0 \ddot{\mathbf{u}} \delta \mathbf{u} \, dV^e \end{aligned} \quad (3.19)$$

$$\begin{aligned} (\delta \hat{\mathbf{u}}^e)^T \mathbf{K}_e^e \Delta \hat{\mathbf{u}}^e &= \int_{\mathcal{V}} \Delta \mathbf{e} : \mathbb{C} : \dot{\delta} \mathbf{e} \, dV^e + \int_{\mathcal{V}} \boldsymbol{\tau} : \Delta \dot{\delta} \mathbf{e} \, dV^e \\ &= \int_{\mathcal{V}} \Delta \mathbf{E} : \mathbb{C} : \delta \mathbf{E} \, dV^e + \int_{\mathcal{V}} \mathbf{S} : \Delta \delta \mathbf{E} \, dV^e \end{aligned} \quad (3.20)$$

$$\begin{aligned} (\delta \hat{\mathbf{u}}^e)^T (\mathbf{D}^e \Delta \hat{\mathbf{u}}^e + \mathbf{K}_v^e \Delta \hat{\mathbf{u}}^e) &= \int_{\mathcal{V}} (\Delta \dot{\mathbf{e}} : \mathbb{V}) : \dot{\delta} \mathbf{e} \, dV^e \\ &= \int_{\mathcal{V}} (\Delta \dot{\mathbf{E}} : \mathbb{V}) : \delta \mathbf{E} \, dV^e \end{aligned} \quad (3.21)$$

$$(\delta \hat{\mathbf{u}}^e)^T \mathbf{M}^e \Delta \hat{\mathbf{u}}^e = \int_{\mathcal{V}} \rho_0 \Delta \ddot{\mathbf{u}} \delta \mathbf{u} \, dV^e \quad (3.22)$$

Genuine external loads as well as the forces that neighboring elements exert on the nodes contribute to $\hat{\mathbf{f}}_{\text{ext}}^e$. Obviously, $\hat{\mathbf{f}}_{\text{int}}^e$ denotes the nodal forces due to internal deformation and inertia. Tangential stiffness and damping matrices $\mathbf{K}^e = \mathbf{K}_e^e + \mathbf{K}_v^e$ and \mathbf{D}^e are measures for the element's resistance against incremental nodal displacements and velocities, respectively. The mass matrix \mathbf{M}^e is a measure for forces which originate from a change in nodal accelerations. It occurs as well in (3.19) as part of the internal forces, which may be rewritten as $\hat{\mathbf{f}}_{\text{int}}^e = \mathbf{M}^e \hat{\mathbf{u}}^e + \hat{\mathbf{f}}_{\text{res}}^e$.

Total and Updated Lagrangian representations of the entities above are fully equivalent. The UL formulation is usually associated with less expensive calculations in order to model geometric nonlinearity [Bathe 2002], but the available constitutive equations and software environment may favor the implementation of the TL form.

Remark: The presented equations were derived by introducing virtual displacement test functions, and are therefore referred to as displacement or kinematically based FEM. Elements based on this approach may under certain conditions behave too constrained, leading to numerical problems or significant inaccuracies (e.g. volumetric locking, see 3.2.3). Mixed formulations which additionally utilize, for example, stress variations help to overcome these disadvantages. Their derivation is nevertheless similar to the above and therefore omitted here. See A.3.2 for a brief introduction.

3.2 Finite Elements

From the element concept introduced in 3.1.3, specific conditions for the element formulation can be deduced, such that by mesh refinement, convergence towards the exact continuum solution is guaranteed. Standard FEM textbooks like those of Bathe [2002], Zienkiewicz and Taylor [2005], Betten [1998], Felippa [2001] cover this issue thoroughly. They describe, amongst others, the class of isoparametric elements as suitable to solve problems which demand continuity in terms of displacements as, for example, equation (3.2). These elements are characterized by the use of identical interpolation functions for coordinates and displacements alike, justifying the term shape functions. The H1-element as the non-viscous hexahedral UL representative will subsequently serve as an example to illustrate the implementation methodology, before elements capable of modeling incompressible visco-elastic materials are discussed.

3.2.1 Voigt notation

The Voigt notation allows components of symmetric stress and strain tensors to be assembled in vector form. They are used in conjunction with matrices that contain the components of minor symmetric fourth-order tensors. The vectors and matrices in question are subsequently marked by underlines to make them distinguishable from tensors. The Voigt representation of equation (2.35) reads

$$\delta \underline{\mathbf{S}} = \underline{\mathbb{C}} : \delta \underline{\mathbf{E}} \quad (3.23)$$

with

$$\underline{\mathbb{C}} = \begin{bmatrix} C^{1111} & C^{2211} & C^{3311} & C^{1211} & C^{2311} & C^{1311} \\ C^{1122} & C^{2222} & C^{3322} & C^{1222} & C^{2322} & C^{1322} \\ C^{1133} & C^{2233} & C^{3333} & C^{1233} & C^{2333} & C^{1333} \\ C^{1112} & C^{2212} & C^{3312} & C^{1212} & C^{2312} & C^{1312} \\ C^{1123} & C^{2223} & C^{3323} & C^{1223} & C^{2323} & C^{1323} \\ C^{1113} & C^{2213} & C^{3313} & C^{1213} & C^{2313} & C^{1313} \end{bmatrix}$$

$$\underline{\mathbf{S}} = [S_{11} \ S_{22} \ S_{33} \ S_{12} \ S_{23} \ S_{13}]^T$$

$$\underline{\mathbf{E}} = [E_{11} \ E_{22} \ E_{33} \ 2E_{12} \ 2E_{23} \ 2E_{13}]^T.$$

The factor 2 in front of the shear strain components is essential for the validity of (3.23).

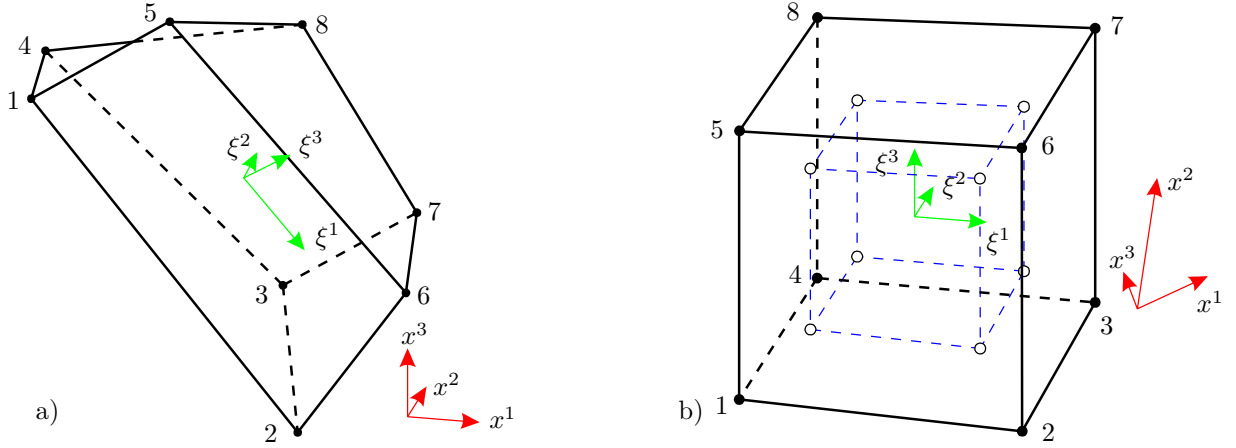


Figure 3.1: Arbitrary H1-element in (a) global cartesian and (b) natural representation. Element nodes are displayed and consistently numbered in (a) and (b); integration points displayed in (b) only.

3.2.2 The H1-element (UL)

This hexahedral element is formed by eight corner nodes which define a natural coordinate system $\{\xi^1, \xi^2, \xi^3\}$, such that the nodal coordinates $\hat{\xi}_n^i$ are either 1 or -1 , and $x_i(\boldsymbol{\xi}) = h_n(\boldsymbol{\xi}) \hat{x}_i^n$.¹ The partition of unity $\sum_n h_n(\boldsymbol{\xi}) = 1$ and $h_n(\hat{\boldsymbol{\xi}}_m) = \delta_n^m$ may be deduced from (3.14) as mandatory requirements for the description of rigid body movements and for the consistency of the element mesh. Trilinear shape functions are established as the standard approach to meet those requirements.

$$h_n(\boldsymbol{\xi}) = \frac{1}{8}(1 + \hat{\xi}_n^1 \xi^1)(1 + \hat{\xi}_n^2 \xi^2)(1 + \hat{\xi}_n^3 \xi^3) \quad (3.24)$$

In accordance with (A.50), the Jacobian matrix \mathbf{J} is introduced as $J_{ij} = \partial x_j / \partial \xi^i$. This allows for the calculation of displacement derivatives with respect to global coordinates, and thus leads to the strain items of (3.10) and (3.12).

$$u_{i,\mathbf{x}}(\mathbf{x}) = h_{n,\mathbf{x}}(\mathbf{x}) \hat{u}_i^n = \mathbf{J}^{-1} h_{n,\boldsymbol{\xi}}(\boldsymbol{\xi}(\mathbf{x})) \hat{u}_i^n \quad (3.25)$$

Finally, equations (3.18) to (3.22) may be evaluated numerically after substituting dV by $\det \mathbf{J} d\xi^1 d\xi^2 d\xi^3$ and setting the respective integration intervals to $\{-1, 1\}$.

An interpolation matrix $\mathbf{h}(\mathbf{x})$ based on (3.14) and strain-displacement matrices $\mathbf{b}(\mathbf{x})$

¹ As any variable in this chapter refers to the elements domain, the upper index e as well as a special notation for interpolated quantities are omitted. n and m denote node numbers, i runs through the coordinates. In subsequent chapters h_n will be written as h^n due to lack of space.

are introduced for convenient notation, such that

$$\Delta \mathbf{u} = \mathbf{h}(\mathbf{x}) \Delta \hat{\mathbf{u}} \quad \text{and} \quad \Delta \underline{\mathbf{e}} = \mathbf{b}_1(\mathbf{x}) \Delta \hat{\mathbf{u}}. \quad (3.26)$$

Neither in TL nor UL description, the linear mapping through \mathbf{b}_1 is sufficient for the consideration of arbitrary great deformations. For example, the stiffness matrix provided in (3.20) is generally subdivided into

$$\mathbf{K}_e = \mathbf{K}_l + \mathbf{K}_{nl} = \int_V \mathbf{b}_l^T \underline{\underline{\mathbf{c}}} \mathbf{b}_l dV + \int_V \mathbf{b}_{nl}^T \underline{\underline{\boldsymbol{\tau}}}^* \mathbf{b}_{nl} dV \quad (3.27)$$

where \mathbf{b}_{nl} is nonlinear in terms of the shape functions. The remaining items are assembled to

$$\hat{\mathbf{f}}_{\text{int}} = \int_V \mathbf{b}_l^T \underline{\underline{\boldsymbol{\tau}}} dV \quad (3.28)$$

$$\mathbf{M} = \int_V \rho \mathbf{h}_1^T \mathbf{h}_1 dV. \quad (3.29)$$

The interpolation matrices \mathbf{h}_1 , \mathbf{b}_l , \mathbf{b}_{nl} of the H1-element are provided in basic FEM textbooks, and are reproduced in section 3.2.4. The two different arrangements $\underline{\underline{\boldsymbol{\tau}}}$ and $\underline{\underline{\boldsymbol{\tau}}}^*$ of the Kirchhoff stress will be elaborated there as well, along with the extension to viscous behavior.

\mathbf{M} denotes the consistent mass matrix in (3.29). In most dynamic analyses, diagonal lumped mass matrices are used instead [Hinton et al. 1976], assigning the elements mass directly to its nodes. This leads to small errors concerning angular momentum. As long as the motion is not dominated by highly accelerated rotations, these errors are of little significance, and become irrelevant with decreasing element size.

All integrals are numerically evaluated using full quadrature (i.e. by use of eight integration points, see (A.67)).

3.2.3 Volumetric locking

Displacement based elements of low order are known to develop spurious locking effects during the analysis of near-incompressibility problems. This includes the simulation of rubber-like materials, and of biologic tissues whose major component is water.

For infinitesimal deformations and linear elasticity, the locking effect can be explained as in [Freischläger 2000]: Separating an element's deformation energy into volumetric and

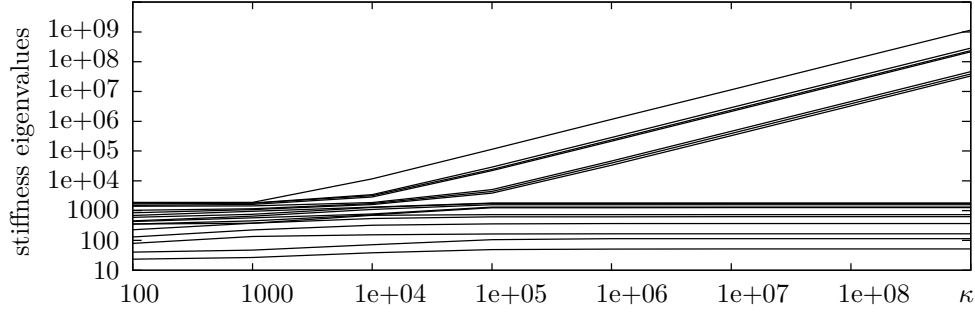


Figure 3.2: 6 of the 18 non-zero eigenvalues of an H1 element increase unboundedly along with the bulk modulus κ .

deviatoric contributions gives

$$\begin{aligned}
 \Pi_{\text{int}} &= \Pi_{\text{dev}} + \Pi_{\text{vol}} \\
 &= G \int_{\mathcal{V}} \boldsymbol{\epsilon}_{\text{dev}} : \boldsymbol{\epsilon}_{\text{dev}} \, dV + \frac{3}{2} \kappa \int_{\mathcal{V}} \boldsymbol{\epsilon}_{\text{vol}} : \boldsymbol{\epsilon}_{\text{vol}} \, dV \\
 &= G \int_{\mathcal{V}} (\boldsymbol{\epsilon}_{\text{dev}})^2 \, dV + \frac{\kappa}{2} \int_{\mathcal{V}} (\text{tr } \boldsymbol{\epsilon})^2 \, dV
 \end{aligned} \tag{3.30}$$

with $\boldsymbol{\epsilon}_{\text{vol}} = \text{tr } \boldsymbol{\epsilon} \cdot \mathbf{I}$ and $\boldsymbol{\epsilon}_{\text{dev}} = \boldsymbol{\epsilon} - \boldsymbol{\epsilon}_{\text{vol}}$. For near-incompressible materials, the bulk modulus κ is typically several orders of magnitude greater than the shear modulus G . Equation (3.30) illustrates the pointwise equivalence of material incompressibility ($\kappa = \infty$) and a kinetic constraint $\text{tr } \boldsymbol{\epsilon} = 0$. Also, with $\kappa \rightarrow \infty$ and $\text{tr } \boldsymbol{\epsilon} \neq 0$ anywhere in the element the second term is of positive value, and becomes significant for very small $\text{tr } \boldsymbol{\epsilon}$. This insight can be extended to the nonlinear case with

$$\Delta \Pi_{\text{vol}} = \kappa \int_{\mathcal{V}} (J - 1) \Delta J \, dV \tag{3.31}$$

which equals zero only if the dilatation $J=1$ throughout the element and not just in an integral sense. Therefore even small volume preserving nodal displacements may result in $\Pi_{\text{vol}} \gg \Pi_{\text{dev}}$, corresponding to a spurious increase of the element's stiffness.

An eigenvalue analysis (Fig. 3.2) illustrates the coupling of isovolumetric deformation modes to an increasing bulk modulus. This effect is less pronounced in higher-order elements. However, in large-scale computations first-order approaches are often preferred due to their inherent simplicity and efficiency. Also, higher order elements tend to be more difficult to manage in terms of automated mesh generation, model manipulations and the simulation of interaction phenomena such as contact or friction.

Incompressibility locking occurs in two-dimensional elements as well, and solutions to

the problem have been proposed as early as in the mid-seventies. Subsequent proposals to inhibit locking in volume elements were based on mixed variational formulations, penalty methods, B-matrix manipulations, enhanced natural and assumed strain concepts, sub-grid methods, and on reduced or selective numerical integration. Some of those methods have been shown to be equivalent or to lead to identical results under certain conditions [Yeo 1996, Djoko et al. 2004, Zhang et al. 2007]. On the other hand, some more recent elements incorporate several of those methods in order to compensate for disadvantages in special cases of geometrical nonlinearity and material behavior, and to provide a reasonable compromise between the contradicting objectives element performance (distortion insensitivity, coarse mesh accuracy, convergence behavior), computational costs, general applicability, and implementational effort. An outline on various approaches is given in the appendix A.3.

3.2.4 The $\bar{\mathbf{F}}$ -bar element

The name F-bar (or $\bar{\mathbf{F}}$) denotes elements with a modified deformation gradient in general. Nonlinear EAS-elements [Simo et al. 1993] with $\bar{\mathbf{F}} = \mathbf{F} + \tilde{\mathbf{F}}$ belong to that group, but subsequently only modifications to the volumetric part of the deformation gradient shall be considered. This limitation is reasonable as only volumetric locking poses problems in the given context, and the additive enhancement of the EAS-elements does not reliably prevent locking for the large deformation incompressible case [see De Souza Neto et al. 1996, Wriggers and Reese 1997, Freischläger 2000].

Based on the volumetric decomposition of the deformation gradient $\mathbf{F} = \mathbf{F}_{\text{vol}} \mathbf{F}_{\text{dev}} = J^{\frac{1}{3}} \mathbf{F}_{\text{dev}}$ the modification of \mathbf{F} is performed by introducing an assumed element variable θ to replace the compatible dilatation J .

$$\bar{\mathbf{F}} = \left(\frac{\theta}{J} \right)^{\frac{1}{3}} \mathbf{F} \quad (3.32)$$

As shown in section 3.2.3, θ needs to be constant in the elements domain in order to circumvent volumetric locking.

To derive an appropriate θ , one might start from a Hu-Washizu functional typical for mixed methods, with independent strain ($\bar{\mathbf{F}}$), pressure (p), and dilatation (θ) fields.

$$\Pi_{\text{int}} = \int W(\bar{\mathbf{F}}) dV + \int p(J - \theta) dV \quad (3.33)$$

In order to derive a displacement based element, the last two terms should vanish, leading to

$$\theta = \frac{v}{V} = \frac{1}{V} \int_V J \, dV. \quad (3.34)$$

When applied on element level, this approach is also known as mean dilatation method [Nagtegaal et al. 1974], with $\theta = \theta_N$ representing the exact ratio between current and referenced element volume. A less expensive approach with no variational basis was proposed for 2D by Moran et al. [1990].

$$\theta_M = J_c \quad (3.35)$$

The index c marks the elements center, hence θ_M matches the volume ratio precisely only for parallel epipeds and few other selected geometries.

The modification of \mathbf{F} leads to modified strain items whose variations differ considerably from their isoparametric counterparts. To derive a more general formulation, the exponent $\frac{1}{3}$ in (3.32) will be replaced by $\frac{k}{3}$. According to the value of k , a weighted modification between the pure isoparametric element ($k=0$) and a pure F-bar element ($k=1$) is available.

The modification (3.32) has to be applied to every deformation item. Adopting the same linearization rules as for (3.8) gives¹

$$\Delta \bar{\mathbf{e}} = \Delta \mathbf{e} + \frac{k}{3} \left(\frac{\Delta \theta}{\theta} - \frac{\Delta J}{J} \right) \mathbf{I} \quad (3.36)$$

$$\begin{aligned} \Delta \delta \bar{\mathbf{e}} &= \Delta \delta \mathbf{e} + \frac{2k}{3} \left(\frac{\delta \theta}{\theta} - \frac{\delta J}{J} \right) \Delta \mathbf{e} + \frac{2k}{3} \left(\frac{\Delta \theta}{\theta} - \frac{\Delta J}{J} \right) \delta \mathbf{e} \\ &\quad + \frac{2k^2}{9} \left(\frac{\delta \theta}{\theta} - \frac{\delta J}{J} \right) \left(\frac{\Delta \theta}{\theta} - \frac{\Delta J}{J} \right) \mathbf{I} \\ &\quad + \frac{k}{3} \left(\frac{\Delta J \delta J}{J^2} - \frac{\Delta \theta \delta \theta}{\theta^2} \right) \mathbf{I} + \frac{k}{3} \left(\frac{\Delta \delta \theta}{\theta} - \frac{\Delta \delta J}{J} \right) \mathbf{I} \end{aligned} \quad (3.37)$$

¹ Since linearized and variational expressions are formally identical, the latter is not quoted.

$$\begin{aligned}
\Delta \bar{\mathbf{e}} &= \Delta \mathbf{e} + \frac{2k}{3} \left(\frac{\dot{\theta}}{\theta} - \frac{\dot{J}}{J} \right) \Delta \mathbf{e} + \frac{2k}{3} \left(\frac{\Delta \theta}{\theta} - \frac{\Delta J}{J} \right) \dot{\mathbf{e}} \\
&+ \frac{2k^2}{9} \left(\frac{\dot{\theta}}{\theta} - \frac{\dot{J}}{J} \right) \left(\frac{\Delta \theta}{\theta} - \frac{\Delta J}{J} \right) \mathbf{I} \\
&+ \frac{k}{3} \left(\frac{\Delta J}{J^2} \dot{J} - \frac{\Delta \theta}{\theta^2} \dot{\theta} \right) \mathbf{I} + \frac{k}{3} \left(\frac{\Delta \dot{\theta}}{\theta} - \frac{\Delta \dot{J}}{J} \right) \mathbf{I}.
\end{aligned} \tag{3.38}$$

A modification operator $\langle \cdot \rangle$ is introduced, such that the assumed dilatation may be defined as $\theta = \langle J \rangle$. Based on the approaches of Nagtegaal and Moran, it is specified as

$$\langle \cdot \rangle_N = \frac{1}{V} \int \cdot \, dV \quad \text{and} \quad \langle \cdot \rangle_M = \cdot_c. \tag{3.39}$$

The unresolved expressions in the above equations may now be determined as

$$\begin{aligned}
\frac{\delta J}{J} &= \delta u_{k;k} & \frac{\Delta J}{J} &= \Delta u_{k;k} & \frac{\Delta \delta J}{J} &= \Delta u_{k;k} \delta u_{l;l} - \Delta u_{k;l} \delta u_{l;k} \\
\frac{\dot{J}}{J} &= \dot{u}_{k;k} & \frac{\Delta \dot{J}}{J} &= \Delta u_{k;k} \dot{u}_{l;l} + \Delta \dot{u}_{k;k} - \Delta u_{k;l} \delta u_{l;k}
\end{aligned} \tag{3.40}$$

and

$$\begin{aligned}
\frac{\delta \theta}{\theta} &= \langle \delta u_{k;k} \rangle & \frac{\Delta \theta}{\theta} &= \langle \Delta u_{k;k} \rangle & \frac{\Delta \delta \theta}{\theta} &= \langle \Delta u_{k;k} \delta u_{l;l} \rangle - \langle \Delta u_{k;l} \delta u_{l;k} \rangle \\
\frac{\dot{\theta}}{\theta} &= \langle \dot{u}_{k;k} \rangle & \frac{\Delta \dot{\theta}}{\theta} &= \langle \Delta u_{k;k} \dot{u}_{l;l} \rangle + \langle \Delta \dot{u}_{k;k} \rangle - \langle \Delta u_{k;l} \delta u_{l;k} \rangle.
\end{aligned} \tag{3.41}$$

$\delta \bar{\mathbf{e}}$, $\Delta \bar{\mathbf{e}}$, $\Delta \delta \bar{\mathbf{e}}$ and $\Delta \dot{\bar{\mathbf{e}}}$ are hereby entirely resolved in component form. Hence, equations (3.19), (3.20) and (3.21) may be discretized anew, utilizing the modified instead of the regular deformation quantities. In the subsequent expressions, the material's responses to the modified deformations will be marked by an overbar, i.e. $\bar{\tau}$, $\bar{\mathbf{e}}$, and $\bar{\mathbf{v}}$.

Eq. (3.38) merits special attention. Like $\Delta \mathbf{e}$ in (3.12), $\Delta \bar{\mathbf{e}}$ depends on $\Delta \mathbf{u}$ and $\Delta \dot{\mathbf{u}}$ alike. Therefore, it contributes to both, damping and stiffness matrix.

3.2.4.1 The static case

Analogously to (3.28), the element forces of an F-bar element are

$$\hat{\mathbf{f}} = \int \bar{\mathbf{b}}_1^T \bar{\boldsymbol{\tau}} \, dV \tag{3.42}$$

and, disregarding viscosity and thereby \mathbf{K}_v , the stiffness matrix is derived in the form $\mathbf{K} = \mathbf{K}_l + \mathbf{K}_{nl1} + \mathbf{K}_{nl2}$ as

$$\mathbf{K}_l = \int \bar{\mathbf{b}}_l^T \underline{\underline{\mathbf{c}}} \bar{\mathbf{b}}_l dV \quad (3.43)$$

$$\mathbf{K}_{nl1} = \int \mathbf{b}_{nl}^T \underline{\underline{\boldsymbol{\tau}}}^* \mathbf{b}_{nl} dV \quad (3.44)$$

$$\begin{aligned} \mathbf{K}_{nl2} = & \frac{2k}{3} \int \mathbf{b}_l^T \underline{\underline{\boldsymbol{\tau}}} \bar{\mathbf{h}}_1 dV + \frac{2k}{3} \int \bar{\mathbf{h}}_1^T \underline{\underline{\boldsymbol{\tau}}}^T \mathbf{b}_l dV + \frac{2k^2}{9} \int \text{tr} \bar{\boldsymbol{\tau}} \bar{\mathbf{h}}_1^T \bar{\mathbf{h}}_1 dV \\ & + \frac{k}{3} \int \text{tr} \bar{\boldsymbol{\tau}} \bar{\mathbf{h}}_2 dV + \frac{k}{3} \int \text{tr} \bar{\boldsymbol{\tau}} \bar{\mathbf{h}}_3 dV. \end{aligned} \quad (3.45)$$

Internal force vector and linear stiffness matrix do not differ from their H1 complements, except for the use of the modified strain and, consequently, of $\bar{\mathbf{b}}_l$ instead of \mathbf{b}_l . The analogy is likewise evident for the nonlinear stiffness, as \mathbf{K}_{nl1} corresponds to the nonlinear expression of the conventional element. However, \mathbf{K}_{nl2} is inherent to the F-bar elements solely.

The strain-displacement matrices introduced in the equations above are given as

$$\mathbf{b}_l = [\mathbf{b}_l^1 \dots \mathbf{b}_l^8]_{6 \times 24} \quad \mathbf{b}_{nl} = [\mathbf{b}_{nl}^1 \dots \mathbf{b}_{nl}^8]_{9 \times 24} \quad \bar{\mathbf{b}}_l = [\bar{\mathbf{b}}_l^1 \dots \bar{\mathbf{b}}_l^8]_{6 \times 24} \quad (3.46)$$

with the following submatrices.

$$\mathbf{b}_l^n = \begin{bmatrix} h_{;1}^n & 0 & 0 \\ 0 & h_{;2}^n & 0 \\ 0 & 0 & h_{;3}^n \\ h_{;2}^n & h_{;1}^n & 0 \\ 0 & h_{;3}^n & h_{;2}^n \\ h_{;3}^n & 0 & h_{;1}^n \end{bmatrix}_{6 \times 3} \quad \mathbf{b}_{mod}^n = \begin{bmatrix} \langle h_{;1}^n \rangle - h_{;1}^n & \langle h_{;2}^n \rangle - h_{;2}^n & \langle h_{;3}^n \rangle - h_{;3}^n \\ \langle h_{;1}^n \rangle - h_{;1}^n & \langle h_{;2}^n \rangle - h_{;2}^n & \langle h_{;3}^n \rangle - h_{;3}^n \\ \langle h_{;1}^n \rangle - h_{;1}^n & \langle h_{;2}^n \rangle - h_{;2}^n & \langle h_{;3}^n \rangle - h_{;3}^n \\ 0 & 0 & 0 \\ 0 & 0 & 0 \\ 0 & 0 & 0 \end{bmatrix}_{6 \times 3}$$

$$\mathbf{b}_{nl}^n = \begin{bmatrix} (h_{;x}^n)^T & \mathbf{0} & \mathbf{0} \\ \mathbf{0} & (h_{;x}^n)^T & \mathbf{0} \\ \mathbf{0} & \mathbf{0} & (h_{;x}^n)^T \end{bmatrix}_{9 \times 3} \quad \bar{\mathbf{b}}_l^n = \mathbf{b}_l^n + \frac{k}{3} \mathbf{b}_{mod}^n$$

Additionally, some strain-interpolation and stress matrices are used which do not corre-

spend to terms in the conventional formulation:

$$\begin{aligned} \bar{\mathbf{h}}_1 &= \begin{bmatrix} \bar{\mathbf{h}}_1^1 & \dots & \bar{\mathbf{h}}_1^8 \end{bmatrix}_{1 \times 24} \\ \bar{\mathbf{h}}_2 &= \begin{bmatrix} \bar{\mathbf{h}}_2^{11} & & \\ & \ddots & \\ & & \bar{\mathbf{h}}_2^{88} \end{bmatrix}_{24 \times 24} \quad \bar{\mathbf{h}}_3 = \begin{bmatrix} \bar{\mathbf{h}}_3^{11} & & \\ & \ddots & \\ & & \bar{\mathbf{h}}_3^{88} \end{bmatrix}_{24 \times 24} \quad \bar{\underline{\underline{\tau}}}^* = \begin{bmatrix} \bar{\underline{\underline{\tau}}} & \mathbf{0} & \mathbf{0} \\ \mathbf{0} & \bar{\underline{\underline{\tau}}} & \mathbf{0} \\ \mathbf{0} & \mathbf{0} & \bar{\underline{\underline{\tau}}} \end{bmatrix}_{9 \times 9} \end{aligned} \quad (3.47)$$

with

$$\begin{aligned} \bar{\mathbf{h}}_1^n &= \begin{bmatrix} \langle \mathbf{h}_{,\mathbf{x}}^n \rangle - \mathbf{h}_{,\mathbf{x}}^n \end{bmatrix}_{1 \times 3} \\ \bar{\mathbf{h}}_2^{mn} &= \begin{bmatrix} \mathbf{h}_{,1}^m \mathbf{h}_{,1}^n - \langle \mathbf{h}_{,1}^m \mathbf{h}_{,1}^n \rangle & \mathbf{h}_{,2}^m \mathbf{h}_{,1}^n - \langle \mathbf{h}_{,2}^m \mathbf{h}_{,1}^n \rangle & \mathbf{h}_{,3}^m \mathbf{h}_{,1}^n - \langle \mathbf{h}_{,3}^m \mathbf{h}_{,1}^n \rangle \\ \mathbf{h}_{,1}^m \mathbf{h}_{,2}^n - \langle \mathbf{h}_{,1}^m \mathbf{h}_{,2}^n \rangle & \mathbf{h}_{,2}^m \mathbf{h}_{,2}^n - \langle \mathbf{h}_{,2}^m \mathbf{h}_{,2}^n \rangle & \mathbf{h}_{,3}^m \mathbf{h}_{,2}^n - \langle \mathbf{h}_{,3}^m \mathbf{h}_{,2}^n \rangle \\ \mathbf{h}_{,1}^m \mathbf{h}_{,3}^n - \langle \mathbf{h}_{,1}^m \mathbf{h}_{,3}^n \rangle & \mathbf{h}_{,2}^m \mathbf{h}_{,3}^n - \langle \mathbf{h}_{,2}^m \mathbf{h}_{,3}^n \rangle & \mathbf{h}_{,3}^m \mathbf{h}_{,3}^n - \langle \mathbf{h}_{,3}^m \mathbf{h}_{,3}^n \rangle \end{bmatrix}_{3 \times 3} \\ \bar{\mathbf{h}}_3^{mn} &= \begin{bmatrix} \langle \mathbf{h}_{,1}^m \mathbf{h}_{,1}^n \rangle - \langle \mathbf{h}_{,1}^m \rangle \langle \mathbf{h}_{,1}^n \rangle & 0 & 0 \\ 0 & \langle \mathbf{h}_{,2}^m \mathbf{h}_{,2}^n \rangle - \langle \mathbf{h}_{,2}^m \rangle \langle \mathbf{h}_{,2}^n \rangle & 0 \\ 0 & 0 & \langle \mathbf{h}_{,3}^m \mathbf{h}_{,3}^n \rangle - \langle \mathbf{h}_{,3}^m \rangle \langle \mathbf{h}_{,3}^n \rangle \end{bmatrix}_{3 \times 3} \end{aligned}$$

The terms of $\bar{\mathbf{h}}_3$ become zero for assumed dilatations like Moran's θ_M which is evaluated at only one specific point of the element.

3.2.4.2 The viscous case

The consideration of general viscosity results in the appearance of damping and viscous stiffness matrix \mathbf{D} and \mathbf{K}_v , as shown in (3.21). Their separate deduction from (3.21) is straightforward, once the component description of $\Delta \bar{\bar{\mathbf{e}}}$ is derived from (3.38) ff.:

$$\Delta \bar{\bar{\mathbf{e}}}_{ij} = \frac{1}{2} \left(\Delta \bar{\bar{u}}_{i;j} + \Delta \bar{\bar{u}}_{j;i} + \bar{\bar{u}}_{k;i} \Delta \bar{\bar{u}}_{k;j} + \bar{\bar{u}}_{k;j} \Delta \bar{\bar{u}}_{k;i} \right) \quad (3.48)$$

with

$$\begin{aligned}\Delta \bar{u}_{i,j} &= \Delta \dot{u}_{i,j} + \frac{k}{3} \left((\langle \Delta \dot{u}_{k;k} \rangle - \Delta \dot{u}_{k;k}) \delta_{ij} + (\langle \dot{u}_{k;k} \rangle - \dot{u}_{k;k}) \Delta u_{i,j} + \right. \\ &\quad \left. (\langle \Delta u_{k;k} \rangle - \Delta u_{k;k}) \left(\dot{u}_{i,j} + \frac{k}{3} (\langle \dot{u}_{k;k} \rangle - \dot{u}_{k;k}) \delta_{ij} \right) + (\dot{u}_{k;l} \Delta u_{l,k} - \langle \dot{u}_{k;l} \Delta u_{l,k} \rangle) \delta_{ij} \right) \\ \bar{u}_{i,j} &= \dot{u}_{i,j} + \frac{k}{3} (\langle \dot{u}_{k;k} \rangle - \dot{u}_{k;k}) \delta_{ij} \\ \Delta \bar{u}_{i,j} &= \Delta u_{i,j} + \frac{k}{3} (\langle \Delta u_{k;k} \rangle - \Delta u_{k;k}) \delta_{ij}.\end{aligned}$$

Collecting those terms which are associated with either $\Delta \dot{\mathbf{u}}$ or $\Delta \mathbf{u}$ and subsequent discretization gives

$$\mathbf{D} = \int \bar{\mathbf{b}}_1^T \underline{\underline{\mathbf{v}}} \bar{\mathbf{b}}_1 dV \quad (3.49)$$

$$\mathbf{K}_v = \int \mathbf{b}_v^T \underline{\underline{\mathbf{v}}} \bar{\mathbf{b}}_1 dV \quad (3.50)$$

with $\bar{\mathbf{b}}_1$ from (3.46) and

$$\mathbf{b}_v = [\mathbf{b}_v^1 \dots \mathbf{b}_v^8]_{6 \times 24} \quad \mathbf{b}_v^n = \mathbf{b}_{v1}^n + \frac{k}{3} \left(2\mathbf{b}_{v2}^n + \mathbf{b}_{v3}^n - \langle \mathbf{b}_{v3}^n \rangle + (\langle \dot{\mathbf{u}}_{k;k} \rangle - \dot{\mathbf{u}}_{k;k}) \bar{\mathbf{b}}_1^n \right). \quad (3.51)$$

The three additional matrices which occur only in the viscous context read

$$\begin{aligned}\mathbf{b}_{v1}^n &= \begin{bmatrix} \bar{u}_{1,1} h_{,1}^n & \bar{u}_{2,1} h_{,1}^n & \bar{u}_{3,1} h_{,1}^n \\ \bar{u}_{1,2} h_{,2}^n & \bar{u}_{2,2} h_{,2}^n & \bar{u}_{3,2} h_{,2}^n \\ \bar{u}_{1,3} h_{,3}^n & \bar{u}_{2,3} h_{,3}^n & \bar{u}_{3,3} h_{,3}^n \\ \bar{u}_{1,1} h_{,2}^n + \bar{u}_{1,2} h_{,1}^n & \bar{u}_{2,1} h_{,2}^n + \bar{u}_{2,2} h_{,1}^n & \bar{u}_{3,1} h_{,2}^n + \bar{u}_{3,2} h_{,1}^n \\ \bar{u}_{1,2} h_{,3}^n + \bar{u}_{1,3} h_{,2}^n & \bar{u}_{2,2} h_{,3}^n + \bar{u}_{2,3} h_{,2}^n & \bar{u}_{3,2} h_{,3}^n + \bar{u}_{3,3} h_{,2}^n \\ \bar{u}_{1,1} h_{,3}^n + \bar{u}_{1,3} h_{,1}^n & \bar{u}_{2,1} h_{,3}^n + \bar{u}_{2,3} h_{,1}^n & \bar{u}_{3,1} h_{,3}^n + \bar{u}_{3,3} h_{,1}^n \end{bmatrix}_{6 \times 3} \\ \mathbf{b}_{v2}^n &= \begin{bmatrix} \bar{u}_{1,1} (\langle h_{,1}^n \rangle - h_{,1}^n) & \bar{u}_{1,1} (\langle h_{,2}^n \rangle - h_{,2}^n) & \bar{u}_{1,1} (\langle h_{,3}^n \rangle - h_{,3}^n) \\ \bar{u}_{2,2} (\langle h_{,1}^n \rangle - h_{,1}^n) & \bar{u}_{2,2} (\langle h_{,2}^n \rangle - h_{,2}^n) & \bar{u}_{2,2} (\langle h_{,3}^n \rangle - h_{,3}^n) \\ \bar{u}_{3,3} (\langle h_{,1}^n \rangle - h_{,1}^n) & \bar{u}_{3,3} (\langle h_{,2}^n \rangle - h_{,2}^n) & \bar{u}_{3,3} (\langle h_{,3}^n \rangle - h_{,3}^n) \\ (\bar{u}_{1,2} + \bar{u}_{2,1}) (\langle h_{,1}^n \rangle - h_{,1}^n) & (\bar{u}_{1,2} + \bar{u}_{2,1}) (\langle h_{,2}^n \rangle - h_{,2}^n) & (\bar{u}_{1,2} + \bar{u}_{2,1}) (\langle h_{,3}^n \rangle - h_{,3}^n) \\ (\bar{u}_{2,3} + \bar{u}_{3,2}) (\langle h_{,1}^n \rangle - h_{,1}^n) & (\bar{u}_{2,3} + \bar{u}_{3,2}) (\langle h_{,2}^n \rangle - h_{,2}^n) & (\bar{u}_{2,3} + \bar{u}_{3,2}) (\langle h_{,3}^n \rangle - h_{,3}^n) \\ (\bar{u}_{1,3} + \bar{u}_{3,1}) (\langle h_{,1}^n \rangle - h_{,1}^n) & (\bar{u}_{1,3} + \bar{u}_{3,1}) (\langle h_{,2}^n \rangle - h_{,2}^n) & (\bar{u}_{1,3} + \bar{u}_{3,1}) (\langle h_{,3}^n \rangle - h_{,3}^n) \end{bmatrix}_{6 \times 3}\end{aligned}$$

$$\mathbf{b}_{v3}^n = \begin{bmatrix} \bar{u}_{1,1}h_{,1}^n + \bar{u}_{2,1}h_{,2}^n + \bar{u}_{3,1}h_{,3}^n & \bar{u}_{1,2}h_{,1}^n + \bar{u}_{2,2}h_{,2}^n + \bar{u}_{3,2}h_{,3}^n & \bar{u}_{1,3}h_{,1}^n + \bar{u}_{2,3}h_{,2}^n + \bar{u}_{3,3}h_{,3}^n \\ \bar{u}_{1,1}h_{,1}^n + \bar{u}_{2,1}h_{,2}^n + \bar{u}_{3,1}h_{,3}^n & \bar{u}_{1,2}h_{,1}^n + \bar{u}_{2,2}h_{,2}^n + \bar{u}_{3,2}h_{,3}^n & \bar{u}_{1,3}h_{,1}^n + \bar{u}_{2,3}h_{,2}^n + \bar{u}_{3,3}h_{,3}^n \\ \bar{u}_{1,1}h_{,1}^n + \bar{u}_{2,1}h_{,2}^n + \bar{u}_{3,1}h_{,3}^n & \bar{u}_{1,2}h_{,1}^n + \bar{u}_{2,2}h_{,2}^n + \bar{u}_{3,2}h_{,3}^n & \bar{u}_{1,3}h_{,1}^n + \bar{u}_{2,3}h_{,2}^n + \bar{u}_{3,3}h_{,3}^n \\ 0 & 0 & 0 \\ 0 & 0 & 0 \\ 0 & 0 & 0 \end{bmatrix}_{6 \times 3}$$

All F-bar element matrices relevant for the linearization of the work equation (3.17) are provided at this point. The stiffness matrix has to be assembled from the linear, nonlinear and viscous components $\mathbf{K} = \mathbf{K}_1 + \mathbf{K}_{n1} + \mathbf{K}_{n2} + \mathbf{K}_v$. Damping matrix and internal force vector are calculated directly, and the mass matrix may be adopted from the regular H1 element.

Viscous stiffness and damping matrix of the H1 element may be derived from the matrix definitions of the F-bar element with $k=0$ and $\langle \cdot \rangle = \bullet$.

The previous equations describe the F-bar element the way it has been implemented, except for the usual simplifications concerning sparse matrices. Examples for the element's behavior and comparisons follow in section 3.2.7.

3.2.5 Inconsistent F-bar element

The name “F-bar element” has been used by De Souza Neto et al. [1996] for a slightly different approach to the F-bar idea. The element in concern eliminates volumetric locking as well and is less expensive than the just presented. A severe disadvantage of the formulation is the asymmetry of the stiffness matrix as shown below.

De Souza Neto et al. use the same deviatoric-volumetric split as presented before, utilizing the approach of equation (3.35):

$$\bar{\mathbf{F}} = \left(\frac{J_c}{J} \right)^{\frac{1}{3}} \mathbf{F}. \quad (3.52)$$

In contrast to the consistent method in 3.2.4 they apply this modification exclusively to the stresses in the variational formulation. With $\bar{\boldsymbol{\sigma}} = \boldsymbol{\sigma}(\bar{\mathbf{F}})$ they define

$$\delta W_{\text{int}} = \int \bar{\boldsymbol{\sigma}} : \mathring{\boldsymbol{\epsilon}} \, dv \quad (3.53)$$

for the static case.

In order to derive a more general description for this work, the exponent in (3.52) is

again expanded by k , and the assumed dilatation - not necessarily the one at the element's centroid - is denoted θ . Cauchy and Kirchhoff stress are then linked through $\bar{\boldsymbol{\sigma}} = \frac{J^{k-1}}{\theta^k} \bar{\boldsymbol{\tau}}$ and an adaptation of the previous expression to the form of equation (3.8) reads

$$\delta W_{\text{int}} = \int \left(\frac{J}{\theta} \right)^k \bar{\boldsymbol{\tau}} : \delta \mathbf{e} \, dV. \quad (3.54)$$

In contrast to (3.8) the linearization has to be conducted with respect to three terms, leading to

$$\begin{aligned} \Delta \delta W_{\text{int}} = & \int \left(\frac{J}{\theta} \right)^k \left(\frac{k}{3} \left(\frac{\Delta J}{J} - \frac{\Delta \theta}{\theta} \right) \bar{\boldsymbol{\tau}} : \delta \mathbf{e} \right. \\ & \left. + (\Delta \bar{\mathbf{e}} : \bar{\mathbf{c}} + \Delta \bar{\mathbf{e}} : \bar{\mathbf{v}}) : \delta \mathbf{e} + \bar{\boldsymbol{\tau}} : \Delta \delta \mathbf{e} \right) + \rho_0 \Delta \ddot{\mathbf{u}} \delta \mathbf{u} \, dV. \end{aligned} \quad (3.55)$$

A transformation back to the form of (3.53) would simplify this equation, but to emphasize the similarities to the consistent F-bar and isoparametric formulation, the current representation shall be kept.

3.2.5.1 The static case

When velocity and acceleration dependence are disregarded, equation (3.55) becomes

$$\begin{aligned} \Delta \delta W_{\text{int}} = & \int \left(\frac{J}{\theta} \right)^k \Delta \mathbf{e} : \bar{\mathbf{c}} : \delta \mathbf{e} \, dV + \int \left(\frac{J}{\theta} \right)^k \bar{\boldsymbol{\tau}} : \Delta \delta \mathbf{e} \, dV \\ & + \frac{k}{3} \int \left(\frac{J}{\theta} \right)^k \left(\frac{\Delta J}{J} - \frac{\Delta \theta}{\theta} \right) (\mathbf{I} \bar{\mathbf{c}} - \bar{\boldsymbol{\tau}}) : \delta \mathbf{e} \, dV. \end{aligned} \quad (3.56)$$

Again, first and second part are almost identical to the respective linear and nonlinear expressions \mathbf{K}_l and \mathbf{K}_{nl} of the isoparametric element (3.20), (3.27). As intended, only the stress and material tensor differ since they rely on the modified deformation gradient. The favorable structure of the regular strain-displacement matrix remains therefore untouched.

$$\hat{\mathbf{f}} = \int \bar{\mathbf{b}}_l^T \bar{\boldsymbol{\tau}} \, dV \quad (3.57)$$

Another advantage over the F-bar element of the previous section is the less expensive additional stiffness. However, the discretization of that last term

$$\mathbf{K}_{\text{add}} = \frac{k}{3} \int \left(\frac{J}{\theta} \right)^k \mathbf{b}_1^T (\underline{\underline{\mathbf{C}}} \mathbf{I} - \bar{\boldsymbol{\tau}}) \bar{\mathbf{h}}_1 \, dV \quad (3.58)$$

with $\mathbf{I}^T = [1 \, 1 \, 1 \, 0 \, 0 \, 0]$ and $\bar{\mathbf{h}}_1$ according to (3.47) reveals the asymmetry of the stiffness matrix. As already pointed out by the inventors, this element is very efficient in explicit calculations or in conjunction with materials that produce asymmetric tangent moduli anyway.

3.2.5.2 The viscous case

Damping and viscous additional stiffness matrices are also very similar to those of the consistent F-bar element, see (3.49) and (3.50). The mass matrix may be adopted without modification from the H1 element (3.29).

$$\mathbf{D} = \int \left(\frac{J}{\theta} \right)^k \bar{\mathbf{b}}_1^T \underline{\underline{\mathbf{D}}} \mathbf{b}_1 \, dV \quad (3.59)$$

$$\mathbf{K}_v = \int \left(\frac{J}{\theta} \right)^k \mathbf{b}_v^T \underline{\underline{\mathbf{D}}} \mathbf{b}_1 \, dV \quad (3.60)$$

The influence of viscosity leads in F-bar and H1 formulations alike to an additional viscous stiffness matrix \mathbf{K}_v which is usually asymmetric. The disadvantageous asymmetric \mathbf{K}_{add} of the inconsistent F-bar element becomes therefore irrelevant, and under arbitrary viscous conditions the element is potentially more efficient than the consistent F-bar element.

3.2.6 Reduced integration elements

The constant dilatation needed to avoid volumetric locking might as well be ensured through application of an one-point quadrature rule. The F-bar element based on the approach in (3.35) is an example which might be classified as selective reduced integration (SRI) element.¹ In [Flanagan and Belytschko 1981, Belytschko 1983] approaches to uniform reduced integration (URI) elements were published, utilizing only one integration point and thus uniform strains. This leads to huge cost reductions in explicit computations

¹ Some SRI elements are based on hybrid formulations whose additional variables are not eliminated on the element level. Those elements are not subject of this work as they require specific decoupled material descriptions.

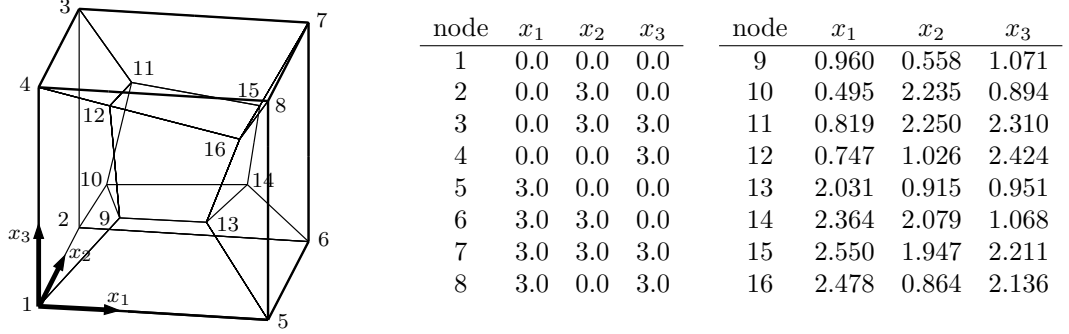


Figure 3.3: Cubical patch geometry, undeformed.

where the calculation of element forces is the most expensive task. And naturally, volumetric locking does not occur. However, in the hexahedral element, the stiffness matrix - based on six independent strain components - has twelve singular modes, on its own often leading to meaningless results globally. A stabilization of these hourglass modes is therefore essential to the application of SRI elements.

A hybrid URI-H1 element has been implemented into `SIang` for comparison. A factor k in the range of 0 to 1 is utilized, which determines how the centroid integration point is weighted against the regular eight integrations points of the H1 element.

3.2.7 Numerical tests

3.2.7.1 Patch test

The basic concept of the patch test is to check the capability of a patch of irregularly shaped elements to exactly reproduce an uniform stress state from a linear deformation state and vice versa. If an element passes the test, it appears suitable to reproduce arbitrary stress states with any desirable accuracy by means of mesh refinement. Compliance with the patch test is not imperative for a well performing element. However, it is considered of great value as validity check and test for implementation accuracy.

The geometry of the present test is taken from Hu and Nagy [1997]. The cubical patch consists of seven elements, for details see Fig. 3.3. It is subjected to a homogeneous displacement field $u_1 = x_1$, $u_2 = (x_1 + x_2)/2$, $u_3 = (2x_1 + x_2 + x_3)/5$, prescribed at the outer nodes. The position of the inner nodes is determined iteratively. A Neo-Hookean material law is utilized with the Kirchhoff stress $\boldsymbol{\tau} = (\ln J)\mathbf{I} + (\mathbf{c} - \mathbf{I})/2$. Analytical results and test deviations may be taken from Tab. 3.1.

As expected, all elements with the exception of $\bar{\mathbf{F}}_{\text{Moran}}$ and URI comply with the patch

τ	H1	maximum error [%]				
		$\bar{\mathbf{F}}_M$	$\bar{\mathbf{F}}_N$	URI _{0.99}	$i\bar{\mathbf{F}}_M$	$i\bar{\mathbf{F}}_N$
2.781	0.0	17.73	0.0	36.76	0.0	0.0
2.031	0.0	21.34	0.0	50.03	0.0	0.0
1.601	0.0	26.27	0.0	61.84	0.0	0.0
0.500	0.0	54.59	0.0	103.84	0.0	0.0
0.250	0.0	79.86	0.0	173.01	0.0	0.0
0.400	0.0	90.85	0.0	217.95	0.0	0.0

Table 3.1: Analytical Kirchhoff stress and maximum deviation in the patch. URI-element with $k = 0.99$ for convergence.

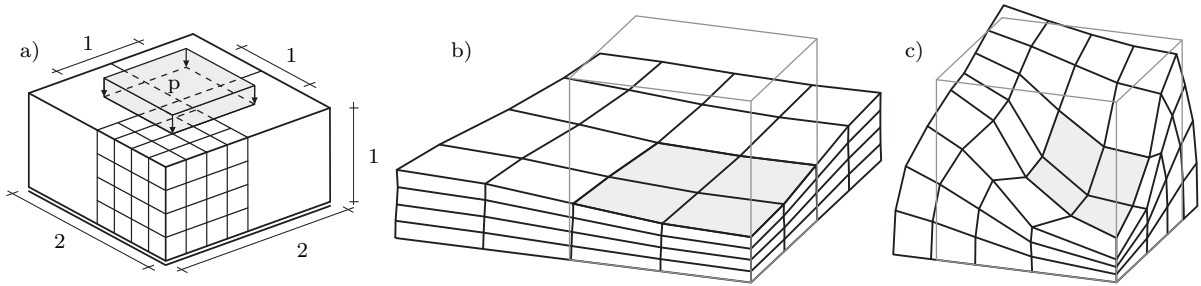


Figure 3.4: Indented block. a) Full descriptive sketch b) Quarter block: Locking (H1) c) No locking ($\bar{\mathbf{F}}$)

test. The failure of the former is caused by the element shapes which deviate significantly from parallel-pipeds. A premise to the element formulation is therefore invalid. The failure of the URI element is caused by the rank deficiency of its stiffness matrix. To enforce convergence at all, the weighting coefficient was set to $k = 0.99$, thereby slightly enhancing the URI element's stiffness matrix with that of an H1 element.

3.2.7.2 Indentation of a near-incompressible block

This test is a common tool to study the convergence behavior of finite elements in the incompressible range. It consists of a cuboid which is loaded with even pressure at the center of its upper surface. Due to symmetry constraints, only a quarter needs to be modeled (see Fig. 3.4). Here, meshes with 2, 4, 8, and 16 elements per edge were realized for all four previously introduced element types (H1, URI, $\bar{\mathbf{F}}$ and $i\bar{\mathbf{F}}$).

Fig. 3.5 shows the indentation at the center node of the upper surface with respect to mesh refinement and element type. The H1 elements display the typical locking effect, which becomes less pronounced for finer meshes due to a more homogeneous dilatation within the individual elements. Again, the URI formulation had to be enhanced in order to remain stable. With k set to 0.99, similar results are derived as with the $\bar{\mathbf{F}}$ elements. Both $\bar{\mathbf{F}}$

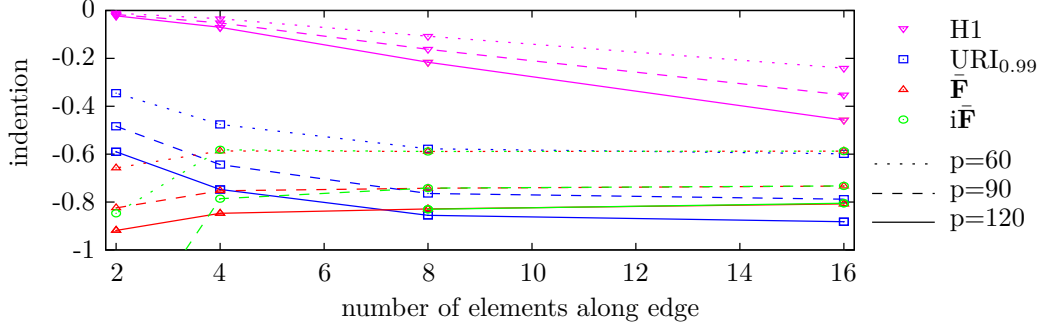


Figure 3.5: Indented block; convergence with mesh refinement. Neo-Hooke material: $\lambda=400900$ $\mu=80$.

and $\bar{\mathbf{iF}}$ elements produce very similar results for the fine mesh configuration, however, $\bar{\mathbf{iF}}$ elements were shown to be inapt for the highly distorted coarse mesh. For either element type, there was no significant difference in the results between Nagtegaal's and Moran's approaches for either element type, thus they are not distinguished in the diagram.

3.2.7.3 Eigenvalue analysis

The eigenvalues of an element provide valuable insight into its locking behavior, e.g. in section 3.2.3 and Fig. 3.2 the unphysical dependence of several eigenvalues on the bulk modulus was illustrated for the isoparametric formulation. An examination of eigenforms associated with those restrained eigenvalues reveals explicitly the critical deformation states. The modal base of a hexahedral element is depicted in Fig. 3.6, where the separation between isochore modes (a-q) and dilatation mode (r) is enforced through a very high bulk modulus. Even though the overall deformations are clearly not homogeneous for modes a-f, they feature identical dilatation values in all integration points. The latter applies to modes g-k as well. Varying dilatation values occur in modes l-q, thereby causing volumetric locking in the H1 element. The effect is illustrated in Tab. 3.2 which contains the eigenvalues of various hexahedral elements and connects them to their respective modes. The Hookean material law was adopted from [Freischläger 2000] to include the values for the EAS formulations in the comparison.

All $\bar{\mathbf{F}}$ and EAS elements display identically locking-free behavior due to the cubic element geometry. The deviations in some of the eigenvalues of the various elements affect inhomogeneous modes only. They result from the different approaches to internal displacement interpolation.

The analysis of $\bar{\mathbf{F}}$, $\bar{\mathbf{iF}}$, and URI elements with irregular shapes confirmed consistent locking-free behaviour, but deviating dilatation-eigenvalues illustrated the inaptness of the

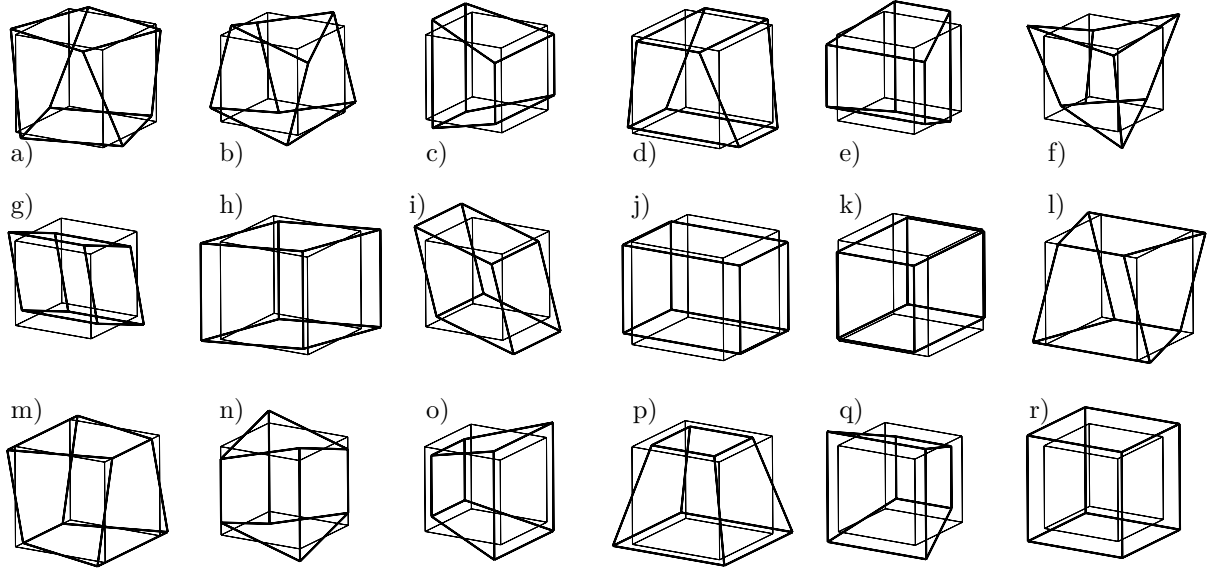


Figure 3.6: Deformation modes of hexahedral elements: torsion (a,b), bending (c-e), corotated warp (f), shear (g-i), tension (j-k), warp (l-n), frustum (o-q), dilatation (r).

mode	H1	$\bar{\mathbf{F}}/\bar{i}\bar{\mathbf{F}}$	URI	H1/P0	H1/E6	H1/E12	H1/E21
7	5.6e+00	5.6e+00	0.0e+00	5.6e+00	3.7e+00	3.7e+00	5.6e+00
8	5.6e+00	5.6e+00	0.0e+00	5.6e+00	3.7e+00	3.7e+00	5.6e+00
9	1.7e+01	6.2e+00	0.0e+00	6.2e+00	3.7e+00	3.7e+00	5.6e+00
10	1.7e+01	6.2e+00	0.0e+00	6.2e+00	5.6e+00	5.6e+00	5.6e+00
11	1.7e+01	6.2e+00	0.0e+00	6.2e+00	5.6e+00	5.6e+00	5.6e+00
12	2.2e+01	9.3e+00	0.0e+00	9.3e+00	1.7e+01	1.1e+01	1.1e+01
13	3.3e+01	9.3e+00	0.0e+00	9.3e+00	1.7e+01	1.1e+01	1.1e+01
14	3.3e+01	9.3e+00	0.0e+00	9.3e+00	1.7e+01	1.1e+01	1.1e+01
15	3.3e+01	1.7e+01	0.0e+00	1.7e+01	2.2e+01	2.2e+01	2.2e+01
16	3.3e+01	1.7e+01	0.0e+00	1.7e+01	3.3e+01	3.3e+01	3.3e+01
17	3.3e+01	1.7e+01	0.0e+00	1.7e+01	3.3e+01	3.3e+01	3.3e+01
18	9.3e+04	2.2e+01	0.0e+00	2.2e+01	3.3e+01	3.3e+01	3.3e+01
19	9.3e+04	3.3e+01	3.3e+01	3.3e+01	3.3e+01	3.3e+01	3.3e+01
20	9.3e+04	3.3e+01	3.3e+01	3.3e+01	3.3e+01	3.3e+01	3.3e+01
21	5.6e+05	3.3e+01	3.3e+01	3.3e+01	3.9e+01	3.3e+01	3.3e+01
22	5.6e+05	3.3e+01	3.3e+01	3.3e+01	3.9e+01	3.3e+01	3.3e+01
23	5.6e+05	3.3e+01	3.3e+01	3.3e+01	3.9e+01	3.3e+01	3.3e+01
24	2.5e+06	2.5e+06	2.5e+06	2.5e+06	2.5e+06	2.5e+06	2.5e+06

Table 3.2: Eigenvalues of a cubic element (geometry: $1 \times 1 \times 1$, material: $E=100$, $\nu=0.49999$). Bold values mark the homogeneous deformation modes g-k and r in Fig. 3.6. Highlighted values correspond to locking modes. Columns 5 to 8 taken from [Freischläger 2000].

Moran formulation for non-parallel edged geometries.

3.2.7.4 Linearization quality

Although each of the presented elements converges quadratically in a Newton-Raphson iteration, the number of necessary iteration steps may differ for the same problem. This is due to the specific nonlinear character of the element in concern, which directly affects the nonlinearity of the global equations. When comparing element efficiency, this effect should be taken into account, additionally to the costs on element level.

An appropriate way to derive at least a qualitative predication is to compare the tangent stiffness matrix \mathbf{K} with a pseudo-stiffness matrix \mathbf{K}_f that is assembled from the change in element forces due to a single nodal displacement Δu . In a geometrically or physically nonlinear setting, the value of that displacement Δu may have a significant impact on the result of this comparison.

The assessment is based on an error value calculated through

$$e = \frac{\left\| \mathbf{K} - \frac{\sum_i \mathbf{K}_f(\hat{\mathbf{u}} + \Delta \hat{\mathbf{u}}_i) - \mathbf{K}_f(\hat{\mathbf{u}})}{\Delta u^*} \right\|}{\|\mathbf{K}\|} \quad (3.61)$$

where $\Delta \hat{\mathbf{u}}_i$ denotes the incremental nodal displacement vector whose elements are zero except for the i -th which is Δu . Δu^* is its unit-free relative length, normalized with respect to the elements dimension. Thus, $\Delta u^* = 0.01$ corresponds to a displacement of 1% of the cubic element's edge length.

Results are shown in Fig. 3.7. A significant difference in the behavior of the various element types is not detectable, not in other tested, irregularly shaped configurations either. The error in the range $\Delta u^* < 10^{-8}$ is a result of the general computational inaccuracy, while the error which increases with Δu^* directly represents the nonlinearity in strains. Obviously, none of the implemented elements performs significantly different from the H1 element.

3.3 Solution techniques

The solutions of FE equations are trivial only for static, linear problems. Otherwise, special techniques are required to obtain solutions reliably and with the aspired accuracy. The utilized algorithms are presented in the following overview.

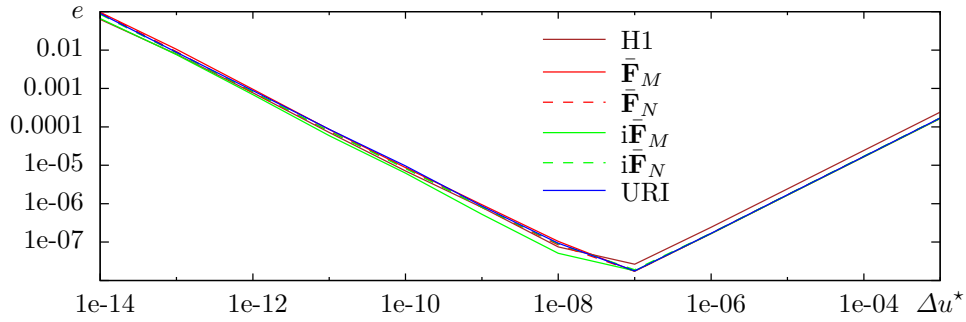


Figure 3.7: Linearization error in a hexahedral element of various types: H1, $\bar{\mathbf{F}}$, $i\bar{\mathbf{F}}$, and URI.

3.3.1 Iteration procedures

3.3.1.1 Load controlled iteration

The most frequently used algorithm to follow an equilibrium path in nonlinear calculations is the Newton-Raphson method, mathematically based on a first-order Taylor expansion of the considered function. A linearized term as given in (3.17) is therefore essential.

Starting from an equilibrium state as identified by (3.16), the next equilibrium state corresponding to a prescribed load increment is sought. The superscript (n, i) indicates a variable at load step n and iteration step i , a single index (n) marks the equilibrium state. The initial deformation state $\hat{\mathbf{u}}^{(n)}$ with the corresponding internal forces $\hat{\mathbf{f}}_{\text{int}}(\hat{\mathbf{u}}^{(n)})$ needs a modification $\Delta\hat{\mathbf{u}}^{(n+1)}$, such that

$$\hat{\mathbf{f}}_{\text{ext}}^{(n+1)} - \hat{\mathbf{f}}_{\text{int}}(\hat{\mathbf{u}}^{(n)} + \Delta\hat{\mathbf{u}}^{(n+1)}) = \mathbf{0}. \quad (3.62)$$

This reflects a purely statical approach. Defining $\hat{\mathbf{u}}^{(n+1,0)} = \hat{\mathbf{u}}^{(n)}$, $\mathbf{K}^{(n+1,i)} = \mathbf{K}(\hat{\mathbf{u}}^{(n+1,i)})$ and $\mathbf{f}^{(n+1,i)} = \mathbf{f}(\hat{\mathbf{u}}^{(n+1,i)})$, the iteration proceeds as follows:

$$\hat{\mathbf{u}}^{(n+1,i+1)} = \hat{\mathbf{u}}^{(n+1,i)} + \left(\mathbf{K}^{(n+1,i)}\right)^{-1} \left(\hat{\mathbf{f}}_{\text{ext}}^{(n+1)} - \hat{\mathbf{f}}_{\text{int}}^{(n+1,i)}\right). \quad (3.63)$$

The latter part of (3.63) represents the displacement increment at iteration step i , $\Delta\hat{\mathbf{u}}^{(n+1,i)}$, which converges to zero when equilibrium is approached. A one-dimensional interpretation is illustrated in Fig. 3.8.

The computation of the stiffness matrix and its processing is the most time consuming part of the iteration procedure. Depending on the characteristics of the problem, a modified Newton-Raphson method may prove to be more efficient: In contrast to (3.63), the stiffness matrix is not updated in every iteration step, and $\mathbf{K}^{(n+1,i)}$ is replaced by $\mathbf{K}^{(n)}$. In some

cases, the update is abdicable throughout the whole deformation process. This initial stiffness method corresponds to the substitution of $\mathbf{K}^{(n+1,i)}$ by $\mathbf{K}^{(0)}$. Both simplifications result in a significant decrease of computational effort per iteration step, at the cost of a diminished convergence rate and ability.

An effective approach to speed up convergence, especially for Newton-Raphson methods, is provided with the method of conjugated lines [Crisfield 1982] or line-search method.

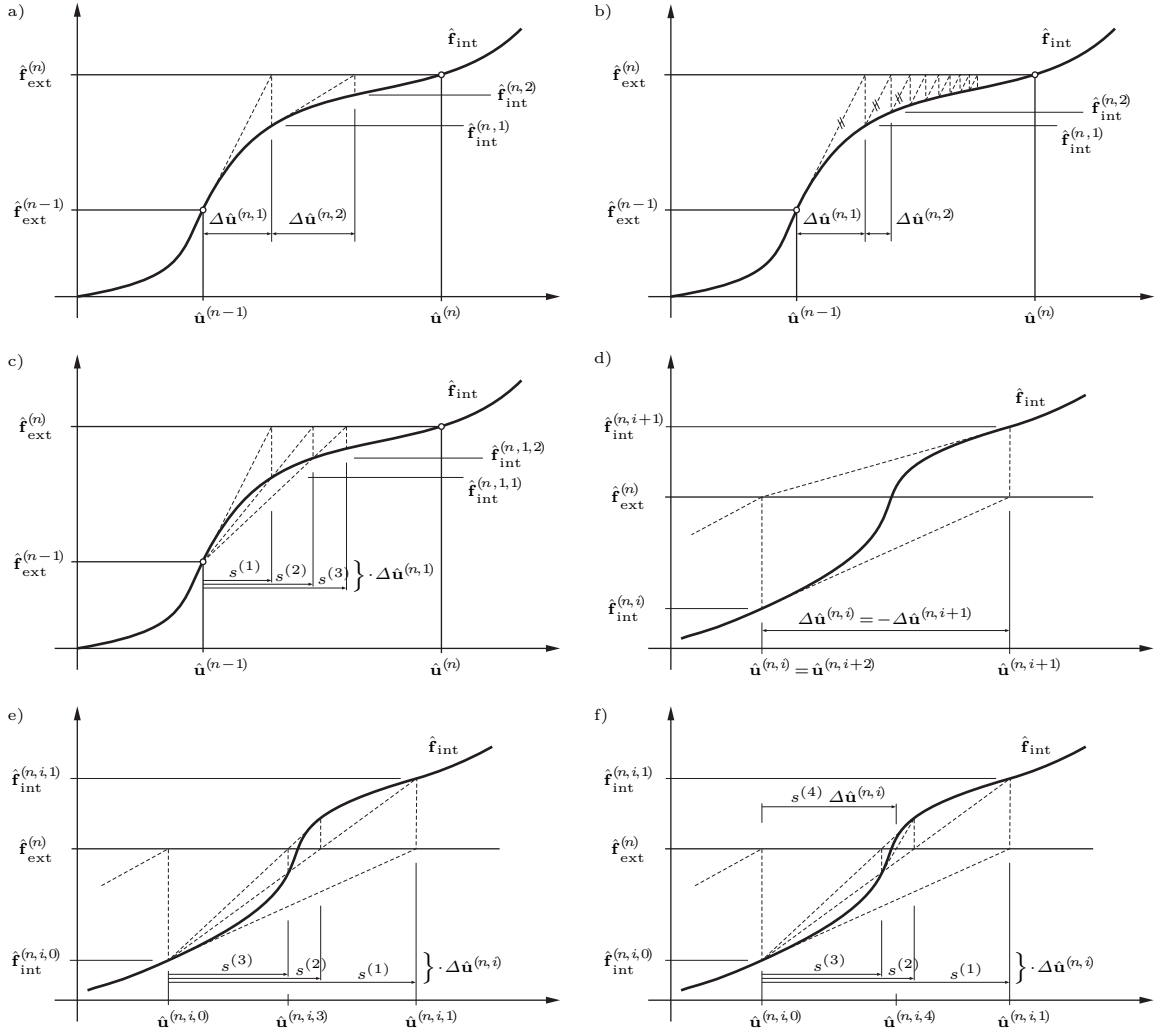


Figure 3.8: Illustration on iteration procedures a) Newton-Raphson method b) modified Newton-Raphson method c) line-search extrapolation d) divergence at inflection point e) line-search interpolation f) enhanced linesearch interpolation with $s^{(1)} = s_u^{(1)}$, $s^{(2)} = s_u^{(2)}$, $s^{(3)} = s_l^{(3)}$, $s^{(4)} = s_u^{(4)}$

3.3.1.2 Iteration acceleration

The line-search algorithm may be utilized to speed up iterative solution techniques as the above-mentioned, or to provide convergence where they would possibly fail. In contrast to manual step-length manipulation, the displacement increment $\Delta \hat{\mathbf{u}}^{(n+1,i)}$ is scaled by a factor $s^{(k)}$ which is a function of the energy increment during the iteration step. By applying this concept to (3.63) one derives

$$\hat{\mathbf{u}}^{(n+1,i+1,k)} = \hat{\mathbf{u}}^{(n+1,i)} + s^{(k)} \Delta \hat{\mathbf{u}}^{(n+1,i)} \quad (3.64)$$

with $s^{(0)}=0$ and $s^{(1)}=1$. The energy increment during the line-search substep is approximated as

$$g^{(k)} = \Delta \hat{\mathbf{u}}^{(n+1,i)} (\hat{\mathbf{f}}_{\text{ext}}^{(n+1)} - \hat{\mathbf{f}}_{\text{int}}^{(n+1,i+1,k)}) \quad (3.65)$$

and the scaling factor accordingly, evaluated by simple interpolation as

$$s^{(k+1)} = s^{(k)} \frac{g^{(0)}}{g^{(0)} - g^{(k)}}. \quad (3.66)$$

See Fig. 3.8:c,e for an illustration. A convenient enhancement of this method may be achieved by updating the referenced interpolation boundaries in (3.66). Introducing the lower and upper values s_l and s_u gives

$$s^{(k+1)} = s_l^{(k)} + (s_u^{(k)} - s_l^{(k)}) \frac{g_l^{(k)}}{g_l^{(k)} - g_u^{(k)}}. \quad (3.67)$$

Starting with $s_l^{(1)} = s^{(0)}$, $s_u^{(1)} = s^{(1)}$, $s^{(2)}$ becomes the new $s_l^{(2)}$ or $s_u^{(2)}$, depending on the value of $g^{(2)}$, which becomes either $g_l^{(2)}$ or $g_u^{(2)}$ accordingly. The line-search ends as soon as $|g^{(k)}/g^{(0)}|$ drops below a given threshold or a maximum number of steps is performed. In the latter case the applied $s^{(k)}$ is the one which refers to the smallest $|g^{(k)}|$ calculated during the procedure.

In the multidimensional case, it is necessary to restrict the maximum extrapolation range of $s^{(k)}$, as the direction of $\Delta \hat{\mathbf{u}}^{(n+1,i)}$ needs to be updated as well. This is due to the approximative character of (3.65) which is precisely orthogonal only for $k=0$. The postulation of a target $g^{(k)}=0$ is inapt for the same reason. In many cases, a conservative approach, as for example, $0.1 \leq s^{(k)} \leq 1.2$ with an enhancement threshold $|g^{(k)}/g^{(0)}| < |0.5|$

provides a significant acceleration compared to the regular Newton-Raphson iteration technique [Matthies and Strang 1979, Felippa 2001]. Still, for strong nonlinearity it appeared adequate to omit the line-search algorithm (3.65) until convergence problems indeed occur.

3.3.1.3 Displacement controlled iteration

Load controlled iteration schemes may often fail when the deformation process comprises stages of zero-stiffness, e.g. when viscous material behavior is involved. Displacement controlled methods can overcome this limitation. The base for the following approach is a distinction between degree of freedom with unknown ($\hat{\mathbf{u}}_1$) and controlled ($\hat{\mathbf{u}}_2$) nodal displacements, here handled as if assembled successively: $\hat{\mathbf{u}} = [\hat{\mathbf{u}}_1, \hat{\mathbf{u}}_2]$. This separation applies to $\hat{\mathbf{f}}_{\text{int}} = [\hat{\mathbf{f}}_{\text{int},1}, \hat{\mathbf{f}}_{\text{int},2}]$ and $\hat{\mathbf{f}}_{\text{ext}} = [\hat{\mathbf{f}}_{\text{ext},1}, \hat{\mathbf{f}}_{\text{ext},2}]$ accordingly. The stiffness matrix relating $\Delta\hat{\mathbf{f}}_{\text{int}}$ and $\Delta\hat{\mathbf{u}}$ can then be disassembled to

$$\mathbf{K} = \begin{bmatrix} \mathbf{K}_{11} & \mathbf{K}_{12} \\ \mathbf{K}_{21} & \mathbf{K}_{22} \end{bmatrix}. \quad (3.68)$$

The resultant iterative equation (3.69) is very similar to equation (3.63).

$$\hat{\mathbf{u}}_1^{(n+1,i+1)} = \hat{\mathbf{u}}_1^{(n+1,i)} + \left(\mathbf{K}_{11}^{(n+1,i)}\right)^{-1} \left(\hat{\mathbf{f}}_{\text{ext},1}^{(n+1)} - \hat{\mathbf{f}}_{\text{int},1}^{(n+1,i)} - \mathbf{K}_{12}^{(n+1,i)} \hat{\mathbf{u}}_2^{(n+1)}\right) \quad (3.69)$$

The iteration is conducted with respect to the unknown displacements only, whereas the controlled displacements act as unaffected inputs. If of interest, the external reaction forces $\mathbf{f}_{\text{ext},2}^{(n+1)}$ acting on the displacement-controlled nodes can be determined afterwards.

Approaches to reduce iteration efforts may be applied as in the previous two sections, although the omittance of the stiffness update per iteration step may have a lesser effect since only the submatrix \mathbf{K}_{11} has to be inverted.

3.3.2 Time integration

Within the spatial discretization framework of the FEM, a discretization in the time domain is indispensable in order to account for the nonlinearities during dynamic simulations. Strategies to satisfy the governing differential equations sequentially at subsequent time steps, e.g. Euler, Taylor and Runge-Kutta methods, rely on the computation of time derivatives through finite difference techniques. They are categorized as explicit or implicit, depending on whether they incorporate approximations of state variables at the respective

following time step as well. They differ in terms of solution stability, costs, and accuracy, depending specifically on the problem to be solved. For a general overview and advice on the choice of methods see for example Harrach [2017]. Here, central difference and Newmark methods are elaborated with specific focus on viscous material behavior.

3.3.2.1 Central finite difference method

Denoting successive nodal quantities at equidistant time intervals Δt by upper left indices $t - \Delta t$, t , $t + \Delta t$, \dots , the central difference approximations of the displacement derivatives read

$${}^t\dot{\mathbf{u}} = (2\Delta t)^{-1} \left({}^{t+\Delta t}\mathbf{u} - {}^{t-\Delta t}\mathbf{u} \right) \quad (3.70)$$

$${}^t\ddot{\mathbf{u}} = (\Delta t)^{-2} \left({}^{t+\Delta t}\mathbf{u} - 2{}^t\mathbf{u} + {}^{t-\Delta t}\mathbf{u} \right). \quad (3.71)$$

This follows from the application of a midpoint rule and the linearization of the velocity within the time steps. Utilizing these substitutions and lumped nodal masses for the evaluation of the equilibrium equation (3.16) at time t allows for a direct determination of the displacements ${}^{t+\Delta t}\mathbf{u}$.

$${}^{t+\Delta t}\mathbf{u} = \Delta t^2 \mathbf{M}^{-1} \left({}^t\hat{\mathbf{f}}_{\text{ext}} - {}^t\hat{\mathbf{f}}_{\text{res}} \right) + 2{}^t\mathbf{u} - {}^{t-\Delta t}\mathbf{u} \quad (3.72)$$

The accuracy and boundedness of the solution is - as with other explicit methods - contingent on whether the Δt is chosen smaller than a critical step width.

In (3.72) appears the term ${}^t\hat{\mathbf{f}}_{\text{res}}$, which may depend on nodal velocities in case of viscous materials. Accordingly, its evaluation relies on an initial assumption and subsequent iterations with ${}^{t+\Delta t}\mathbf{u}^{(i+1)} = {}^{t+\Delta t}\mathbf{u}^{(i)} + \Delta \mathbf{u}^{(i+1)}$. All methods listed in 3.3.1 are appropriate for this purpose, exemplary

$$\Delta \mathbf{u}^{(i+1)} = \left(\frac{1}{\Delta t^2} \mathbf{M} + \frac{1}{2\Delta t} {}^t\mathbf{K}_{\text{v}}^{(i)} \right)^{-1} \left({}^t\hat{\mathbf{f}}_{\text{ext}} - {}^t\hat{\mathbf{f}}_{\text{res}}^{(i)} - \mathbf{M} {}^t\ddot{\mathbf{u}}^{(i)} \right) \quad (3.73)$$

denotes the regular Newton-Raphson scheme. Herein, \mathbf{K}_{v} marks the viscosity matrix

$${}^t\mathbf{K}_{\text{v}}^{(i)} = \frac{\partial {}^t\hat{\mathbf{f}}_{\text{res}}^{(i)}}{\partial {}^t\dot{\mathbf{u}}} \quad (3.74)$$

and the factor $\frac{1}{2\Delta t}$ stems from the evaluation of $\frac{\partial {}^t\dot{\mathbf{u}}}{\partial {}^{t+\Delta t}\mathbf{u}}$ specifically for the central difference

method (3.70). This general approach could not be located in the literature. While there is a direct, non-iterative solution to (3.72) in the case of constant damping coefficients (where the damping matrix corresponds to $2 \Delta t \mathbf{K}_v$), the proposed iteration allows for the solution of coupled systems with $\hat{\mathbf{f}}_{\text{res}}(\hat{\mathbf{u}}, \dot{\hat{\mathbf{u}}}) \neq \hat{\mathbf{f}}_{\text{res}}(\hat{\mathbf{u}}) + \hat{\mathbf{f}}_{\text{res}}(\dot{\hat{\mathbf{u}}})$ as well.

The computation of the viscosity matrix contradicts the typical small-costs-per-step advantage of a central difference approach. Few occasional updates after several time steps may prove sufficient though, depending on the sensitivity of the element forces on the velocities. In case of stronger nonlinearities, the approximation quality and fitness of the central difference remains doubtful anyway, reconsidering its fundamental assumption (3.70).

The following direct iteration scheme provides a less expensive solution. However, compared to (3.73) it will more often fail to converge, as the derivatives of the internal forces are not taken into account.

$$\Delta \hat{\mathbf{u}}^{(i+1)} = \Delta t^2 \mathbf{M}^{-1} \left({}^t \hat{\mathbf{f}}_{\text{res}}^{(i-1)} - {}^t \hat{\mathbf{f}}_{\text{res}}^{(i)} \right) \quad (3.75)$$

3.3.2.2 Newmark method

When the time steps required by the central difference method are neither feasible nor demanded, other methods such as the one by Newmark [1959] may provide a robust solution more effectively. Newmark proposed

$${}^{t+\Delta t} \hat{\mathbf{u}} = {}^t \hat{\mathbf{u}} + {}^t \dot{\hat{\mathbf{u}}} \Delta t + \left((0.5 - \beta) {}^t \ddot{\hat{\mathbf{u}}} + \beta {}^{t+\Delta t} \ddot{\hat{\mathbf{u}}} \right) \Delta t^2 \quad (3.76)$$

$${}^{t+\Delta t} \dot{\hat{\mathbf{u}}} = {}^t \dot{\hat{\mathbf{u}}} + \left((1 - \gamma) {}^t \ddot{\hat{\mathbf{u}}} + \gamma {}^{t+\Delta t} \ddot{\hat{\mathbf{u}}} \right) \Delta t \quad (3.77)$$

as approximations to displacements and velocities at time $t + \Delta t$. The parameters γ and β determine the method's properties, containing as special cases the linear acceleration method ($\beta = \frac{1}{6}, \gamma = \frac{1}{2}$), central difference method ($\beta = 0, \gamma = \frac{1}{2}$), and others. For a discussion on their behavior see, e.g., [Ogden 1997]. The implicit and unconditionally stable method originally suggested by Newmark uses $\beta = \frac{1}{4}, \gamma = \frac{1}{2}$. It is also known as averaged acceleration or trapezoidal rule.

Following a rearrangement of (3.76) and (3.77), the equilibrium equation (3.16) may be restated at time $t + \Delta t$

$${}^{t+\Delta t} \hat{\mathbf{u}} = \beta \Delta t^2 \mathbf{M}^{-1} \left({}^{t+\Delta t} \hat{\mathbf{f}}_{\text{ext}} - {}^{t+\Delta t} \hat{\mathbf{f}}_{\text{res}} \right) + (0.5 - \beta) \Delta t^2 {}^t \ddot{\hat{\mathbf{u}}} + \Delta t {}^t \dot{\hat{\mathbf{u}}} + {}^t \hat{\mathbf{u}} \quad (3.78)$$

with both ${}^{t+\Delta t}\hat{\mathbf{u}}$ and ${}^{t+\Delta t}\hat{\mathbf{f}}_{\text{res}}$ being unknown. For linear visco-elastic material behavior, the explicit solution may be taken from textbooks. In general though, an iterative calculation of these variables is necessary. Defining as before

$$\mathbf{K}_{\text{v}} = \frac{\partial \hat{\mathbf{f}}_{\text{res}}}{\partial \dot{\mathbf{u}}} \quad \mathbf{K}_{\text{e}} = \frac{\partial \hat{\mathbf{f}}_{\text{res}}}{\partial \hat{\mathbf{u}}} \quad \mathbf{K}_{\text{vem}} = \frac{\gamma}{\beta \Delta t} \mathbf{K}_{\text{v}} + \mathbf{K}_{\text{e}} + \frac{1}{\beta \Delta t^2} \mathbf{M} \quad (3.79)$$

the displacement increment for a Newton-Raphson scheme is derived. The evaluation of $\frac{\partial {}^{t+\Delta t}\dot{\mathbf{u}}}{\partial {}^{t+\Delta t}\hat{\mathbf{u}}}$ for Newmark's method led to the factor $\frac{\gamma}{\beta \Delta t}$.

$$\Delta \hat{\mathbf{u}}^{(i+1)} = {}^{t+\Delta t}\mathbf{K}_{\text{vem}}^{(i)-1} \left({}^{t+\Delta t}\hat{\mathbf{f}}_{\text{ext}} - {}^{t+\Delta t}\hat{\mathbf{f}}_{\text{res}}^{(i)} - \mathbf{M} {}^{t+\Delta t}\ddot{\mathbf{u}}^{(i)} \right) \quad (3.80)$$

Utilizing a modified Newton-Raphson technique, ${}^{t+\Delta t}\mathbf{K}_{\text{vem}}^{(i)}$ may be substituted by ${}^t\mathbf{K}_{\text{vem}} = {}^{t+\Delta t}\mathbf{K}_{\text{vem}}^{(0)}$ in many cases, avoiding the stiffness computation in every iteration step. Equivalent to (3.75) a speed-up may be achieved through a direct iteration, again at the risk of an impaired convergence.

$$\Delta \hat{\mathbf{u}}^{(i+1)} = \beta \Delta t^2 \mathbf{M}^{-1} \left({}^{t+\Delta t}\hat{\mathbf{f}}_{\text{res}}^{(i-1)} - {}^{t+\Delta t}\hat{\mathbf{f}}_{\text{res}}^{(i)} \right) \quad (3.81)$$

Like the central difference scheme presented before, the Newmark formulation does not demand an initially decoupled description of viscous and elastic forces. The decoupled and linear viscous versions can be derived by introducing the appropriate simplifications to (3.78) and (3.80).

Chapter 4

A general model of skeletal muscle

A wide variety of approaches is currently utilized and effective for the assessment of mechanical aspects in vertebrate physiology - from small rigid body simulations, to models which comprise fine details of joints, ligaments, cartilage and bone structures, to highly sophisticated models that even consider metabolic and electro-chemical processes. Research objectives cover very diverse fields, like implant and trauma medicine, training and sport sciences, occupational safety, product design, paleontology and forensics. Given that context, one single, general physiological model could not possibly be effective in all of these applications.

The present work aims to describe a model of skeletal muscle that is generally applicable at the scale of whole-body to full muscle simulations, and within the domain of active and passive locomotion, occupational safety, impact simulation and physiological testing for muscle properties.

4.1 Properties of skeletal muscle

A comprehensive description of skeletal muscle behavior and functionality may easily cover several books, and still be considered basic in many aspects. The complex chemical, neural and thermomechanical mechanisms which drive and control the muscle are still subject to fundamental research. However, accepting certain limitations, reliable theories are available, covering for example the mechanical behavior of muscles. In the following section a description of the muscle physiology is provided, which should suffice as foundation to the models explained afterwards. Neural and metabolic implications will barely be considered. Standard texts recommended for the further interested reader are McMahon [1984], Pollack

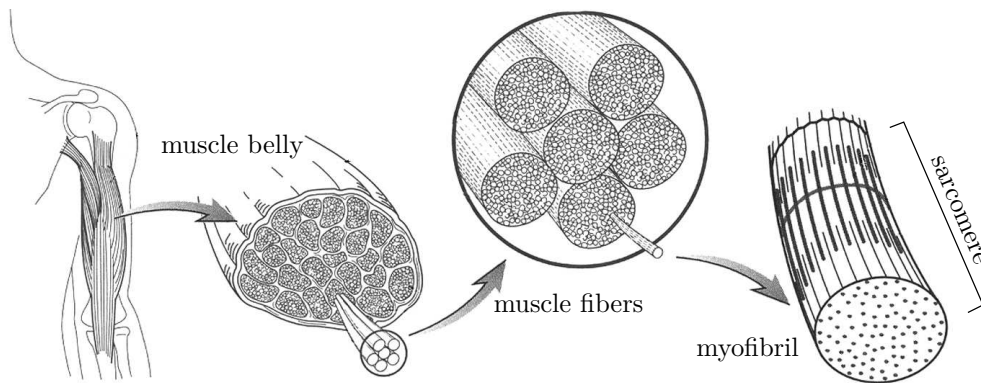


Figure 4.1: Muscle anatomy, adopted from Lieber [2002].

[1990], Winters and Woo [1990], and Herzog [2000].

4.1.1 Muscle physiology

The main functions of skeletal muscle are generation, short time recuperation and dissipation of mechanical energy, the first being the most exclusive one. It is achieved by generating tension forces between origin and insertion of the muscle. Adequate motor control presumed, these forces result in coordinated movements, locomotion and stabilization of the body.

The structure of a muscle - apart from tendons and tendon sheets (aponeuroses) - is depicted in Fig. 4.1. The muscle belly consists of muscle bundles (fascicles) which again contain several muscle fibers (cells). Every fiber, bundle, and muscle is surrounded by connective tissue and membranes which among other tasks ensure their nutritional supply and responsiveness. Within a muscle fiber, myofibrils are arranged in parallel, themselves constructed from series of sarcomeres, the smallest contractile units. Fig. 4.2 illustrates how the sarcomere is bordered by Z-lines which intersect the thin myofilaments in the so-called I-band. Thick myofilaments form the A-band. They slide between the thin filaments and connect with them via crossbridges when the muscle contracts. Thick and thin filaments are often referred to as myosin and actin filaments, as these two proteins are their main respective components.

4.1.2 Contraction mechanism

The sliding filament and crossbridge theories were introduced by Huxley and Hanson [1954], Huxley and Niedergerke [1954], and Huxley [1957], and - with some adjustments - have been

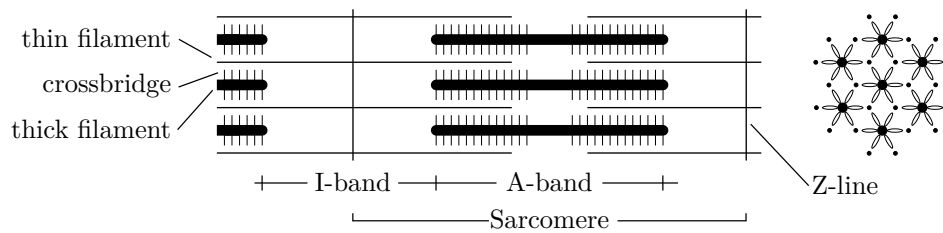


Figure 4.2: Schematic illustration of the sarcomere, longitudinal and transversal section.

confirmed ever since. They proposed that the myosin molecules from the thick filaments attach to certain proteins on the thin filaments, bend and detach again. The respective sarcomere contracts during this cyclic process and so does the whole muscle fiber.

The contraction is initiated by an electrochemical stimulus from the motor neuron. It is propagated along the cell's surface and makes the sarcotubular system permeable to Ca^{2+} ions which migrate into the myofibrils. They bind to troponin and thereby activate the attachment sites on the thin filament. The myosin heads may now attach, deform through the breakdown of ATP to ADP¹, and detach. The strike length amounts to 5–10nm. Neighboring myosin heads and attachment sites are offset in a way that enables a smooth sliding mechanism.

Gordon et al. [1966] were the first to describe the force-length relationship of a single sarcomere. The graph in Fig. 4.3 refers to frog skeletal muscle, but is almost identical to those obtained for cat, humans, and other mammals. The respective slack lengths are commonly specified in the range from 2.1 to 2.7 μm . Absolute forces are hardly comparable as they depend very much and differently on experimental conditions like, e.g., temperature.

It is important to emphasize the isometric nature of the underlying experiment, i.e. the forces were measured at fixed lengths. If the descending limb referred to a general displacement-force function, the softening behavior would destabilize the muscle fibers. The activation of a fiber with sarcomeres of different initial lengths at the descending limb would make the shorter ones contract and the longer ones extend. This effect has indeed been observed [Julian and Morgan 1979], but following some creepage, equilibrium is achieved and subsequently a positive stiffness verified. Force enhancement - the increase in force when an already activated sarcomere is stretched - is not only essential for inter-sarcomere stability, but also on whole muscle level for effective motion control.

In experimental contexts, eccentric, concentric, isometric, isotonic, and isokinetic con-

¹ ATP/ADP - adenosine tri-/diphosphate. Said chemical reaction is known as Lohmann reaction.

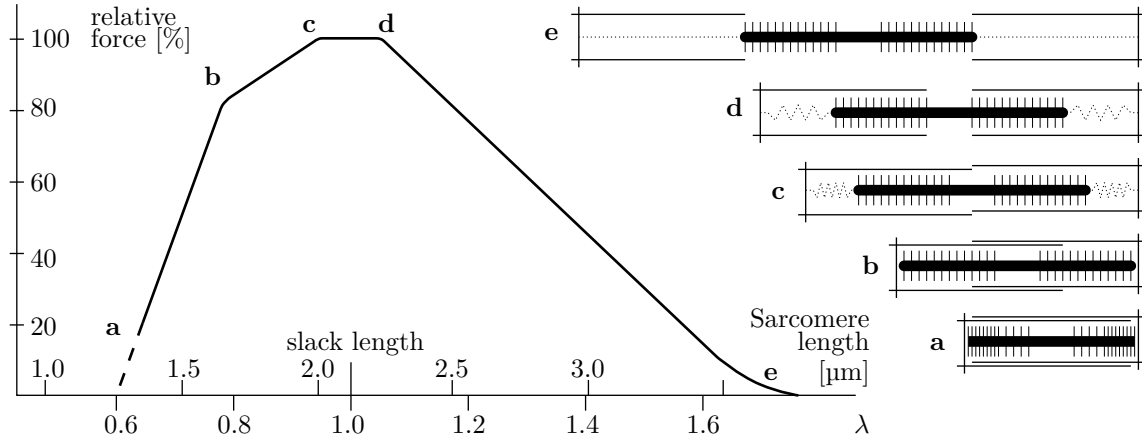


Figure 4.3: Isometric tension vs. length curve and corresponding appearance of the sarcomere.

traction are distinguished, denoting shortening and lengthening contraction, contraction at constant length, constant force, or constant velocity, respectively.

4.1.3 Activation mechanism

Muscles are organized in motor units that contain several muscle fibers which are all innervated via the same pathway, the motor neuron. The fibers of a motor unit do therefore always contract and relax simultaneously. The contraction force depends on the firing rate of the motor neuron: The response to single stimulations with sufficiently long intervals in between are single force twitches. A second stimulation before the force twitch subsides will increase its magnitude and duration. With increasing frequency of the stimulation the overlap increases, the force curve becomes smoother, and eventually fused (Fig. 4.4) at a frequency that may vary between 20–120Hz, depending on the particular muscle and temperature.

The characteristic form of a single twitch depends on the metabolic and structural properties of the fiber, i.e. the fiber type, as well as the motor neuron diameter. The resultant time courses of single twitches vary significantly in length and height. E.g., contraction times in humans vary from below 10ms in eye muscles to beyond 100ms in locomotion muscles. The underlying reasons are varying metabolic and structural properties, and different motor neuron diameters.

Muscle contraction may as well be induced artificially through electrodes that are either placed on the skin, in the muscle body (percutaneous, accessed via needle-puncture) or implanted in the proximity of the motor neuron. Surface electrodes are obviously non-

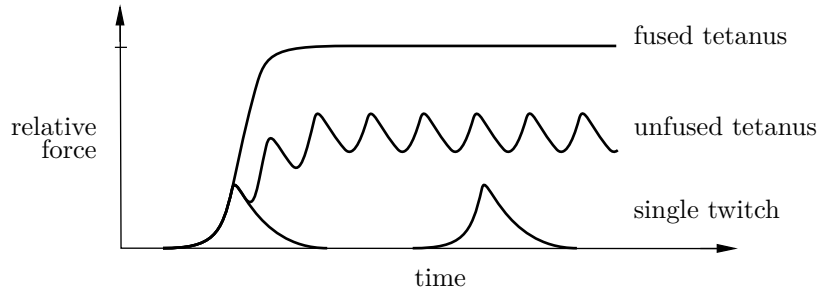


Figure 4.4: Schematic force evolution vs. time for different stimulation frequencies.

invasive, but they are also not suitable for the stimulation of profound muscles, require higher voltages to be effective, and act less selective than the subcutaneous options. Implant electrodes require surgery, but presuming intact innervation of the muscle, only the motor neuron needs to be stimulated to propagate the signal throughout the muscle. In contrast, surface and percutaneous placements often require an array of electrodes in order to avoid locally damaging currents. All three methods are capable of inducing full tetanic activation, mimicking the natural frequency-modulated stimulation in conjunction with a sufficient signal amplitude.

4.1.4 Muscle geometry and force

Force-length characteristics of a muscle follow directly from its architecture, which often appears as an optimized solution targeting on maximum performance. Most sarcomeres work in and close to the plateau region of Fig. 4.3. A major factor on the relation between working ranges of muscle and sarcomeres is the pennation angle α , defined as the angle between fiber orientation and the muscle's line of pull. The effective fiber force is proportional to $\cos \alpha$ and the number of parallel fibers is reversely proportional to $\cos \alpha$, so the physiological cross-sectional area

$$A_{\text{pcs}} = \frac{\text{muscle volume}}{\text{optimal fiber length}} \quad (4.1)$$

is an appropriate measure to estimate the maximum isometric force of a muscle. The proportionality factor amounts typically to $20 - 40 \text{ N/cm}^2$. The optimal fiber length is determined by the optimal lengths of the enclosed sarcomeres, corresponding to the slack length in Fig. 4.3.

The simplification lies here in the assumption of an uniform pennation angle which may lead to inaccurate results. Some classical examples for different fiber arrangements

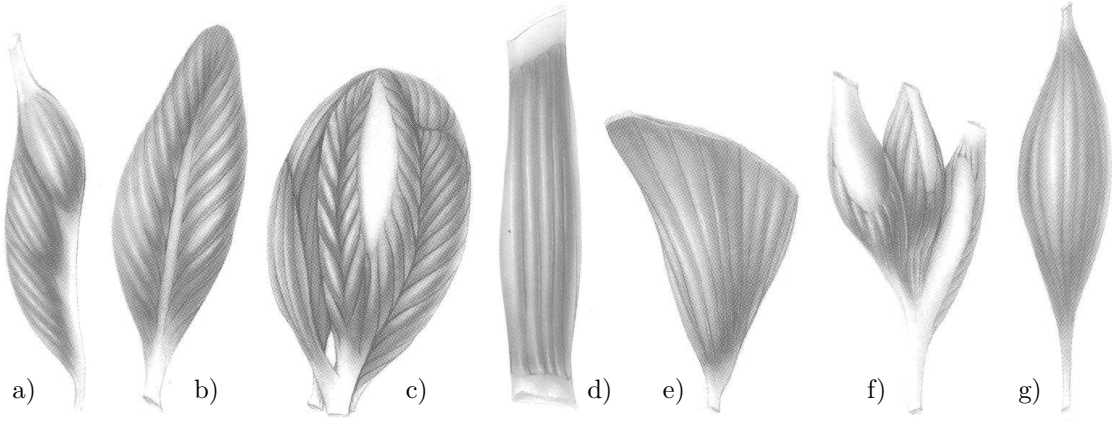


Figure 4.5: Various pennation types. a) unipennate b) bipennate c) multipennate d) strap with tendinous intersections e) triangular f) tricipital g) fusiform [Company 2002].

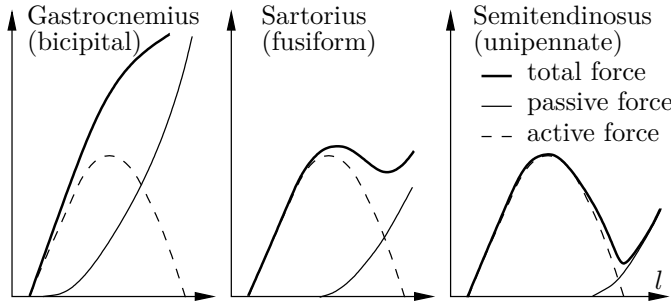


Figure 4.6: Schematic isometric force-length functions of frog muscles [Epstein and Herzog 1998].

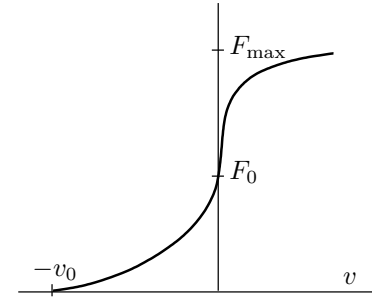


Figure 4.7: Force-velocity curve, based on [Hill 1938, Katz 1939].

are given in Fig. 4.5. The variety in muscle architecture illustrates the variety in functional tasks. Maximum force as well as the range in which force can be generated are correspondingly variable, even if neglecting the size effect. Individual muscles in a group of agonists are designed to physiologically complement each other, usually in a way that each muscle's working range coincides roughly with its mean optimal fiber length. The amount of connective tissue is to some extent dependent on the muscle architecture too, such that the passive properties vary according to Fig. 4.6.

Apparently, the length dependence of the active force in a muscle is much smoother than possibly expected from a sarcomere's behavior. This is an effect of slight variations in lengths between parallel and serial sarcomeres, and to a lesser extent minor deviations of intrinsic sarcomere properties and fiber recruitment patterns.

Contraction velocity acts as a further major influence on the active force. From some of the first experiments conducted and published by Hill [1938], the inverse relation between a

muscle's active force and its contraction velocity was derived for full activation, concentric motion and near-optimal length (see Fig. 4.7). These data, generated from quick release experiments, were shown to be compliant with theoretical thermodynamic considerations regarding the heat generation of a shortening muscle. While similar energy considerations were inconclusive in the eccentric range (until the sliding filament theory was established), the first experimental data investigating active force versus lengthening velocity were made available at about the same time by Katz [1939].

Considering muscle in arbitrary settings, neither isometric nor isokinetic, experimental data indicate a scaling of the muscle force by both length- and velocity dependent factors. Specific proposals and assumptions are discussed in section 4.2.

4.1.5 Three-dimensional properties

The muscle properties addressed so far refer exclusively to results and experiments where quantities in the line of pull were recorded. As this work aims at a spatial representation, some additional remarks concerning three-dimensional muscle behavior are necessary.

Near-incompressibility is clearly the mechanically most relevant characteristic of any dense soft tissue. Due to this property, muscle activation will have an immediate and significant effect also on stresses and stiffness perpendicular to the fiber direction. Specifics of the passive muscle's transversal properties impact the active behavior to a much lesser extent, and although the micro-mechanical molecular processes are well understood, no consistent mechanical description for the cross-fiber behavior has been established. Research is mostly focused on the tetanic muscle (see section 4.3), and few experiments investigate its passive three-dimensional properties.

Strumpf et al. [1993] reported the in-fiber direction stiffness of a passive canine diaphragm to be significantly smaller than its transverse stiffness, but activation reversed this relation. In bi-axial experiments on activated cardiac muscle Humphrey and Yin [1987], Hunter and Smaill [1988] and Guccione et al. [1993] found the stiffness in fiber direction to be two to five times higher than the transverse stiffness. For passive skeletal muscle under compression, Van Looke et al. [2006] found the stiffness to be twice as high in transversal direction than along the fibers, while under tension Morrow et al. [2010] measured longitudinal stiffness to be roughly twenty times as high as in the transverse direction. Bosboom et al. [2001b] conducted in vivo transversal compression experiments on the relaxed rat tibialis anterior muscle. Weichert et al. [2011] investigated passive behavior on cubic muscle samples under various loading condition, and Siebert et al. [2014]

assessed lateral mechanical behavior of isolated rat muscles at different activation states in what appears to be the most recent approach to the topic. While those studies provide valuable data, a comprehensive systematic investigation of strain and activation dependent three-dimensional muscle properties is still lacking.

4.2 Review and extension of straight-line models

Straight-line models (SLM) of muscle, i.e. models which represent the muscle or its fibers as line elements, date back to the beginning of the previous century. Aside from being still the method of choice for many simulations, they also serve as basis for the constitutive descriptions of higher dimensional models.

They are often classified as either rheological or biophysical, dating back to the models invented by A.V. Hill and A.F. Huxley, respectively. Several models of both kinds will be explained subsequently. The fiber properties associated with the three-dimensional model developed in this work will heavily rely on these one-dimensional descriptions.

4.2.1 Rheological models

Hill [1938] stated in the summary of his famous paper that skeletal muscle may be considered as a serial ‘two-component system, the one component being undamped and elastic, the other being governed by the characteristic equation $(F+a)(v+b)=\text{const.}$ ’ which refers to the shortening range of Fig. 4.7. The formula proposed by Hill is commonly rewritten as

$$F = \frac{F_0^{\text{opt}} b - a v}{b - v} \quad (4.2)$$

with the constants a and b representing the asymptotes of the hyperbola in the concentric range. Here, the contraction velocity v is negative during shortening. Hill’s two components will be denoted serial elastic (SE) and contractile element (CE). Typically, the effect of the CE is scaled with activation and a parallel elastic element (PE) is supplemented, for otherwise a passive muscle could not exert a force as shown in Fig. 4.6.

Closely related to Hill’s proposal, other rheological models have been developed, some of them depicted in Fig. 4.8. The variety in the properties of the utilized springs, dashpots and CEs add to the diversity of the available models. However, the three element model remains by far the most popular, as it may be adapted to a wide range of applications with

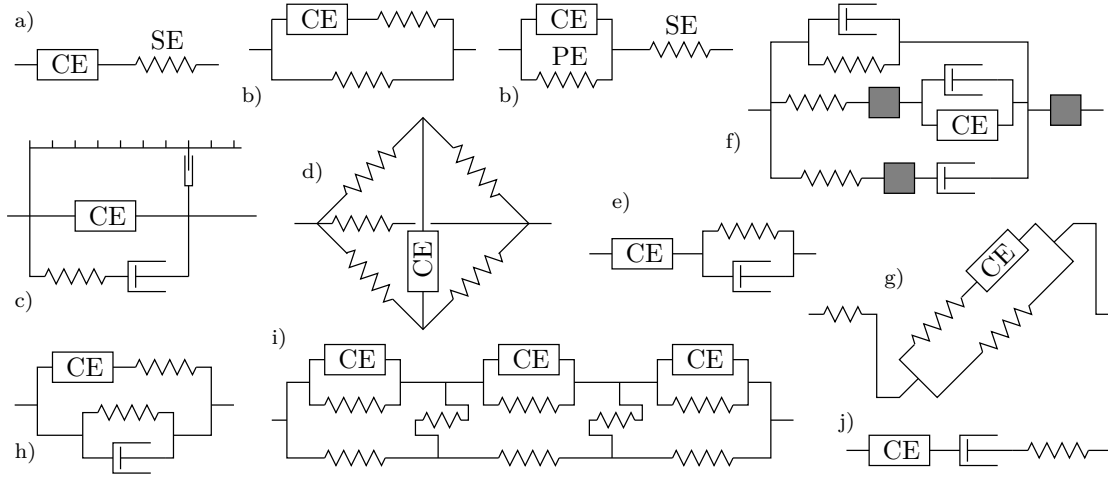


Figure 4.8: Rheological models for muscle. a) Hill [1938] b) i.e. Winters and Woo [1990] c) Forcinito et al. [1998], with elastic rack d) Vain [2001] e) Van der Linden [1998] f) Tamura and Saito [2002], with inertia g) Zajac [1989] h) Durfee and Palmer [1994] i) Yücesoy [2003] j) Ding et al. [1998].

satisfying accuracy and at reasonable costs.

An intrinsic shortcoming of rheological models is their purely phenomenological, lumped-parameter nature. This makes an association between model and muscle components futile, and analytical parameter assessment difficult. E.g., the popular connotation of the serial elastic element (SE) in Fig. 4.8:a as the tendon’s equivalent appears inadequate because cross-bridges and aponeuroses contribute significantly to the series elasticity.

Still, due to the physiology of the samples used in [Hill 1938] and similar works (i.e. frog sartorius muscle, 32mm long and 0.35mm thick) the findings can be transferred from the whole-muscle level onto representative parallel-fibered muscle units. Zajac [1989] embedded this in a model which included pennation and a separate elastic element representing the tendon. This allows for the reapplication of identified parameters to muscles with different architecture, and finally the derivation of higher-dimensional continuum models.

Remark: Most publications addressing the one-dimensional properties of skeletal muscle deal with force, displacement and velocity measures, like the experiments they are referring to. When quoting from such papers a transcription from force to nominal stress ($P = F/A_0$), from length to stretch ($\lambda = l/l_{\text{opt}}$), and from velocity to stretch velocity ($\dot{\lambda} = v/l_{\text{opt}}$) is conducted. Due to the linear relation between those respective items the original functions require little modifications; essentially only an adaptation of parameters.

Despite the continuum mechanic quantities involved, the terms “force-length” and “force-velocity” will be kept. Indices and markers remain unchanged as well.

4.2.1.1 The elastic elements

Serial and parallel elastic elements in the rheological three element model assume simultaneously the functions of tendons, aponeuroses, collagenous fibers and connective tissue. In the context of a three-dimensional modeling approach, these structural elements will be modeled individually, or - considering the model resolution in FEA - they will be regarded as a multitude of various elastic elements. Accordingly, there is no equivalent to the elastic elements of the three element model in the present work's three-dimensional approach. A detailed discussion of their properties is therefore omitted.

4.2.1.2 The contractile element

In contrast to the above, the contractile element in rheological models mimics muscle behavior only, and the properties of muscle fibers in this work's three-dimensional approach are directly derived from the rheological CE descriptions.

As previous explained, the stress generated by the CE is derived as a function of isometric force at optimal length, activation level, contraction velocity, length when activated and instantaneous length. Fatigue and other effects of contraction history will be disregarded at this stage. A proper functional description may be based on the scaling functions

$$f_1(\lambda_{\text{act}}, \lambda) = P_0/P_0^{\text{opt}} \quad (4.3)$$

$$f_{\text{act}}(\alpha, t) = P_{\text{CE}|\dot{\lambda}=0}/P_0. \quad (4.4)$$

P_0^{opt} represents the maximum isometric stress at optimal length. Accordingly, P_0 is the maximum isometric stress at activation length. The activation function f_{act} is time dependent and smoothes alleged jumps of the activation state α , sharing the same co-domain $[0, 1]$. For example, upon full stimulation the muscle stress rises steadily from zero to the tetanic stress in Fig. 4.4.

Supported by the findings of Edman [1979; 1988] and others, some authors [Van Leeuwen 1991, Van der Linden 1998, Meier and Blickhan 2000] suggest a similar scaling function to account for the velocity dependence of the CE's stress:

$$f_v(\dot{\lambda}) = P_{\text{CE}}/P_{\text{CE}|\dot{\lambda}=0}, \quad (4.5)$$

assuming independence of f_v from other state variables. The resultant $P_{\text{CE}} = f_v f_{\text{act}} f_1 P_0^{\text{opt}}$ is computationally convenient, but its validity is limited to near-full-force contractions

($\alpha \approx 1$). The maximum shortening velocity v_0 (see Fig. 4.7) was shown to correlate with the activation state [Petrofsky and Phillips 1981, Chow and Darling 1999], and lengths below the optimal length have an influence on the force-velocity relation as well [Stern 1974, Van Soest 1992].

A comprehensive model for submaximal activation states was presented by Günther [1997], where f_v is a function of f_{act} , f_1 , $\dot{\lambda}$, λ , and muscle specific parameters. That approach (4.13) will be discussed in detail and expanded on later in this chapter.

Force-length relations

The length dependent scaling factor f_1 accounts for the activation-length dependence of the muscle stress. Several functional descriptions are compared below. For brevity, only the function segments with $f_1 > 0$ are presented, everywhere else applies $f_1 = 0$.

A recurrent approach to model f_1 is the parabolic function (4.6), albeit with some variation in its parameter a (Günther [1997]: $a = 0.54$, Epstein and Herzog [1998]: $a = 0.6$, Scovil and Ronsky [2006]: $a = 0.72$).

$$f_1 = 1 - \frac{1}{a^2} (\lambda_{\text{act}} - 1)^2 \quad \text{for } 1 - a < \lambda_{\text{act}} < 1 + a \quad (4.6)$$

Bovendeerd [1990], who for cardiac muscle only described the ascending limb of the force-length function, proposed

$$f_1 = 1 + \frac{1}{a} (\lambda_{\text{act}} - 1) - \sqrt{\frac{1}{a^2} (\lambda_{\text{act}} - 1)^2 + b} \quad \text{for } \lambda_{\text{act}} > 1 - a \frac{1 - b}{2} \quad (4.7)$$

with $a = 1.538$, $b = 0.01$. Otten [1987] and Van der Horst [2002] utilized the exponential function

$$f_1 = \exp \left(-\frac{1}{a^{b_2}} (\lambda_{\text{act}}^{b_1} - 1)^{b_2} \right) \quad (4.8)$$

with $a = 0.54$, $b_1 = 1$, $b_2 = 2$, and another exponential description is provided in [Van der Linden 1998]:

$$f_1 = \begin{cases} \exp \left(-b_1 (\lambda_{\text{act}} - 1)^4 \right) & \text{for } \lambda_{\text{act}} \leq 1 \\ \exp \left(-b_2 (\lambda_{\text{act}} - 1)^3 \right) & \text{for } \lambda_{\text{act}} > 1 \end{cases} \quad (4.9)$$

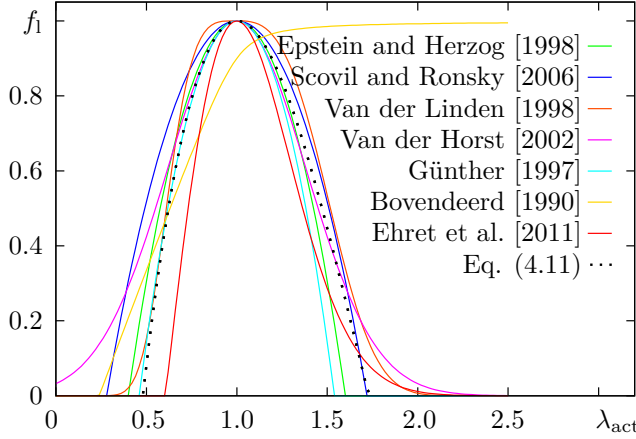


Figure 4.9: Isometric force-length functions. Approach (4.11) is here parameterized to approximate Günther [1997] and Scovil and Ronsky [2006].

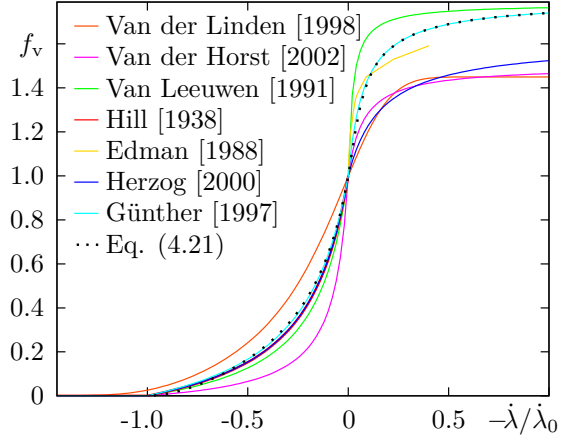


Figure 4.10: Force-velocity functions. Approach (4.21) is here parameterized to approximate Günther [1997].

with $b_1 = 30$ and $b_2 = 5$. Ehret et al. [2011] proposed

$$f_l = \left(1 + \frac{1}{a_c}(\lambda_{\text{act}} - 1)\right) \exp\left(-\frac{1}{2a_c^2}(\lambda_{\text{act}} - 1)^2 - \frac{1}{a_c}(\lambda_{\text{act}} - 1)\right) \quad \text{for } \lambda_{\text{act}} \geq 1 - a_c \quad (4.10)$$

with $a_c = 0.395$.

All of the mentioned functions are displayed in Fig. 4.9.

The exponential functions and their gradients are steady and possess positive values for every real-valued λ . This may improve the convergence behavior in iterative computations over the more realistic approaches in accordance with (4.6). The latter are adequate as long as the algorithms do either not demand steadiness, or λ does not exceed the physiological range during computation.

For this work, a third order polynomial function is proposed (4.11). It allows for distinct and independent maximum and minimum stretch values at which force can be exerted, and is better suited for curve fitting to asymmetric experimental data than (4.6).

$$f_l = 1 + \frac{1}{a_e^2 a_c^2} \left((\lambda_{\text{act}} - 1)^3 (a_e - a_c) - (\lambda_{\text{act}} - 1)^2 (a_e^2 + a_c^2 - a_e a_c) \right). \quad (4.11)$$

This description is derived from the boundary conditions $f_l(1) = 1$, $f'_l(1) = 0$, $f_l(1 - a_c) = 0$, $f_l(1 + a_e) = 0$. It contains as special case the parabola of (4.6) with $a = a_e = a_c$. The indexes e and c mark parameters in the eccentric and concentric range, respectively.

Several authors [Meier and Blickhan 2000, Tamura and Saito 2002, Till et al. 2008, Siebert et al. 2015] applied Gordon's multi-linear force-length curve for sarcomeres directly

to muscle models. This appears appropriate only if the sarcomere properties' variation and length non-uniformities that may exist initially or develop during contraction are considered in the model, possibly by including a probabilistic approach. These non-uniformities in sarcomere length are thought to be the main reason for the divergence between isometric sarcomere and muscle force-length relations [Herzog 2007]. Already the actual measurements in [Gordon et al. 1966], which refer to a fiber segment and not to a single sarcomere, are not quite as piece-wise linear as the proposed function suggests.

Force-velocity relations

Most formulae to calculate P_{CE} originate from the hyperbolic functions developed by Hill [1938], and from data by Aubert [1956]:

$$P_{CE} = \begin{cases} \frac{P_0^{\text{opt}} b_c - a_c \dot{\lambda}}{b_c - \dot{\lambda}} & \text{for } \dot{\lambda}_0 \leq \dot{\lambda} \leq 0 \\ \frac{P_0^{\text{opt}} b_e - a_e \dot{\lambda}}{b_e - \dot{\lambda}} & \text{for } \dot{\lambda} > 0 \end{cases} \quad (4.12)$$

For $\dot{\lambda} < \dot{\lambda}_0$ applies $P_{CE}=0$, which is omitted here and in subsequent equations.

The above relations were derived from maximally activated muscles at optimal lengths, and different proposals followed on how to incorporate activation and length dependence. Günther [1997] developed a model which will be considered as a reference in this work:

$$P_{CE} = \begin{cases} f_{\text{act}} f_l P_0^{\text{opt}} \frac{g_{\text{act}} B_{\text{rel}} + g_l A_{\text{rel}} \dot{\lambda}}{g_{\text{act}} B_{\text{rel}} - \dot{\lambda}} & \text{for } \dot{\lambda}_0 \leq \dot{\lambda} \leq 0 \\ f_{\text{act}} f_l P_0^{\text{opt}} \left(1 + \frac{(c_r - 1)(g_l A_{\text{rel}} + 1)c_s \dot{\lambda}}{(c_r - 1)g_{\text{act}} B_{\text{rel}} + (g_l A_{\text{rel}} + 1)c_s \dot{\lambda}} \right) & \text{for } \dot{\lambda} > 0 \end{cases} \quad (4.13)$$

This can be derived from (4.12) in several steps:

1. transcription of the eccentric hyperbola to not depend on its asymptotes a_e and b_e , but instead on a slope factor c_s and a ratio c_r , with

$$\frac{dP_{CE}}{d\dot{\lambda}} \Big|_{\dot{\lambda} \rightarrow 0+} = c_s \frac{dP_{CE}}{d\dot{\lambda}} \Big|_{\dot{\lambda} \rightarrow 0-} \quad \text{and} \quad c_r = P_{\text{max}}/P_0 \quad (4.14)$$

2. substituting P_0^{opt} with $P_{CE|\dot{\lambda}=0} = f_{\text{act}} f_l P_0^{\text{opt}}$

3. eliminating a_c and b_c by introducing the muscle independent invariants

$$A_{\text{rel}} = -a_c / (f_{\text{act}} P_0^{\text{opt}}) \quad \text{and} \quad B_{\text{rel}} = b_c / \lambda_{\text{opt}} = b_c \quad (4.15)$$

4. scaling of A_{rel} by g_l and B_{rel} by g_{act} , which then results in

$$\dot{\lambda}_0 = -\frac{g_{\text{act}} B_{\text{rel}}}{g_l A_{\text{rel}}}. \quad (4.16)$$

Thus, a scalable description of the force-velocity relation is derived. In conjunction with the following functions, which were already proposed by Van Soest [1992], Günther [1997] achieved an activation and stretch dependent downscaling of the maximum shortening velocity as it has been observed experimentally.

$$g_{\text{act}} = \begin{cases} 1 & \text{for } f_{\text{act}} > 0.3 \\ f_{\text{act}}/0.3 & \text{else} \end{cases} \quad g_l = \begin{cases} 1 & \text{for } \lambda_{\text{act}} > \lambda_{\text{opt}} \\ f_l^{-1} & \text{else} \end{cases} \quad (4.17)$$

One of the few approaches which does not comply with (4.2) is given in [Van der Linden 1998]:

$$f_v = \frac{c_r}{1 + c_1 \exp(-c_2 \sinh(c_3 \frac{\dot{\lambda}}{\dot{\lambda}_0} + c_3 \frac{1}{2}))} \quad (4.18)$$

Like in Van der Linden's force-length relation (4.9), this exponential form leads to positive values throughout the domain, and accordingly to small deviations from Günther's curve; i.e. $f_v(\dot{\lambda}_0) \neq 0$. Its steady derivative can be of great merit during iterative computations. However, for $\dot{\lambda}/\dot{\lambda}_0 > 8$, the double exponential denominator term exceeds $1.798 \cdot 10^{308}$, the limit for double precision numbers. While physiologically irrelevant, equation (4.18) is therefore inapt as a general force-velocity description for computational purposes.

For this work, a new force-velocity function is proposed (4.21) which accounts for activation dependence as in (4.13), keeps scalability as in (4.5), and resolves some numerical disadvantages of the pure double hyperbolic descriptions.

For reference, Günther's formula (4.13) is transcribed to a compliant parameter set

$$f_v = \begin{cases} \frac{1 - \frac{\dot{\lambda}}{\dot{\lambda}_0}}{1 + c_c \frac{\dot{\lambda}}{\dot{\lambda}_0}} & \text{for } \dot{\lambda}_0 \leq \dot{\lambda} \leq 0 \\ \frac{1 - c_{e1} \frac{\dot{\lambda}}{\dot{\lambda}_0}}{1 - c_{e2} \frac{\dot{\lambda}}{\dot{\lambda}_0}} & \text{for } \dot{\lambda} > 0, \end{cases} \quad (4.19)$$

with

$$\dot{\lambda}_0 = -\frac{g_{\text{act}} B_{\text{rel}}}{g_l A_{\text{rel}}} \quad c_c = \frac{1}{g_l A_{\text{rel}}} \quad c_{e1} = \frac{c_r c_s (1 + c_c)}{c_r - 1} \quad c_{e2} = \frac{c_s (1 + c_c)}{c_r - 1} \quad (4.20)$$

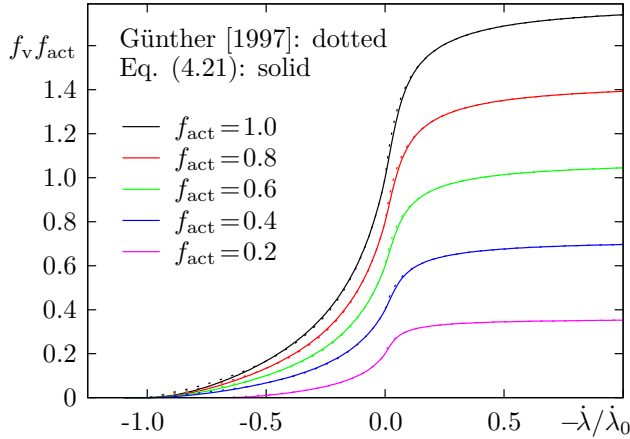


Figure 4.11: f_v dependence on f_{act} according to Günther [1997].

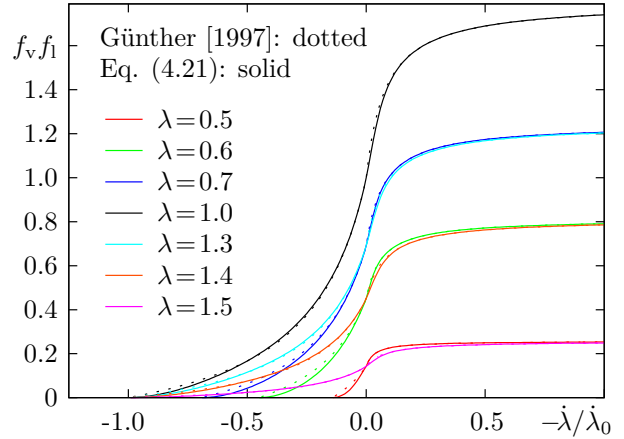


Figure 4.12: f_v dependence on f_l according to Günther [1997] (here mapped to λ via eq. (4.6)).

a form which is very similar to the ones proposed by Van Leeuwen [1991], Epstein and Herzog [1998], and Van der Horst [2002]. But whereas c_c , c_{e1} , c_{e2} , and λ_0 are considered constants by those authors, here they represent functions of f_{act} and f_l as in Günther's approach. Consequently, f_v is only dependent on $\dot{\lambda}$ in the former case, while in the latter it depends as well on α , t , and λ via (4.17).¹ These dependencies are visualized in Fig. 4.11 and Fig. 4.12.

The proposed function (4.21) mimics the double hyperbolic form of (4.19) and (4.13) closely, but maintains a steady derivative. Its concentric range is based on a quadratic parabola, modified by a third order polynomial denominator to maintain the functional values of the hyperbola in $\dot{\lambda} = 0$ and $\dot{\lambda} = \dot{\lambda}_0$, and its gradient in $\dot{\lambda} = 0$. Additionally, a zero-gradient in $\dot{\lambda} = \dot{\lambda}_0$ is enforced. The hyperbolic base function is kept in the eccentric range, but an exponential term is added to ensure a steady derivative towards the concentric domain. The parameter k determines the curvature of the modified function in the eccentric proximity of $\dot{\lambda} = 0$. A value of $k = 40$ is appropriate [Edman 1988].

$$f_v = \begin{cases} \frac{\left(1 - \frac{\dot{\lambda}}{\dot{\lambda}_0}\right)^2}{1 - (1 - c_c)\frac{\dot{\lambda}}{\dot{\lambda}_0} + (3 - 2c_c)\left(\frac{\dot{\lambda}}{\dot{\lambda}_0}\right)^2 - (2 - c_c)\left(\frac{\dot{\lambda}}{\dot{\lambda}_0}\right)^3} & \text{for } \dot{\lambda}_0 \leq \dot{\lambda} \leq 0 \\ \frac{1 - c_{e1}\frac{\dot{\lambda}}{\dot{\lambda}_0}}{1 - c_{e2}\frac{\dot{\lambda}}{\dot{\lambda}_0}} - \frac{(1 + c_c - c_{e1} + c_{e2})\frac{\dot{\lambda}}{\dot{\lambda}_0}}{\exp\left(-k\frac{\dot{\lambda}}{\dot{\lambda}_0}\right)} & \text{for } \dot{\lambda} > 0 \end{cases} \quad (4.21)$$

¹ It is noteworthy, that different sets of parameters, i.e. $\{A_{\text{rel}}, B_{\text{rel}}, c_s, c_r\}$ or $\{\dot{\lambda}_0, c_c, c_{e1}, c_{e2}\}$, which describe the hyperbolic function f_v for the specific case $f_l = f_{\text{act}} = 1$ identically, do not produce identical descriptions of f_v otherwise.

Diagrams Fig. 4.11 and Fig. 4.12 show the excellent agreement of (4.21) with Günther's description, while providing the numerically advantageous steady derivatives. The proposed form may serve as substitution for any of the aforementioned double hyperbolic functions by applying the conversions from (4.20).

Note, that g_{act} and g_l in (4.20) are functions of f_{act} and f_l , respectively (see (4.17)). Concentric parabolic functions that are defined in terms of $\{\dot{\lambda}_0, c_c\}$ may be enhanced by substituting c_c with c_c/g_l , and $\dot{\lambda}_0$ with $\dot{\lambda}_0 g_{\text{act}}/g_l$ in order to account for activation and stretch dependence in accordance with (4.13).

Activation function

Following either neural or artificial stimulus, the calcium release into the muscle cell and thereby the active force increase rapidly. For full whole-muscle contractions, the activation includes also the accumulative activation of the muscles' various motor units. Despite the complexity of activation patterns and the underlying processes, the activation-driven force development can be modeled through successive superposition of comparatively simple activation scaling functions f_{act} (4.4), which include the time-dependent transition between an initial and a targeted activation states. This applies similarly to activation and deactivation dynamics, although they may be parametrized differently.

Van Leeuwen and Kier [1997] suggested a sinusoidal function for zero-to-full activation, which may be generalized for arbitrary intervals to

$$f_{\text{act}} = \begin{cases} \alpha_1 & \text{if } t < t_0 \\ \alpha_1 + \Delta\alpha \left(\frac{1}{2} - \frac{1}{2} \cos \left(\frac{\pi(t - t_0)}{|\Delta\alpha|t_a} \right) \right)^c & \text{if } t_0 < t < t_0 + |\Delta\alpha|t_a \\ \alpha_2 & \text{else} \end{cases} \quad (4.22)$$

for an activation switch from α_1 to α_2 by $\Delta\alpha$. The time t_0 denotes the time of the onset of α_2 ; t_a is the time to complete a full activation. To model a different slope for deactivation, t_a could be substituted by an independent parameter t_d leading to a less steep activation decay.

Johansson et al. [2000] proposed

$$f_{\text{act}} = \begin{cases} \alpha_1 & \text{if } t < t_0 \\ \alpha_1 + \Delta\alpha (1 - \exp(-c(t - t_0))) & \text{if } t_0 < t \end{cases} \quad (4.23)$$

where c was chosen identically for increasing and decreasing activation. The bracketed term will never amount to 1 precisely, hence, in order to convert the respective parameters t_a and c between (4.22) and (4.23), an approximation is required. Substituting $\Delta\alpha$ by $0.999\Delta\alpha$ leads to the relation $c=6.908/t_a$.

There are more sophisticated approaches to muscle activation than the presented, some of which account for very specific metabolic effects. But the more detailed the descriptions become, the less adequate they appear within the framework of a rheological model and the macro-scale perspective in this work. A progression to further accurateness leads to the so-called biophysical models that are discussed briefly in the next section.

4.2.2 Biophysical models

Along with his cross-bridge hypothesis, Huxley [1957] presented a mathematical model for the cross-bridge formation. Assuming rate parameter functions $f(x)$ for attachment/bonding, and $g(x)$ for detachment/unbonding of the active interacting sites on thick and thin filaments, the time rate of the proportion of the attached cross-bridges $n(x, t)$ was derived.

$$\frac{dn}{dt} = (1 - n)f(x) - ng(x) \quad (4.24)$$

See Fig. 4.13 for an illustration. With a cross-bridge force of $F=kx$ and introducing the sliding velocity $v(t)$ via its integral relation to $x(t)$, Huxley was able to match Hill's force-velocity observations in the shortening range. In the eccentric range, the theory matched the data by Katz [1939] only qualitatively, and the force predictions due to rapid length changes were poor.

An enhancement to the model was provided in [Huxley and Simmons 1971] by the introduction of three distinct stable attachment states. A transition between those states, not necessarily corresponding to a relative displacement of the filaments, led to a more realistic behavior at high strain rates.

Far more sophisticated biophysical models of sarcomere contraction have been proposed since then. As molecular kinematics became observable with astonishing resolution, models of cross-bridge kinetics became very detailed [Holmes and Geeves 2000, Arakelian et al. 2015]. In addition to the larger number of identified attachment states, variables were introduced which govern, e.g., Ca^{2+} transients and diffusion [Shames et al. 1996, Wexler et al. 1997] and the ATP hydrolysis cycle [Ferenczi et al. 2005].

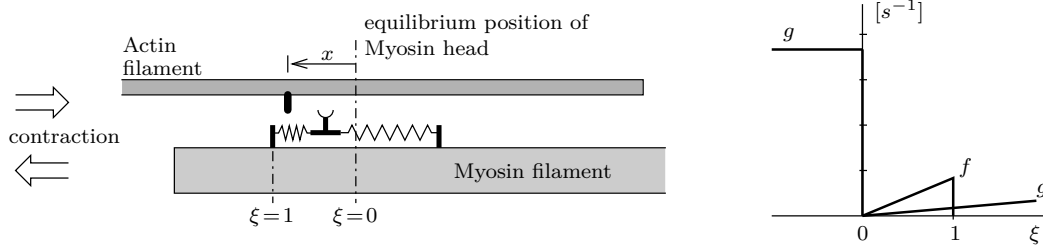


Figure 4.13: Huxley's original model [Huxley 1957], and the attachment (f) and detachment (g) rate functions for a stimulated cross-bridge.

These models tend to agree exceptionally well with the data they are compared to. However, a general and significant disadvantage of all biophysical models is their extremely expensive computational basis. Even Huxley's two-state model appears as inappropriate for whole muscle simulations. Zahalak and Ma [1990] introduced the Distribution-Moment model, an integral, probabilistic approach to (4.24), providing similar solutions on the macroscopic scale more efficiently. Nonetheless, it is far more expensive than comparable rheological models, and its use is advantageous only when the link to metabolic processes and cross-bridge behavior are of interest.

As that is not the case in this work, biophysical models are not considered further.

4.3 History of three-dimensional muscle models

The earliest three-dimensional models of biological soft tissues dealt with ligaments, tendons and skin. Comparatively late, in a previous edition of [Fung 1993], the author extended the idea of transverse isotropy to muscle, suggesting an exponential, isotropic strain-energy function for the passive behavior and an unspecified time- and Ca^{2+} -dependent function to factor in the fiber properties. Following this concept, Humphrey and Yin [1987] developed a cardiac muscle model considering different fiber types, but not activation dynamics. This was included by Hunter and Smaill [1988] who distinguished between full and non-activation. Bovendeerd [1990] presented a sophisticated model of the left ventricle during a cardiac cycle, with sarcomere geometry and certain timing parameters as input, and using CE- and SE-length as internal variables. The constitutive description is specific to the ventricle structure, and the activation pattern is not suitable for generalization either. As in Hunter and Smaill's case, the working range of the sarcomeres was limited to the ascending limb and plateau of the force-length curve, typical for cardiac muscle. Weiss et al. [1996] developed an extended Mooney-Rivlin description for transversely isotropic

biotissues which was implemented into the finite element code NIKE3D (Lawrence Livermore National Laboratory) and has been referenced by some of the following authors. Maurel [1998] proposed a combination of Humphrey and Yin's and Zajac's models for the CHARM toolkit (EU ESPRIT Project), which to some extent has been realized by Martins et al. [1998]. However, the emphasis of those works were visualization and three-dimensional geometry generation for an upper torso based on the Visible Human Data Set (U.S. National Library of Medicine). Kojic et al. [1998] published another utilization of the two-element Hill-type approach in 3D without detailing his (compressible) passive constitutive model. The first to ever utilize a Distribution-Moment model to describe the active properties of muscle in a 3D context were Gielen [1998] and, based on that work, Maenhout [2002]. Their models incorporated a simple mechanism of Ca^{2+} -release and -uptake for the activation process. Probably due to performance issues, the presented examples were limited to planar, quasi-2D slices. Investigating inertia effects during contraction, Johansson et al. [2000] and Meier and Blickhan [2000] implemented a muscle model into ANSYS, including arbitrary activation levels of Hill-type fibers embedded in an isotropic Mooney-Rivlin material. The stresses were scaled through Gordon's force-length relationship and an exponential function for the activation process. Oomens et al. [2003] pursued the work of Gielen, utilizing an enhanced description of the Ca^{2+} -dynamics and an isotropic Neo-Hookean passive behavior. In an attempt to research compression induced muscle damage, Breuls [2003] presented a multilevel model. Since his main concern was prolonged loading in immobilized patients though, neither activation nor contraction dynamics were taken into account. In [Teran et al. 2005], an approach to derive B-spline fiber representations from the Visible Human Data Set was presented, and a follow-up article by Blemker et al. [2005] included a muscle model based on the one of Weiss in NIKE3D. It comprises sarcomere length-dependence and on/off activation. Tang et al. [2007] enhanced the model of Kojic et al. to incorporate fatigue effects. In a straightforward approach to utilize established 1D muscle implementations in a 3D context, Hedenstierna et al. [2008] investigated the limits of combined solid/truss models. Lu et al. [2010] implemented a basic visco-elastic anisotropic material law for muscle in LS-DYNA, and for detailed studies on how the electro-chemical principles on sarcomere-level comply with phenomenological findings, chemo-electro-mechanical models as in [Heidlauf and Röhrle 2014] were developed. Most recently, Spyrou et al. [2017] proposed a two-scale approach with a high-resolution differentiation between muscle fibers and extracellular matrix on the fine scale, and a deduced representative volume element for both on the coarser level.

4.4 Proposed modeling approach

The previous section illustrates the variety of muscle models that were utilized in 3D simulations of skeletal muscle. Most of the simulations were either adapted to a very specific environment and not generally applicable, or limited by a lack of truly three-dimensional reference data. Even with exclusive regard to passive muscle behavior, very few data were published that are suitable for validation purposes, and, accordingly, there are very few validated material models.

The publication of Weichert et al. [2011] stands out in that regard, and the proposed and tested material description therein - which also opens for anisotropic behavior in the non-excited muscle - serves as a base for the description of passive muscle behavior in this work. Selected other material models that have often been utilized for the passive description of muscle were implemented during the course of this work as well, and will be addressed below.

The conventional additive superposition of active and passive contributions to the muscle's behavior will be maintained, as well as the consideration of active behavior in fiber direction only. While the latter constitutes a limitation to the model, no publications could be found which indicate a benefit from the consideration of direct activation effects in more than one dimension.

The fundamentals for the modeling of both, active and passive behavior, were elaborated in section 4.2 and section 2.3, respectively. Section 2.3.6 specifically described how the muscle fiber's one-dimensional constitutive laws are incorporated into a three-dimensional framework. This section only presents the selected specific realizations of those approaches.

4.4.1 Proposed passive constitutive equations

During the course of this work, several isotropic Rivlin-type materials were implemented in order to comply with and reproduce findings of previous publications. Rivlin's generalized material law is defined as

$$W_{\text{dev}}(\hat{I}_1, \hat{I}_2) = \sum_{p,q} \alpha_{pq} (\hat{I}_1 - 3)^p (\hat{I}_2 - 3)^q \quad (4.25)$$

which only describes the deviatoric share of the work equation. Neo-Hooke ($\alpha_{10} \neq 0$), Mooney-Rivlin ($\alpha_{10} \neq 0, \alpha_{01} \neq 0$), and Yeoh ($\alpha_{10} \neq 0, \alpha_{20} \neq 0, \alpha_{30} \neq 0$) material formulations can be derived from (4.25). These three models are popular in the simulation of rubber-like

materials, and common in the simulation of biotissue. In the aforementioned order, they read

$$W = c_1(\hat{I}_1 - 3) + W_{\text{vol}} \quad (4.26)$$

$$W = c_1(\hat{I}_1 - 3) + c_2(\hat{I}_2 - 3) + W_{\text{vol}} \quad (4.27)$$

$$W = c_1(\hat{I}_1 - 3) + c_2(\hat{I}_1 - 3)^2 + c_3(\hat{I}_1 - 3)^3 + W_{\text{vol}}. \quad (4.28)$$

The above constitutive descriptions are confined to isotropic behavior. For this work's model and the simulations conducted here (see chapter 5), the consideration of the anisotropy of the passive muscle was considered crucial. The chosen anisotropic strain-energy function

$$W = \frac{\mu}{4\alpha} (\exp \left[\alpha \left(\frac{w_0}{3} \tilde{I}_1 + w_p \tilde{I}_4 - 1 \right) \right] - 1) + \frac{\mu}{4\beta} (\exp \left[\beta \left(\frac{w_0}{3} \tilde{I}_2 + w_p \tilde{I}_5 - 1 \right) \right] - 1) + W_{\text{vol}} \quad (4.29)$$

is based on [Ehret et al. 2011], and has been verified and adapted to passive muscle properties by Weichert et al. [2011]. Weichert et al. investigated cubic samples of coney muscle during compression tests, with fiber orientations at 0° , 45° , and 90° towards the compression direction. Superficial deformation and force were monitored closely, and the material parameters were identified through (a) adaptation to an idealized homogeneous deformation state, and (b) adaptive FEM computations. The two identified parameter sets are

$$\text{a) } \alpha = 8.5224, \beta = 6.875 \cdot 10^{-4}, \mu = 1518.7 \text{ Pa}, w_0 = 0.824 \quad (4.30)$$

$$\text{b) } \alpha = 7.54, \beta = 1.0 \cdot 10^{-3}, \mu = 2226.0 \text{ Pa}, w_0 = 0.762 \quad (4.31)$$

with $w_p = 1 - w_0$. See Fig. 4.15 for a depiction. The latter set is chosen as starting point for the simulations and subsequent optimization in section 5.1.

The work due to volumetric deformation W_{vol} is set to $\frac{1}{2} \kappa (J - 1)^2$ across all material laws in the course of this work, with κ denoting the compression modulus, and the dilatation J as defined in equation (2.5)¹. There are various other approaches, but Fig. 4.14 illustrates their conformity in the range of small dilatation and thus in the present context.

¹ Dilatation $J = I_3^{\frac{1}{2}} = \hat{I}_3 = \tilde{I}_3^{\frac{1}{2}}$. Refer to section 2.3.4 ff. for the invariants utilized above, and for the derivation of stress functions and material tensors from the above strain-energy functions.

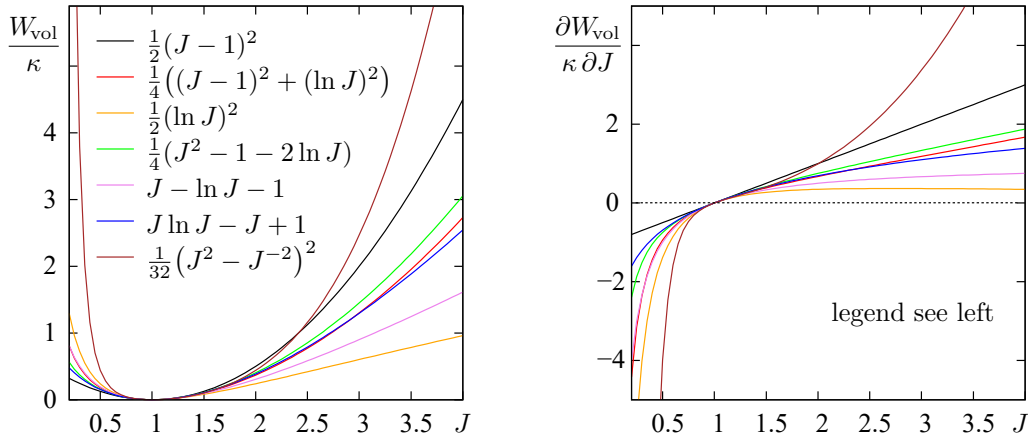


Figure 4.14: Comparison of different approaches for W_{vol} . Function and derivative progression.

4.4.2 Proposed active constitutive equations

The modeling of active stress is based on the scaled approach described in section 4.2.1.2 for the contractile element.

$$P_{\text{CE}} = f_v f_{\text{act}} f_1 P_0^{\text{opt}} \quad (4.32)$$

Several of the there presented scaling functions were implemented, but for the subsequent simulations, the newly proposed functions (4.11) and (4.21) along with (4.23) were selected to describe f_1 , f_v , and f_{act} , respectively.

4.4.3 Complementary: aponeurosis constitutive equations

Naturally, when considering muscle behavior, the respective aponeuroses may need to be considered as well. This is the case for one of the subsequent model applications. Thus a suitable constitutive description was derived and is listed here.

Also aponeuroses display strong anisotropy, with higher stiffness and exponential stress-strain relation in fiber direction. They undergo smaller strains than muscle fibers during active or passive muscle contraction. For the active case, maximum stretch values between 5% and 10% were published (Scott and Loeb [1995], Monti et al. [2003], Azizi and Roberts [2009], Siebert et al. [2015]). It is therefore not necessary to utilize a constitutive description that covers the nonlinearities which occur beyond that range.

The chosen material model for aponeuroses is therefore a straightforward combination of an isotropic Neo-Hookean law (4.26) with a fiber stress description that was fitted to

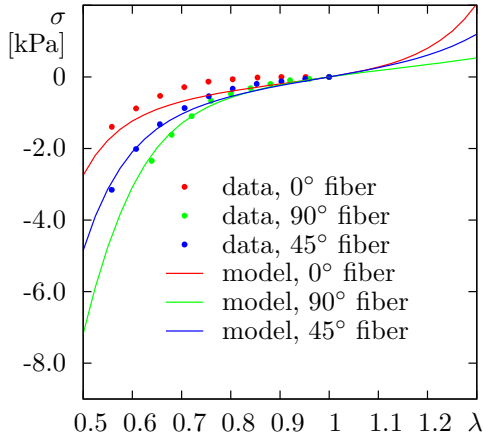


Figure 4.15: Comparison, (4.29) with parameter set b and data from Weichert et al..

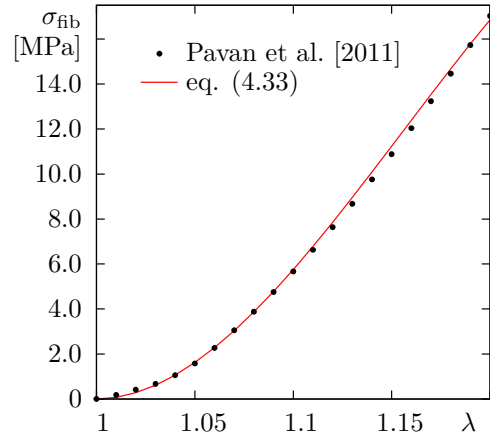


Figure 4.16: Aponeurosis stress vs. stretch, model and data comparison.

the data of Pavan et al. [2011]:

$$\sigma_{\text{fib}} = a(\lambda - 1)^2 + b(\lambda^2 - 1)^2 \quad \text{for } \lambda \geq 1 \quad (4.33)$$

with $a = 2153.5$ MPa, $b = -357.9$ MPa, $c_1 = 2.08$ MPa, $\kappa = 5.55$ MPa. For infinitesimal strains, the latter two values correspond to a linear elastic law with Young's modulus of 10MPa and a Poisson ratio of 0.2. There are few data [Cutts et al. 1991] to support a choice for lateral aponeurosis properties, but deviations are negligible as the stiffness perpendicular to the fiber direction is too small to have a significant effect on muscle deformation. This is evident from the literature and became also apparent from the computations in this work.

4.5 Validation example: Squid tentacle strike

4.5.1 Introduction

While the term ‘skeletal muscle’ points clearly to the muscle’s specific purpose of complementing a skeletal system, there are instances of identical muscles acting independently of any mobile skeletal base. They are referred to as muscular hydrostats. Almost always, these muscles are subject to complex activation patterns and therefore unsuitable for model validation purposes. However, some straightforward, maximum activation contractions occur with the objective of prey capture. This was verified by Van Leeuwen et al. [2000] who compared snatch mechanisms of squid tentacles, frog tongues, and chameleon tongues.



Figure 4.17: *Loligo pealei*. a) specimen with extended tentacles [NOAA Central Library] b) schematic diagram of tentacle [Kier 2016]: AN axial nerve cord, CM circular muscle, HM helical muscle, LM longitudinal muscle, SLM superficial longitudinal muscle, TM transverse muscle.

The former is described in detail in [Kier and Van Leeuwen 1997] and shall be reproduced subsequently to illustrate the required steps for such a simulation, and to verify the current implementation.

Kier and Van Leeuwen monitored tentacle strikes of *Loligo pealei*, a squid species of about 30cm length, with eight arms and two tentacles (see Fig. 4.17). The tentacle consists of two functional units: The muscular stalk which elongates rapidly when striking, and the terminal club which is equipped with suckers to grasp the prey. The extensor muscles are oriented transversely within the stalk. Their contraction translates into longitudinal stretch and drives the club forward. The club itself does not deform significantly until contact with the prey is established. A minor fraction of the stalk is occupied by longitudinal, circumferential and spiral muscle fibers, which remain passive during the snatch phase.

Van Leeuwen and Kier [1997] suggested that the extraordinary rapidity of the strike is the result of optimized, nonuniform sarcomere lengths in the extensor muscles along the tentacle stalk. They developed a 1D disc model to reproduce the experimental observations, and to determine the actual sarcomere lengths computationally. The contraction dynamics was broken down to the level of myosin head action in order to derive adjusted phenomenological descriptions similar to Fig. 4.3 and Fig. 4.7. Based on an extensive set of known and estimated parameters, Kier and Van Leeuwen performed an optimization of few variables with respect to maximum terminal club velocity (see lower section of Tab. 4.1). This approach led to results that agree very well with their actual measurements. In this chapter, and based on the same set of muscle parameters, they are reproduced by means of this work's 3D model.

symbol	definition	value	unit
tentacle properties			
l_{s0}	initial stalk length	53.143	mm
l_{c0}	initial club length	39.857	mm
r_0	initial stalk radius	3.7	mm
ϱ	mass density	1050	kg m ⁻³
A_{cl0}/A_{c0}	fraction of longitudinal muscle in stalk cross-section	79.86	-
η	fraction of extensor muscles in stalk surface cross-section	0.7	-
α	relative surface mass increase to account for water inertia	0.08	-
reference muscle properties			
$l_{\text{myo,ref}}$	optimum reference thick (myosin) filament length	1.58	μm
$l_{\text{act,ref}}$	optimum reference thin (actin) filament length	2.24	μm
$l_{\text{sarc0,ref}}$	optimum reference sarcomere length	2.37	μm
l_{bz}	length of bare zone on thick filament	0.14	μm
l_z	width of z-disc	0.06	μm
$\dot{\lambda}_{\text{min,ref}}$	minimum unloaded reference stretch rate	-17	s ⁻¹
$\sigma_{\text{max,ref}}$	maximum isometric reference stress	280	kPa
t_a	time delay between initial and full activation	40	ms
optimization results			
$l_{\text{myo},1}$	optimum thick filament length at stalk base (independent)	0.9707	μm
$l_{\text{myo},50}$	optimum thick filament length at stalk end (independent)	0.4997	μm
$l_{\text{act},1}$	optimum thin filament length at stalk base	1.2099	μm
$l_{\text{act},50}$	optimum thin filament length at stalk end	0.5976	μm
$l_{\text{sarc0},1}$	optimum sarcomere length at stalk base	1.3399	μm
$l_{\text{sarc0},50}$	optimum sarcomere length at stalk end	0.7276	μm
$\dot{\lambda}_{\text{min},1}$	minimum unloaded stretch rate at stalk base	-30.07	s ⁻¹
$\dot{\lambda}_{\text{min},50}$	minimum unloaded stretch rate at stalk end	-55.37	s ⁻¹
$\sigma_{\text{max},1}$	maximum isometric stress at stalk base	161.53	kPa
$\sigma_{\text{max},50}$	maximum isometric stress at stalk end	69.94	kPa

Table 4.1: Model parameters utilized by Kier and Van Leeuwen [1997].

4.5.2 Model derivation

4.5.2.1 Reference model

The model of Kier and Van Leeuwen builds on a geometrical coupling of strictly one-dimensional descriptions of transverse contraction dynamics and passive longitudinal elasticity, thereby omitting the utilization of a three-dimensional material law. Figure 4.18 visualizes their modeling approach. There, the tentacle consists of one rigid terminal club, and 50 stalk disc elements with two initially independent variables each: Radius r_i and width b_i . By defining the disc's volume $V_i = \pi b_i r_i^2$ to be constant, the degree of freedom is reduced to just one per element. This coupling condition postulates perfect incompressibility. Therefore, all kinematic variables can be expressed in terms of the longitudinal

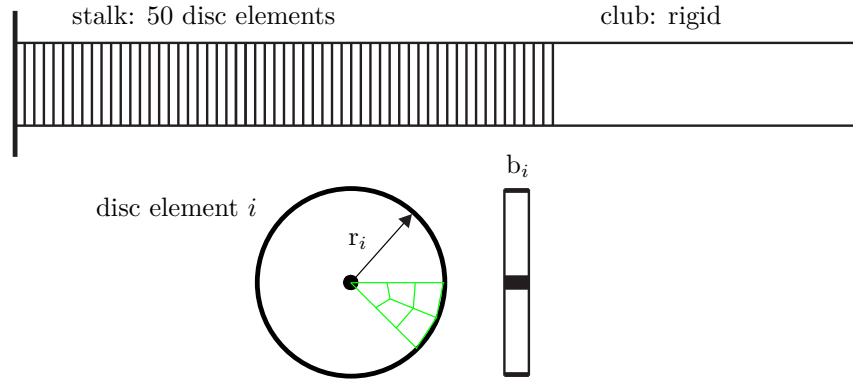


Figure 4.18: Black: illustration of the segmented tentacle model of Kier and Van Leeuwen [1997]. Green: FE model cross-section.

displacements of the disc interfaces. With the resultant linear equation system, Kier and Van Leeuwen followed an explicit time integration scheme to model the tentacle strike.

Fortunately, and in contrast to most 1D studies on skeletal muscle, Kier and Van Leeuwen also provided cross-sectional measures in their publications, which are essential for the 3D simulation of hydrostats. Hence, 1D stresses rather than just forces can be referred to. The interrelation is $P_l(\lambda_l) = f(\lambda_l)/A$, with P_l the longitudinal component of the nominal stress tensor \mathbf{P} , and f the force acting in longitudinal direction. λ denotes the stretch and A the undeformed cross-sectional area. Indices l and t mark longitudinal and transversal reference, respectively. The Cauchy stress amounts to $\sigma_l(\lambda_l) = \lambda_l P_l(\lambda_l)$. This relation is strictly valid only for incompressible continua, but for near-incompressibility the error is small of higher order, and thus negligible.

4.5.2.2 Finite element model and computation

The mesh used here for the finite element simulation is of similar simplicity as the reference model. Utilizing the latter's symmetries, only a quarter of the tentacle cross-section was modeled (see fig. 4.18). The elementation in longitudinal direction was adopted from the reference. The previously introduced F-bar elements were used, and the central difference scheme (see section 3.3.2) was applied for time integration.

4.5.2.3 Passive material adaptation

A recurring task during 3D modeling of muscle tissue is the transcription of constitutive laws into three dimensions. It is common practice to utilize 1D data for calibration and verification of 3D models; first and foremost due to the intricacy of an experimental deter-

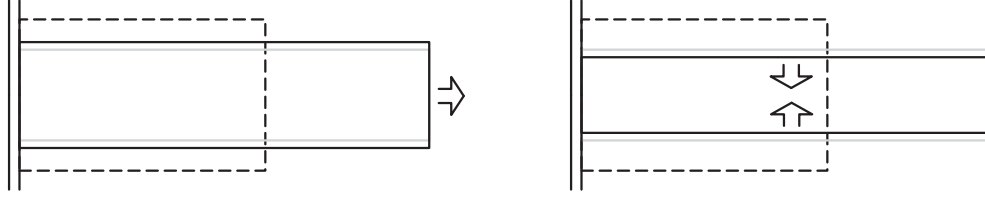


Figure 4.19: Effect of tension (l) and lateral compression (r) on dilatation. Grey reference shape resembles perfectly isovolumetric deformation with identical longitudinal strain.

mination of conclusive 3D data, but also due to the wealth and quality of readily available 1D data. Data from hydrostats are particularly expedient for verifications, as shown by Meier and Blickhan [2000], Liang et al. [2006], and Tang et al. [2009]. Measurements on these structures reveal more about their passive properties than comparable data of skeletal muscles, in which fibers are roughly aligned with the external loads. But this special quality also requires an adaptation approach that is distinct from the common postulation of force-equivalence in fiber direction [Winkel and Schleichardt 2011].

In the present context, an equivalent three-dimensional constitutive description of the passive material needs to be obtained. Equation (4.34) defines the deformation state which corresponds to the 1D longitudinal stretch λ_1 , and accounts for the dilatation that occurs in the 3D simulation.

$$\mathbf{F}(\lambda_1) = \mathbf{F}(\lambda_1, J(\lambda_1)) = \begin{bmatrix} \lambda_1 & 0 & 0 \\ 0 & (J/\lambda_1)^{\frac{1}{2}} & 0 \\ 0 & 0 & (J/\lambda_1)^{\frac{1}{2}} \end{bmatrix} \quad (4.34)$$

The relation between stretch and dilatation depends on the material model. Once an appropriate law is determined - here the Yeoh law - specific material parameters can be adapted. The governing equation for the adaptation is usually based on a force-equivalent approach (4.35), equating the force-stretch relation of 1D and 3D models in the line of action.

$$\boldsymbol{\sigma}(\mathbf{F}(\lambda_1)) = \begin{bmatrix} \sigma_{1D}(\lambda_1) & 0 & 0 \\ 0 & 0 & 0 \\ 0 & 0 & 0 \end{bmatrix} \quad (4.35)$$

This approach is reasonable when fiber direction and line of action coincide, e.g. in regular skeletal muscles. However, a deviating equivalent-pressure approach was developed for the present example. It reproduces the stress state as it typically occurs in hydrostats, where

elongation is driven by transversal contraction (see Fig. 4.19).

For this, the geometrically enforced incompressibility is reconsidered as an incompressible hydrostatic material, so the transversal compression σ_t required to elicit the same longitudinal stretch as the longitudinal stress σ_{1D} in (4.35) amounts to

$$\sigma_t = -\sigma_{1D}. \quad (4.36)$$

The passive material law is now supposed to resolve the incompressibility constraint as well as to account for the predefined longitudinal passive stress. This can be done by superposing the latter $\sigma_{1D}(\lambda_l)$ with the hydrostatic stress state; i.e. $\sigma_t = \sigma_l$. For static deformation states, equilibrium requires both longitudinal stress components to add up to zero, i.e. $\sigma_l + \sigma_{1D} = 0$ in accordance with (4.36). Therefore only the transversal stress components $\sigma_t = \sigma_{1D}$ contribute to the combined pressure.

$$p_{eq}(\lambda_l) = -\frac{1}{3} \text{tr}(\boldsymbol{\sigma}) = \frac{2}{3} \sigma_{1D}(\lambda_l) \quad (4.37)$$

The proposed equivalent-pressure approach aims at reproducing that pressure in a 3D framework. The corresponding stress state is

$$\boldsymbol{\sigma}(\mathbf{F}(\lambda_l)) = \begin{bmatrix} 0 & 0 & 0 \\ 0 & -\frac{3}{2} p_{eq}(\lambda_l) & 0 \\ 0 & 0 & -\frac{3}{2} p_{eq}(\lambda_l) \end{bmatrix} \quad (4.38)$$

thus accounting for the transverse contraction as the pressure-generating mechanism.

In [Kier and Van Leeuwen 1997], the authors utilized the following exponential description for the passive stress-stretch function:

$$P_{1D}(\lambda_l) = 133.11 \text{kPa} (\lambda_l - 1)^{2.26} \quad (4.39)$$

This corresponds well with the Yeoh type material description mentioned in section 4.4.1. Thus, equation (4.39) was evaluated at $\lambda_l = 1.2/1.45/1.773^1$ in order to provide the required support points for the Yeoh parameter deduction. The parameters were then obtained by means of a least square curve fitting procedure, based on (4.28), (4.34) and either (4.35) or (4.38). The former led to the Yeoh parameter set in accordance with the traditional equivalent-force approach (4.40), the latter to the parameter set in accordance with the

¹ The value 1.773 refers to the application limit of (4.39) in the cited paper.

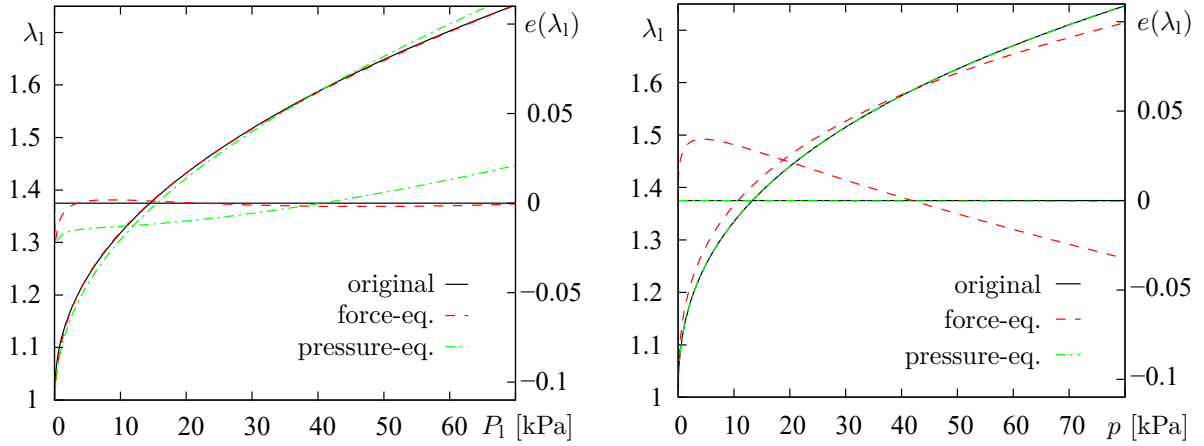


Figure 4.20: Comparison of original data from [Kier and Van Leeuwen 1997] with the deduced 3D material's passive behavior. Longitudinal stretch vs. tension stress P_1 (left) and vs. lateral pressure p (right). Depiction of equivalent-force (4.35) and equivalent-pressure modeling approach (4.38), with the respective relative deviation error e .

equivalent-pressure approach (4.41).

$$a_{10} = 1140.3\text{Pa} \quad a_{20} = 11014.5\text{Pa} \quad a_{30} = 796.6\text{Pa} \quad (4.40)$$

$$a_{10} = 1141.3\text{Pa} \quad a_{20} = 11013.6\text{Pa} \quad a_{30} = 716.1\text{Pa} \quad (4.41)$$

The bulk modulus κ was presumed to $2 \cdot 10^7$ Pa.

The resultant passive model behavior is shown in Fig. 4.20. As expected, the force-equivalent approach provides a material description which mimics the original's 1D behavior well for longitudinal tension. In contrast, the material derived from the pressure-equivalent approach coincides very well with the original material under transversal contraction or compression. The error plots show also the equivalent-pressure data to be closer to the original data under tension, than the equivalent-force data are under compression. This observation is, however, specific to the application and not valid in general.

4.5.2.4 Active material adaptation

Sarcomere characteristics in the tentacle vary from stalk base to end. As already mentioned in [Kier and Van Leeuwen 1997], the stalk was divided into 50 elements in order to reflect this in the model's active properties. The proximal $l_{\text{myo},1}$ and the distal $l_{\text{myo},50}$ were handled as independent variables in Kier and Van Leeuwen's optimization, presuming a linear evolution along the stalk length. $l_{\text{act},i}$, $l_{\text{sarc}0,i}$, $\dot{\lambda}_{\text{min},i}$ and $\sigma_{\text{max},i}$ were expressed by $l_{\text{myo},i}$ and a set of reference muscle parameters (see Tab. 4.1). For the present 3D model, the

factor	parameters
f_{act}	$\Delta\alpha = 1, t_a = 40 \text{ ms}, c = 15$
f_v	$c_c = 4, c_{e1} = 55.232, c_{e2} = 30.24$
f_l	$\lambda_a = 0.57, \lambda_b = 0.769,$ $\lambda_c = 1 - 0.07 \mu\text{m} l_{\text{sarc}0}^{-1},$ $\lambda_d = 1 + 0.07 \mu\text{m} l_{\text{sarc}0}^{-1},$ $\lambda_e = 1.769 - 0.13 \mu\text{m} l_{\text{sarc}0}^{-1},$ $f_l(\lambda_b) = 1 - \frac{l_{\text{sarc}0} - 0.619 \mu\text{m}}{4.902 l_{\text{sarc}0} - 1.275 \mu\text{m}}$

Table 4.2: Parameters for scaling factors of active stress.

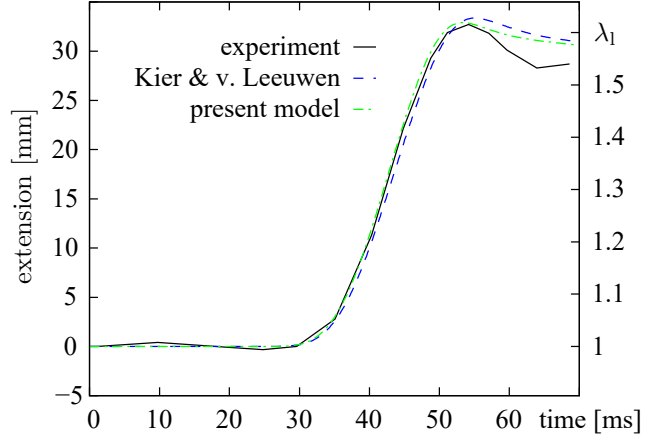


Figure 4.21: Tentacle strike comparison.

variables are transformed to follow the scaling approach from 4.2.1: f_{act} according to (4.22), f_v according to (4.19), and f_l according to Fig. 4.3. The resultant active parameters are listed in Tab. 4.2.

4.5.2.5 Results and evaluation

The validity of the derived material formulation and the model is verified in a 3D simulation of the tentacle strike. Taking advantage of its rotational symmetry, only a quarter of the stalk was modeled by F-bar elements. The element size was chosen analogously to the original model; mass distribution and inertial effects of the surrounding water were fully reproduced from Kier and Van Leeuwen in order to confine the comparison to material effects.

Results from the 3D simulation show excellent agreement with the original 1D model data (see Fig. 4.21). The deviation from the experimental data beyond the point of maximum extension occurs in both simulations. Kier and Van Leeuwen attributed this to partial activation of the longitudinal contractor muscles once the tentacle has reached its maximum length.

The example illustrates the general validity of the present model, and how the pressure-equivalent approach allows for an expedient adaptation of the passive hydrostat material formulation to the one-dimensional reference. However, in this and in the original tentacle strike simulation occur minor deviations between 1D and 3D results. These may be attributed to a fundamental flaw immanent to any such adaptation. While in 1D the stress state within the tissue matrix depends on λ_l only, it depends on the nine components of the deformation gradient in 3D. The exploitation of symmetries may reduce the dependence

to only transversal and longitudinal stretch like in the current case. But the ratio of both is not determined uniquely by the pressure.

Equation (4.38) describes just one prominent stress state for which a set of adequate material parameters can be derived by means of the equivalent-pressure hypothesis. It is convenient to use, since it matches the pure contraction situation at static equilibrium, i.e. with the effective longitudinal stress $\sigma_l + \sigma_{1D} = 0$. But in the context of accelerated motion, this sum does not equal zero, and the ratio between σ_l and σ_t is not constant. Therefore, neither the formula to derive 3D material parameters could remain constant, if the behavior of a 1D model was to be reproduced perfectly.

This ambiguity is caused by the deficiency in information that results directly from the reduction of the real structure to a 1D data set. Every approach to develop a 3D model from this reduced data set requires the selection of a reasonable substitute based on experience or case-specific complementary information.

Chapter 5

Model application

A wide range of applications exists for the muscle model which was introduced in the previous chapter. Utilizing verified material parameters, the example of a squid tentacle stroke was provided there in order to validate the model and its implementation.

In this chapter, novel application samples are investigated by means of the proposed model in order to document its usefulness and versatility.

5.1 Investigations on *M. soleus* of *rattus norvegicus*

5.1.1 Introduction

The modeling of skeletal muscle as proposed in this work requires detailed information on the particular architecture of the muscle concerned. A model based on just a rough description of the external muscle geometry and an averaged pennation angle would not take full advantage of this approach's capabilities. Localized pennation data, fiber geometries and information on the muscle-tendon junction, but also increased precision of parameters like maximum fiber twitch velocity and isometric stress support the accuracy and predictive quality of the model.

To date, very few data sets provide the complete fiber mapping of a muscle, and almost none of them are publicly accessible. However, research in that area is lively and techniques supporting the automated capture of this kind of data are ever-evolving, especially those which follow noninvasive approaches [Lansdown et al. 2007, Sinha et al. 2011, Noorkoiv et al. 2010, Oudeman et al. 2016]. These noninvasive methods have distinct limitations

regarding scanning time and quality of border identification between different tissue types. Also, they do not accomplish the level of spatial resolution that invasive or combined methods may. Usually, the latter require less expensive technical equipment, and are particularly appropriate when the objective comprises the determination of parameters which demand dissection measures anyway.

One such invasive approach was presented by Stark [2008], Stark and Schilling [2010], who developed the techniques and a reliable procedure to simultaneously acquire fiber course data and contractile force data of single muscles in *rattus norvegicus*. Mr. Stark kindly authorized and supported the use of their data within the bounds of this work.

Stark [2008] investigated the fiber mapping of the soleus muscle of five laboratory rats (*rattus norvegicus*, Wistar strain). From each specimen, left and right soleus muscles were extracted, fixed in a clamping device and shock frozen - one in relaxed state and the respective other in the state of isometric tetanic contraction. The corresponding contraction force was recorded. Subsequently, histological sections were prepared to acquire data on the muscle architecture and further parameters.

Although the body weight varied significantly between the rats, left and right muscles from the same animal showed excellent conformity. Taking symmetry into regard, this justifies the consideration of either as the relaxed, respectively stimulated, representation of the other.

The results from one pair of soleus muscles (from animal #7 in Stark [2008]), is used as reference in the subsequent analyses. Starting from the relaxed state and based on the muscle architecture from this source, the tetanic isometric contraction will be simulated in order to derive the modified architectural representation of the stimulated state.

5.1.2 Data base

Stark [2008] captured data from the m. triceps surae of twelve laboratory rats. Both components of the m. triceps surae - i.e. m. soleus and m. gastrocnemius (Fig. 5.1) - were considered separately. The most complete data sets were derived from the pair of soleus muscles from male rat #7 (denoted #3 in [Stark and Schilling 2010]), which will therefore serve as reference in this work.

The muscles were taken from the anesthetized animal and fixated in situ at relaxed length, or at contracted length in case of those muscles which were later to be stimulated. The muscles were put in a clamping device, which also allowed for the recording of contraction forces. The left soleus of animal #7 was supramaximally stimulated via the clamps

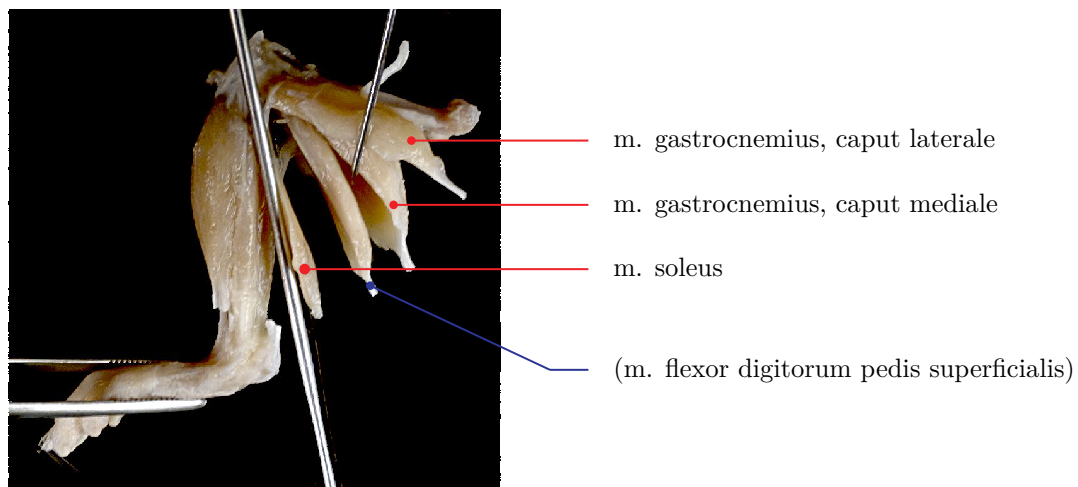


Figure 5.1: *M. triceps surae* (red) of *rattus norvegicus*, picture from [Stark 2008].

(DC 10V, 120Hz, 0.2ms). The right soleus of animal #7 remained relaxed. Either muscle was then shock-frozen in ethanol at -70°C . This step proved to be time critical, since for an ideal result the stimulation had to be maintained throughout the freezing process. A premature relaxation could lead to disturbed fiber paths within the initially contracted muscle. This effect limits the applicability of the overall procedure to muscles with small cross-sections whenever contraction is of concern.

Subsequently, longitudinal serial sections of the frozen muscles were prepared by microtome, each with a thickness of $12\mu\text{m}$. Every fourth section was kept for further histological processing. An immediate fixation in formalin and subsequent treatment with a staining agent led to distinctive dyeing of connective tissue and muscle fibers.

The sections were scanned as unassociated pictures. Post-processing included alignment, image enhancement, artifact removal, and fiber tracing. The latter was based on the evaluation of the fibers' cutting angles and the validity of traces between adjacent sections. The approach eventually led to a volume representation of the muscle geometry, vector field data of fiber orientations, and sets of validated fiber traces. The final coordinate systems defined the x-axis as the muscle's line of action from proximal to distal, and the z-axis in the direction of the greatest lateral dimension (approximately corresponding to the medio-lateral axis).

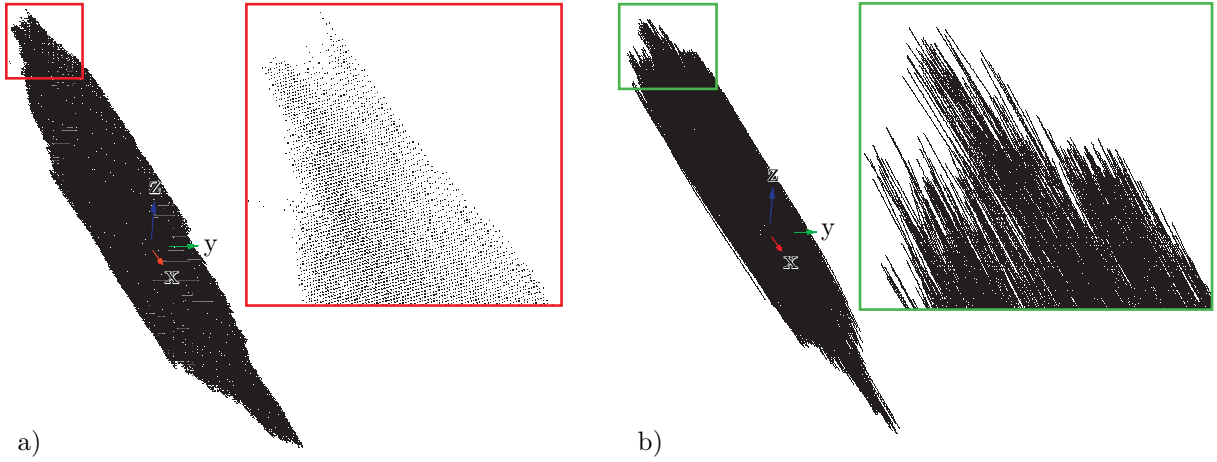


Figure 5.2: Visualization of a) vertex cloud data set and b) fiber trace data set.

5.1.3 Model derivation

5.1.3.1 Mesh generation

The finite element mesh for this work was derived from the 100 μ m spaced vertex cloud which represented the muscle volume. This vertex cloud was provided by Stark, based on the aligned microtome sections. It displays clear derangements and fringes at the border due to the mechanical impact of the microtome sectioning (see Fig. 5.3).

For this work, a cross-sectional area (CSA)-preserving smoothing algorithm was utilized to remove these faults from representative transversal cross-sections. These were then connected to obtain a volume representation of the muscle, which was subsequently meshed with hexaeder elements. These three steps to convert the vertex cloud information into finite element representation were performed in CATIA[®].

The soleus volume representations from Stark [2008] could not be used for the FE model, as they were generated with the sole objective of visualization, and CSA preservation was not ensured.

The digitized geometries comprise significant parts of the Achilles tendon (tendo calcaneus) which was disregarded here. The junction between tendon and distal tendon sheet, which also marks the distal limit of the contractile muscle tissue, was determined by a strong shift in the gradient of the CSA along the longitudinal muscle axis (see Fig. 5.4). The CSA at the identified distal location coincides well with the CSA at the proximal insertion of the soleus; which is to be expected as both are structured similarly and need to transfer the same forces.

Aponeuroses were modeled by membrane elements of varying thickness. (The particular

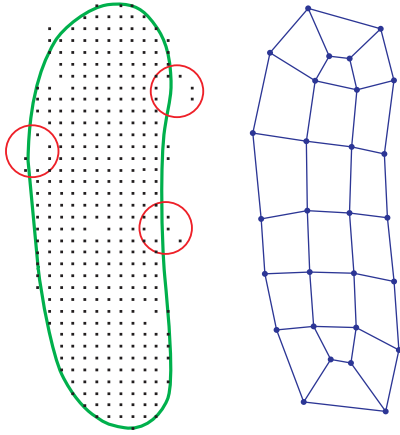


Figure 5.3: Vertex cloud cross-section (black), smoothed border (green), microtone distortions (red), and deduced mesh cross-section (blue).

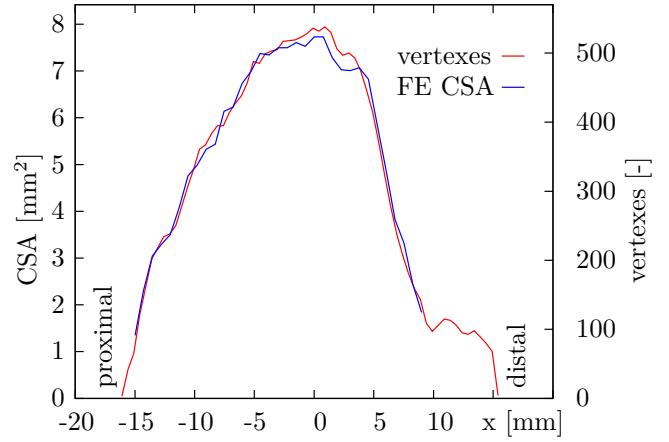


Figure 5.4: Comparison of model CSA and number of original vertexes per cross-section (relaxed).

elements for this purpose were built by manipulating the four-noded *SLang* shell element [Bucher 2013] to not possess any bending stiffness.) They were implemented as surface elements to the previously described hexaeder mesh. Their size and shape was determined by the spread of fiber trace endpoints. The fiber tracing algorithm from Stark [2008] omitted invalid or disturbed data and lead almost exclusively to fiber traces which span from one aponeurosis to the other. Their endpoints provide therefore a valid base for the determination of the aponeuroses' shape.

The aponeuroses' thickness could not be deduced from the original data sets. Instead, the thickness was derived from the overall CSA and it's gradient, the local inclination of aponeurosis with respect to the longitudinal muscle axis, the local alignment angle between aponeuroses and attached fibers, and the premise of a constant weighting factor γ for aponeurosis cross-sectional area (CSA_a) with respect to muscle cross-sectional area (CSA_m).

The details are as follows: In the relaxed state, proximal and distal aponeurosis do not overlap in longitudinal direction, and for the biggest cross-section applies $\max CSA = \max CSA_m$. From

$$CSA(x) = CSA_m(x) + CSA_a(x) \quad (5.1)$$

$$\max CSA = CSA_m(x) + \gamma \cdot CSA_a(x) \quad (5.2)$$

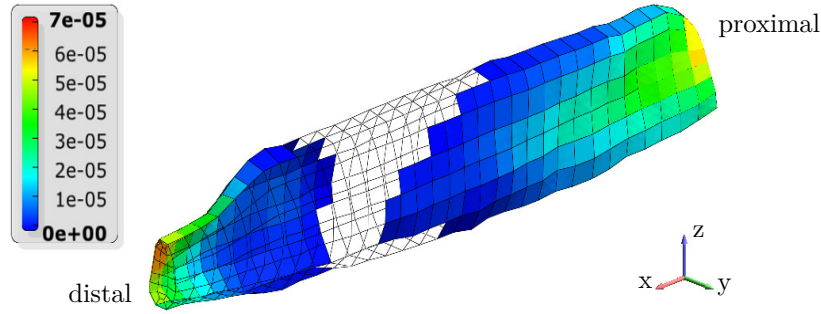


Figure 5.5: FE model with aponeuroses thickness [m].

follows

$$\text{CSA}_a(x) = \frac{1}{\gamma - 1} (\max \text{CSA} - \text{CSA}(x)). \quad (5.3)$$

Based on Cutts et al. [1991], γ is set to 31.0. $\text{CSA}_a(x)$ describes the complete aponeurosis' area within a specific soleus cross-section determined by x . The actual element thickness is then derived by weighting its share of the aponeurosis circumference at that section with the integrated effective force from muscle fibers which are directly or indirectly attached to this part of the aponeurosis. The latter contributes the dependance on the aponeurosis-fiber alignment angles. This approach may be rephrased as the simple assumption, that the aponeurosis thickness is proportional to its loads.

A depiction of the resultant aponeuroses element thickness is provided in Fig. 5.5.

5.1.3.2 Fiber mapping

Along with [Stark and Schilling 2010], the authors published several data files which may be downloaded from the journal's website. They contain vertex coordinates along with the respective fiber orientation vectors for both, contracted and relaxed muscles of animal #7.

Based on these data sets, the fiber orientation was interpolated at every Gauss point of the FE model. The response surface functionality of `SIang` (smoothing factor 2, see Fig. 5.6 for illustration) was utilized to derive the interpolated vector coordinates. For fiber orientation within the aponeuroses, the interpolated direction vectors were projected onto the aponeuroses' planes.

Fig. 5.7 shows the fiber orientations within the aponeuroses and the muscle body, where each colored line represents the direction for one element's integration point.

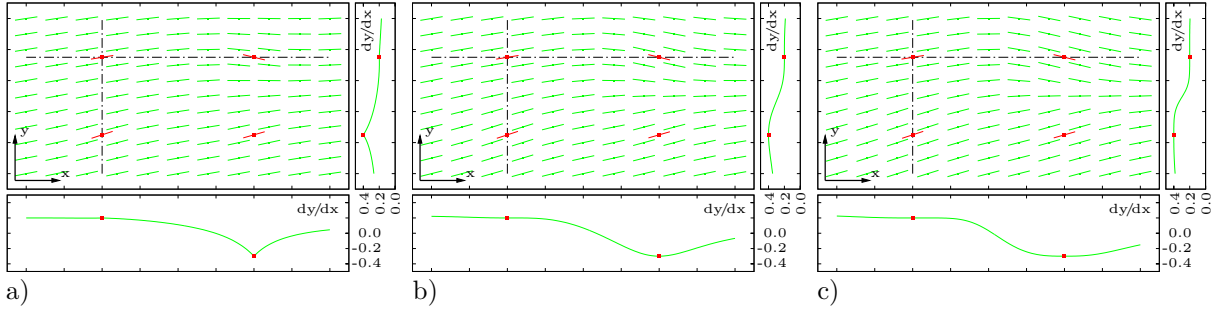


Figure 5.6: SI_{ang} response surface interpolation of an arbitrary 2D vector field with different smoothing factors: 1.0 (a), 2.0 (b), 3.0 (c). Depiction of support points and vectors (red), and interpolation results (green). Dash-dot lines mark the paths of the depicted dy/dx courses.

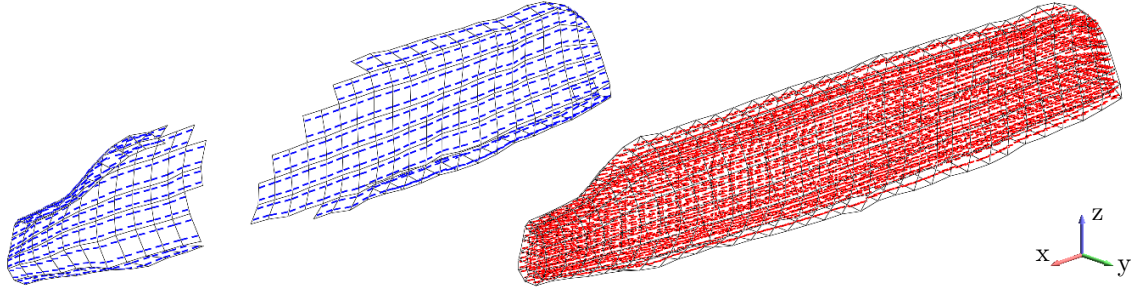


Figure 5.7: FE model fiber directions in aponeuroses (left) and muscle body (right).

5.1.3.3 Constitutive descriptions

The actual contraction of the soleus samples was predetermined by Stark through the specific flexion of the rat's hind limb during sample preparation. This posture corresponded to the muscle's optimal length where the maximum force was expected to occur. The muscle was kept at this length throughout the contraction and freezing process, hence activation dynamics, length change or contraction velocity did not affect the measurement results. Accordingly, (4.32) was simplified for the simulation, and the maximum isometric fiber stress was set to $22\text{N}/\text{cm}^2$, in accordance with the measurements of [Stark 2008].

The base strain-energy function (4.29) was used with default parameters (4.31) for the initial computation. Later, as described in section 5.1.5, parameters were adapted to specifically fit the soleus data at hand.

The aponeuroses material model was utilized as introduced in section 4.4.3, along with the parameters provided there.

5.1.3.4 Boundary conditions

Nodes of both, proximal and distal model surfaces were restrained in longitudinal (x-) direction. Selected nodes of these surfaces were also restrained in lateral directions (y, z) to provide positional stability. Beyond this, displacements were not restricted.

5.1.4 Computation

The contracted equilibrium state was derived following a Newton-Raphson approach with line-search enhancement as described in section 3.3.1. Starting from the relaxed state at the length imposed by Stark on the contracted muscle, the activation parameter f_{act} was increased from 0 to 1 in several steps. This supports a robust computation, and is not related to a physiological activation process.

In the following sections, the resultant, fully activated model state will be compared to Stark's actual data from the contracted muscle.

5.1.5 Results, optimization and evaluation

5.1.5.1 Geometry alignment

The simulation is based on geometry data from the relaxed right soleus, and results after the simulated contraction shall be compared to original data from the left contracted soleus. It is therefore necessary to mirror one geometry and align it with the other in a first step.

As mentioned before, Stark [2008] defined local coordinate systems such that the maximum lateral dimension would occur in z-direction, roughly aligned with the physiological medio-lateral orientation. Hence, the mirroring is performed with respect to the x-y-plane.

However, the alignment utilized for this work does not follow the original approach. While the cross-section's major and minor dimensions are clearly distinct from each other (see Fig. 5.3), the identification of the actual maximum could be strongly impaired by minor flaws in the geometric data (e.g., distortions in the vertex cloud as in Fig. 5.3), or the FE mesh data (e.g., the position of surface nodes). Also, due to the deformation caused by the contraction itself, the direction of the maximum lateral dimension identified from the contracted muscle's geometry is unlikely to coincide with the direction derived from the relaxed muscle.

Instead, in order to provide a reliable base for the comparison, FE and original geometries are aligned by first aligning their centers of gravity, and a subsequent alignment of

their principal inertial axes. This approach was applied to the reference data base of the contracted muscle, and led to a corrective rotation of 5.08° around the x-axis, and minor corrections of 1.28° and 1.61° around y- and z- axes, respectively.

5.1.5.2 Shape alteration during contraction

Due to volume preservation, the shortening of the soleus is accompanied with a significant lateral expansion, resulting in a characteristically altered CSA distribution. Fig. 5.8 compares the actual measurements with simulation results that are based on the initial parameter set (4.31) of the constitutive description (4.29). This simulation clearly exaggerates the mass shift from the proximal end towards the muscle belly.

The discrepancy between computed and measured CSA course calls for an adaptation of the model. A parametrized modification of either initial geometry, fiber course, or active stress does not appear meaningful in the present context, whereas the origin of the actual values of the passive material parameters are not as well-documented. Fig. 5.8 also depicts simulation results which were derived through optimization of these parameters, and which agree much better with the measurements.

The goal of matching the computed CSA data as closely as possible with the measured CSA data was implemented by minimizing the root-mean-square (RMS) of the difference between both data vectors. The optimization process - utilizing successively evolutionary algorithms (EA) and adaptive response surface method (ARSM) - was controlled with optiSLang® [Dynardo GmbH 2015]. The derived parameter set is:

$$\alpha = 35.05, \beta = 1.120, \mu = 5955.2\text{Pa}, w_0 = 0.9072 \quad (5.4)$$

The RMS minimization between computed and measured CSA course is a very obvious choice for an optimization objective in the present context and with the available data. However, some material parameters may have little impact on the objective in the given situation. In order to assess the quality of the adapted parameters, the sensitivity of the objective with respect to these parameters should be considered whenever data fitting is performed. Here, parameters were independently varied in the range of 80% to 120% with respect to their values in equation (5.4). The weighting parameter w_0 is close to its limit value of 1.0, hence the variation is performed with respect to the complementary term $1-w_0$. Results are depicted in Fig. 5.9. Clearly, the variation of the parameter β is of little significance to the selected optimization objective. This is due to the specific structure

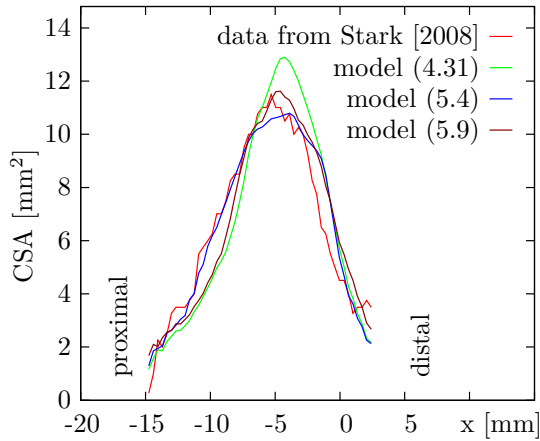


Figure 5.8: Comparison of original and computed CSA of the contracted soleus, based on Weichert et al.'s and optimized parameter sets.

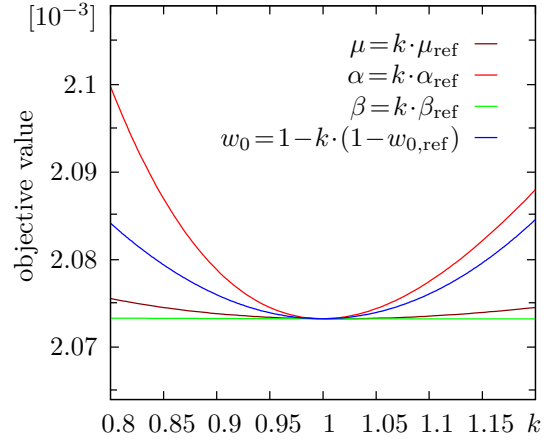


Figure 5.9: Sensitivity of the CSA optimization objective with respect to individual parameters. Optimization results (5.4) are used as reference.

of the work equation (4.29) in conjunction with the absence of any lateral loading in the experiment.

This case illustrates well how reliable material parameters must be derived from a wider, carefully assembled experimental base, and how different findings may be weighted.

5.1.5.3 Contraction force

Stark also recorded the maximum contraction force of the soleus, right before shock-freezing the muscle. The major nerve branch was stimulated at 120Hz, and full tetanic contraction was ensured. The corresponding maximum force amounted to 2.09N. The simulation with the original material parameters (4.31) led to a contraction force of 1.95N, while a simulation with the parameters determined in (5.4) led to 1.51N. This confirms the findings from the previous section, that CSA curve fitting based on the available data is in itself not sufficient for the reliable identification of material parameters.

Another optimization was conducted with the objective to minimize the deviation from the measured muscle force and identify the respective material parameters. However, this objective was shown to be inadequate, as the difference between computed and measured force amounts to numerically zero for multiple parameter sets within and outside the parameters' plausible range of (4.31) and (5.4). The parameters for arbitrary three of

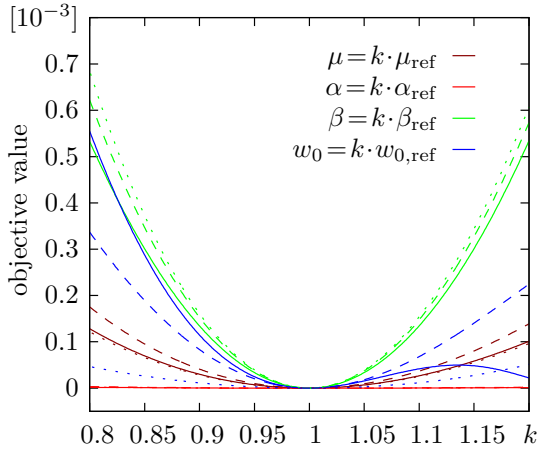


Figure 5.10: Sensitivity of force optimization objective with respect to individual parameters. Optimization results (5.5) (solid), (5.6) (dashed), (5.7) (dotted) are used as reference.

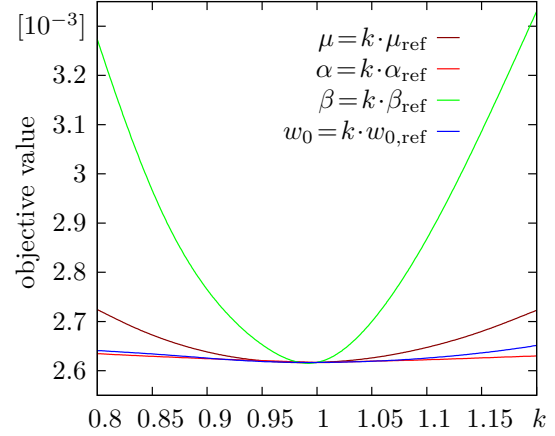


Figure 5.11: Sensitivity of the combined force/CSA optimization objective with respect to individual parameters. Optimization results (5.9) are used as reference.

these optima are listed in (5.5) et seq. for illustration.

$$\alpha = 24.01, \beta = 1.080, \mu = 1571.8\text{Pa}, w_0 = 0.5547 \quad (5.5)$$

$$\alpha = 29.45, \beta = 0.8078, \mu = 1929.2\text{Pa}, w_0 = 0.4247 \quad (5.6)$$

$$\alpha = 38.48, \beta = 0.7851, \mu = 1014.4\text{Pa}, w_0 = 0.2095 \quad (5.7)$$

The corresponding sensitivities are depicted in Fig. 5.10. Other than in the previous section, the parameter α is of little significance and the parameter β is (locally) significant to the current force optimization objective, thus indicating that the two objectives may complement each other well.

5.1.5.4 Combined shape and contraction force optimization

In order to derive a set of parameters which accounts for both, contraction force and CSA course, a final optimization was performed with respect to a combination of the previous objectives. They were weighted such that a 1% deviation of the simulated force F_{sim} from the measured value F_{exp} corresponds to a 1% RMS deviation of the computed CSA course with respect to the RMS value of the measured CSA course in x-direction:

$$f_{\text{obj}} = \left| \frac{F_{\text{sim}} - F_{\text{exp}}}{F_{\text{exp}}} \right| + \left| \frac{\text{rms}(\text{CSA}_{\text{sim}}) - \text{rms}(\text{CSA}_{\text{exp}})}{\text{rms}(\text{CSA}_{\text{exp}})} \right| \quad (5.8)$$

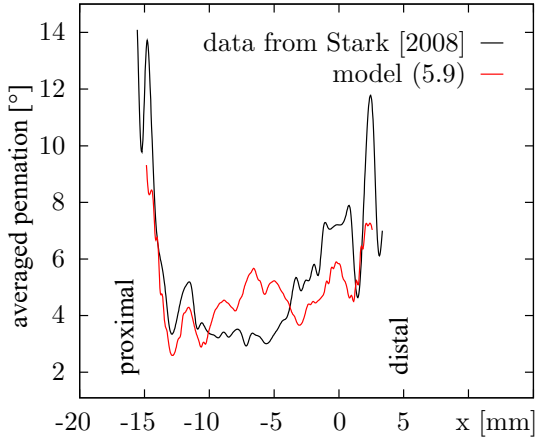


Figure 5.12: Comparison of averaged pennation angles of the contracted rat soleus muscle; original vs. simulated.

α	β	μ [Pa]	w_0	equation
CSA optimized, section 5.1.5.2				
35.05	1.120	5955.2	0.9072	(5.4)
force optimized, section 5.1.5.3				
24.01	1.080	1571.8	0.5547	(5.5)
29.45	0.8078	1929.2	0.4247	(5.6)
38.48	0.7851	1014.4	0.2095	(5.7)
combined objective, section 5.1.5.4				
40.55	0.7626	1005.1	0.1786	(5.9)

Table 5.1: Overview over parameter sets for material law (4.29) as derived from optimizing the contraction simulation with different objectives.

This weighing is somewhat arbitrary. It should ideally be based on accuracy, sensitivity and reliability of the comparison values, i.e. of the measurements. However, this information is not available at this point.

$$\alpha = 40.55, \beta = 0.7626, \mu = 1005.1 \text{ Pa}, w_0 = 0.1786 \quad (5.9)$$

The combined approach led to the parameter set (5.9). The resultant force complies with the measured force of 2.09N; the CSA course is depicted in Fig. 5.8 as well. Relative parameter sensitivities are shown in Fig. 5.11.

5.1.5.5 Fascicle orientation

One further potential means to validate or determine material parameters is the comparison of the fascicle orientation after contraction. However, comparison between reported data and computation results based on the parameters of equation (5.9) gave mediocre results (see Fig. 5.12), and the optimization of material parameters within reasonable bounds did not lead to a significantly lessened misalignment between the two curves.

Several factors are likely to contribute to this behavior: For the simulation, the proximal and distal ends of the muscle are modeled plane in the relaxed state, and are presumed to remain plane during contraction. This approach may be unrealistic, especially in conjunction with the potentially distorting clamping mechanism of the experiment. Relative offsets between fibers at both ends may cause the pennation disparity shown in proximal and distal positions of the graph, and they may impact the pennation in the muscle body.

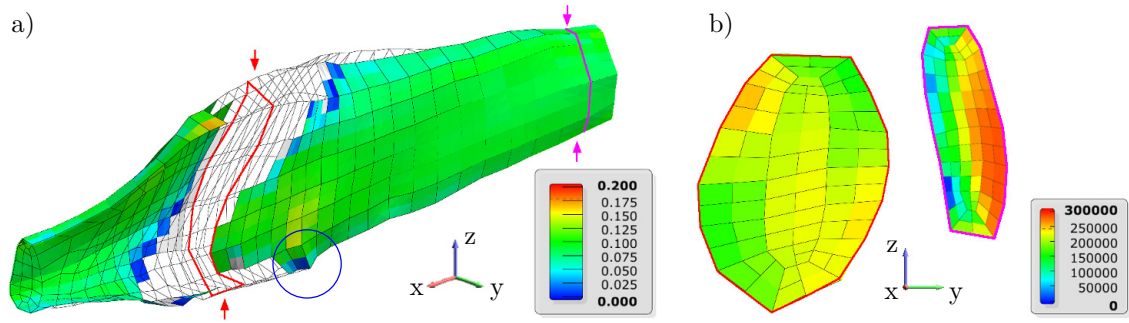


Figure 5.13: Contracted soleus. a) aponeurosis strain in fiber directions b) lateral pressure distribution (in the element planes marked on the left) [Pa].

Pennation may also be affected by inconsistencies in the reference data of Stark [2008], which stem from the different objectives and various data processing approaches of that work (e.g., for the contracted geometry, the number of available grid points with directional information amounts to less than 1/15th of that of the relaxed geometry). And due to the way the model has been deduced from different data sets (see section 5.1.3), there are artifacts where fibers are not perfectly aligned with the surface of the 3D representation, resulting in small non-physiological model areas (see protruding corner in blue circle in Fig. 5.13).

As the computed pennation angle is much more sensitive to such errors than the aforementioned CSA and contraction force, these issues render the current data unfeasible for an optimization with respect to fiber orientation.

5.1.6 Summary

Based on an extensive geometric data set of contracted and relaxed rat's m. soleus by Stark [2008], a detailed three-dimensional model of that muscle was developed. The model included detailed descriptions of aponeuroses and muscle fiber geometry, and transversely isotropic material behavior as deduced in section 4.4. The contraction process was simulated, starting from the relaxed soleus geometry, and resulting in a fully activated representation of that muscle. Material parameters were initially taken from Weichert et al. [2011], and subsequently optimized for compliance with Stark's data of the contracted muscle. The utilized optimization objectives comprised the minimization of deviations from the measured course of cross-sectional area and from the measured contraction force. The course of averaged pennation data proved to be insufficiently consistent for optimization purposes.

Implementing the optimized parameters, and following a corrective alignment based on the orientation of the principal inertial axes, simulation results and measurements show good agreement. Muscle pressure and aponeurosis stress distribution are plausible and well within the physiological range reported from other measurements in comparable contraction scenarios. The overall approach to modeling and simulation was validated and is expected to perform as well in different settings.

Furthermore, the investigation clearly illustrates that more physiological samples and complementing simulations are required to determine an optimization objective which may be used to not only reliably derive material properties, but, subsequently, also to identify experimental or modeling shortcomings, to evolve material models, and to ultimately increase simulation quality.

5.2 Muscle activation as means of injury prevention

5.2.1 Introduction

In anticipation of impact forces or sudden accelerations, conditioned defensive reflexes do often include muscle tensioning which involves both, agonist and respective antagonist muscles. The objective of such contractions is clearly not coordinated movement, but rather the utilization of an increased stiffness of the muscles, and thus the potential protection they may provide. A quantification of such effects is currently lacking, and areas of advantageous application have only insufficiently been identified.

In light of the inadequacy of natural reflex conditioning with respect to the hazards of modern technologies and artificial environments, huge efforts are made to keep the associated risks at a minimum. In fact, safety systems have themselves become a highly innovative field of research and development.

Passenger cars are an outstanding illustration of this circumstance. A regular modern car subjects its occupants to velocities that were unforeseeable for the wide public just hundred years ago. The associated risks are very obvious, but were hardly addressed during the pioneering years of the automobile. Only with cars becoming less exclusive and accessible to a significant part of the population, the awareness of these risks grew on behalf of the manufacturers and regulating authorities. Subsequently, passenger safety became increasingly important in car design. Occupant protection, along with accident avoidance, is one major objective in that process. The typical approach is to establish safety zones around the occupants which must not be penetrated by any items of the car

interior, and to restrain the occupants from moving out of that zone. Especially the latter requires in-depth knowledge of occupant kinematics and injury thresholds.

Extensive data mining was and is undertaken to generate a wide statistical base on the course of accidents, occurrence probabilities, and damage inflicted. Because this information was traditionally acquired by policemen or insurance experts, the inclusion of medical injury assessments in statistically relevant numbers is a rather recent development¹. Although the variance in human physiology is acknowledged to have significant influence on injury mechanisms and severity, only lately the influence of the instantaneous muscle tensing on passenger kinematics has been studied. Here, this approach shall be taken one step further, and the local effect of muscle tension on the outcome of a potentially damaging impact will be investigated.

5.2.2 Background

Many studies which relate car crash injury data to passenger parameters evidence the significance of the latter. Weight, age, gender, BMI (body mass index), height and other factors do strongly influence injury probability and severity in otherwise identical accident scenarios. Some correlations may be attributed to physique-specific posture, body weight distribution or positioning of seat belts, which in turn influence the occupant's kinematic during a crash [Dischinger et al. 1995, Tsunetoshi et al. 2006, Kent et al. 2010]. But there is also a distinct dependence on structural parameters. For example, the comparatively high risk of fractures and fatalities in the elderly can be attributed directly to diminished bone mineral density and a loss of skeletal elasticity due to the ossification of cartilage [Mercier et al. 1999, Zhang et al. 2000, Yoganandan et al. 2007]. Duprey et al. [2008] also demonstrated a similar, but less pronounced, gender dependence.

These latter relations support the assumption that also factors like body composition and, in case of skeletal muscles, instantaneous activation will affect injury probability and severity.

However, while BMI data have been recorded in several occupant injury studies, more detailed data on body composition were rarely acquired. Given that samples for these kind of studies cannot be preselected, a great number of individual cases would be necessary to reliably capture the subtle distinctions of different soft tissue types in injury scenarios, e.g. slack muscle and adipose tissue. Kent et al. [2010] attempted to identify specific injury

¹ Data bases containing injury assessments: CCIS (Co-operative Crash Injury Study - UK), NASS/CDS (National Automotive Sampling System/Crashworthiness Data System - USA)

patterns in the obese on the base of sled tests with PMHS (post mortal human subjects), but were unable to separate the effects of obesity and weight due to their strong correlation.

While these investigations of the relation between body composition and injury severity in car crashes are difficult due to the lack of sufficient data, an investigation of the muscle tension effect in humans is practically impossible during potentially harmful crash situations. One sample instance of this effect was reported in [Tencer et al. 2002]. Femoral fracture due to a rear-end collision was shown to occur more often in the bumping driver's right than in the left leg. This type of fracture is commonly caused by insufficiently restraining lap belts, resulting in a forward motion of the lower torso and the knee hitting the dashboard. Ruan et al. [2008] could validate Tencer et al.'s hypothesis, that tension in the extensors (m. quadriceps femoris) of the right leg due to hard braking generates longitudinal pressure and a bending moment in the femur, thereby increasing the risk of fracture.

There are few studies investigating muscle damage due to stationary pressure [Bosboom et al. 2003, Gefen et al. 2005], but further sources of real-world data or publications regarding the influence of muscle contraction in dynamic impact scenarios with humans could not be acquired. Several animal studies on the topic are available. E.g., Crisco et al. [1996] exposed rat gastrocnemius muscle to a blunt lateral impact while either relaxed or fully tensed, and evaluated the damage to the muscle tissue itself (result: tensed muscle took less damage). However, as more complex experiments would not yield transferable results for humans, these investigations are generally restricted to similar fundamental relations.

A reliable modeling and simulation base is essential to assess the effects and potential benefits of muscle tension, voluntary or imposed, in accident scenarios.

5.2.3 Sample object: Thorax

Beyond the obvious kinematic or postural examples, there are many more scenarios worth considering when investigating muscle activation as a means of injury prevention. E.g.:

- Selective contraction of limb muscles may counteract potentially harmful bending stresses in bones caused by external loads (e.g. biceps femoris contraction during the aforementioned dashboard collision).
- Contraction of torso muscles may help maintaining the blood supply to the brain under high inferior acceleration forces (comparable to a pilot's pressure suit).

- Simultaneous contraction of agonists and antagonists may impose compressive stresses where otherwise harmful shear stresses would dominate (e.g. the effect of simultaneous erector spinae and rectus abdominis contraction on the spine under transversal torso loads).
- Contraction of muscles which cover bones may serve to disperse loads and prevent local trauma (e.g. semispinales contraction protecting the cervical spine from local impact loads)
- Contraction of abdominal muscle may help shielding sensitive organs from external impact loads.

Et cetera. Subsequently, the consequences of anterior thorax muscle activation during an automobile front-impact are considered, specifically with respect to potential rib fractures from seatbelt restraints.

In general, rib fractures alone are not regarded as severe injuries in healthy adults, with an AIS injury rating¹ of 1 (single rib fracture) or 2 (two to three fractured ribs). However, rib fractures can contribute to far more severe thoracic injuries such as lung and heart laceration. And while the occurrence of rib fractures in automobile crash scenarios does not necessarily point to more severe organ injuries, the latter are unlikely to occur in the absence of a rib fracture. (E.g., Thor and Gabler [2008] studied NASS² data of frontal crashes and identified AIS2+ lung injuries in 7% of occupants with broken ribs, whereas rib fractures were diagnosed in 45% of those with AIS2+ lung injury.)

The specific choice of the sample object was also made due to the availability of a thorax geometry representation at the Institute of Structural Mechanics (ISM) at the Bauhaus University Weimar, and the thorax research conducted there [Drücker 2002, Bruhin et al. 2005, Schneider 2012].

5.2.4 Model derivation

The thorax model which was developed at the ISM helped assess different thorax closure techniques subsequent to median sternotomy [Drücker 2002, Bruhin et al. 2005]. The

¹ The AIS (Abbreviated Injury Scale) rates the severity of individual injuries from 0 (minor) to 6 (maximum). It is revised and regularly updated by the Association for the Advancement of Automotive Medicine. The AIS is not based on, but loosely correlating with the odds of mortality, with 6 also paraphrased as certain death. ² The NASS (National Automotive Sampling System) is based on a continued collection of crash data by the NHTSA (National Highway Traffic Safety Administration) with specific emphasis on injury mechanisms.

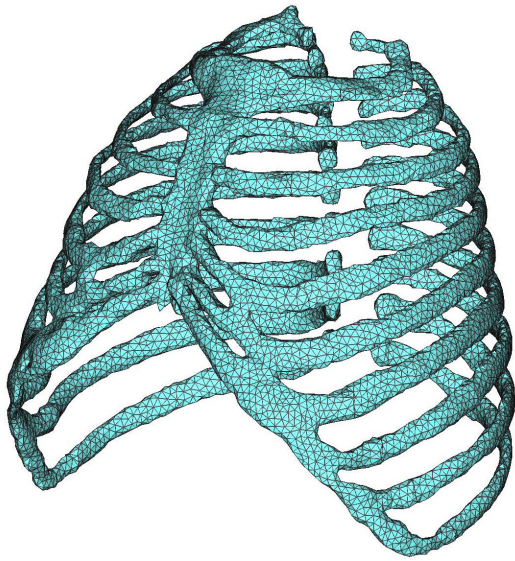


Figure 5.14: Triangularized thorax geometry model from Bruhin et al. [2005].



Figure 5.15: Transversal thorax cryosection, width=432mm (Visible Human Project, U.S. National Library of Medicine).

model comprised a triangularized geometry/finite element representation of the thorax (Fig. 5.14), and complex constraint definitions to account for realistic spine kinematics and spine-rib coupling. Muscles were represented through one-dimensional forces only.

5.2.4.1 Mesh generation and fiber mapping

The model in this work is utilized to assess the local effect of muscle activation at the seat belt contact area. Hence, a reduced modeling approach was followed, with only two representative ribs and the enclosing muscle. Ribs 3 and 4 from the ISM thorax model were chosen. In order to avoid non-physiological stress peaks in the ribs, and to allow for a smooth mesh transition to the muscle, the triangular rib representation was dismissed. Center splines and rib cross-sections were determined, and elliptic tube sections (in the detailed model area) and stiffness-equivalent beam cross-sections (elsewhere) were defined (see Fig. 5.16). The detailed, tubular part of the ribs was modeled by means of four-node shell elements. This part of the ribs extends beyond the core model in order to keep stress disturbances from the beam-tube transition out of the assessed region.

The muscular structure was modeled from the interspace between 4th and 5th rib inferior to the interspace between 2th and 3th rib superior. Laterally, the dimension was determined to sufficiently extend beyond the belt contact area. The thickness of the pectoral muscle layer was derived from cryosections of the Visual Human Project (VHP, U.S.

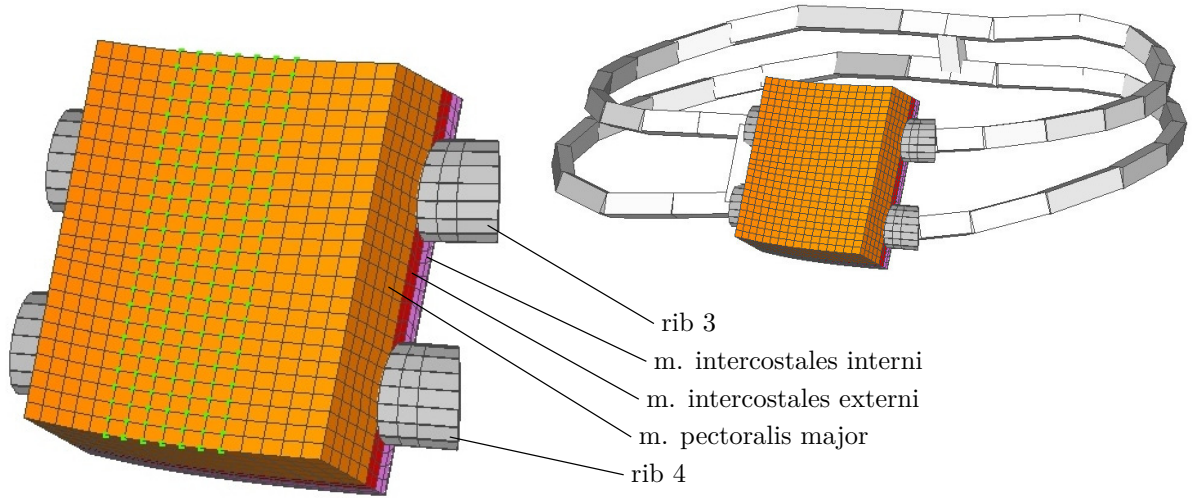


Figure 5.16: Derived FE model of ribs 3 and 4, with added muscle structures.

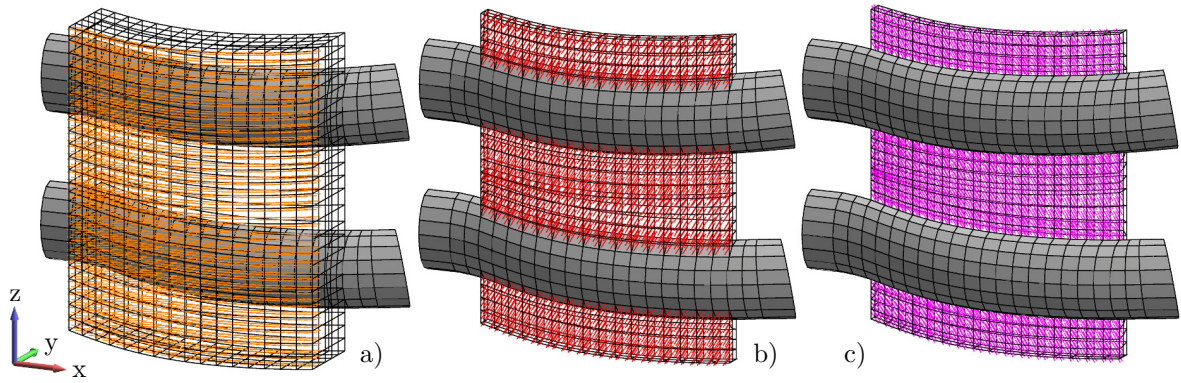


Figure 5.17: Fiber course in the three muscle layers (depicted at integration points of the foremost element layer only): a) m. pectoralis major b) m. intercostales externi c) m. intercostales interni

National Library of Medicine, Fig. 5.15). Outer and inner intercostales muscles were modeled to comply with the rib geometries. Pennation information had to be gathered from anatomical drawings. Estimates at few selected points served as supports for the interpolation of fiber direction vectors at integration points. See Fig. 5.17 for a visualization of the fiber course.

5.2.4.2 Constitutive descriptions

For all three muscles in the simulation, the strain-energy function (4.29) was used in conjunction with the parameter sets derived in section 5.1. Active muscle properties were modeled as described in section 4.2.1.2: activation by (4.23), strain and strain rate

dependence by (4.11) and (4.21), respectively. The utilized parameters are provided in Tab. 5.2.

Ribs were modeled as hollow tubes. In reality, ribs possess no single-cavity marrow-filled center, but are interfused with spongy bone structures. But the stiffness of this trabecular bone amounts to less than 5% of the stiffness of the outer cortical bone [Li et al. 2010]. Hence, it has little structural relevance and may be disregarded as long as investigations do not account for the actual damage or fracture mechanisms of ribs. The present simulation does consider neither, and strains remain below 5% within the ribs, so a linear elastic material model was chosen for cortical bone. The Poisson ratio was determined to 0.3 and the Young's modulus to 13.5GPa. The latter was taken from Subit et al. [2013] and presents a reasonable average with respect to other literature values (Zioupos et al. [2008]: 16.1GPa, Kemper et al. [2007]: 13.9GPa, Li et al. [2010]: 11.5GPa).

5.2.4.3 Loading

The loading scenario is based on a 30mph rigid barrier crash test in accordance with U.S. Federal Motor Vehicle Safety Standard (FMVSS) No. 208. Kent et al. [2007] and other publications propose a validated one-dimensional three-mass spring damper model to derive thorax deceleration during this particular and similar scenarios. It accounts for the delayed reaction of internal and posterior thoracic structures. The resultant acceleration loads (see Fig. 5.18) were applied in the simulation at hand.

The belt deceleration was imposed directly in the designated contact area, whereas the delayed mass forces were accounted for as pressure loads on rib loop and anterior muscle surface.

5.2.4.4 Boundary conditions

Nodes in the belt contact area were constrained to remain plane; the curvature of the belt is disregarded. Also, all four surfaces that intersect muscle fibers were modeled with individual planar constraints. Rib nodes in the medial and lateral surface planes were excepted from these constraints to allow for independent bending. The rib loop was restrained at the spinal nodes such that only motion perpendicular to the spine is permitted.

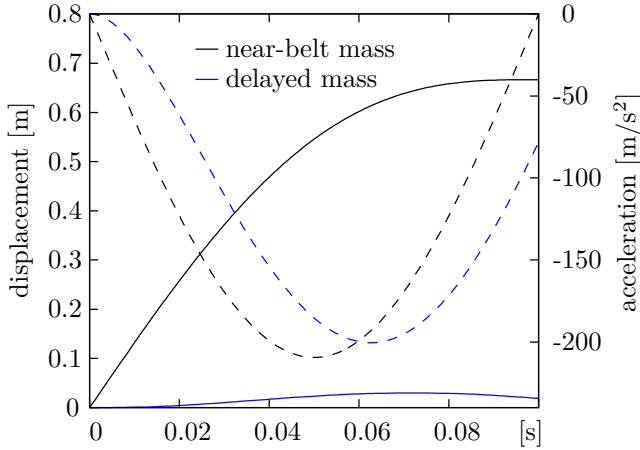


Figure 5.18: Model motion for 30mph rigid barrier crash test. (Accelerations dashed. Displacement of delayed mass shown relative to belt displacement.)

factor	eq.	parameters
f_{act}	(4.23)	$\alpha_1 = 0$ $\Delta\alpha = 1$ $c = 2.996$
f_v	(4.21)	$\dot{\lambda}_0 = -20$ $c_c = 4$ $c_{e1} = 55.232$ $c_{e2} = 30.24$ $k = 40$
f_l	(4.11)	$a_c = 0.52$ $a_e = 0.73$

Table 5.2: Contraction parameters

5.2.5 Computation

The simulation covers the 0.1 s impact time shown in Fig. 5.18 plus any preceding contraction time. Referring to that scale, the onset of contraction was varied between -0.3 s and $+0.1$ s, the latter corresponding to a contraction-free impact.

Equilibrium states during the impact process were derived following the Newmark procedure from equation (3.80).

5.2.6 Results and evaluation

5.2.6.1 Rib fracture probability

The major concern of the present study is to investigate whether and to what extent the effect of muscle activation may reduce the occurrence of rib fractures in the given accident scenario. This is deduced from an assessment of maximum rib bending moments. Fig. 5.19 displays their course for various contraction onset times, i.e. with different contraction states while exposed to the same impact environment. The advantageous decrease in the rib's bending moment with increased muscle tension is evident; it amounts to 23% if the activation is initiated at least 0.1 s before the impact.

Anterior rib fracture moments are reported in the area of 2.0 to 2.5 Nm [Cormier et al. 2005, Pezowicz and Glowacki 2012]. There are many more publications regarding the fracture strength of ribs, but although the (US-)National Highway Traffic Safety Administration provides guidance on how to capture data from a standardized rib bending test

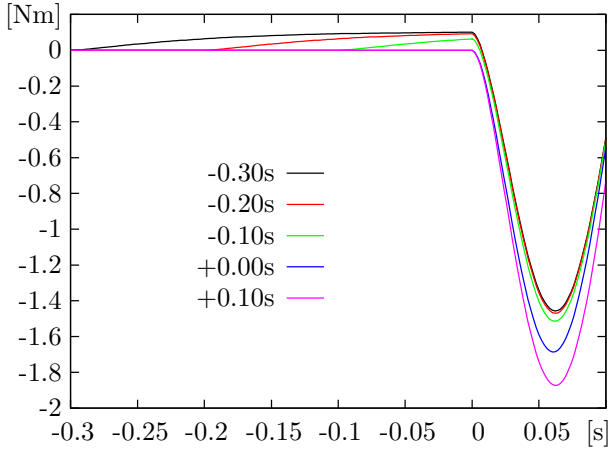


Figure 5.19: Maximum rib bending moment for different activation onsets

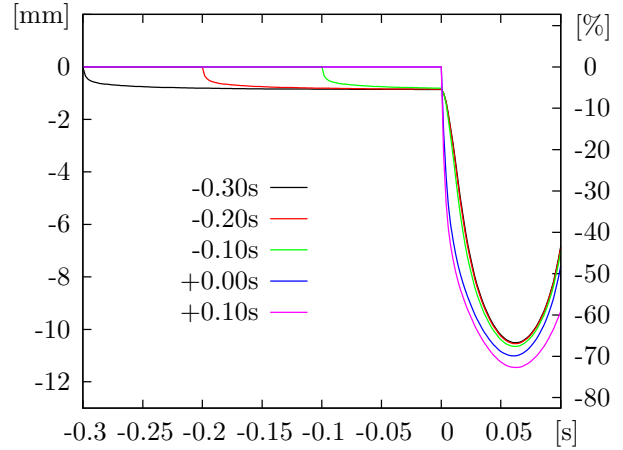


Figure 5.20: Maximum muscle indentation below belt for different activation onsets

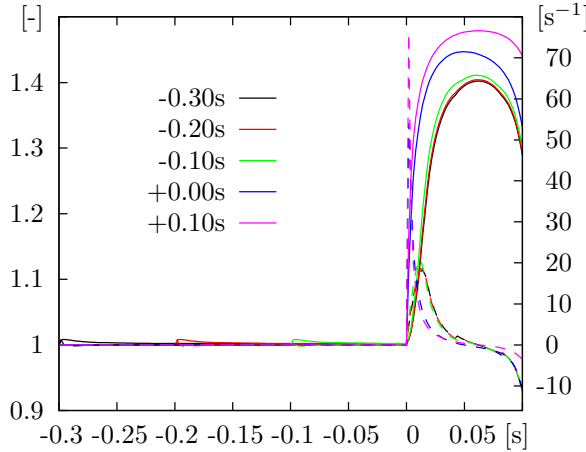


Figure 5.21: Maximum fiber strain (solid) and strain rate (dashed) for different activation onsets

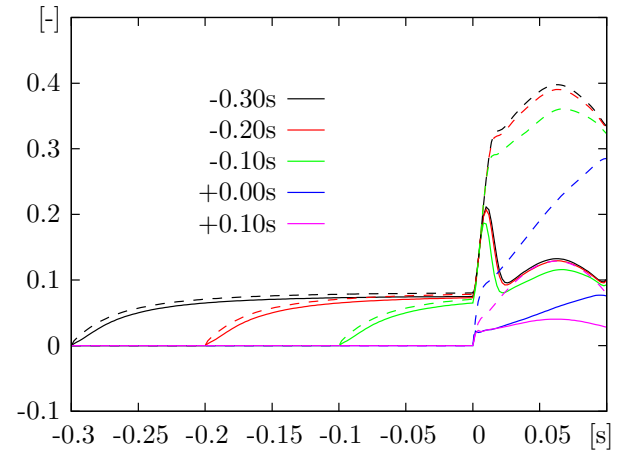


Figure 5.22: Maximum cross-fiber (solid) and along-fiber (dashed) shear strain for different activation onsets

procedure [NHTSA 2014], few published data are actually comparable. Often, forces are presented without reference geometries, strains without cross-sections, or equivalent stresses without clear definition. Nonetheless, the coefficient of variation¹ c_v of either result - fracture moment, fracture force or fracture stress - can often be deduced, and the comparison is valid:

- Stitzel [2003]: $c_v = 48.7\%$ (59 samples, 2 female/2 male subjects)
- Kemper et al. [2005]: $c_v = 28.5\%$ (117 samples, 3 f./3 m. subjects, age 18-67)

¹ c_v is also referred to as relative standard deviation, defined as standard derivation divided by mean.

- Granik and Stein [1973]: $c_v = 29.2\%$ (subjects pre-selected, 5 of 15 excluded)
- Subit et al. [2013]: $c_v = 22.8\%$ (10 samples, 3 subjects, age 54-71)
- Agnew et al. [2014]: $c_v = 60.9\%$ (test samples, 10 f./33 m. subjects, age 9-92)
- Stein and Granik [1976]: $c_v = 35.6\%$ (218 samples, 79 subj., age 27-83, c_v age-corrected)
- Cormier et al. [2005]: $c_v = 66\%$ (52 samples, 2 f./2 m. subjects, age 61-71)
- Pezowicz and Glowacki [2012]: $c_v = 32\%$ (33 samples, 17 f. subjects, age 10-22).

Of the above, the first two studies examined samples of cortical rib bone, the other ones tested intact rib segments in bending setups. The numbers illustrate an overall significant variation between the subjects, with a strong dependence on age and gender. The variance within one individual cannot be deduced from these data. However, three of the above publications provide more details, e.g. the assignment of results to specific ribs, rib positions or donors: Agnew et al. [2014] tested complete ribs, and provided the number of tested ribs per subject along with the individual mean and variation of the fracture stress. Cormier et al. [2005] and Stitzel [2003] tested rib segments and provided the results per rib, segment origin (anterior, lateral, posterior) and subject.

For further evaluation, data were confined here to sets which comprised at least four tests per individual and segment location. Also, only data from the middle ribs (ribs 3 to 8) were considered. 22 such individual sets were identified; the respective coefficients of variation are:

- Stitzel [2003]: $c_v = 28.6/28.8/27.8/29.4/16.7/23.9/17.9 \%$
- Agnew et al. [2014]: $c_v = 18.7/22.8/16.2/24.9/36.3/23.4/23.8/7.3/27.0/33.4 \%$
- Cormier et al. [2005]: $c_v = 29.1/23.5/31.6/20.5/26.6 \%$

averaging to a coefficient of variation for rib fracture characteristics of $c_v = 24.5\%$ with a standard variation of $\sigma(c_v) = 6.5\%$. The data sets are not sufficiently conclusive with respect to age and gender to derive a more precise estimate for the 38 year old male VHP donor on which the present computation was based (see Fig. 5.15).

The individual fracture data sets from Cormier et al. [2005] and Stitzel [2003] do not agree on one specific distribution type, but are clustered around a hypothetical uniform distribution. Likewise, the complete set of all rib fracture data is best approximated as uniformly distributed, although the data range (54% to 131% of the mean, see Fig. 5.23) reflects the slight non-uniformity.

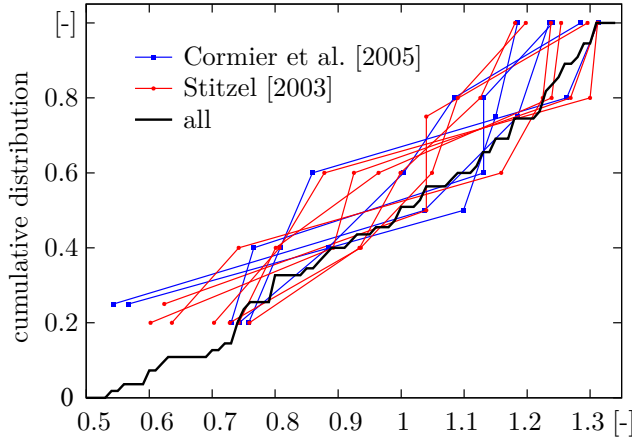


Figure 5.23: Cumulative fracture distribution vs. mean-normalized fracture parameter. Individual data sets and accumulated data.

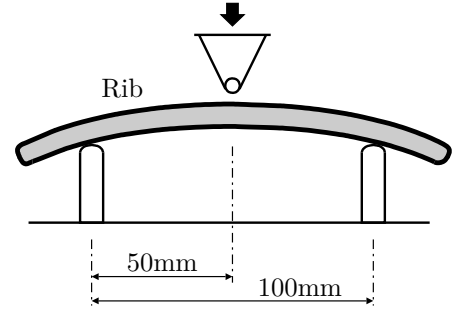


Figure 5.24: Rib fracture test setup according to [NHTSA 2014], also adopted by Stitzel [2003]

For an ideal uniform distribution, the standard variation σ amounts to 28.9% of the distribution interval, and the interval range is $\pm 1.73\sigma$. Thus, if the realization of an uniformly distributed fracture parameter changes by 1σ within the distribution interval, the fracture probability changes by 28.9% accordingly.

With these data as reference, the effect of muscle tone in the simulated scenario can be assessed: The maximum reduction in rib bending moment amounts to 23%, and was shown to occur when the pectoralis major muscle is fully activated. This corresponds to $0.94c_v$ with $c_v = 24.5\%$ as derived above. Hence, presuming the mean as reference point, the reduction of the rib bending moment by way of muscle activation results in a reduced fracture probability of up to 27.1%.

5.2.6.2 Muscle indention and tissue injury

The level of muscle tissue injury cannot be deduced directly from the present simulation, because there are no comparison data, adequate theories or models available. Overall, there are few studies regarding the damage mechanisms involved, and none was found to address the influence of contraction.

Pressure was frequently proposed as a damage indicator [Bosboom et al. 2001a, Breuls 2003], but the exclusive subject of those investigations were sores from prolonged load application. Ceelen et al. [2008] and Oomens et al. [2014] followed the same objective, but validated two separate damage mechanisms in animal studies: ischaemic damage (semi-static pressure-related and caused by the occlusion of blood vessels) and deformation dam-

age (related to shear strains orthogonal to the fiber direction). Whereas the former should have little bearing in the present impact simulation, the latter is likely to be relevant here. However, a quantitative assessment of the deformation damage was not deduced. Also, due to the nature of their experiments - only lateral muscle compression was considered - Ceelen et al. and Oomens et al. did not identify along-fiber shear and fiber strain as damage indicators, which Ito et al. [2009] proposed in a theoretical approach.

It appears likely that excessive strain in any direction will result in tissue damage. Unfortunately though, there are no verified injury thresholds available for deformations other than fiber strain and strain rate (which are covered by a wealth of sport- and exercise-related publications, e.g. Garrett et al. [1987], Friden and Lieber [1992], Taniguchi et al. [2003]). Reported failure strains in fiber direction lie in the range of 25% to 50%. Data show this threshold to be significantly diminished in case of extreme eccentric strain rates, and slightly increased with activation. These two effects act antithetic in the present scenario, as shown in Fig. 5.21: The impact simulation with relaxed muscle fibers (contraction onset +0.10s) produces the highest strain rates, whereas further progressed contractions result in lesser strain rates. Also, the relaxation of muscle fibers prevents the build-up of significant shear stresses, and thus the aforementioned potential damage indicators cross-fiber (deduced from I'_3 in (2.43)) and along-fiber shear strain (I'_4 in (2.43)) increase with the activation level. This is well illustrated in Fig. 5.22.

The comparison of relaxed vs. fully contracted muscle provides no clear conclusion as to which scenario leads to lesser injury in the pectoralis major. Significantly higher maximum fiber strains (+19%) and strain rates (factor 4) indicate higher damage probability or more severe damage in the relaxed configuration, respectively, while higher shears strains (factor 3) indicate the opposite. The former values lie within a range that was shown to be critical in some cases, whereas no comparison values are available for the latter. Aside from the apparent lack of thresholds, these damage indicators are likely to be insufficient for a definite assessment. Considering the microstructure of muscle tissue, strain and pressure gradients may as well have an impact on inflicted damage; and an integral consideration - strong localized vs. lesser extended damage - may prove favorable to assess healing chances and thus damage severity.

Given the vagueness in the prediction of muscle injury, it shall be pointed out that skeletal muscle injury is always regarded as minor ($\text{AIS} \leq 1$) and will be of secondary interest in a severe injury scenario.

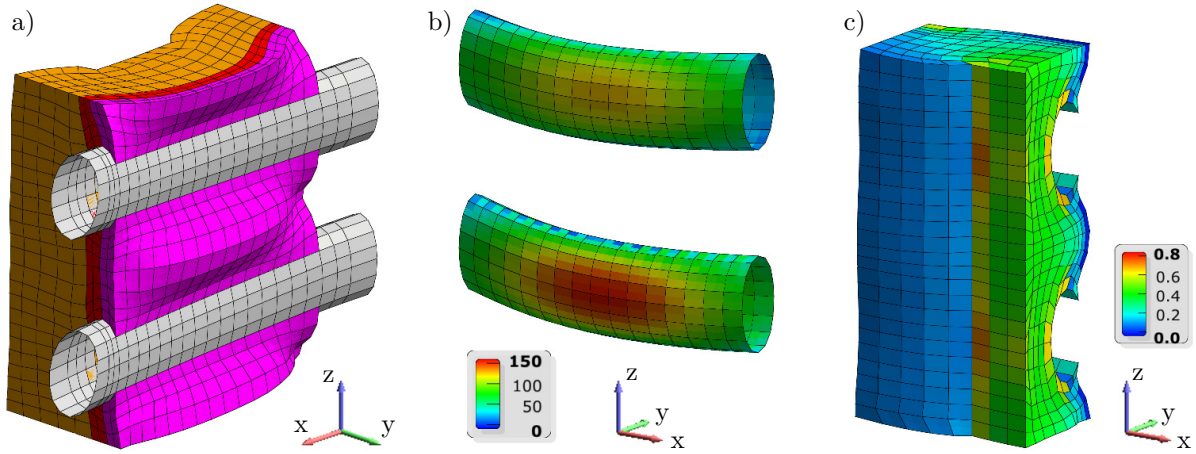


Figure 5.25: Depiction of structure at +0.07s, with activation onset at -0.1 s before impact (see 5.2.5): a) posterior view of deformed structure b) rib bending stress σ_{xx} c) pressure (model bisected) [MPa].

5.2.7 Summary and discussion

The results provided in the previous sections clearly validate the initial hypothesis that muscle activation has a significant potential for injury prevention. For the specific setting of a 30mph rigid barrier car impact, it was derived that rib fracture probability for a belted car occupant could be reduced by means of a timely activation of the m. pectoralis major. The activation should be triggered at least 0.2s before impact in order to fully benefit from the effect, i.e. decrease the fracture probability by 27%.

A quantitative assessment of the - potentially less severe - tissue damage could not be provided due to the lack of established damage thresholds.

The presented model allows the investigation of the localized protective effect of the contracted muscle. The consideration of postural or joint manipulations by means of muscle control, and their implication on loading and whole-body kinematics exceed the scope of this simulation. Currently, this exceeds the scope of a fully three-dimensional model approach in general - not due to a limitation of the underlying methods and algorithms, but rather due to the immense efforts required for the geometrical modeling of free-form geometries with multiple anisotropic materials. At least when isolated, said considerations are more effectively undertaken by using the established straight-line models (see 4.2).

Chapter 6

Conclusion

6.1 Summary

A model for the simulation of active skeletal muscle has been developed, implemented, validated and applied in this work.

It is founded on a finite element approach and a continuum description of muscle, which accounts for anisotropy by means of continuous fiber vector fields. Fiber kinematics as well as visco-elastic properties and activation control patterns are considered for the muscle dynamics.

Herein documented is the development of finite elements capable of handling semi-incompressible material behavior, the development of functions to describe the muscle fiber properties, and their incorporation into an adequate three-dimensional constitutive framework. The different steps are compared to and match positively against various alternative approaches, and overall prove to be advantageous with respect to completeness and general applicability.

Two application studies were conducted a) on the contraction behavior of rat soleus muscles and the determination of relevant muscle parameters, and b) on the impact of upper body constitution on likelihood and severity of specific seatbelt injuries which vehicle occupants may experience in an automobile crash scenario. Either study provided meaningful results and led to further validation of this work's approach.

For all involved domains, scientific context and foundations are provided.

6.2 Discussion and outlook

One major motivation for this work was the lack of a generally applicable simulation framework for researching active muscle behavior, the generation of motion and force, while considering three-dimensional constraints and interaction. The present work provides such a framework, and also the basis for further extension in terms of variables to consider (e.g. fatigue and recovery) and model enhancements (e.g. constitutive descriptions).

Specifically the need for the latter is illustrated well by examples in sections 4 and 5, for which reference solutions are established. While the material models utilized here were successfully optimized to closely mimic the objectives and thus provide worthwhile results, the deviation between different fitting parameter sets indicate that a further enhancement of the base material model would be meaningful. However, such efforts have to be based on extensive coordinated testing, far beyond the mostly independent small sample examinations which are currently published. Such a structured approach to investigate muscle behavior thoroughly and in three dimensions appears to be a significant and essential step to further advance the quality of simulation.

An automated, non-invasive capturing of muscle geometries (and also of the geometries of aponeuroses, tendons, origin and insertion sites) could be another contributor to simulation advancement. Several disadvantages of the shock-freezing method applied in the rat soleus study were already named. But current progress in that field is significant: Especially Live-MRT is an extremely promising means for better physiological interpretation of high-resolution images.

The study on seatbelt injuries illustrates the potential of the developed model. But it also illustrates a significant enhancement potential in the way such a complex scenario needs to be simplified. In order to derive reasonable boundary conditions, the study had to rely on several results from preceding publications which could not be fully validated. The consideration of different coupled models appears to be essential for future efficient, thorough simulations. In the present context, rigid body and finite element models, straight line and 3D models, and possibly also complementing models on different scales would allow for a more complete model and thus advance flexibility and reliability of the simulation.

Appendix

A.1 Mathematical preliminaries

This section gives a short outline on tensor calculus and notation. For more extensive information on the topic consider the corresponding chapters in mechanics textbooks, e.g. Betten [1987], Ogden [1997], Weichert and Başar [2000], Itskov [2009], or Iben [1995], Lippmann [1996] for a rather mathematical approach.

Einstein summation convention applies throughout this work, except for indices in brackets. The notational convention from chapter 2.1.1 regarding the physical interpretation of upper and lower case variables does not apply here. Instead, the following notation is used: first-order tensors are denoted by bold lower-case letters, second-order tensors by bold upper-case letters, higher-order tensors by double-struck letters. Non-bold letters of either case denote scalars.

A.1.1 Tensor calculus

A.1.1.1 Base systems

An arbitrary basis is formed by independent base vectors in covariant $\{\mathbf{g}_i\} = \{\mathbf{g}_1, \mathbf{g}_2, \dots, \mathbf{g}_n\}$ or contravariant notation $\{\mathbf{g}^i\}$. The terms co- and contravariant refer to the index position only and do not reflect any physical constraint. The relation between the dual bases is postulated as

$$\mathbf{g}_i \cdot \mathbf{g}^j = \delta_i^j \tag{A.1}$$

with the Kronecker symbol $\delta_i^j = \delta^{ij} = \delta_{ij} = \{1 \forall i=j, 0 \forall i \neq j\}$, stating that each base vector is perpendicular to the complementary set of base vectors in the opposite notation. Metric

coefficients $g_{ij} = \mathbf{g}_i \cdot \mathbf{g}_j$ and $g^{ij} = \mathbf{g}^i \cdot \mathbf{g}^j$ are used to convert between the dual bases.

$$\mathbf{g}_i = g_{ij} \mathbf{g}^j, \quad \mathbf{g}^i = g^{ij} \mathbf{g}_j \quad (\text{A.2})$$

An orthonormal or Cartesian basis $\{\mathbf{e}_i\}$ consists of perpendicular unit vectors. As a consequence, co- and contravariant base vectors are identical and $g_{ij} = \delta_{ij}$, $g^{ij} = \delta^{ij}$.

A.1.1.2 Vectors and vector operations

According to the previous section, a first-order tensor is represented by

$$\mathbf{a} = a_i \mathbf{g}^i = a^i \mathbf{g}_i \quad (\text{A.3})$$

in symbolic or indicial notation, respectively.

Scalar product, tensor product, cross product, box product: These four basic operations are defined as

$$\mathbf{a} \cdot \mathbf{b} = \mathbf{b} \cdot \mathbf{a} = a_i b^i = a^i b_i = a_i b_j g^{ij} = a^i b^j g_{ij} \quad (\text{A.4})$$

$$\mathbf{a} \otimes \mathbf{b} = a^i b^j \mathbf{g}_i \otimes \mathbf{g}_j = a^i b_j \mathbf{g}_i \otimes \mathbf{g}^j = a_i b^j \mathbf{g}^i \otimes \mathbf{g}_j = a_i b_j \mathbf{g}^i \otimes \mathbf{g}^j \quad (\text{A.5})$$

$$\mathbf{a} \times \mathbf{b} = -\mathbf{b} \times \mathbf{a} = \varepsilon_{ijk} a^i b^j \mathbf{g}^k = \varepsilon^{ijk} a_i b_j \mathbf{g}_k \quad (\text{A.6})$$

$$\langle \mathbf{a} \mathbf{b} \mathbf{c} \rangle = \mathbf{a} \cdot (\mathbf{b} \times \mathbf{c}) = \varepsilon_{ijk} a^i b^j c^k = \varepsilon^{ijk} a_i b_j c_k = \det[\mathbf{a}, \mathbf{b}, \mathbf{c}] \quad (\text{A.7})$$

respectively, with $\mathbf{a} \otimes \mathbf{b}$ also written as \mathbf{ab} , and the permutation or Levi-Cevita symbol ε .

$$\varepsilon_{ijk} = \varepsilon^{ijk} = \begin{cases} 1 & \text{if } (i, j, k) \text{ is an even permutation of } (1, 2, 3) \\ -1 & \text{if } (i, j, k) \text{ is an odd permutation of } (1, 2, 3) \\ 0 & \text{else} \end{cases} \quad (\text{A.8})$$

Eqs. (A.6) and (A.7) are valid in the three-dimensional Euclidean space \mathbb{R}^3 only.

The geometrical interpretation of scalar, cross and box product in \mathbb{R}^3 yield scaled projection length $\mathbf{a} \cdot \mathbf{b} = \|\mathbf{a}\| \|\mathbf{b}\| \cos \phi_{(\mathbf{a}, \mathbf{b})}$, spanned area $A_{(\mathbf{a}, \mathbf{b})} = \|\mathbf{a} \times \mathbf{b}\| = \|\mathbf{a}\| \|\mathbf{b}\| \sin \phi_{(\mathbf{a}, \mathbf{b})}$, and spanned volume $V_{(\mathbf{a}, \mathbf{b}, \mathbf{c})} = \langle \mathbf{a} \mathbf{b} \mathbf{c} \rangle$. When applied to base vectors, this illustrates how the metric coefficients (A.2) describe indeed the geometrical characteristics of a given basis.

In general, $\|\bullet\|$ denotes the Euclidean norm of a tensor. Accordingly, $\|\mathbf{a}\| = \sqrt{\mathbf{a} \cdot \mathbf{a}}$ is

the length of the vector \mathbf{a} .

A.1.1.3 Higher-order tensors and tensor operations

Second- or higher-order tensors may be derived from or deconstructed into a combination of tensors of lower order (as in, e.g., eq. (A.5)). According to their components' notation, they are called covariant, contravariant, or mixed tensors:

$$\mathbf{A} = A_{ij}\mathbf{g}^i\mathbf{g}^j = A^{ij}\mathbf{g}_i\mathbf{g}_j = A^i_j\mathbf{g}_i\mathbf{g}^j = A_i^j\mathbf{g}^i\mathbf{g}_j. \quad (\text{A.9})$$

For brevity, the following descriptions are based on second-order tensors in covariant notation only. Neither transference to contravariant or mixed tensor representations nor the use of higher-order tensors produce any irregular results.

Tensor products: Several tensor products may be defined. Unless explicitly stated otherwise, the term will refer to the regular version, consistent with (A.5), e.g.

$$\mathbf{A} \otimes \mathbf{B} = A_{ij}B_{kl}\mathbf{g}^i\mathbf{g}^j\mathbf{g}^k\mathbf{g}^l. \quad (\text{A.10})$$

Three further tensor products - only applicable to dyads - will be used in this work:

$$\mathbf{A} \oplus \mathbf{B} = A_{ik}B_{lj}\mathbf{g}^i\mathbf{g}^j\mathbf{g}^k\mathbf{g}^l \quad (\text{A.11})$$

$$\mathbf{A} \ominus \mathbf{B} = A_{il}B_{kj}\mathbf{g}^i\mathbf{g}^j\mathbf{g}^k\mathbf{g}^l \quad (\text{A.12})$$

$$\mathbf{A} \odot \mathbf{B} = 1/2(\mathbf{A} \oplus \mathbf{B} + \mathbf{A} \ominus \mathbf{B}) \quad (\text{A.13})$$

The operational symbols $\oplus \ominus \odot$ are used differently by some authors.

Contraction: Simple and double contraction of arbitrary tensors is denoted as in the following example.

$$\mathbf{A} \cdot \mathbf{B} = (A_{ij}\mathbf{g}^i\mathbf{g}^j)(B_{kl}\mathbf{g}^k\mathbf{g}^l) = A_{ij}g^{jk}B_{kl}\mathbf{g}^i\mathbf{g}^l = A_{ij}B_l^j\mathbf{g}^i\mathbf{g}^l = A_i^k B_{kl}\mathbf{g}^i\mathbf{g}^l \quad (\text{A.14})$$

$$\mathbf{A} : \mathbf{B} = (A_{ij}\mathbf{g}^i\mathbf{g}^j) : (B_{kl}\mathbf{g}^k\mathbf{g}^l) = A_{ij}g^{ik}g^{jl}B_{kl} = A_{ij}B^{ij} = A^{kl}B_{kl} \quad (\text{A.15})$$

$$\mathbb{A} : \mathbf{B} = (A_{ijkl}\mathbf{g}^i\mathbf{g}^j\mathbf{g}^k\mathbf{g}^l) : (B_{mn}\mathbf{g}^m\mathbf{g}^n) = A_{ijkl}B^{kl}\mathbf{g}^i\mathbf{g}^j = A_{ij}^{mn}B_{mn}\mathbf{g}^i\mathbf{g}^j \quad (\text{A.16})$$

In this work, an omitted operation symbol marks a dyadic product between first-order tensors, but a simple contraction when at least one higher-order tensor is present (i.e.

$\mathbf{ab} = \mathbf{a} \otimes \mathbf{b}$, but $\mathbf{AB} = \mathbf{A} \cdot \mathbf{B}$). The Euclidean norm of a second-order tensor is computed as $\|\mathbf{A}\| = \sqrt{\mathbf{A} : \mathbf{A}}$.

Some sources (e.g. Itskov [2009]) conflict with definition (A.16) and would contract $\mathbf{g}^j \cdot \mathbf{g}^m$ and $\mathbf{g}^k \cdot \mathbf{g}^n$ instead. This may have implications on the nomenclature of identity tensors, transposition rules, symmetries and derivatives.

Transposition and symmetry: The transposition of a second-order tensor \mathbf{A} is uniquely defined as

$$\mathbf{A}^T = (A_{ij} \mathbf{g}^i \mathbf{g}^j)^T = A_{ij} \mathbf{g}^j \mathbf{g}^i. \quad (\text{A.17})$$

A symmetric tensor is characterized by $\mathbf{A}^T = \mathbf{A}$, a skew-symmetric tensor by $\mathbf{A}^T = -\mathbf{A}$. Any tensor may be split up into its symmetric and skew-symmetric parts.

$$\mathbf{A} = \text{sym } \mathbf{A} + \text{skew } \mathbf{A} \quad (\text{A.18})$$

$$\text{sym } \mathbf{A} : \mathbf{B} = \text{sym } \mathbf{A} : \mathbf{B}^T = \text{sym } \mathbf{A} : \text{sym } \mathbf{B} \quad (\text{A.19})$$

A symmetric second-order tensor of dimension n comprises only $n(n+1)/2$ independent components. One representation which emphasizes this property for a symmetric \mathbf{A} is

$$\mathbf{A} = \sum_{i=1}^n A_{ii} \mathbf{g}^i \mathbf{g}^i + \sum_{i=2}^n \sum_{j=1}^{i-1} A_{ij} (\mathbf{g}^i \mathbf{g}^j + \mathbf{g}^j \mathbf{g}^i). \quad (\text{A.20})$$

The transposition of a fourth-order tensor is defined by

$$\mathbf{B} : \mathbb{A}^T : \mathbf{C} = \mathbf{C} : \mathbb{A} : \mathbf{B} \quad (\text{A.21})$$

$$\mathbf{B} : \mathbb{A}^t : \mathbf{C} = \mathbf{B} : \mathbb{A} : \mathbf{C}^T \quad (\text{A.22})$$

which with the convention of (A.15) leads to $A_{ijkl} = (\mathbb{A}^T)_{klij}$ and $A_{ijkl} = (\mathbb{A}^t)_{ijlk}$. Likewise, there are also several types of symmetries for fourth-order tensors. Major symmetry denotes $\mathbb{A} = \mathbb{A}^T$ or $A_{ijkl} = A_{klij}$, whereas right minor symmetry denotes $\mathbb{A} = \mathbb{A}^t$ or $A_{ijkl} = A_{ijlk}$, and left minor symmetry can be written as $\mathbb{A}^T = (\mathbb{A}^T)^t$ or $A_{ijkl} = A_{jikl}$. Super symmetry denotes the simultaneous occurrence of all three symmetries. In this work, the symmetry operator “sym” marks major symmetrization when applied to fourth-order tensors.

$$\text{sym } \mathbb{A} = 1/2(\mathbb{A} + \mathbb{A}^T) \quad (\text{A.23})$$

Identity tensor: Identity tensors are derived from the following properties.

$$\mathbf{I} \cdot \mathbf{a} = \mathbf{a} \cdot \mathbf{I} = \mathbf{a} \quad (\text{A.24})$$

$$\mathbb{I} : \mathbf{A} = \mathbf{A} : \mathbb{I} = \mathbf{A} \quad (\text{A.25})$$

$$\mathbb{I}^t : \mathbf{A} = \mathbf{A} : \mathbb{I}^t = \mathbf{A}^T \quad (\text{A.26})$$

With (A.15), this leads to

$$\mathbf{I} = \mathbf{g}_i \mathbf{g}^i = \delta_j^i \mathbf{g}_i \mathbf{g}^j \quad (\text{A.27})$$

$$\mathbb{I} = \delta_k^i \delta_l^j \mathbf{g}_i \mathbf{g}_j \mathbf{g}^k \mathbf{g}^l \quad (\text{A.28})$$

$$\mathbb{I}^t = \delta_l^i \delta_k^j \mathbf{g}_i \mathbf{g}_j \mathbf{g}^k \mathbf{g}^l. \quad (\text{A.29})$$

Because of $\mathbf{I} = g_{ij} \mathbf{g}^i \mathbf{g}^j$ and (A.2), the identity tensor \mathbf{I} is also referred to as metric tensor. A super-symmetric identity tensor is defined as $\mathbb{I}^s = (\mathbb{I} + \mathbb{I}^t)/2$ with $\mathbb{I}^s : \mathbf{A} = \mathbf{A} : \mathbb{I}^s = \text{sym } \mathbf{A}$.

Trace, spherical and deviatoric tensor: The trace of a second-order tensor is defined through a double contraction (A.15) with the identity tensor.

$$\text{tr } \mathbf{A} = \mathbf{A} : \mathbf{I} = (A_{ij} \mathbf{g}^i \mathbf{g}^j) : (g^{kl} \mathbf{g}_k \mathbf{g}_l) = A_i^i \quad (\text{A.30})$$

The deviatoric-spherical split can be introduced according to

$$\mathbf{A} = \text{dev } \mathbf{A} + \text{sph } \mathbf{A} \quad \text{with} \quad \text{sph } \mathbf{A} = \frac{1}{3}(\text{tr } \mathbf{A}) \mathbf{I}. \quad (\text{A.31})$$

Power function: Power functions are used with integer exponents only, as in

$$\mathbf{A}^2 = \mathbf{A} \mathbf{A} \quad \mathbf{A}^0 = \mathbf{I} \quad \mathbf{A} \mathbf{A}^{-1} = \mathbf{I} \quad \mathbf{A}^{-2} = \mathbf{A}^{-1} \mathbf{A}^{-1}. \quad (\text{A.32})$$

Eigenvalues and eigenvectors: The search for nontrivial solutions of the 3D eigenvalue problem $(\mathbf{A} - \lambda \mathbf{I}) \mathbf{n} = \mathbf{0}$ always leads to the characteristic equation

$$\det(\mathbf{A} - \lambda \mathbf{I}) = 0 = \lambda^3 - I_1(\mathbf{A}) \lambda^2 + I_2(\mathbf{A}) \lambda - I_3(\mathbf{A}) \quad (\text{A.33})$$

from which the three eigenvalues λ_i and subsequently the corresponding eigenvectors \mathbf{n}_i may be derived. I_1 , I_2 , and I_3 are the principal invariants of \mathbf{A} , see (A.37). If the

eigenvectors are distinct, they form a Cartesian basis in which \mathbf{A} is defined as

$$\mathbf{A} = \sum_{i=1}^3 \lambda_i \mathbf{n}_i \otimes \mathbf{n}_i \quad (\text{A.34})$$

with

$$\mathbf{A}^\alpha = \sum_{i=1}^3 (\lambda_i)^\alpha \mathbf{n}_i \mathbf{n}_i \quad \ln \mathbf{A} = \sum_{i=1}^3 \ln \lambda_i \mathbf{n}_i \mathbf{n}_i \quad \exp \mathbf{A} = \sum_{i=1}^3 \exp \lambda_i \mathbf{n}_i \mathbf{n}_i. \quad (\text{A.35})$$

From $(\mathbf{A}^\alpha - \lambda^\alpha \mathbf{I}) \mathbf{n} = \mathbf{0}$ for any α and (A.33) follows the Cayley-Hamilton theorem which states that every second-order tensor fulfills its own characteristic equation. An expansion of the resultant equation by \mathbf{A}^{-1} yields

$$\mathbf{A}^{-1} = \frac{1}{I_3(\mathbf{A})} (\mathbf{A}^2 - I_1(\mathbf{A}) \mathbf{A} + I_2(\mathbf{A}) \mathbf{I}). \quad (\text{A.36})$$

Invariants: Every isotropic function $f(\mathbf{A})$ may be expressed as a function of \mathbf{A} 's principal traces $\text{tr } \mathbf{A}^k$. Based on these, arbitrary sets of invariants may be deduced for specific applications. E.g., coefficients of a tensor's characteristic polynomial (A.33) form a set of invariants often referred to as principal invariants. For a three-dimensional second-order tensor \mathbf{A} , these principal invariants read:

$$\begin{aligned} I_1(\mathbf{A}) &= \text{tr } \mathbf{A} \\ I_2(\mathbf{A}) &= \frac{1}{2} \left((\text{tr } \mathbf{A})^2 - \text{tr } \mathbf{A}^2 \right) \\ I_3(\mathbf{A}) &= \frac{1}{3} \text{tr } \mathbf{A}^3 - \frac{1}{2} \text{tr } \mathbf{A} \text{tr } \mathbf{A}^2 + \frac{1}{6} (\text{tr } \mathbf{A})^3 = \det \mathbf{A} \end{aligned} \quad (\text{A.37})$$

An isotropic function $f(\mathbf{A}, \mathbf{B})$ which depends on two independent symmetric second-order tensors $\mathbf{A}, \mathbf{B} \in \text{Sym}^3$, can be expressed as a function of the following principal traces:

$$\text{tr } \mathbf{A}, \text{tr } \mathbf{A}^2, \text{tr } \mathbf{A}^3, \text{tr } \mathbf{B}, \text{tr } \mathbf{B}^2, \text{tr } \mathbf{B}^3, \text{tr}(\mathbf{AB}), \text{tr}(\mathbf{A}^2 \mathbf{B}), \text{tr}(\mathbf{AB}^2), \text{tr}(\mathbf{A}^2 \mathbf{B}^2) \quad (\text{A.38})$$

Following this pattern, a dependence on \mathbf{A} and a normalized vector \mathbf{n} can be fully incorporated through $f(\mathbf{A}, \mathbf{n} \otimes \mathbf{n})$. In that case, five elements of (A.38) are redundant due to $\|\mathbf{n}\| = 1$. Only two additional invariants I_4 and I_5 are required to complement (A.37), such

that $f(\mathbf{A}, \mathbf{n} \otimes \mathbf{n}) = f(I_1, I_2, I_3, I_4, I_5)$. A common choice for I_4 and I_5 is

$$\begin{aligned} I_4(\mathbf{A}, \mathbf{n}) &= \text{tr}(\mathbf{A}\mathbf{n} \otimes \mathbf{n}) = \mathbf{n} \cdot \mathbf{A}\mathbf{n} \\ I_5(\mathbf{A}, \mathbf{n}) &= \text{tr}(\mathbf{A}^2\mathbf{n} \otimes \mathbf{n}) = \mathbf{n} \cdot \mathbf{A}^2\mathbf{n}. \end{aligned} \quad (\text{A.39})$$

A.1.1.4 Tensor differentiation

Derivatives of tensor functions: Tensor functions are differentiable if the Gâteaux derivative exists, such that

$$f(\mathbf{A})_{,\mathbf{A}} : \mathbf{X} = \left. \frac{d}{d\varepsilon} f(\mathbf{A} + \varepsilon\mathbf{X}) \right|_{\varepsilon=0} \quad (\text{A.40})$$

for arbitrary \mathbf{X} , given that $\mathbf{A} + \mathbf{X}$ is an admissible operation. The subscript comma marks the partial derivative with respect to the subsequent subscript quantity.

The above applies as well for the differentiation of higher-order tensor-valued functions, e.g. $\mathbf{b}(\mathbf{a})$ and $\mathbf{B}(\mathbf{A})$. The corresponding derivatives are

$$f(\mathbf{A})_{,\mathbf{A}} = \frac{\partial f(\mathbf{A})}{\partial A_{ij}} \mathbf{g}_i \mathbf{g}_j \quad \mathbf{b}(\mathbf{a})_{,\mathbf{a}} = \frac{\partial b_i(\mathbf{a})}{\partial a_j} \mathbf{g}^i \mathbf{g}_j \quad \mathbf{B}(\mathbf{A})_{,\mathbf{A}} = \frac{\partial B_{ij}(\mathbf{A})}{\partial A_{kl}} \mathbf{g}^i \mathbf{g}^j \mathbf{g}_k \mathbf{g}_l \quad (\text{A.41})$$

presuming the base vectors are independent of \mathbf{a} and \mathbf{A} , respectively.

If non-ambiguous, the derivative arguments in parentheses will be henceforth omitted.

Specific tensor function derivatives: The derivatives for the principal isotropic (A.37) and transversely isotropic invariants (A.39) read

$$\begin{aligned} I_1(\mathbf{A})_{,\mathbf{A}} &= \mathbf{I} \\ I_2(\mathbf{A})_{,\mathbf{A}} &= I_1 \mathbf{I} - \mathbf{A}^T \\ I_3(\mathbf{A})_{,\mathbf{A}} &= I_3 \mathbf{A}^{-T} = (\mathbf{A}^2)^T - I_1 \mathbf{A}^T + I_2 \mathbf{I} \end{aligned} \quad (\text{A.42})$$

and

$$\begin{aligned} I_4(\mathbf{A}, \mathbf{n})_{,\mathbf{A}} &= \mathbf{n} \otimes \mathbf{n} \\ I_5(\mathbf{A}, \mathbf{n})_{,\mathbf{A}} &= \mathbf{n} \otimes \mathbf{A}\mathbf{n} + \mathbf{n}\mathbf{A} \otimes \mathbf{n}. \end{aligned} \quad (\text{A.43})$$

The following rule applies for the differentiation of principal traces in general:

$$(\text{tr } \mathbf{A}^k)_{,\mathbf{A}} = k(\mathbf{A}^{k-1})^T. \quad (\text{A.44})$$

For arbitrary second-order tensors holds

$$\mathbf{A}_{,\mathbf{A}} = \mathbb{I} \quad (\text{A.45})$$

$$(\mathbf{A}^{-1})_{,\mathbf{A}} = -\mathbf{A}^{-1} \oplus \mathbf{A}^{-1}. \quad (\text{A.46})$$

However, derivatives with respect to symmetric tensors are non-unique due to the reduced number of independent components in those tensors (see (A.20)). It is common convention - not mathematical necessity - to disregard the skew-symmetric content of these derivatives, and utilize the unique symmetric derivative exclusively. The above then becomes (with $\mathbf{A} = \text{sym} \mathbf{A}$)

$$\mathbf{A}_{,\mathbf{A}} = (\mathbb{I} + \mathbb{I}^t)/2 = \mathbf{I} \odot \mathbf{I} = \mathbb{I}^s \quad (\text{A.47})$$

$$(\mathbf{A}^{-1})_{,\mathbf{A}} = -\mathbf{A}^{-1} \odot \mathbf{A}^{-1}. \quad (\text{A.48})$$

Tensor transformation: With a_i and \tilde{a}_i being the components of \mathbf{a} in two arbitrary coordinate systems x^i and \tilde{x}^i , the identity $\mathbf{a} = a_i \mathbf{g}^i = \tilde{a}_i \tilde{\mathbf{g}}^i$ and (A.1) yield the transformation rules for independent base vectors

$$\tilde{\mathbf{g}}_i = \frac{\partial \mathbf{a}}{\partial \tilde{x}^i} = \frac{\partial \mathbf{a}}{\partial x^j} \frac{\partial x^j}{\partial \tilde{x}^i} = \mathbf{g}_j \frac{\partial x^j}{\partial \tilde{x}^i} \quad \tilde{\mathbf{g}}^i = \mathbf{g}^j \frac{\partial \tilde{x}^i}{\partial x^j} \quad (\text{A.49})$$

which are hereby defined as tangent vectors to the corresponding coordinate isolines. (A.49) leads to the covariant and contravariant transformation rules for tensors undergoing a one-to-one mapping from x^i to \tilde{x}^i coordinates.

$$\tilde{a}_i = \frac{\partial x^j}{\partial \tilde{x}^i} a_j \quad \tilde{a}^i = \frac{\partial \tilde{x}^i}{\partial x^j} a^j \quad \tilde{A}_{ij} = \frac{\partial x^k}{\partial \tilde{x}^i} \frac{\partial x^l}{\partial \tilde{x}^j} A_{kl} \quad (\text{A.50})$$

These rules are applicable to tensors of different order and notation analogously.

Coordinate derivatives: For the definition of the partial coordinate derivatives of

base vectors, the Christoffel symbol Γ is introduced:

$$\mathbf{g}_{i,j} = \frac{\partial \mathbf{g}_i}{\partial x^j} = \Gamma_{ij}^k \mathbf{g}_k \quad \mathbf{g}_{,j}^i = -\Gamma_{jk}^i \mathbf{g}^k \quad \Gamma_{jk}^i = \Gamma_{kj}^i \quad (\text{A.51})$$

The partial derivative of a second-order tensor follows from the chain rule.

$$\begin{aligned} \mathbf{A}_{,i} &= \frac{\partial \mathbf{A}}{\partial x^i} = A_{,i}^{kl} \mathbf{g}_k \mathbf{g}_l + A^{kl}_{,i} \mathbf{g}_{k,i} \mathbf{g}_l + A^{kl} \mathbf{g}_k \mathbf{g}_{l,i} \\ &= (A_{,i}^{kl} + \Gamma_{ij}^k A^{jl} + \Gamma_{ij}^l A^{kj}) \mathbf{g}_k \mathbf{g}_l \\ &= A^{kl}|_i \mathbf{g}_k \mathbf{g}_l \end{aligned} \quad (\text{A.52})$$

Herein, $A_{,i}^{kl}$ is the partial derivative of A^{kl} with respect to x^i , and $A^{kl}|_i$ is its covariant derivative (since it obeys the covariant transformation rule in (A.50)). Other covariant derivatives are

$$\begin{aligned} a^i|_j &= a^i_{,j} + \Gamma_{jk}^i a^k \\ a_i|_j &= a_{i,j} - \Gamma_{ij}^k a_k \\ A_{kl}|_i &= A_{kl,i} - \Gamma_{ik}^j A_{jl} - \Gamma_{il}^j A_{kj}. \end{aligned} \quad (\text{A.53})$$

The coordinate differentiation of the metric coefficients (A.2) yields $\Gamma_{ij}^k = 0$ and $A^{kl}|_i = A_{,i}^{kl}$ for all Cartesian base systems.

Nabla operator, gradient, divergence, curl: The Nabla operator $\nabla = \mathbf{g}^i \partial / \partial x^i$ is used to define several frequently used operators, e.g. gradient, divergence and curl (the latter also often referred to as rotation):

$$\nabla \mathbf{a} = \frac{\partial \mathbf{a}}{\partial x^i} \mathbf{g}^i = a_j|_i \mathbf{g}^j \mathbf{g}^i = \mathbf{a}_{,x} = \text{grad } \mathbf{a} \quad (\text{A.54})$$

$$\nabla \cdot \mathbf{a} = \mathbf{g}^i \cdot \frac{\partial \mathbf{a}}{\partial x^i} = a^i|_i = \text{grad } \mathbf{a} : \mathbf{I} = \text{div } \mathbf{a} \quad (\text{A.55})$$

$$\nabla \times \mathbf{a} = \mathbf{g}^i \frac{\partial}{\partial x^i} \times \mathbf{a} = \varepsilon^{ijk} a_j|_i \mathbf{g}_k = \text{curl } \mathbf{a} \quad (\text{A.56})$$

The Nabla operator as in (A.54) and (A.55) is applicable analogously to scalar- and tensor-

valued fields. The following rules apply:

$$\begin{aligned}
\text{grad}(a \mathbf{b}) &= a \text{grad } \mathbf{b} + \mathbf{b} \otimes \text{grad } a \\
\text{grad}(\mathbf{a} \cdot \mathbf{b}) &= (\text{grad } \mathbf{a})^T \mathbf{b} + (\text{grad } \mathbf{b})^T \mathbf{a} \\
\text{grad}(a \mathbf{B}) &= a \text{grad } \mathbf{B} + \mathbf{B} \otimes \text{grad } a \\
\text{grad}(\mathbf{A} \mathbf{b}) &= \mathbf{b} \cdot \text{grad}(\mathbf{A}^T) + \mathbf{A} \cdot \text{grad } \mathbf{b}
\end{aligned} \tag{A.57}$$

$$\begin{aligned}
\text{div}(a \mathbf{b}) &= a \text{div } \mathbf{b} + \mathbf{b} \cdot \text{grad } a \\
\text{div}(\mathbf{a} \mathbf{b}) &= \mathbf{a} \text{div } \mathbf{b} + \text{grad } \mathbf{a} \cdot \mathbf{b} \\
\text{div}(a \mathbf{B}) &= a \text{div } \mathbf{B} + \mathbf{B} \otimes \text{grad } a \\
\text{div}(\mathbf{A} \mathbf{b}) &= \mathbf{A}^T : \text{grad } \mathbf{b} + \mathbf{b} \cdot \text{div}(\mathbf{A}^T) \\
\text{div}(\mathbf{a} \times \mathbf{b}) &= \mathbf{b} \cdot \text{curl } \mathbf{a} - \mathbf{a} \cdot \text{curl } \mathbf{b}.
\end{aligned} \tag{A.58}$$

In this work, $(\text{grad } \mathbf{a})_{ij}$ denotes $\partial a_i / \partial x_j$. Some authors, e.g. [Tai 1994], use interchanged indices.

A.1.1.5 Linearization

Any sufficiently smooth function $f(\mathbf{x})$ of a tensor-valued quantity \mathbf{x} may be approximated by a first-order Taylor expansion, i.e. by linearization at $\mathbf{x} = \bar{\mathbf{x}}$:

$$f(\bar{\mathbf{x}} + \Delta \mathbf{x}) \approx f(\bar{\mathbf{x}}) + f(\mathbf{x})_{,\mathbf{x}} \Big|_{\mathbf{x}=\bar{\mathbf{x}}} \Delta \mathbf{x}. \tag{A.59}$$

This may be generalized to

$$f(\mathbf{x} + \Delta \mathbf{x}) \approx f(\mathbf{x}) + \Delta f(\mathbf{x}, \Delta \mathbf{x}). \tag{A.60}$$

The linearization operator $\Delta(\bullet)$ marks the increment of a field quantity, here $\Delta \mathbf{x}$. It is also utilized as Gâteaux operator, e.g. to mark the linearized increment of the function $f(\mathbf{x})$ due to $\Delta \mathbf{x}$.

$$\Delta f(\mathbf{x}, \Delta \mathbf{x}) = \frac{d}{d\varepsilon} f(\mathbf{x} + \varepsilon \Delta \mathbf{x}) \Big|_{\varepsilon=0} \tag{A.61}$$

For brevity or clarity, the following terms may be used interchangeable for $f = f(\mathbf{x})$:

$$\Delta f = \Delta(f(\mathbf{x})) = \Delta f(\mathbf{x}, \Delta \mathbf{x}) = \Delta_{\mathbf{x}} f(\mathbf{x}) = \Delta_{\mathbf{x}} f \quad (\text{A.62})$$

From the identity (A.61) follows the applicability of superposition, product and chain rule.

$$\Delta_{\mathbf{x}}(f(\mathbf{x}) + g(\mathbf{x})) = \Delta_{\mathbf{x}} f(\mathbf{x}) + \Delta_{\mathbf{x}} g(\mathbf{x}) \quad (\text{A.63})$$

$$\Delta_{\mathbf{x}}(f(\mathbf{x}) \cdot g(\mathbf{x})) = \Delta_{\mathbf{x}} f(\mathbf{x}) \cdot g(\mathbf{x}) + f(\mathbf{x}) \cdot \Delta_{\mathbf{x}} g(\mathbf{x}) \quad (\text{A.64})$$

$$\Delta_{\mathbf{x}}(f(g(\mathbf{x}))) = \Delta_{[\Delta_{\mathbf{x}} g(\mathbf{x})]} f(g(\mathbf{x})) \quad (\text{A.65})$$

For multivariable tensor functions,

$$\Delta f = \Delta(f(\mathbf{x}_1, \mathbf{x}_2, \dots)) = \Delta_{\mathbf{x}_1} f(\mathbf{x}_1, \mathbf{x}_2, \dots) + \Delta_{\mathbf{x}_2} f(\mathbf{x}_1, \mathbf{x}_2, \dots) + \dots \quad (\text{A.66})$$

applies. All of the above rules for the scalar-valued tensor functions f and g are valid for higher-order functions as well.

A.1.2 Numerical integration

In FEM applications, integrals over the elements domain are hardly ever evaluated analytically. The integral of a polynomial shape function of order $2n - 1$ may be determined by means of the n -point Gauss-Legendre quadrature.

$$\int_{-1}^1 f(\xi) d\xi = \sum_{i=1}^n c_i f(\xi_i) \quad (\text{A.67})$$

For the usual range of natural coordinates $-1 \leq \xi \leq 1$, integration point coordinates ξ_i and weights c_i may be taken out of textbooks. The accuracy of the computed integral is limited by these inputs and computing precision only.

A.2 Complementary continuum mechanics

This section provides some complementary information and formulae referenced in the continuum mechanics chapter (2) of the main text. Only tensor fields in the Euclidean space \mathbb{R}^3 are considered, and any index is supposed to run from 1 to 3 unless stated otherwise.

A.2.1 Transformation and deformation

Push-forward (Φ_*) and pull-back (Φ^*): These operators map tensor components from the undeformed basis into the deformed or vice versa. In view of (2.4) which gives $\mathbf{g}_i = \mathbf{F}\mathbf{G}_i$, the push-forward for a second-order tensor reads $\Phi_*(\mathbf{A}) = A^{ij}\mathbf{g}_i\mathbf{g}_j = \mathbf{F}^T(A^{ij}\mathbf{G}_i\mathbf{G}_j)\mathbf{F}$. Generally holds

$$\begin{aligned} \Phi_*(\cdot) &= \mathbf{F}(\cdot)\mathbf{F}^T & \Phi^*(\cdot) &= \mathbf{F}^{-1}(\cdot)\mathbf{F}^{-T} & \text{for contravariant components} \\ \Phi_*(\cdot) &= \mathbf{F}^{-T}(\cdot)\mathbf{F}^{-1} & \Phi^*(\cdot) &= \mathbf{F}^T(\cdot)\mathbf{F} & \text{for covariant components.} \end{aligned} \quad (\text{A.68})$$

The fourth-order spatial elasticity tensor $\mathbb{c} = c^{ijkl}\mathbf{g}_i\mathbf{g}_j\mathbf{g}_k\mathbf{g}_l$ is according to (2.36) expressible as the push-forward of \mathbb{C} .

$$\mathbb{c} = \Phi_*\mathbb{C} = C^{ijkl}(\mathbf{F}\mathbf{G}_i)(\mathbf{G}_j\mathbf{F}^T)(\mathbf{F}\mathbf{G}_k)(\mathbf{G}_l\mathbf{F}^T) = C^{ijkl}\mathbf{g}_i\mathbf{g}_j\mathbf{g}_k\mathbf{g}_l \quad (\text{A.69})$$

Obviously, $c^{ijkl} = C^{ijkl}$ applies.

Deformation tensors: The components F_j^i of \mathbf{F} (2.4) form a Jacobi matrix which describes an invertible and orientation preserving transformation. Accordingly, it always holds that $J = \det \mathbf{F} > 0$. For reference, the inverse and transposed forms of \mathbf{F} are quoted:

$$\begin{aligned} \mathbf{F}^{-1} &= \mathbf{G}_i\mathbf{g}^i = \frac{\partial X^i}{\partial x_j}\mathbf{e}_i\mathbf{e}^j = \text{grad } \mathbf{X} \\ \mathbf{F}^T &= \mathbf{G}^i\mathbf{g}_i = \frac{\partial x^j}{\partial X^i}\mathbf{e}^i\mathbf{e}_j \\ \mathbf{F}^{-T} &= \mathbf{g}^i\mathbf{G}_i = \frac{\partial X^i}{\partial x_j}\mathbf{e}^j\mathbf{e}_i \end{aligned} \quad (\text{A.70})$$

Polar decomposition: The deformation of $d\mathbf{X}$ - described through the mapping $d\mathbf{x} = \mathbf{F} d\mathbf{X}$ - may also be regarded as sequential rotation and stretch. Depending on their order, right and left polar decomposition are distinguished.

$$\mathbf{F} = \mathbf{R}\mathbf{U} = \mathbf{v}\mathbf{R} \quad (\text{A.71})$$

Herein, \mathbf{U} and \mathbf{v} are the symmetric right and left stretch tensors¹; \mathbf{R} is the orthogonal rotation tensor. Since $\mathbf{C} = \mathbf{U}^2$ and $\mathbf{c} = \mathbf{v}^2$, these three tensors can be computed from the eigenvalues of \mathbf{C} and \mathbf{c} (A.34).

Divergence theorem: Also named Gauss' integral theorem or Gauss-Green theorem, where \mathcal{S} is the surface boundary of a volume \mathcal{V} with \mathbf{n} as outward unit normal vector field on \mathcal{S} .

$$\int_{\mathcal{S}} \mathbf{A} \cdot \mathbf{n} \, dA = \int_{\mathcal{V}} \operatorname{div} \mathbf{A} \, dV. \quad (\text{A.72})$$

Transport theorem: From (A.42) and (A.55) follows

$$\dot{J} = \frac{\partial J}{\partial \mathbf{F}} \frac{\partial \mathbf{F}}{\partial t} = J \mathbf{F}^{-T} : \dot{\mathbf{F}} = J \mathbf{I} : \operatorname{grad} \mathbf{v} = J \operatorname{div} \mathbf{v} \quad (\text{A.73})$$

which in conjunction with (A.72) may be used to derive Reynold's transport theorem

$$\frac{d}{dt} \int_{\mathcal{V}} f(\mathbf{x}, t) \, dv = \int_{\mathcal{V}} \frac{\partial f(\mathbf{x}, t)}{\partial t} \, dv + \int_{\mathcal{S}} f(\mathbf{x}, t) \mathbf{v} \cdot \mathbf{n} \, da. \quad (\text{A.74})$$

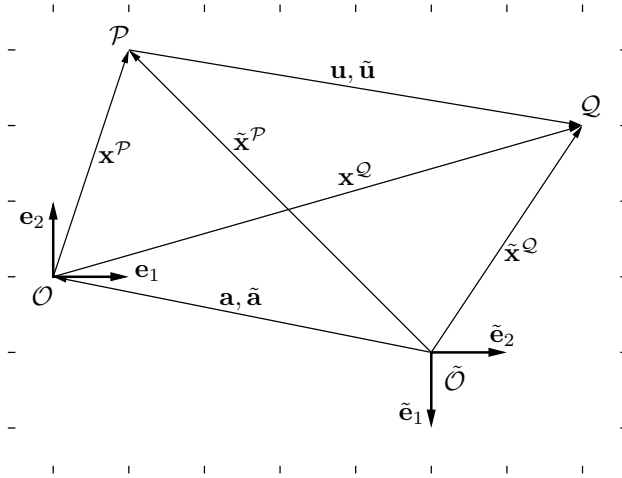
A.2.2 Objectivity

Many textbooks on continuum mechanics introduce the concept of objective tensors to explain the compliance of constitutive laws with the principle of material objectivity. The concept is introduced rather dogmatically and even with substantial contradictions in different books. Therefore a summary is presented.

By definition, every tensor (though not its components) is independent of any basis and could therefore be referred to as objective. In the given context, a tensor field is considered objective, if it is monitored identically by different observers who agree on reference configuration and measures for space, mass and time.

A change of observer may be regarded as change of origin and basis. Two observers \mathcal{O} and $\tilde{\mathcal{O}}$ monitoring the movement of a body \mathcal{B} will record its deformation differently: A material point \mathcal{P} observed by \mathcal{O} at place \mathbf{x} and at time t is identified by $\tilde{\mathcal{O}}$ at $\tilde{\mathbf{x}}$ and \tilde{t} , where the tilde marks all quantities associated with a specific event, but observed by $\tilde{\mathcal{O}}$

¹ This notation of \mathbf{v} is limited to this “polar decomposition” subsection, otherwise \mathbf{v} refers to the velocity vector.



i	\mathbf{e}_i	$\mathbf{e}_{\tilde{i}}$	$\tilde{\mathbf{e}}_i$	$\tilde{\mathbf{e}}_{\tilde{i}}$
1	$\begin{bmatrix} 1 \\ 0 \end{bmatrix}$	$\begin{bmatrix} 0 \\ 1 \end{bmatrix}$	$\begin{bmatrix} 0 \\ -1 \end{bmatrix}$	$\begin{bmatrix} 1 \\ 0 \end{bmatrix}$
2	$\begin{bmatrix} 0 \\ 1 \end{bmatrix}$	$\begin{bmatrix} -1 \\ 0 \end{bmatrix}$	$\begin{bmatrix} 1 \\ 0 \end{bmatrix}$	$\begin{bmatrix} 0 \\ 1 \end{bmatrix}$

i	$x_i^{\mathcal{P}}$	$x_{\tilde{i}}^{\mathcal{P}}$	$\tilde{x}_i^{\mathcal{P}}$	$\tilde{x}_{\tilde{i}}^{\mathcal{P}}$	i	a_i	$a_{\tilde{i}}$
1	1	-3	-4	-4	1	0	-1
2	3	1	4	-4	2	1	0

i	$x_i^{\mathcal{Q}}$	$x_{\tilde{i}}^{\mathcal{Q}}$	$\tilde{x}_i^{\mathcal{Q}}$	$\tilde{x}_{\tilde{i}}^{\mathcal{Q}}$
1	7	-2	2	-3
2	2	7	3	2

$$[Q_{ij}] = \begin{bmatrix} 0 & -1 \\ 1 & 0 \end{bmatrix}$$

Figure A.1: Illustration to the comments on objectivity. The tables exemplify the notation with regard to the objects in the sketch. Consider the ticks surrounding the sketch as scale.

instead of \mathcal{O} . Fig. A.1 illustrates the configuration. Obviously,

$$\tilde{\mathbf{x}} = \mathbf{x} + \mathbf{a} \quad (\text{A.75})$$

applies, where \mathbf{a} is the vector connecting the reference points of \mathcal{O} and $\tilde{\mathcal{O}}$. Introducing two associated Cartesian bases $\{\mathbf{e}_i\}$ and $\{\tilde{\mathbf{e}}_i\}$, the coordinate vectors of \mathcal{P} may be written as

$$\begin{aligned} \mathbf{x} &= x_i \mathbf{e}_i = x_{\tilde{j}} \tilde{\mathbf{e}}_j \\ \tilde{\mathbf{x}} &= \tilde{x}_i \mathbf{e}_i = \tilde{x}_{\tilde{j}} \tilde{\mathbf{e}}_j. \end{aligned} \quad (\text{A.76})$$

The tilde at the index marks a tensor component referring to the basis $\{\tilde{\mathbf{e}}_i\}$. (Note, that this does not require the tensor to be perceived by $\tilde{\mathcal{O}}$.) Stipulating the use of identical measures for time intervals and lengths by any observer, an orthonormal rotation matrix $\mathbf{Q} = \mathbf{e}_i \otimes \tilde{\mathbf{e}}_i$ maps between the base vectors.

$$\mathbf{e}_i = \mathbf{Q} \tilde{\mathbf{e}}_i \quad (\text{A.77})$$

The components of \mathbf{Q} read $Q_{ij} = Q_{\tilde{i}\tilde{j}} = \tilde{\mathbf{e}}_i \cdot \mathbf{e}_j$. With $Q_{ij} \tilde{\mathbf{e}}_i = \mathbf{e}_j$ one derives

$$\tilde{x}_{\tilde{i}} = Q_{ij} x_j + a_{\tilde{i}} \quad (\text{A.78})$$

$$\tilde{x}_{\tilde{i}} = x_{\tilde{i}} + a_{\tilde{i}}. \quad (\text{A.79})$$

The frequently used notation $\tilde{\mathbf{x}} = \mathbf{Q}\mathbf{x} + \mathbf{a}$ is misleading without further remarks, as it would be expected to work regardless of the utilized bases, which is refuted by (A.79).

To prove the identity of two tensors, their components with regard to the same basis need to be equal. Therefore, (A.79) shows that coordinates are not objective. However, the distance between material points and their displacements are objective in terms of this definition, easily shown by $\mathbf{u} = \mathbf{x}^{\mathcal{Q}} - \mathbf{x}^{\mathcal{P}}$, $\tilde{\mathbf{u}} = \tilde{\mathbf{x}}^{\mathcal{Q}} - \tilde{\mathbf{x}}^{\mathcal{P}}$ and

$$\tilde{u}_{\tilde{i}} = \tilde{x}_{\tilde{i}}^{\mathcal{Q}} - \tilde{x}_{\tilde{i}}^{\mathcal{P}} = x_i^{\mathcal{Q}} - x_i^{\mathcal{P}} = u_i. \quad (\text{A.80})$$

Here, \mathbf{u}_i is the component of \mathbf{u} as perceived by \mathcal{O} , but in reference to the base $\{\tilde{\mathbf{e}}_i\}$.

Keeping in mind that this property - the identity of components with regard to the same base - is the only criterion to prove two tensor's identity, and thus to verify observer indifference, simplifications may appear convenient. By restricting any tensor marked by a tilde, i.e. observed by $\tilde{\mathcal{O}}$, to be expressed in terms of $\{\tilde{\mathbf{e}}_i\}$ only, and likewise any tensor without tilde to be expressed with respect to $\{\mathbf{e}_i\}$, equation (A.78) is deduced in its popular form

$$\tilde{\mathbf{x}} = \mathbf{Q}\mathbf{x} + \mathbf{a} \quad (\text{A.81})$$

and $\tilde{\mathbf{u}} = \mathbf{Q}\mathbf{u}$. Accordingly, (2.2) yields

$$\tilde{\mathbf{g}}_i = \frac{\partial \tilde{\mathbf{x}}}{\partial X_i} = \frac{\partial \mathbf{Q}\mathbf{x}}{\partial X_i} = \mathbf{Q}\mathbf{g}_i. \quad (\text{A.82})$$

A premise for the latter is the agreement of the distinctive observers on the material coordinates X_i . This restriction is significant as it requires them to utilize the same origin and basis in the reference state when $\mathbf{x} \equiv \mathbf{X}$ at $t_0 = \tilde{t}_0$. An unrestricted formulation would require an additional constant mapping.

Since the agreement now leads to $\tilde{\mathbf{G}}_i = \mathbf{G}_i$, the transformation behavior of a tensor depends on whether it is based on \mathbf{g}_i (A.83), \mathbf{G}_i (A.84), or both (A.85).

$$\begin{aligned} \tilde{a}(\tilde{\mathbf{x}}, \tilde{t}) &= a(\mathbf{x}, t) \\ \tilde{\mathbf{a}}(\tilde{\mathbf{x}}, \tilde{t}) &= \mathbf{Q}(t)\mathbf{a}(\mathbf{x}, t) \\ \tilde{\mathbf{A}}(\tilde{\mathbf{x}}, \tilde{t}) &= \mathbf{Q}(t)\mathbf{A}(\mathbf{x}, t)\mathbf{Q}^T(t) \end{aligned} \quad (\text{A.83})$$

$$\begin{aligned}
\tilde{a}(\tilde{\mathbf{x}}, \tilde{t}) &= a(\mathbf{x}, t) \\
\tilde{\mathbf{a}}(\tilde{\mathbf{x}}, \tilde{t}) &= \mathbf{a}(\mathbf{x}, t) \\
\tilde{\mathbf{A}}(\tilde{\mathbf{x}}, \tilde{t}) &= \mathbf{A}(\mathbf{x}, t)
\end{aligned} \tag{A.84}$$

$$\tilde{\mathbf{A}}(\tilde{\mathbf{x}}, \tilde{t}) = \mathbf{Q}(t) \mathbf{A}(\mathbf{x}, t) \tag{A.85}$$

Therefore, all deformation, strain and stress measures introduced in 2.1.2 and (2.27) are objective: \mathbf{c} , \mathbf{e} , $\boldsymbol{\tau}$ and $\boldsymbol{\sigma}$ comply with (A.83), \mathbf{C} , \mathbf{E} , \mathbf{P} and \mathbf{S} with (A.84), and \mathbf{F} with (A.85). As referenced in the main text, some authors mention these three types as Eulerian, Lagrangian, and two-point objectivity, while others acknowledge exclusively either (A.83) or (A.84) as objectivity equations. Material frame invariance of constitutive equations is achieved whenever $W(\mathbf{C})$, $W(\mathbf{QF})$, or $W(\mathbf{QcQ}^T)$ are independent of \mathbf{Q} .

Noting that $\tilde{\mathbf{F}} = \mathbf{QF}$, the equivalence of these three notations becomes apparent. For deformation-dependent spatial tensor functions, equation (A.83) may be cited in its common form as

$$\tilde{\mathbf{A}}(\tilde{\mathbf{F}}) = \tilde{\mathbf{A}}(\mathbf{QF}) = \mathbf{Q} \mathbf{A}(\mathbf{F}) \mathbf{Q}^T \quad \text{or} \quad \tilde{\mathbf{A}} = \mathbf{Q} \mathbf{A} \mathbf{Q}^T. \tag{A.86}$$

This transformation rule is valid only for Eulerian tensors defined with respect to \mathbf{g}_i , but as mentioned before, is frequently used to legitimize the labeling of a tensor as *objective tensor*. It remains remarkable, that this label appears regularly in engineering literature, but in none of the textbooks on tensor calculus consulted during the course of this work.

The aforementioned transformation rules apply to rate measures as well. With the time derivation of (A.82):

$$\dot{\tilde{\mathbf{g}}}_i = \dot{\mathbf{Q}} \mathbf{g}_i + \mathbf{Q} \dot{\mathbf{g}}_i \tag{A.87}$$

follows the compliance of specific derivatives such as the Lie-derivative of Eulerian tensors, e.g. $\dot{\mathbf{e}}$, with (A.86). The time derivative of Lagrangian tensors, e.g. $\dot{\mathbf{E}}$, complies with (A.84).

A.2.3 Invariants addendum

A.2.3.1 Invariants conversion

In section 2.3.4 of the main text, invariants from [Criscione et al. 2001] were cited, highlighting their potential for parameter identification in conjunction with a successive mapping to the principal invariants. The conversion formulae are based on the original source, but comprise several necessary corrections:

$$\begin{aligned}
 I_1 &= I_1'^{\frac{2}{3}} \left(I_2'^2 (1 + I_4'^2) + I_2'^{-1} (I_3'^2 + I_3'^{-2}) \right) \\
 I_2 &= I_1'^{\frac{4}{3}} \left(I_2'^{-2} (1 + I_3'^4 + I_3'^{-4}) + I_2' (1 + I_4'^2) (I_3'^2 + I_3'^{-2}) \right. \\
 &\quad \left. + I_2'^4 (1 + I_4'^2)^2 + I_1' I_4'^2 (I_3'^2 \sin^2 \gamma + I_3'^{-2} \cos^2 \gamma) \right) \\
 I_3 &= I_1'^2 \\
 I_4 &= I_1'^{\frac{4}{3}} I_2'^2 \\
 I_5 &= I_1'^{\frac{4}{3}} I_2'^4 (1 + I_4'^2)
 \end{aligned} \tag{A.88}$$

$$\begin{aligned}
 I_1' &= I_3^{\frac{1}{2}} \\
 I_2' &= I_3^{-\frac{1}{6}} I_4^{\frac{1}{2}} \\
 I_3' &= \left(\frac{I_1 I_4 - I_5}{2\sqrt{I_3 I_4}} + \sqrt{\left(\frac{I_1 I_4 - I_5}{2\sqrt{I_3 I_4}} \right)^2 - 1} \right)^{\frac{1}{2}} \\
 I_4' &= \sqrt{I_5 I_4^{-2} - 1} \\
 I_5' &= \frac{I_1 I_4 I_5 + I_1 I_4^3 + 2I_3 I_4 - I_5^2 + 2I_2 I_4^2 - I_5 I_4^2 - 2I_1^2 I_4^2}{(I_5 - I_4^2) \sqrt{(I_1 I_4 - I_5)^2 - 4I_3 I_4}}
 \end{aligned} \tag{A.89}$$

Likewise, the invariants from [Ehret et al. 2011] can be converted as follows:

$$\begin{aligned}
 I_2 &= \tilde{I}_2 \tilde{I}_3 \\
 I_5 &= \tilde{I}_1 \tilde{I}_4 - \tilde{I}_2 \tilde{I}_3 + \tilde{I}_3 \tilde{I}_5
 \end{aligned} \tag{A.90}$$

$$\begin{aligned}
 \tilde{I}_2 &= I_2 I_3^{-1} \\
 \tilde{I}_5 &= (I_5 - I_1 I_4 + I_2) I_3^{-1}
 \end{aligned} \tag{A.91}$$

For all other than the above indices, $I_i = \tilde{I}_i$ applies.

A.2.3.2 Invariants derivatives

The derivatives of invariants of (\mathbf{C}, \mathbf{N}) are essential for the deduction of the generalized formula in section 2.3.5. Note that also the differentiation with respect to \mathbf{c} is conducted with the invariants based on \mathbf{C} and \mathbf{N} .

Derivatives of principal invariants I_i : The invariants are introduced in section 2.3.2. Compliant with (A.42) and (A.43), the derivatives are

$$\begin{aligned}
 I_{1,\mathbf{C}} &= \mathbf{I} & I_{1,\mathbf{c}} &= \mathbf{I} \\
 I_{2,\mathbf{C}} &= I_1 \mathbf{I} - \mathbf{C} & I_{2,\mathbf{c}} &= I_1 \mathbf{I} - \mathbf{c} \\
 I_{3,\mathbf{C}} &= I_3 \mathbf{C}^{-1} & I_{3,\mathbf{c}} &= I_3 \mathbf{c}^{-1} \\
 I_{4,\mathbf{C}} &= \mathbf{N} \otimes \mathbf{N} & I_{4,\mathbf{c}} &= I_4(\mathbf{n} \otimes \mathbf{n}) \\
 I_{5,\mathbf{C}} &= \mathbf{N} \otimes \mathbf{C}\mathbf{N} + \mathbf{N}\mathbf{C} \otimes \mathbf{N} & I_{5,\mathbf{c}} &= I_4(\mathbf{n} \otimes \mathbf{c}\mathbf{n} + \mathbf{n}\mathbf{c} \otimes \mathbf{n}).
 \end{aligned} \tag{A.92}$$

Derivatives of modified invariants \hat{I}_i : See (2.41) for the invariants. $\hat{\mathbf{C}} = J^{-\frac{2}{3}} \mathbf{C}$.

$$\begin{aligned}
 \hat{I}_{1,\mathbf{C}} &= \hat{I}_3^{-\frac{2}{3}}(\mathbf{I} - \frac{1}{3}\hat{I}_1\hat{\mathbf{C}}^{-1}) & \hat{I}_{1,\mathbf{c}} &= \mathbf{I} - \frac{1}{3}\hat{I}_1\hat{\mathbf{c}} \\
 \hat{I}_{2,\mathbf{C}} &= \hat{I}_3^{-\frac{2}{3}}(\hat{I}_1\mathbf{I} - \hat{\mathbf{C}} - \frac{2}{3}\hat{I}_2\hat{\mathbf{C}}^{-1}) & \hat{I}_{2,\mathbf{c}} &= \hat{I}_1\mathbf{I} - \hat{\mathbf{c}} - \frac{2}{3}\hat{I}_2\hat{\mathbf{c}} \\
 \hat{I}_{3,\mathbf{C}} &= \frac{1}{2}\hat{I}_3^{-\frac{1}{3}}\hat{\mathbf{C}}^{-1} & \hat{I}_{3,\mathbf{c}} &= \hat{I}_3^{-\frac{1}{3}}\hat{\mathbf{c}}^{-1} \\
 \hat{I}_{4,\mathbf{C}} &= \hat{I}_3^{-\frac{2}{3}}(\mathbf{N} \otimes \mathbf{N} - \frac{1}{3}\hat{I}_4\hat{\mathbf{C}}^{-1}) & \hat{I}_{4,\mathbf{c}} &= \hat{I}_4(\mathbf{n} \otimes \mathbf{n} - \frac{1}{3}\hat{\mathbf{c}}^{-1}) \\
 \hat{I}_{5,\mathbf{C}} &= \hat{I}_3^{-\frac{2}{3}}(\mathbf{N} \otimes \hat{\mathbf{C}}\mathbf{N} + \mathbf{N}\hat{\mathbf{C}} \otimes \mathbf{N} - \frac{2}{3}\hat{I}_5\hat{\mathbf{C}}^{-1}) & \hat{I}_{5,\mathbf{c}} &= \hat{I}_4(\mathbf{n} \otimes \hat{\mathbf{c}}\mathbf{n} + \mathbf{n}\hat{\mathbf{c}} \otimes \mathbf{n}) - \frac{2}{3}\hat{I}_5\hat{\mathbf{c}}^{-1}
 \end{aligned} \tag{A.93}$$

Derivatives of invariants based on Ehret et al. [2011] \tilde{I}_i : See (2.42) for the invariants.

$$\begin{aligned}
 \tilde{I}_{1,\mathbf{C}} &= \mathbf{I} & \tilde{I}_{1,\mathbf{c}} &= \mathbf{I} \\
 \tilde{I}_{2,\mathbf{C}} &= -\mathbf{C}^{-2} & \tilde{I}_{2,\mathbf{c}} &= -\mathbf{c}^{-2} \\
 \tilde{I}_{3,\mathbf{C}} &= \tilde{I}_3 \mathbf{C}^{-1} & \tilde{I}_{3,\mathbf{c}} &= \tilde{I}_3 \mathbf{c}^{-1} \\
 \tilde{I}_{4,\mathbf{C}} &= \mathbf{N} \otimes \mathbf{N} & \tilde{I}_{4,\mathbf{c}} &= \tilde{I}_4(\mathbf{n} \otimes \mathbf{n}) \\
 \tilde{I}_{5,\mathbf{C}} &= -\mathbf{C}^{-1}\mathbf{N} \otimes \mathbf{N}\mathbf{C}^{-1} & e\tilde{I}_{5,\mathbf{c}} &= \tilde{I}_5(\mathbf{n} \otimes \mathbf{n}) + \tilde{I}_4(\mathbf{n} \otimes \mathbf{c}^{-1}\mathbf{n} + \mathbf{n}\mathbf{c}^{-1} \otimes \mathbf{n})
 \end{aligned} \tag{A.94}$$

A.2.4 Material tensor addendum to section 2.3.5

A.2.4.1 Derivatives for material tensor (eq. 2.46)

Here, W_i and W_{ij} substitute $\partial W / \partial I_i$ and $\partial^2 W / (\partial I_i \partial I_j)$, respectively.

$$\begin{aligned} \frac{\partial(W_1 \mathbf{I})}{\partial \mathbf{C}} &= \left[W_{11} \mathbf{I} + W_{12}(I_1 \mathbf{I} - \mathbf{C}) + W_{13} I_3 \mathbf{C}^{-1} \right. \\ &\quad \left. + W_{14} \mathbf{N} \otimes \mathbf{N} + W_{15}(\mathbf{N} \otimes \mathbf{C} \mathbf{N} + \mathbf{N} \mathbf{C} \otimes \mathbf{N}) \right] \otimes \mathbf{I} \end{aligned} \quad (\text{A.95})$$

$$\begin{aligned} \frac{\partial(W_2(I_1 \mathbf{I} - \mathbf{C}))}{\partial \mathbf{C}} &= \left[W_{21} \mathbf{I} + W_{22}(I_1 \mathbf{I} - \mathbf{C}) + W_{23} I_3 \mathbf{C}^{-1} \right. \\ &\quad \left. + W_{24} \mathbf{N} \otimes \mathbf{N} + W_{25}(\mathbf{N} \otimes \mathbf{C} \mathbf{N} + \mathbf{N} \mathbf{C} \otimes \mathbf{N}) \right] \otimes (I_1 \mathbf{I} - \mathbf{C}) \\ &\quad + W_2(\mathbf{I} \otimes \mathbf{I} - \mathbf{I} \odot \mathbf{I}) \end{aligned} \quad (\text{A.96})$$

$$\begin{aligned} \frac{\partial(W_3 I_3 \mathbf{C}^{-1})}{\partial \mathbf{C}} &= \left[W_{31} \mathbf{I} + W_{32}(I_1 \mathbf{I} - \mathbf{C}) + W_{33} I_3 \mathbf{C}^{-1} \right. \\ &\quad \left. + W_{34} \mathbf{N} \otimes \mathbf{N} + W_{35}(\mathbf{N} \otimes \mathbf{C} \mathbf{N} + \mathbf{N} \mathbf{C} \otimes \mathbf{N}) \right] \otimes I_3 \mathbf{C}^{-1} \\ &\quad + W_3 I_3 (\mathbf{C}^{-1} \otimes \mathbf{C}^{-1} - \mathbf{C}^{-1} \odot \mathbf{C}^{-1}) \end{aligned} \quad (\text{A.97})$$

$$\begin{aligned} \frac{\partial(W_4 \mathbf{N} \otimes \mathbf{N})}{\partial \mathbf{C}} &= \left[W_{41} \mathbf{I} + W_{42}(I_1 \mathbf{I} - \mathbf{C}) + W_{43} I_3 \mathbf{C}^{-1} \right. \\ &\quad \left. + W_{44} \mathbf{N} \otimes \mathbf{N} + W_{45}(\mathbf{N} \otimes \mathbf{C} \mathbf{N} + \mathbf{N} \mathbf{C} \otimes \mathbf{N}) \right] \otimes \mathbf{N} \otimes \mathbf{N} \end{aligned} \quad (\text{A.98})$$

$$\begin{aligned} \frac{\partial(W_5(\mathbf{N} \otimes \mathbf{C} \mathbf{N} + \mathbf{N} \mathbf{C} \otimes \mathbf{N}))}{\partial \mathbf{C}} &= \left[W_{51} \mathbf{I} + W_{52}(I_1 \mathbf{I} - \mathbf{C}) + W_{53} I_3 \mathbf{C}^{-1} + W_{54} \mathbf{N} \otimes \mathbf{N} \right. \\ &\quad \left. + W_{55}(\mathbf{N} \otimes \mathbf{C} \mathbf{N} + \mathbf{N} \mathbf{C} \otimes \mathbf{N}) \right] \otimes (\mathbf{N} \otimes \mathbf{C} \mathbf{N} + \mathbf{N} \mathbf{C} \otimes \mathbf{N}) \\ &\quad + W_5 ((\mathbf{N} \otimes \mathbf{N}) \odot \mathbf{I} + \mathbf{I} \odot (\mathbf{N} \otimes \mathbf{N})) \end{aligned} \quad (\text{A.99})$$

A.2.4.2 Derivatives for material tensor (eq. 2.51)

Here, W_i and W_{ij} substitute $\partial W / \partial \hat{I}_i$ and $\partial^2 W / (\partial \hat{I}_i \partial \hat{I}_j)$, respectively.

$$\begin{aligned}
& \partial \left(W_1 \hat{I}_3^{-\frac{2}{3}} (\mathbf{I} - \frac{1}{3} \hat{I}_1 \hat{\mathbf{C}}^{-1}) \right) / \partial \mathbf{C} \\
&= \hat{I}_3^{-\frac{4}{3}} \left(\left[W_{11} \mathbf{I} + W_{12} (\hat{I}_1 \mathbf{I} - \hat{\mathbf{C}}) + W_{14} \mathbf{N} \otimes \mathbf{N} + W_{15} (\mathbf{N} \otimes \hat{\mathbf{C}} \mathbf{N} + \mathbf{N} \hat{\mathbf{C}} \otimes \mathbf{N}) \right. \right. \\
&\quad \left. \left. - \left(\frac{1}{3} W_{11} \hat{I}_1 + \frac{2}{3} W_{12} \hat{I}_2 - \frac{1}{2} W_{13} \hat{I}_3 + \frac{1}{3} W_{14} \hat{I}_4 + \frac{2}{3} W_{15} \hat{I}_5 \right) \hat{\mathbf{C}}^{-1} \right] \otimes (\mathbf{I} - \frac{1}{3} \hat{I}_1 \hat{\mathbf{C}}^{-1}) \right. \\
&\quad \left. - \frac{1}{3} W_1 (\mathbf{C}^{-1} \otimes \mathbf{I} + \mathbf{I} \otimes \hat{\mathbf{C}}^{-1} - \frac{1}{3} \hat{I}_1 \hat{\mathbf{C}}^{-1} \otimes \hat{\mathbf{C}}^{-1} - \hat{I}_1 \mathbf{C}^{-1} \odot \mathbf{C}^{-1}) \right) \quad (\text{A.100})
\end{aligned}$$

$$\begin{aligned}
& \partial \left(W_2 \hat{I}_3^{-\frac{2}{3}} (\hat{I}_1 \mathbf{I} - \hat{\mathbf{C}} - \frac{2}{3} \hat{I}_2 \hat{\mathbf{C}}^{-1}) \right) / \partial \mathbf{C} \\
&= \hat{I}_3^{-\frac{4}{3}} \left(\left[W_{21} \mathbf{I} + W_{22} (\hat{I}_1 \mathbf{I} - \hat{\mathbf{C}}) + W_{24} \mathbf{N} \otimes \mathbf{N} + W_{25} (\mathbf{N} \otimes \hat{\mathbf{C}} \mathbf{N} + \mathbf{N} \hat{\mathbf{C}} \otimes \mathbf{N}) \right. \right. \\
&\quad \left. \left. - \left(\frac{1}{3} W_{21} \hat{I}_1 + \frac{2}{3} W_{22} \hat{I}_2 - \frac{1}{2} W_{23} \hat{I}_3 + \frac{1}{3} W_{24} \hat{I}_4 + \frac{2}{3} W_{25} \hat{I}_5 \right) \hat{\mathbf{C}}^{-1} \right] \right. \\
&\quad \otimes (\hat{I}_1 \mathbf{I} - \hat{\mathbf{C}} - \frac{2}{3} \hat{I}_2 \hat{\mathbf{C}}^{-1}) + W_2 (\mathbf{I} \otimes \mathbf{I} - \mathbf{I} \odot \mathbf{I} - \frac{2}{3} (\hat{\mathbf{C}}^{-1} \otimes (\hat{I}_1 \mathbf{I} - \hat{\mathbf{C}}) \\
&\quad \left. \left. + (\hat{I}_1 \mathbf{I} - \hat{\mathbf{C}}) \otimes \hat{\mathbf{C}}^{-1} - \frac{2}{3} \hat{I}_2 \hat{\mathbf{C}}^{-1} \otimes \hat{\mathbf{C}}^{-1} - \hat{I}_2 \hat{\mathbf{C}}^{-1} \odot \hat{\mathbf{C}}^{-1}) \right) \right) \quad (\text{A.101})
\end{aligned}$$

$$\begin{aligned}
& \partial \left(\frac{1}{2} W_3 \hat{I}_3^{\frac{1}{3}} \hat{\mathbf{C}}^{-1} \right) / \partial \mathbf{C} \\
&= \frac{1}{2} \hat{I}_3^{-\frac{1}{3}} \left(\left[W_{31} \mathbf{I} + W_{32} (\hat{I}_1 \mathbf{I} - \hat{\mathbf{C}}) + W_{34} \mathbf{N} \otimes \mathbf{N} + W_{35} (\mathbf{N} \otimes \hat{\mathbf{C}} \mathbf{N} + \mathbf{N} \hat{\mathbf{C}} \otimes \mathbf{N}) \right. \right. \\
&\quad \left. \left. - \left(\frac{1}{3} W_{31} \hat{I}_1 + \frac{2}{3} W_{32} \hat{I}_2 - \frac{1}{2} W_{33} \hat{I}_3 + \frac{1}{3} W_{34} \hat{I}_4 + \frac{2}{3} W_{35} \hat{I}_5 \right) \hat{\mathbf{C}}^{-1} \right] \otimes \hat{\mathbf{C}}^{-1} \right. \\
&\quad \left. + W_3 \left(\frac{1}{4} \mathbf{C}^{-1} \otimes \mathbf{C}^{-1} - \frac{1}{2} \mathbf{C}^{-1} \odot \mathbf{C}^{-1} \right) \right) \quad (\text{A.102})
\end{aligned}$$

$$\begin{aligned}
& \partial \left(W_4 \hat{I}_3^{-\frac{2}{3}} (\mathbf{N} \otimes \mathbf{N} - \frac{1}{3} \hat{I}_4 \hat{\mathbf{C}}^{-1}) \right) / \partial \mathbf{C} \\
&= \hat{I}_3^{-\frac{4}{3}} \left(\left[W_{41} \mathbf{I} + W_{42} (\hat{I}_1 \mathbf{I} - \hat{\mathbf{C}}) + W_{44} \mathbf{N} \otimes \mathbf{N} + W_{45} (\mathbf{N} \otimes \hat{\mathbf{C}} \mathbf{N} + \mathbf{N} \hat{\mathbf{C}} \otimes \mathbf{N}) \right. \right. \\
&\quad \left. \left. - \left(\frac{1}{3} W_{41} \hat{I}_1 + \frac{2}{3} W_{42} \hat{I}_2 - \frac{1}{2} W_{43} \hat{I}_3 + \frac{1}{3} W_{44} \hat{I}_4 + \frac{2}{3} W_{45} \hat{I}_5 \right) \hat{\mathbf{C}}^{-1} \right] \right. \\
&\quad \otimes (\mathbf{N} \otimes \mathbf{N} - \frac{1}{3} \hat{I}_4 \hat{\mathbf{C}}^{-1}) - \frac{1}{3} W_4 (\mathbf{C}^{-1} \otimes \mathbf{N} \otimes \mathbf{N} + \mathbf{N} \otimes \mathbf{N} \otimes \hat{\mathbf{C}}^{-1} \\
&\quad \left. \left. - \frac{1}{3} \hat{I}_4 \hat{\mathbf{C}}^{-1} \otimes \hat{\mathbf{C}}^{-1} - \hat{I}_4 \mathbf{C}^{-1} \odot \mathbf{C}^{-1}) \right) \right) \quad (\text{A.103})
\end{aligned}$$

$$\begin{aligned}
& \partial \left(W_5 \hat{I}_3^{-\frac{2}{3}} (\mathbf{N} \otimes \hat{\mathbf{C}} \mathbf{N} + \mathbf{N} \hat{\mathbf{C}} \otimes \mathbf{N} - \frac{2}{3} \hat{I}_5 \hat{\mathbf{C}}^{-1}) \right) / \partial \mathbf{C} \\
&= \hat{I}_3^{-\frac{4}{3}} \left(\left[W_{51} \mathbf{I} + W_{52} (\hat{I}_1 \mathbf{I} - \hat{\mathbf{C}}) + W_{54} \mathbf{N} \otimes \mathbf{N} + W_{55} (\mathbf{N} \otimes \hat{\mathbf{C}} \mathbf{N} + \mathbf{N} \hat{\mathbf{C}} \otimes \mathbf{N}) \right. \right. \\
&\quad \left. \left. - \left(\frac{1}{3} W_{51} \hat{I}_1 + \frac{2}{3} W_{52} \hat{I}_2 - \frac{1}{2} W_{53} \hat{I}_3 + \frac{1}{3} W_{54} \hat{I}_4 + \frac{2}{3} W_{55} \hat{I}_5 \right) \hat{\mathbf{C}}^{-1} \right] \right. \\
&\quad \otimes (\mathbf{N} \otimes \hat{\mathbf{C}} \mathbf{N} + \mathbf{N} \hat{\mathbf{C}} \otimes \mathbf{N} - \frac{2}{3} \hat{I}_5 \hat{\mathbf{C}}^{-1}) + W_5 \left((\mathbf{N} \otimes \mathbf{N}) \odot \mathbf{I} + \mathbf{I} \odot (\mathbf{N} \otimes \mathbf{N}) \right. \\
&\quad \left. - \frac{2}{3} (\hat{\mathbf{C}}^{-1} \otimes (\mathbf{N} \otimes \hat{\mathbf{C}} \mathbf{N} + \mathbf{N} \hat{\mathbf{C}} \otimes \mathbf{N}) + (\mathbf{N} \otimes \hat{\mathbf{C}} \mathbf{N} + \mathbf{N} \hat{\mathbf{C}} \otimes \mathbf{N}) \otimes \hat{\mathbf{C}}^{-1}) \right. \\
&\quad \left. \left. + \frac{4}{9} \hat{I}_5 \hat{\mathbf{C}}^{-1} \otimes \hat{\mathbf{C}}^{-1} + \frac{2}{3} \hat{I}_5 \hat{\mathbf{C}}^{-1} \odot \hat{\mathbf{C}}^{-1} \right) \right) \quad (\text{A.104})
\end{aligned}$$

A.2.4.3 Derivatives for material tensor (eq. 2.56)

Here, W_i and W_{ij} substitute $\partial W / \partial \tilde{I}_i$ and $\partial^2 W / (\partial \tilde{I}_i \partial \tilde{I}_j)$, respectively.

$$\begin{aligned}
\frac{\partial (W_1 \mathbf{I})}{\partial \mathbf{C}} &= \left[W_{11} \mathbf{I} - W_{12} \mathbf{C}^{-2} + W_{13} \tilde{I}_3 \mathbf{C}^{-1} \right. \\
&\quad \left. + W_{14} \mathbf{N} \otimes \mathbf{N} - W_{15} \mathbf{C}^{-1} \mathbf{N} \otimes \mathbf{N} \mathbf{C}^{-1} \right] \otimes \mathbf{I} \quad (\text{A.105})
\end{aligned}$$

$$\begin{aligned}
\frac{\partial (W_2 \mathbf{C}^{-2})}{\partial \mathbf{C}} &= \left[W_{21} \mathbf{I} - W_{22} \mathbf{C}^{-2} + W_{23} \tilde{I}_3 \mathbf{C}^{-1} \right. \\
&\quad \left. + W_{24} \mathbf{N} \otimes \mathbf{N} - W_{25} \mathbf{C}^{-1} \mathbf{N} \otimes \mathbf{N} \mathbf{C}^{-1} \right] \otimes \mathbf{C}^{-2} \\
&\quad - W_2 (\mathbf{C}^{-2} \odot \mathbf{C}^{-1} + \mathbf{C}^{-1} \odot \mathbf{C}^{-2}) \quad (\text{A.106})
\end{aligned}$$

$$\begin{aligned}
\frac{\partial (W_3 \tilde{I}_3 \mathbf{C}^{-1})}{\partial \mathbf{C}} &= \left[W_{31} \mathbf{I} - W_{32} \mathbf{C}^{-2} + W_{33} \tilde{I}_3 \mathbf{C}^{-1} \right. \\
&\quad \left. + W_{34} \mathbf{N} \otimes \mathbf{N} - W_{35} \mathbf{C}^{-1} \mathbf{N} \otimes \mathbf{N} \mathbf{C}^{-1} \right] \otimes \tilde{I}_3 \mathbf{C}^{-1} \\
&\quad + W_3 \tilde{I}_3 (\mathbf{C}^{-1} \otimes \mathbf{C}^{-1} - \mathbf{C}^{-1} \odot \mathbf{C}^{-1}) \quad (\text{A.107})
\end{aligned}$$

$$\begin{aligned}
\frac{\partial (W_4 \mathbf{N} \otimes \mathbf{N})}{\partial \mathbf{C}} &= \left[W_{41} \mathbf{I} - W_{42} \mathbf{C}^{-2} + W_{43} \tilde{I}_3 \mathbf{C}^{-1} \right. \\
&\quad \left. + W_{44} \mathbf{N} \otimes \mathbf{N} - W_{45} \mathbf{C}^{-1} \mathbf{N} \otimes \mathbf{N} \mathbf{C}^{-1} \right] \otimes \mathbf{N} \otimes \mathbf{N} \quad (\text{A.108})
\end{aligned}$$

$$\begin{aligned}
\frac{\partial(W_5 \mathbf{C}^{-1} \mathbf{N} \otimes \mathbf{N} \mathbf{C}^{-1})}{\partial \mathbf{C}} &= [W_{51} \mathbf{I} - W_{52} \mathbf{C}^{-2} + W_{53} \tilde{I}_3 \mathbf{C}^{-1} \\
&\quad + W_{54} \mathbf{N} \otimes \mathbf{N} - W_{55} \mathbf{C}^{-1} \mathbf{N} \otimes \mathbf{N} \mathbf{C}^{-1}] \otimes \mathbf{C}^{-1} \mathbf{N} \otimes \mathbf{N} \mathbf{C}^{-1} \\
&\quad + W_5 ((\mathbf{C}^{-1} \mathbf{N} \otimes \mathbf{N} \mathbf{C}^{-1}) \odot \mathbf{C}^{-1} + \mathbf{C}^{-1} \odot (\mathbf{C}^{-1} \mathbf{N} \otimes \mathbf{N} \mathbf{C}^{-1}))
\end{aligned} \tag{A.109}$$

A.3 Finite element addendum

A.3.1 Linear elements for finite incompressibility

As mentioned in chapter 3.2.3, various concepts have been published to avoid locking effects during the analysis of near-incompressible solids. Although the pioneering works of Nagtegaal et al. [1974] (mean dilatation method), Malkus and Hughes [1978] and Hughes [1980] (selective reduced integration method, SRI), Flanagan and Belytschko [1981] (reduced integration method with stabilization, RI), Sussman and Bathe [1987] (mixed displacement/pressure method, u/p), and Simo and Rifai [1990] (enhanced assumed strain method, EAS) provided the foundation for the development of many three-dimensional elements, they themselves were often limited to plate or shell formulations. Therefore, those and other sources are not referred to in the following overview, which shall be restricted to papers that actually describe realizations of three-dimensional elements. Still, this overview is not complete in terms of publications, as it is only intended to cover the main developments within the area of research.

In many publications, first-order quadrilateral and hexahedral elements are often indistinguishable by their names. For example, EAS plate elements with four and twelve enhanced modes are often labeled Q1/E4 and Q1/E12 while the related brick element with nine enhanced modes is labeled Q1/E9. To unify element names in the present work, hexahedrons will be denoted by an initial H, tetrahedrons by a T, and quadrilaterals by a Q. The subsequent numbers mark the interpolation order of the displacements, followed by a method-specific token.

Although several papers suggested the application of enhancement methods to hexahedral elements before, Pian and Tong [1986] appear to be the first to have actually realized such a formulation. Based on their hybrid assumed stress Q1/HR-5 element orig-

inating from a Hellinger-Reissner variational formulation [Pian and Sumihara 1984]¹, they developed the H1/HR-18 element with 18 internal parameters. The applicability of this element is limited to geometric and material linearity, but within this limit it is described by several authors as highly efficient and accurate. Sussman [1987], Sussman and Bathe [1987] invented the class of u/p-elements - mixed displacement-pressure formulations that allow for an elimination of the pressure variables on the element level. This facilitates a straightforward inclusion into regular displacement based codes, given decoupled constitutive descriptions are available. By first- and second-order displacement interpolation the elements H1/P0 and H2/P4 were introduced, with constant and linear pressure interpolation, respectively. H1/HR-18 and more frequently H1/P0 serve as standard references to verify the locking behavior of newly developed elements in the near-incompressible case.

Based on Hu-Washizu's variational principle (see A.3.2), the Enhanced-Assumed-Strain method yielded the nonlinear H1/E9 element with nine enhanced strain modes in [Simo and Armero 1992]. Due to apparent instabilities under certain compression conditions, Simo et al. [1993] proposed the improved versions H1/E12 and H1/ME12. With twelve enhanced modes, special quadrature rules and up to 354 internal variables, these elements provide satisfying coarse mesh accuracy, but their computational cost are extraordinarily high. At the same time, Andelfinger and Ramm [1993] published EAS elements with even more enhanced modes, e.g. the H1/E21. Remarkably, even those elements develop rank deficiencies and the associated hourglass modes for stress states with compression [Wriggers and Reese 1996], as well as volumetric locking appeared in the case of distorted geometries [Freischläger 2000]. Wriggers and Korelc [1996] stated that thirty enhanced modes were necessary to avoid any locking in nonlinear applications, however this is hardly feasible and apparently hasn't been realized. Instead, the authors proposed a conjugated gradient method that along with other artificial hourglass control mechanisms which performed better than H1/ME12, but still failed to provide the desired properties for EAS elements with arbitrary geometry and nonlinear deformations. Probably due to the required implementation effort of progressive EAS elements, later formulations as in [Kasper and Taylor 2000, De Sousa et al. 2003] were mostly compared to the classic ones. Still, no universal benchmark or unified test set which includes tests for distortion sensitivity, locking and hourglassing under great deformations has been established.

Meanwhile, Weiss [1994] proposed an augmented Lagrangian iteration procedure to enforce the incompressibility constraint to any desired accuracy. Starting from a compressible

¹ This publication was not available to the author. The comments rely on several reputable recitations.

state the incremental increase of a penalty parameter (i.e. the compression modulus) avoids the ill-conditioning of the stiffness matrix which may occur even in locking-free elements when near-incompressibility is modeled.

De Souza Neto et al. [1996] published the well-performing F-bar formulation, described and enhanced in section 3.2.5, with the known shortcoming of a non-symmetric tangential stiffness matrix.

Hexahedral RI elements with one-point quadrature rule don't display volumetric locking by default, and several efforts were published to further enhance their regular stabilization in order to handle incompressible materials. Stabilization parameters, which needed adjustment by the user and at worst would influence the solution, were a common drawback. The H0/Jet3D element in [Li and Cescotto 1997] utilizes such a parameter, but is reported to provide good results even in the nonlinear range. In contrast, no manual calibration is necessary for the element of Hu and Nagy [1997], which instead is valid only for small deformations. Liu et al. [1998] used a corotated coordinate system and four integration points for the stabilizing terms in their H0/DS formulation. This measure ensures good performance in large deformation analysis without the need for parameter adjustment. Sensitivity to mesh distortion was apparently not tested for. The superior cost advantage of the one-point quadrature element H0 is diminished by weighted superimposition with the regular H1 element as proposed in [Doll et al. 2000]. This stabilization is similar to the k -exponent introduced in section 3.2.4 and still less expensive than comparable fully integrated EAS formulations. Reese et al. [2000] invented the concept of an equivalent parallelepiped to derive the stabilization terms, which along with the solutions are, to some degree, load dependent. Besides, the deviation of the actual element geometry from a parallelepiped leads to diminished accuracy of distorted elements as in other formulations. For these elements in particular, mesh refinement leads to less distorted and therefore more accurate elements. Updates with minor improvements were presented in Puso [2000], and [Reese 2005], where the H0/SP element compared favorable to H1/P0 and H1/ME12 in several tests.

Also linear tetrahedral elements have been enhanced to work properly for near-incompressible situations. Although not as accurate as hexahedrons, they are attractive due the option to reliably generate meshes fully automatically. Taylor [2000] claimed this to be the driving motivation behind his mixed enhanced strain element T1/ME1P1 with independent displacement, pressure and internal strain fields. A similar approach has been followed by Chiumenti et al. [2002] and [Cervera et al. 2003], who additionally applied a

sub-grid method (developed by Hughes [1995]) to relax the incompressibility constraint and avoid the geometrical locking typical for triangular and tetrahedral meshes. The mentioned elements were validated for linear elasticity only. A different idea for the essential constraint relaxation was proposed by De Souza Neto et al. [2003]: Incompressibility was enforced over a patch of elements, which concedes in a dependence of stabilization effectiveness on the size of the patches. The actual elements used were derived by the same strategy as the hexahedrons in [De Souza Neto et al. 1996], resulting in an asymmetric stiffness matrix as well.

Remark: The term *stabilization* has been used without further explanation so far. This is due to the few commonalities the different approaches possess, apart from their purpose. They all provide enhancements to the otherwise rank-deficient stiffness matrix. As the eigenvectors associated with negative eigenvalues have the well known hourglass shapes, the stabilization usually assigns some stiffness to those particular modes. This may be done on element level, for a patch of elements or globally. The stabilizing terms are often derived from orthogonality conditions (as enhanced strains), from Taylor expansions of strain and stress fields (for RI elements), from equivalent normalized elements, or by ad hoc modifications of strains, stresses, gradient or stiffness matrices. It is absolutely recommended to refer to the respective publications to get detailed information on the methods used.

A.3.2 Variational base for mixed element formulations

In equations (3.2) and (3.4), strain-displacement relations were included which are not an integral part of the principle of virtual work. These kinematic field equations, kinematic constraints ($\mathbf{u} = \bar{\mathbf{u}}$ on \mathcal{S}^u) and even constitutive material descriptions may be considered as specific boundary conditions for the formularization of that principle. One approach which instead allows for their direct inclusion is the consideration of a minimum potential energy. It may be written as

$$\delta\Pi = 0 \quad \text{with } \Pi = \Pi_{\text{int}} + \Pi_{\text{ext}} = \int_{\mathcal{B}} W(\mathbf{E}) \, dV + \Pi_{\text{ext}}. \quad (\text{A.110})$$

This is equivalent to the virtual work equation (3.4), apart from the substitution of the term $\mathbf{S} : \delta\mathbf{E}$ by the more general $\delta W(\mathbf{E})$. While ultimately still being a function of the deformation, this allows for the variation of other quantities than just displacements.

To discriminate between independent and dependent variables, an upper index is in-

roduced that will point to an explicit dependence. E.g., \mathbf{E}^u marks a Green-Lagrange strain which depends on the displacements (through kinematic equations), \mathbf{E}^s indicates a dependence on the stress (through constitutive equations) and \mathbf{E} denotes the independent strain variable. Prescribed boundary values are marked by an overbar.¹

The three-field Hu-Washizu variational principle is one exemplary realization of the above approach on which many enhanced finite elements are based. Starting from eq. (A.110), \mathbf{S} and \mathbf{T}^s are introduced as Lagrange multipliers, such that

$$\Pi_{\text{HW}} = \int_{\mathcal{B}} W(\mathbf{E}) dV + \int_{\mathcal{B}} \mathbf{S} : (\mathbf{E}^u - \mathbf{E}) dV + \int_{\mathcal{S}^u} \mathbf{T}^s (\bar{\mathbf{u}} - \mathbf{u}) dA + \Pi_{\text{ext}}. \quad (\text{A.111})$$

The independent variables herein are the displacements \mathbf{u} , the 2nd Piola-Kirchhoff stresses \mathbf{S} , and the Green-Lagrange strains \mathbf{E} .

$\delta\Pi_{\text{HW}}=0$ identifies a stationary potential energy, and derived as the sum of the variations with respect to those three variables

$$\begin{aligned} \delta\Pi_{\text{HW}} = & \int_{\mathcal{B}} \frac{\partial W}{\partial \mathbf{E}} : \delta\mathbf{E} dV + \int_{\mathcal{B}} \mathbf{S} : (\delta\mathbf{E}^u - \delta\mathbf{E}) dV + \int_{\mathcal{B}} \delta\mathbf{S} : (\mathbf{E}^u - \mathbf{E}) dV \\ & - \int_{\mathcal{B}} \rho_0 \mathbf{b} \delta\mathbf{u} dV - \int_{\mathcal{S}^t} (\bar{\mathbf{T}} - \mathbf{T}^s) \delta\mathbf{u} dA + \int_{\mathcal{S}^u} \delta\mathbf{T} (\bar{\mathbf{u}} - \mathbf{u}) dA = 0. \end{aligned} \quad (\text{A.112})$$

The linearization has to be conducted with respect to all three independent variables.

If a uniform discretization would be applied to all three, the resultant element formulations would not deviate from the virtual work based approach. However, while displacements fields in the continuum context are required to be steady even in their discretized form, strains and stresses might be approximated by functions with discontinuities on element boundaries. This allows for the definition and elimination of the stress and strain quantities on element level (leading to enhanced displacement based formulation), globally or independent of the displacement discretization patterns. The F-bar element introduced in section 3.2.4 can be traced to this approach as well, with the independent dilatation being a function of the Green-Lagrange strains.

The Hu-Washizu functional is considered one of the most flexible variational formulations for the derivation of displacement based and mixed finite elements. There are several others of importance though, often overlapping but usually also with distinct advantages. [Wriggers 2009] provides a thorough introduction and overview.

¹ The proposed notation is limited to this section only.

References

- A. M. Agnew, K. Moorhouse, M. Murach, S. E. White, and Y.-S. Kang. Tensile stress in human ribs throughout the lifespan. In *IRCOBI Conference*, 2014.
- Johannes Altenbach and Holm Altenbach. *Einführung in die Kontinuumsmechanik*. B.G. Teubner, 1994.
- U. Andelfinger and E. Ramm. EAS-elements for two-dimensional, three-dimensional, plate and shell structures and their equivalence to HR-elements. *International Journal for Numerical Methods in Engineering*, 36:1311–1337, 1993.
- Claudia Arakelian, Anthony Warrington, Hanspeter Winkler, R.J. Perz-Edwards, Michael K. Reedy, and Kenneth A. Taylor. Myosin S2 origins track evolution of strong binding on actin by azimuthal rolling of motor domain. *Biophysical Journal*, 108(6):1495 – 1502, 2015. ISSN 0006-3495.
- Xavier Aubert. *Le Couplage énergétique de la contraction musculaire*. PhD thesis, Brussels, 1956.
- E. Azizi and T.J. Roberts. Biaxial strain and variable stiffness in aponeuroses. *The Journal of Physiology*, 587:4309–4318, 2009.
- Klaus-Jürgen Bathe. *Finite-Elemente-Methoden*. Springer-Verlag, 2nd edition, 2002.
- T. Belytschko. Correction of article by Flanagan, D. P. and Belytschko, T. *International Journal for Numerical Methods in Engineering*, 19:467, 1983.
- Ted Belytschko. *Nonlinear Finite Element Analysis*. Northwestern University, 1999.
- Josef Betten. *Tensorrechnung für Ingenieure*. B.G. Teubner, 1987.
- Josef Betten. *Finite Elemente für Ingenieure I/II*. Springer-Verlag, 1998.
- S. S. Blemker, P. M. Pinsky, and S. L. Delp. A 3D model of muscle reveals the causes of nonuniform strains in the biceps brachii. *Journal of Biomechanics*, 38:657–665, 2005.
- E. M. H. Bosboom, C. V. C. Bouten, C. W. J. Oomens, H. W. M. Van Straaten, F. P. T. Baaijens, and H. Kuipers. Quantification and localisation of damage in rat muscles after controlled loading; a new approach to study the aetiology of pressure sores. *Medical Engineering and Physics*, 23:195–200, 2001a.
- E. M. H. Bosboom, M. K. C. Hesselink, C. W. J. Oomens, M. R. Drost, and F. P. T. Baaijens. Passive transverse mechanical properties of skeletal muscle under in vivo compression. *Journal of Biomechanics*, 34:1365–1368, 2001b.
- E. M. H. Bosboom, C. V. C. Bouten, C. W. J. Oomens, F. P. T. Baaijens, and K. Nicolay. Quantifying pressure sore-related muscle damage using high resolution MRI. *Journal of Applied Physiology*, 95: 2235–2240, 2003.

- Peter Bovendeerd. *The mechanics of the normal and ischemic left ventricle during the cardiac cycle*. PhD thesis, Rijksuniversiteit Limburg, Maastricht, The Netherlands, 1990.
- Roel G. M. Breuls. *Experimental and Theoretical Analyses of Compression Induced Muscle Damage*. PhD thesis, Technische Universiteit Eindhoven, 2003.
- R Bruhin, U A Stock, J P Drucker, T Azhari, J Wippermann, J M Albes, D Hintze, S Eckardt, C Konke, and T Wahlers. Numerical simulation techniques to study the structural response of the human chest following median sternotomy. *The Annals of Thoracic Surgery*, 80(2):623–630, 2005.
- Christian et al. Bucher. *SLang* - the Structural Language, 5.1.0 edition, 2013.
- K.K. Ceelen, A. Stekelenburg, S. Loerakker, G.J. Strijkers, D.L. Bader, K. Nicolay, F.P. Baaijens, and C.W. Oomens. Compression-induced damage and internal tissue strains are related. *Journal of Biomechanics*, 41(16):3399–3404, 2008.
- M. Cervera, M. Chiumenti, Q. Valverde, and C. A. de Saracibar. Mixed linear/linear simplicial elements for incompressible elasticity and plasticity. *Computer Methods in Applied Mechanics and Engineering*, 192:5249–5263, 2003.
- M. Chiumenti, Q. Valverde, C. Angele de Saracibar, and M. Cervera. A stabilized formulation for incompressible elasticity using linear displacement and pressure interpolations. *Computer Methods in Applied Science and Engineering*, 191:5253–5264, 2002.
- John W. Chow and Warren G. Darling. The maximum shortening velocity of muscle should be scaled with activation. *Journal of Applied Physiology*, 86:1025–1031, 1999.
- Anatomical Chart Company. *Illustrated pocket anatomy: Muscular and skeletal systems study guide*, 2002.
- Joseph M Cormier, Joel D Stitzel, Stefan M Duma, and Fumio Matsuoka. Regional variation in the structural response and geometrical properties of human ribs. In *Annu Proc Assoc Adv Automot Med.*, volume 49, pages 153–170. Association for the Advancement of Automotive Medicine, 2005.
- John C. Criscione, Andrew S. Douglas, and William C. Hunter. Physically based strain invariant set for materials exhibiting transversely isotropic behavior. *Journal of the Mechanics and Physics of Solids*, 49:871–897, 2001.
- J. J. Crisco, K. D. Hentel, W. O. Jackson, K. Goehner, and P. Jokl. Maximal contraction lessens impact response in a muscle contusion model. *Journal of Biomechanics*, 29(10):1291 – 1296, 1996. ISSN 0021-9290.
- M. A. Crisfield. Solution procedure for non-linear structural problems. In *Recent advances in non-linear computational methods*, pages 1–39. Pineridge-Press, 1982.
- A Cutts, Robert McNeill Alexander, and Robert F Ker. Ratios of cross-sectional areas of muscles and their tendons in a healthy human forearm. *Journal of Anatomy*, 176:133–137, 1991.
- R.J. Alves De Sousa, R.M. Natal Jorge, R.A. Fontes Valente, and J.M.A. César de Sá. A new volumetric and shear locking-free 3d enhanced strain element. *Engineering Computations*, 20:896–926, 2003.
- E.A. De Souza Neto, D. Perić, M. Dutko, and D.R.J. Owen. Design of simple low order finite elements for large strain analysis of nearly incompressible solids. *International Journal for Solids and Structures*, 33 (20–22):3277–3296, 1996.

- E.A. De Souza Neto, F.M.A. Pires, and D.R.J. Owen. F-bar-based linear triangles and tetrahedra for finite strain analysis of nearly incompressible solids. Part I: formulation and benchmarking. *International Journal for Numerical Methods in Engineering*, 61(3):353–383, 2003.
- Jun Ding, Stuart A. Binder-Mcleod, and Anthony S. Wexler. Two-step, predictive, isometric force model tested on data from human and rat muscles. *Journal of Applied Physiology*, 85(6):2176–2189, 1998.
- Patricia C. Dischinger, Timothy J. Kerns, and Joseph A. Kufera. Lower extremity fractures in motor vehicle collisions: The role of driver gender and height. *Accident Analysis & Prevention*, 27(4):601 – 606, 1995. ISSN 0001-4575.
- J.K. Djoko, B.P. Lamichhane, B.D. Reddy, and B.I. Wohlmuth. Conditions for equivalence between the Hu-Washizu and related formulations, and computational behavior in the incompressible limit, 2004.
- S. Doll, R. Hauptmann, K. Schweizerhof, and C. Freischläger. On volumetric locking of low-order solid and solid-shell elements for finite elastoviscoplastic deformations and selective reduced integration. *Computational Engineering*, 17(7):874–902, 2000.
- Jan-Peter Drücker. Untersuchungen zur automatischen Erstellung eines numerischen Modells zur Analyse von Brustkorbfixierungstechniken nach operativen Eingriffen. Master’s thesis, Bauhaus University Weimar, 2002.
- Sonia Duprey, Karine Bruyere, and Jean-Pierre Verriest. Influence of geometrical personalization on the simulation of clavicle fractures. *Journal of Biomechanics*, 41(1):200–207, 2008. ISSN 0021-9290.
- William K. Durfee and Karen I. Palmer. Estimation of force- activation, force- length, and force-velocity properties in isolated, electrically stimulated muscle. *IEEE Transactions on Biomedical Engineering*, 41(3):205–216, 1994.
- Dynardo GmbH. *Methods for multi-disciplinary optimization and robustness analysis*, 2015. optiSlang Documentation v. 4.1.2.
- K. A. P. Edman. The velocity of unloaded shortening and its relation to sarcomere length and isometric force in vertebrate muscles fibers. *Journal of Physiology*, 291:139–155, 1979.
- K. A. P. Edman. Double-hyperbolic force-velocity relation in frog muscle fibres. *Journal of Physiology*, 404:301–321, 1988.
- Alexander E. Ehret, Markus Böhl, and Mikhail Itskov. A continuum constitutive model for the active behaviour of skeletal muscle. *Journal of the Mechanics and Physics of Solids*, 59:625–636, 2011.
- Marcelo Epstein and Walter Herzog. *Theoretical models of skeletal muscle: Biological and mathematical considerations*. John Wiley & Sons, Ltd, 1998.
- Carlos A. Felippa. *Nonlinear Finite Element Methods*. University Of Colorado, Boulder, 2001.
- Michael A. Ferenczi, Sergey Y. Bershitsky, Natalia Koubassova, Verl Siththanandan, William I. Helsby, Pierre Panine, Manfred Roessle, Theyencheri Narayanan, and Andrey K. Tsaturyan. The ‘Roll and Lock’ mechanism of force generation in muscle. *Structure*, 13:131–141, 2005.
- D.P. Flanagan and T. Belytschko. A uniform strain hexahedron and quadrilateral with orthogonal hourglass control. *International Journal for Numerical Methods in Engineering*, 17:679, 1981.
- Mario Forcinito, Marcelo Epstein, and Walter Herzog. Can a rheological muscle model predict force depression/enhancement? *Journal of Biomechanics*, 31:1093–1099, 1998.

- Christof Freischläger. *Konzepte zur Formulierung versteifungsfreier Volumenelemente*. PhD thesis, Universität Karlsruhe, 2000.
- Jan Friden and Richard L. Lieber. Structural and mechanical basis of exercise-induced muscle injury. *Medicine & Science in Sports & Exercise*, 24(5):521–530, 1992.
- Y.C. Fung. *Mechanical Properties of Living Tissues*. Springer-Verlag, 2 edition, 1993.
- William E. Garrett, Marc R. Safran, Anthony V. Seaber, Richard R. Glisson, and Beth M. Ribbeck. Biomechanical comparison of stimulated and nonstimulated skeletal muscle pulled to failure. *The American Journal of Sports Medicine*, 15(5):448–454, 1987.
- A. Gefen, N. Gefen, E. Linder-Ganz, and S.S. Margulies. In vivo muscle stiffening under bone compression promotes deep pressure sores. *Journal of Biomechanical Engineering - Transactions of the ASME*, 127: 512–524, 2005.
- Alexander W.J. Gielen. *A continuum approach to the mechanics of contracting skeletal muscle*. PhD thesis, University of Eindhoven, 1998.
- A.M. Gordon, A.F. Huxley, and F.J. Julian. The variation in isometric tension with sarcomere length in vertebrate muscle fibers. *Journal of Physiology*, 184:170–192, 1966.
- Gerald Granik and Ira Stein. Human ribs: Static testing as a promising medical application. *Journal of Biomechanics*, 6(3):237 – 240, 1973. ISSN 0021-9290.
- Ralf Greve. *Kontinuumsmechanik*. Springer-Verlag, 2003.
- J.M. Guccione, L.K. Waldmann, and A.D. McCulloch. Mechanics of active contraction in cardiac muscle: Part II - cylindrical models of the systolic left ventricle. *Journal of Biomechanical Engineering - Transactions of the ASME*, 115:82–90, 1993.
- Michael Günther. *Computersimulation zur Synthetisierung des muskulär erzeugten menschlichen Gehens unter Verwendung eines biomechanischen Mehrkörpermodells*. PhD thesis, Universität Tübingen, 1997.
- Prof. Dr. Bastian von Harrach. *Numerik von Differentialgleichungen*. Goethe-Universität Frankfurt am Main, 2017.
- S. Hedenstierna, P. Halldin, and K. Brodin. Evaluation of a combination of continuum and truss finite elements in a model of passive and active muscle tissue. *Computational Methods in Biomechanics and Biomedical Engineering*, 11(6):1025–5842, 2008.
- Thomas Heidlauf and Oliver Röhrle. A multiscale chemo-electro-mechanical skeletal muscle model to analyze muscle contraction and force generation for different muscle fiber arrangements. *Frontiers in Physiology*, 5:498, 2014. ISSN 1664-042X.
- W. Herzog. Personal correspondence with the author. 2007.
- Walter Herzog, editor. *Skeletal muscle mechanics: From mechanisms to function*. John Wiley & Sons, Ltd, 2000.
- A. Hill. Aspects of invariance in solid mechanics. *Advances in Applied Mechanics*, 18:1–75, 1978.
- Archibald Vivian Hill. The heat of shortening and the dynamic constants of muscle. *Proceedings of the Royal Society*, 126:136–195, 1938.

- E. Hinton, T. Rock, and O. C. Zienkiewicz. A note on mass lumping and related processes in the finite element method. *Earthquake Engrg. Struct. Dynamics*, 4:245–249, 1976.
- K. C. Holmes and M. A. Geeves. The structural basis of muscle contraction. *Philosophical Transactions of The Royal Society: Biological Sciences*, 355:419–431, 2000.
- Gerhard A. Holzapfel. *Nonlinear solid mechanics - A continuum approach for Engineering*. John Wiley & Sons, Ltd, 2000.
- Yu-Kan Hu and L.I. Nagy. A one point quadrature eight-node brick element with hourglass control. *Computers and Structures*, 65(6):893–902, 1997.
- T.G.R. Hughes. Generalization of selective integration procedures of anisotropic and nonlinear media. *International Journal for Numerical Methods in Engineering*, 15:1413, 1980.
- Thomas J. R. Hughes. Multiscale phenomena: Green’s functions, the Dirichlet-to-Neumann formulation, subgrid scale models, bubbles and the origins of stabilized methods. *Computer Methods in Applied Mechanics and Engineering*, 127:387–401, 1995.
- J.D. Humphrey and F.C.P. Yin. A new constitutive formulation for characterizing the mechanical behavior of soft tissues. *Biophysical Journal*, 52:563–570, 1987.
- P.J. Hunter and B.H. Smaill. The analysis of cardiac function: A continuum approach. *Prog. Biophys. Molec. Biol.*, 52:101–164, 1988.
- A. F. Huxley and R. Niedergerke. Structural changes in muscle during contraction. *Nature*, 173:971–973, 1954.
- A. F. Huxley and R. M. Simmons. Proposed mechanism of force generation in striated muscle. *Nature*, 233:533–538, 1971.
- Andrew Fielding Huxley. Muscle structure and theories of contraction. *Prog. Biophys. Biophys. Chem.*, 7: 255–318, 1957.
- H.E. Huxley and J. Hanson. Changes in the cross-striations of muscle during contraction and stretch and their structural interpretation. *Nature*, 173:973–976, 1954.
- Hans Karl Iben. *Mathematik für Ingenieure und Naturwissenschaftler - Tensorrechnung*. B.G. Teubner, 1995.
- D. Ito, E. Tanaka, and S. Yamamoto. A novel constitutive model of skeletal muscle taking into account anisotropic damage. *Journal of the Mechanical Behavior of Biomedical Materials*, 3:85–93, 2009.
- Mikhail Itskov. *Tensor Algebra and Tensor Analysis for Engineers*. Springer, 2 edition, 2009.
- T. Johansson, P. Meier, and R. Blickhan. A finite-element model for the analysis of skeletal muscle. *Journal of Theoretical Biology*, 206:131–149, 2000.
- F.J. Julian and D.L. Morgan. Intersarcomere dynamics during fixed-end tetanic contractions of frog muscle fibres. *Journal of Physiology*, 293:365–378, 1979.
- Eric P. Kasper and Robert L. Taylor. A mixed-enhanced strain method Part II: Geometrically nonlinear problems. *Computers and Structures*, 75:251–260, 2000.

- Bernhard Katz. The relation between force and speed in muscular contraction. *Journal of Physiology*, 96: 45–64, 1939.
- Andrew R Kemper, Craig McNally, Eric A Kennedy, Sarah J Manoogian, Amber L Rath, Tracy P Ng, Joel D Stitzel, Eric P Smith, Stefan M Duma, and Fumio Matsuoka. Material properties of human rib cortical bone from dynamic tension coupon testing. *Stapp Car Crash J*, 49(11):199–230, 2005.
- Andrew R. Kemper, Craig McNally, Clayton A. Pullins, Laura J. Freeman, Stefan M. Duma, and Stephen M. Rouhana. The biomechanics of human ribs: Material and structural properties from dynamic tension and bending tests. *Stapp Car Crash Journal*, 51:235–273, 2007.
- Richard W. Kent, Sergey V. Purtsezov, and Walter D. Pilkey. Limiting performance analysis of a seat belt system with slack. *International Journal of Impact Engineering*, 34(8):1382 – 1395, 2007. ISSN 0734-743X.
- Richard W. Kent, Jason L. Forman, and Ola Bostrom. Is there really a “cushion effect”? A biomechanical investigation of crash injury mechanisms in the obese. *Obesity*, 18:749–753, 2010.
- W. M. Kier and J. L. Van Leeuwen. A kinematic analysis of tentacle extension in the squid loligo pealei. *Journal of Experimental Biology*, 200:41–53, 1997.
- William M. Kier. The musculature of coleoid cephalopod arms and tentacles. *Frontiers in Cell and Developmental Biology*, 4:10, 2016. ISSN 2296-634X.
- M. Kojic, S. Mijailovic, and N. Zdravkovic. Modelling of muscle behavior by the finite element method using Hill’s three-element model. *International Journal for Numerical Methods in Engineering*, 43: 941–953, 1998.
- Drew A Lansdown, Zhaohua Ding, Megan Wadington, Jennifer L Hornberger, and Bruce M Damon. Quantitative diffusion tensor mri-based fiber tracking of human skeletal muscle. *Journal of Applied Physiology*, 103(2):673–681, 2007.
- K.P. Li and S. Cescotto. An 8-node brick element with mixed formulation for large deformation analyses. *Computer Methods in Applied Mechanics and Engineering*, 141:157–204, 1997.
- Zuoping Li, Matthew W. Kindig, Jason R. Kerrigan, Costin D. Untaroiu, Damien Subit, Jeff R. Crandall, and Richard W. Kent. Rib fractures under anterior-posterior dynamic loads: Experimental and finite-element study. *Journal of Biomechanics*, 43:228–234, 2010.
- Y. Liang, R.M. McMeeking, and A.G. Evans. A finite element simulation scheme for biological muscular hydrostats. *Journal of Theoretical Biology*, 242:142–150, 2006.
- Richard L. Lieber. *Skeletal Muscle Structure, Function & Plasticity: The Physiological Basis of Rehabilitation*. Lipincott Williams & Wilkins, 2002.
- Host Lippmann. *Angewandte Tensorrechnung*. Springer-Verlag, 1996.
- W.K. Liu, Yong Guo, Sing Tang, and T. Belytschko. A multiple-quadrature eight-node hexahedral finite element for large deformation elastoplastic analysis. *Computer Methods in Applied Mechanics and Engineering*, 154:69–132, 1998.
- Y.T. Lu, H.X. Zhu, S. Richmond, and J. Middleton. A visco-hyperelastic model for skeletal muscle tissue under high strain rates. *Journal of Biomechanics*, 43(13):2629 – 2632, 2010. ISSN 0021-9290.

- Mascha Maenhout. *Strain fields within contracting skeletal muscle*. PhD thesis, Technische Universiteit Eindhoven, 2002.
- D. M. Malkus and T. J. R. Hughes. Mixed finite element methods-reduced and selective integration techniques: A unification of concepts. *Computer Methods in Applied Mechanics and Engineering*, 15: 63–81, 1978.
- J.A.C. Martins, E.B. Pires, R. Salvado, and P.B. Dinis. A numerical model of passive and active behavior of skeletal muscles. *Computer Methods in Applied Mechanics and Engineering*, 151:419–433, 1998.
- G.T. Mase and G.E. Mase. *Continuum mechanics for engineers*. CRC Press, 1999.
- H. Matthies and G. Strang. The solution of nonlinear finite element equations. *International Journal for Numerical Methods in Engineering*, 14:1613–1626, 1979.
- Walter Maurel. *3D Modeling of the Human Upper Limb including the Biomechanics of Joints, Muscles and Soft Tissues*. PhD thesis, Ecole Polytechnique Federale de Lausanne, 1998.
- Thomas A. McMahon. *Muscles, Reflexes and Locomotion*. Princeton University Press, 1984.
- P. Meier and R. Blickhan. *Skeletal muscle mechanics: From mechanisms to function*, chapter 12: FEM-simulation of skeletal muscle: The influence of inertia during activation and deactivation, pages 207–223. John Wiley & Sons, Ltd, 2000.
- Cletus R. Mercier, Mack C. Shelley, Geneva H. Adkins, and Joyce M. Mercier. Age and gender as predictors of injury severity in broadside and angle vehicular collisions. *Journal of the Transportation Research Board*, 1693:50–61, 1999.
- R.J. Monti, R.R. Roy, H. Zhong, and V.R. Edgerton. Mechanical properties of rat soleus aponeurosis and tendon during variable recruitment in situ. *Journal of Experimental Biology*, 206:3437–3445, 2003.
- B. Moran, M. Ortiz, and C.F. Shih. Formulation of implicit finite element methods for multiplicative finite deformation plasticity. *International Journal for Numerical Methods in Engineering*, 29:483–514, 1990.
- D.A. Morrow, T.L.H. Donahue, G.M. Odegard, and K.R. Kaufman. Transversely isotropic tensile material properties of skeletal muscle tissue. *Journal of the Mechanical Behavior of Biomedical Materials*, 3: 124–129, 2010.
- J.C. Nagtegaal, D.M. Parks, and J.M. Rice. On numerically accurate finite element solutions in the fully plastic range. *Computer Methods in Applied Mechanics and Engineering*, pages 153–177, 1974.
- N. M. Newmark. A method of computation for structural dynamics. *ASCE Journal of Engineering Mechanics Division*, 85:67–94, 1959.
- NHTSA. *NHTSA Test Reference Guide II - Biomechanics Tests*. US DOT, 2014.
- M Noorkoiv, A Stavnsbo, P Aagaard, and A J Blazeovich. In vivo assessment of muscle fascicle length by extended field-of-view ultrasonography. *Journal of Applied Physiology*, 109(6):1974–1979, 2010.
- R.W. Ogden. *Non-Linear Elastic Deformations*. Dover Publications, New York, 1997.
- C. W. J. Oomens, M. Maenhout, C. H. van Oijen, M. R. Drost, and F. P. Baaijens. Finite element modelling of contracting skeletal muscle. *Philosophical Transactions of The Royal Society: Biological Sciences*, 358:1453–1460, September 2003.

- Cees W. J. Oomens, Daniel L. Bader, Sandra Loerakker, and Frank Baaijens. Pressure induced deep tissue injury explained. *Annals of Biomedical Engineering*, 43(2):297–305, 2014. ISSN 1573-9686.
- E. Otten. A myocybernetic model of the jaw system of the rat. *Journal of Neuroscience Methods*, 21: 287–302, 1987.
- Jos Oudeman, Aart J. Nederveen, Gustav J. Strijkers, Mario Maas, Peter R. Luijten, and Martijn Froeling. Techniques and applications of skeletal muscle diffusion tensor imaging: A review. *Journal of Magnetic Resonance Imaging*, 43(4):773–788, 2016.
- P. Pavan, C. Stecco, S. Darwish, A. Natali, and R. De Caro. Investigation of the mechanical properties of the plantar aponeurosis. *Surgical and Radiologic Anatomy*, pages 1–7, 2011. ISSN 0930-1038. 10.1007/s00276-011-0873-z.
- J.S. Petrofsky and C.A. Phillips. The influence of temperature, initial length and electrical activity on force-velocity relationship of the medial gastrocnemius muscle of the cat. *Journal of Biomechanics*, 14 (5):297–306, 1981.
- Celina Pezowicz and Maciej Glowacki. The mechanical properties of human ribs in young adult. *Acta of Bioengineering and Biomechanics*, 14(2):53–60, 2012.
- T. H. H. Pian and K. Sumihara. Rational approach for assumed stress finite elements. *International Journal for Numerical Methods in Engineering*, 20:1685–1695, 1984.
- T. H. H. Pian and P. Tong. Relations between incompatible displacement model and hybrid stress model. *International Journal for Numerical Methods in Engineering*, (22):173–181, 1986.
- G.H. Pollack. *Muscle and Molecules: Uncovering the Principles of Biological Motion*. Ebner and Sons, Seattle, 1990.
- Michael Anthony Puso. A highly efficient enhanced assumed strain physically stabilized hexahedral element. *International Journal for Numerical Methods in Engineering*, 49:1029–1064, 2000.
- S. Reese, P. Wriggers, and B.D. Reddy. A new locking-free brick element formulation for continuous large deformation problems. *Computers and Structures*, 75:291–304, 2000.
- Stefanie Reese. On a physically stabilized one point finite element formulation for three-dimensional finite elasto-plasticity. *Computer Methods in Applied Mechanics and Engineering*, 194:4685–4715, 2005.
- Jesse S. Ruan, Raed El-Jawahri, Saeed Barbat, Stephen W. Rouhana, and Priya Prasad. Impact response and biomechanical analysis of the knee-thigh-hip complex in frontal impacts with a full human body finite element model. *Stapp Car Crash Journal*, 2008.
- Robert Schneider. Simulation der nuss- operationstechnik am menschlichen brustkorb. Master’s thesis, Bauhaus Universität Weimar, 2012.
- S.H. Scott and G.E. Loeb. Mechanical properties of aponeurosis and tendon of the cat soleus muscle during whole-muscle isometric contractions. *Journal of Morphology*, 224(1):73–86, 1995.
- Carol Y. Scovil and Janet L. Ronsky. Sensitivity of a hill-based muscle model to perturbations in model parameters. *Journal of Biomechanics*, 39:2055–2063, 2006.
- David M. Shames, Anthony J. Baker, Michael W. Weiner, and S. Albert Camacho. Ca^{2+} -force relationship of frog skeletal muscle: a dynamic model for parameter estimation. *Modeling in Physiology*, 271:2062–2071, 1996.

- Tobias Siebert, Olaf Till, and Reinhard Blickhan. Work partitioning of transversally loaded muscle: experimentation and simulation. *Computer Methods in Biomechanics and Biomedical Engineering*, 17(3):217–229, 2014. PMID: 22515574.
- Tobias Siebert, Kay Leichsenring, Christian Rode, Carolin Wick, Norman Stutzig, Harald Schubert, Reinhard Blickhan, and Markus Böl. Three-dimensional muscle architecture and comprehensive dynamic properties of rabbit gastrocnemius, plantaris and soleus: Input for simulation studies. *PLOS One*, 10(6):1–20, 2015.
- J.C. Simo and F. Armero. Geometrically nonlinear enhanced strain mixed methods and the method of incompatible modes. *International Journal for Numerical Methods in Engineering*, 33:1413–1449, 1992.
- J.C. Simo and S. Rifai. A class of mixed assumed strain methods and the method of incompatible modes. *International Journal for Numerical Methods in Engineering*, 29:1595–1638, 1990.
- J.C. Simo, F. Armero, and R.L. Taylor. Improved versions of assumed enhanced strain trilinear elements for 3D deformation problems. *Computer Methods in Applied Mechanics and Engineering*, 110:61–112, 1993.
- Usha Sinha, Shantanu Sinha, John A Hodgson, and Reggie V Edgerton. Human soleus muscle architecture at different ankle joint angles from magnetic resonance diffusion tensor imaging. *Journal of Applied Physiology*, 110(3):807–819, 2011.
- L.A. Spyrou, M. Agoras, and K. Danas. A homogenization model of the voigt type for skeletal muscle. *Journal of Theoretical Biology*, 414(Supplement C):50 – 61, 2017. ISSN 0022-5193.
- Heiko Stark. *Die 3D-Architektur der Muskelfaszikel in ausgewählten Muskeln und ihre Relevanz zur Kraftentwicklung*. PhD thesis, Friedrich-Schiller-Universität Jena, 2008.
- Heiko Stark and Nadja Schilling. A novel method of studying fascicle architecture in relaxed and contracted muscles. *Journal of Biomechanics*, 43:2897–2903, 2010.
- I. D. Stein and G. Granik. Rib structure and bending strength: An autopsy study. *Calcified Tissue Research*, 20(1):61–73, 1976. ISSN 1432-0827.
- J. T. Stern. Computer modeling of gross muscle dynamics. *Journal of Biomechanics*, 7:411–428, 1974.
- J. D. Stitzel. *The Role of Local Material Properties in Modeling Fracture Tolerance of the Human Thorax*. PhD thesis, Virginia Polytechnic Institute and State University, 2003.
- R.K. Strumpf, J.D. Humphrey, and F.C.P. Yin. Biaxial mechanical properties of passive and tetanized canine diaphragm. *American Journal of Physiology*, 265:469–475, 1993.
- Damien Subit, Eduardo del Pozo de Dios, Juan Valazquez-Ameijide, Carlos Arregui-Dalmases, and Jeff Crandall. Tensile material properties of human rib cortical bone under quasi-static and dynamic failure loading and inuence of the bone microstucture on failure characteristics. *ArXiv e-prints*, March 2013.
- T. Sussman and K.-J. Bathe. A finite element formulation for nonlinear incompressible elastic and inelastic analysis. *Computers and Structures*, 26:357–409, 1987.
- Theodore D. Sussman. *On the finite element analysis of nonlinear incompressible solids*. PhD thesis, Massachusetts Institute of Technology, 1987.
- Chen-To Tai. A survey of the improper use of grad in vector analysis. *University of Michigan, Technical Report RL*, 909, 1994.

- Yohjiro Tamura and Masami Saito. A rheological motor model for vertebrate skeletal muscle in due consideration of non-linearity. *Journal of Biomechanics*, 35:1273–1277, 2002.
- C.Y. Tang, C.P. Tsui, B. Stojanovic, and M. Kojic. Finite element model of skeletal muscles coupled with fatigue. *International Journal of Mechanical Sciences*, 49:1179–1191, 2007.
- C.Y. Tang, G. Zhang, and C.P. Tsui. A 3d skeletal muscle model coupled with active contraction of muscle fibres and hyperelastic behaviour. *Journal of Biomechanics*, 42:865–872, 2009.
- T. Taniguchi, S. Yamamoto, A. Hayakawa, E. Tanaka, H. Kimpara, and K. Miki. Strain-rate and muscle-tonus dependence of mechanical properties of rabbit tibialis anterior muscle. In *Proceedings of ATEM: International Conference on Advanced Technology in Experimental Mechanics*, 2003.
- Robert L. Taylor. A mixed-enhanced formulation for tetrahedral finite elements. *International Journal for Numerical Methods in Engineering*, 47(1–3):205–227, 2000.
- A.F. Tencer, R. Kaufman, K. Ryan, D.C. Grossman, M.B. Henley, F. Mann, C. Mock, F. Rivara, S. Wang, J. Augenstein, D. Hoyt, and B. Eastman. Femur fractures in relatively low speed frontal crashes: the possible role of muscle forces. *Accident Analysis & Prevention*, 34:1–11, 2002.
- J. Teran, E. Sifakis, S.S. Blemker, V. Ng-Thow-Hing, C. Lau, and R. Fedkiw. Creating and simulating skeletal muscle from the visible human data set. *Transactions on Visualization and Computer Graphics*, 11:317–328, 2005.
- C.P. Thor and H.C. Gabler. The relationship between thoracic organ injuries and associated rib fractures. *Biomed Sci Instrum.* 2008;44:292-7., 44:292–297, 2008.
- Olaf Till, Tobias Siebert, Christian Rode, and Reinhard Blickhan. Characterization of isovelocity extension of activated muscle: A hill-type model for eccentric contractions and a method for parameter determination. *Journal of Theoretical Biology*, 255(2):176 – 187, 2008. ISSN 0022-5193.
- C.A. Truesdell and W. Noll. *The Nonlinear Field Theories*. Springer-Verlag, 1965.
- Araki Tsunetoshi, Oka Chiaki, and Tsutsumi Sadami. Injury mechanisms and clinical features of intra-abdominal seat belt injuries of motor vehicles. *Journal of the Japanese Association for the Surgery of Trauma*, 20(2):79–85, 2006.
- Arved Vain. The phenomenon of mechanical stress transmission in skeletal muscles. *Tartu University Press*, 2001.
- Marika J. Van der Horst. *Human head neck response in frontal, lateral and rear end impact loading*. PhD thesis, Technische Universiteit Eindhoven, 2002.
- B.J.J.J. Van der Linden. *Mechanical modeling of skeletal muscle functions*. PhD thesis, Universiteit Twente, 1998.
- J. L. Van Leeuwen. Optimum power output and structural design of sarcomeres. *Journal of Theoretical Biology*, 149:229–256, 1991.
- J.L. Van Leeuwen and W.M. Kier. Functional design of tentacles in squid: Linking sarcomere ultrastructure to gross morphological dynamics. *Phil. Trans. R. Soc. Lond. B*, 352:551–571, 1997.
- Johan L. Van Leeuwen, Jurriaan H. De Groot, and William M. Kier. Evolutionary mechanics of protrusible tentacles and tongues. *Netherlands Journal of Zoology*, 50:113–139, 2000.

- M. Van Looke, C.G. Lyons, and C.K. Simms. A validated model of passive muscle in compression. *Journal of Biomechanics*, 39:2999–3009, 2006.
- A.J. Van Soest. *Jumping from structure to control: a simulation study of explosive movements*. PhD thesis, Vrije Universiteit Amsterdam, 1992.
- C. Weichert, K. Leichsenring, T. Siebert, and M. Böl. Passive muscle behaviour - experimental and numerical investigations. *Proc. Appl. Math. Mech.*, 11:135–136, 2011.
- Dieter Weichert and Yavuz Başar. *Nonlinear continuum mechanics of solids*. Springer-Verlag, 2000.
- Jeffrey A. Weiss. *A constitutive model and finite element representation for transversely isotropic soft tissues*. PhD thesis, University of Utah, 1994.
- Jeffrey A. Weiss, Bradley N. Maker, and Sanjay Govindjee. Finite element implementation of incompressible, transversely isotropic hyperelasticity. *Computer Methods in Applied Mechanics and Engineering*, 135:107–128, 1996.
- Anthony S. Wexler, Jun Ding, and Stuart A. Binder-Macleod. A mathematical model that predicts skeletal muscle force. *IEEE Transactions on Biomedical Engineering*, 44(5):337–348, 1997.
- Benjamin Winkel and Axel Schleichardt. On the derivation of passive 3d material parameters from 1d stress-strain data of hydrostats. *Journal of Biomechanics*, 44:2113–2117, 2011.
- Jack M. Winters and Savio L.-Y. Woo, editors. *Multiple Muscle Systems - Biomechanics and movement organization*. Springer-Verlag, 1990.
- P. Wriggers. *Mixed Finite Element Methods - Theory and Discretization*, pages 131–177. Springer Vienna, Vienna, 2009. ISBN 978-3-211-99094-0.
- P. Wriggers and J. Korelc. On enhanced strain methods for small and finite deformations of solids. *Computational Mechanics*, 18:413–428, 1996.
- P. Wriggers and S. Reese. A note on enhanced strain methods for large deformations. *Computer Methods in Applied Mechanics and Engineering*, 135:201–209, 1996.
- P. Wriggers and S. Reese. On deficiencies of enhanced strain methods in large elastic compression states. *Computer Methods in Applied Mechanics and Engineering*, 1997.
- B. C. Yeo, S. T. und Lee. Equivalence between enhanced assumed strain method and assumed stress hybrid method based on the Hellinger-Reissner principle. *International Journal for Numerical Methods in Engineering*, 39:3083–3099, 1996.
- Narayan Yoganandan, Frank A. Pintar, Brian D. Stemper, Thomas A. Gennarelli, and John A. Weigelt. Biomechanics of side impact: Injury criteria, aging occupants, and airbag technology. *Journal of Biomechanics*, 40(2):227 – 243, 2007. ISSN 0021-9290.
- Can Ali Yücesoy. *Intra-, inter-, and extramuscular myofascial force transmission: A combined finite element modeling and experimental approach*. PhD thesis, Technische Universiteit Eindhoven, 2003.
- G. I. Zahalak and S.-P. Ma. Muscle activation and contraction: constitutive relations based directly on cross-bridge kinetics. *Journal of Biomechanical Engineering - Transactions of the ASME*, 112:52–62, 1990.

- Felix E. Zajac. Muscle and tendon: properties, models, scaling and applications to biomechanics and motor control. *Critical Reviews in Biomedical Engineering*, 17(4):359–411, 1989.
- Canhui Zhang, Dongdong Wang, Jianlin Zhang, Wei Feng, and Qian Huang. On the equivalence of various hybrid finite elements and a new orthogonalization method for explicit element stiffness formulation. *Finite Elements in Analysis and Design*, 43:321–332, 2007.
- Jun Zhang, Joan Lindsay, Kathy Clarke, Glenn Robbins, and Yang Mao. Factors affecting the severity of motor vehicle traffic crashes involving elderly drivers in ontario. *Accident Analysis & Prevention*, 32(1): 117 – 125, 2000. ISSN 0001-4575.
- O.C. Zienkiewicz and R.C. Taylor. *The finite element method for solid and structural mechanics*. Elsevier Butterworth-Heinemann, 6 edition, 2005.
- Peter Zioupos, Ulrich Hansen, and John D. Currey. Microcracking damage and the fracture process in relation to strain rate in human cortical bone tensile failure. *Journal of Biomechanics*, 41(14):2932–2939, 2008. ISSN 0021-9290.